Closeout for U.S. Department of Energy

Final Technical Report for University of Arizona grant
DOE Award Number DE-FG03-95ER40906
From 1 February 1995 to 31 January 2004
Grant title: Theory and Phenomenology of Strong and Weak High Energy Physics (Task A) and Experimental Elementary Particle Physics (Task B)
(DOE/ER/40906-1)

I Introduction

The following pages describe the high energy physics program at the University of Arizona which was funded by DOE grant DE-FG03-95ER40906, for the period 1 February 1995 to 31 January 2004. In this report, emphasis was placed on more recent accomplishments. This grant was divided into two tasks, a theory task (Task A) and an experimental task (Task B but called Task C early in the grant period) with separate budgets.

Faculty supported by this grant, for at least part of this period, include, for the theory task, Adrian Patrascioiu (now deceased), Ina Sarcevic, and Douglas Toussaint., and, for the experimental task, Elliott Cheu, Geoffrey Forden, Kenneth Johns, John Rutherfoord, Michael Shupe, and Erich Varnes.

Grant monitors from the Germantown DOE office, overseeing our grant, changed over the years. Dr. Marvin Gettner covered the first years and then he retired from the DOE. Dr. Patrick Rapp worked with us for just a few years and then left for a position at the University of Puerto Rico. Dr. Kathleen Turner took his place and continues as our grant monitor.

The next section of this report covers the activities of the theory task (Task A) and the last section the activities of the experimental task (Task B).

II.1 LATTICE GAUGE THEORY - Doug Toussaint

Doug Toussaint does research involving lattice gauge simulations of QCD. In the grant period now ending this included Tom Burch, a graduate student who has gone on to a postdoctoral position at Regensberg. Kostas Orginos (postdoc) was here from 1997-2000, and has now moved on to BNL. Eric Gregory (postdoc) is currently at Arizona, and is supported 1/3 by this grant and 2/3 by a grant from the DOE SciDAC program. Their major research effort is the use of numerical techniques to study QCD, the theory of the strong interaction. The goals of this work are to verify the theory by calculating properties of hadrons, to calculate hadronic matrix elements needed to extract fundamental parameters of the standard model, and to understand the behavior of QCD at high temperature and density, as in the early universe or relativistic heavy ion collisions or the interiors of neutron stars. Most of this work is done in the MILC (MIMD lattice computations) collaboration, which consists of eleven physicists at eight institutions. This group is carrying out computations on parallel machines at the DOE supercomputer centers at ORNL and NERSC, the NSF supercomputer centers, and on the new Linux cluster at Fermilab.

QCD simulations with three quark flavors

The main thrust of our research is lattice QCD including the effects of dynamical quarks. We have developed and implemented an improved form of the Kogut-Susskind, or staggered, lattice fermion formulation which eliminates the lowest order effects of the lattice discretization, and have used this formulation to generate lattices, or "snapshots of the gauge fields", at a range of quark masses. We have done this for a wide range of light quark masses at a lattice spacing of approximately 0.12 fm, and for three sets of quark mass at a lattice spacing of about 0.09 fm. Currently we are working to extend these simulations to a light quark mass of 0.1 times the strange quark mass. This is still a little over twice the real world light quark mass, but it is the smallest light quark mass for which large scale zero temperature simulations have been done. The MILC collaboration has used these lattices to study the hadron spectrum, decay constants of b-quark mesons, masses of exotic hybrid mesons, the structure of the QCD vacuum, the potential between a static quark and antiquark, and other quantities. Other groups, either independently or in collaboration with MILC members, have used these configurations to study charmonium and bottomonium spectroscopy, decays of heavy-light mesons, and the form factor of the nucleon.

We have made all but the most recent of these configurations available to the lattice community through the "gauge connection" archive at NERSC, from which they can be downloaded over the web.

Figure1 shows a compilation of several quantities for which the systematic errors are under good control computed on these lattices, divided by their experimental value[1]. These include our results and results of other groups using lattices generated the MILC collaboration. The inclusion of the dynamical quark effects improves agreement with experiment for these quantites (and therefore presumably for quantities that are not known experimentally).

The following table shows the status of our lattice generation with the Asqtad action as of July 2003. Runs marked with an "R" are still in progress. The two "coarse lattice" runs with a strange

quark mass $am_s = 0.03$ and the $28^3 \times 64$ run with $am_a = 0.01/0.05$ are being done with SciDAC resources at ORNL. The runs with $am_q = 0.005/0.05$ and $am_q = 0.0031/0.031$ are in progress, and we have applied for computer time at NERSC and at the PACI centers to continue these runs.

$am_{u,d}/am_s$	m_π/m_ρ	$10/g^2$	lats.	a/r_1
quenched	na	8.00	408 N	0.3762(8)
0.02/na	0.50	7.20	547	0.3744(11)
0.40/0.40	0.94	7.35	332 N	0.3766(10)
0.20/0.20	0.89	7.15	341 N	0.3707(10)
0.10/0.10	0.79	6.96	339 N	0.3730(14)
0.05/0.05	0.68	6.85	425 N	0.3742(15)
0.04/0.05	0.63	6.83	351 N	0.3765(14)
0.03/0.05	0.58	6.81	564 N	0.3775(12)
0.02/0.05	0.51	6.79	484 N	0.3775(12)
0.01/0.05	0.39	6.76	637 N	0.3846(12)
0.01/0.05*	0.39	6.76	219 R	0.3801(17)
0.007/0.05	0.34	6.76	474 N	0.3782(14)
0.005/0.05	0.30	6.76	149 R	0.3794(23)
0.03/0.03		6.79	186 R	
0.01/0.03		6.75	45 R	
quenched	na	8.40	415 N	0.2686(6)
0.031/0.031	0.67	7.18	496	0.2613(8)
0.0124/0.031	0.50	7.11	515 N	0.2697(10)
0.0062/0.031	0.38	7.09	521 N	0.2712(8)
0.0031/0.031*		7.08	R	

Parameters of the improved action simulations
$r_1 \approx 0.34 - 0.32$ fm
N = Posted at NERSC: `http://qcd.nersc.gov`
R = Currently running
Coarse lattices are $20^3 \times 64$ (* $28^3 \times 64$)
Fine lattices are $28^3 \times 96$ (* $40^3 \times 96$)

In order to handle the different machines, we have developed a portable QCD code where the machine specific communication routines are isolated in a single file, with a different version for each machine. This code has been made available to the lattice community, and has been used by several other collaborations.

Hadron spectrum with three quark flavors

The calculation of the masses of strongly interacting particles (hadrons) has been a long term objective of lattice gauge theorists. The masses of many of these particles are very well determined experimentally, so their calculation serves as a test of our methods and eventually of QCD.

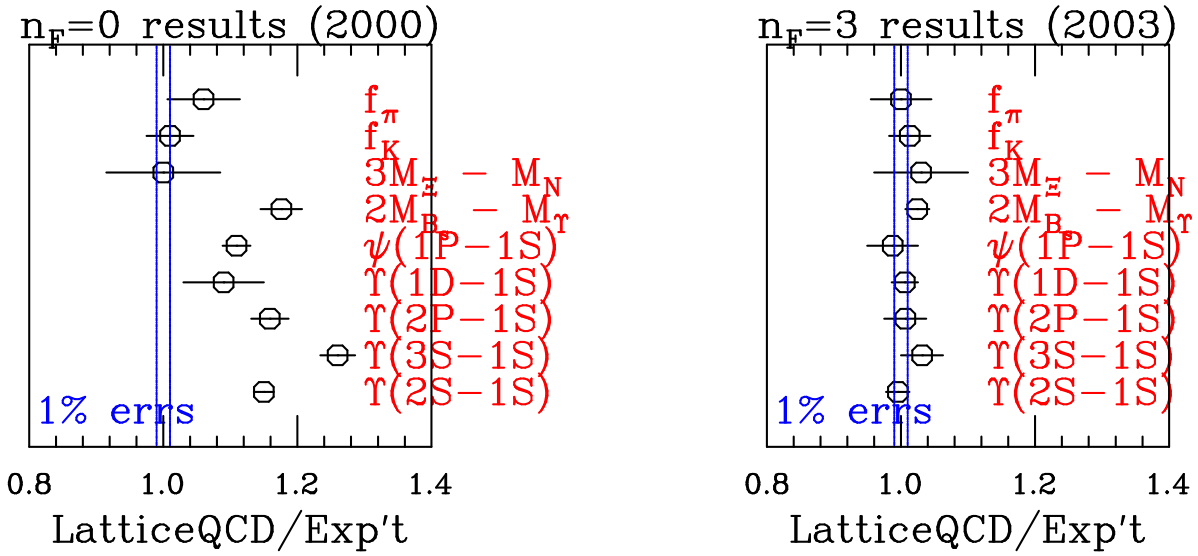

Figure 1: Improvement in consistency of some well understood QCD quantities with the inclusion of three flavors of dynamical quarks. (from hep-lat/0304004)

There are a number of particles, such as glueballs and particles with exotic quantum numbers, whose existence is predicted by QCD, but which have not yet been definitively observed. Accurate calculations of their masses and decay properties would aid experimentalists searching for them.

We are calculating the masses of the lightest hadron states, including those with strange valence quarks, as the improved-action lattices are generated. We have completed spectrum calculations on the $a \approx 0.12$ fm quenched and dynamical lattices. Among the interesting results of this study is the first simulation of a meson decay in full QCD, where we see an avoided level crossing between a 0^{++} meson state, the a_0, and a two meson $\pi + \eta$ state as a function of quark mass. This is shown in Fig. 3. A second important result is a demonstration the that mass ratio "J" suggested by the UKQCD collaboration is in better agreement with experiment when the effects of dynamical quarks are included, as illustrated in Fig. 2 The "fine" lattices that we are now generating, together with the spectrum computations on the older coarse lattices, will allow us to begin extrapolating to the continuum limit, and the results with a range of light quark masses will allow us to explore extrapolations to the chiral limit.

In principle, masses of excited states can be extracted from our propagators, but this is technically difficult. We are exploring these possibilities, and have reported preliminary results at the Lattice-03 conference.

Physics of light pseudoscalars:

Lattice computation of the masses and decay constants of light pseudoscalar mesons, namely the π and K, offers a unique opportunity to check our lattice methods to high precision, and to calculate phenomenologically important physical quantities that are difficult or impossible to obtain with controlled errors by other methods. Crucial to this is the inclusion of nondegenerate sea and valence quarks and the effects of taste symmetry breaking in chiral perturbation theory[2, 3], which allows us to use lattice data at unphysical quark masses to compute these quantities at the physical masses. Note that a further systematic error of previous lattice calculations — having

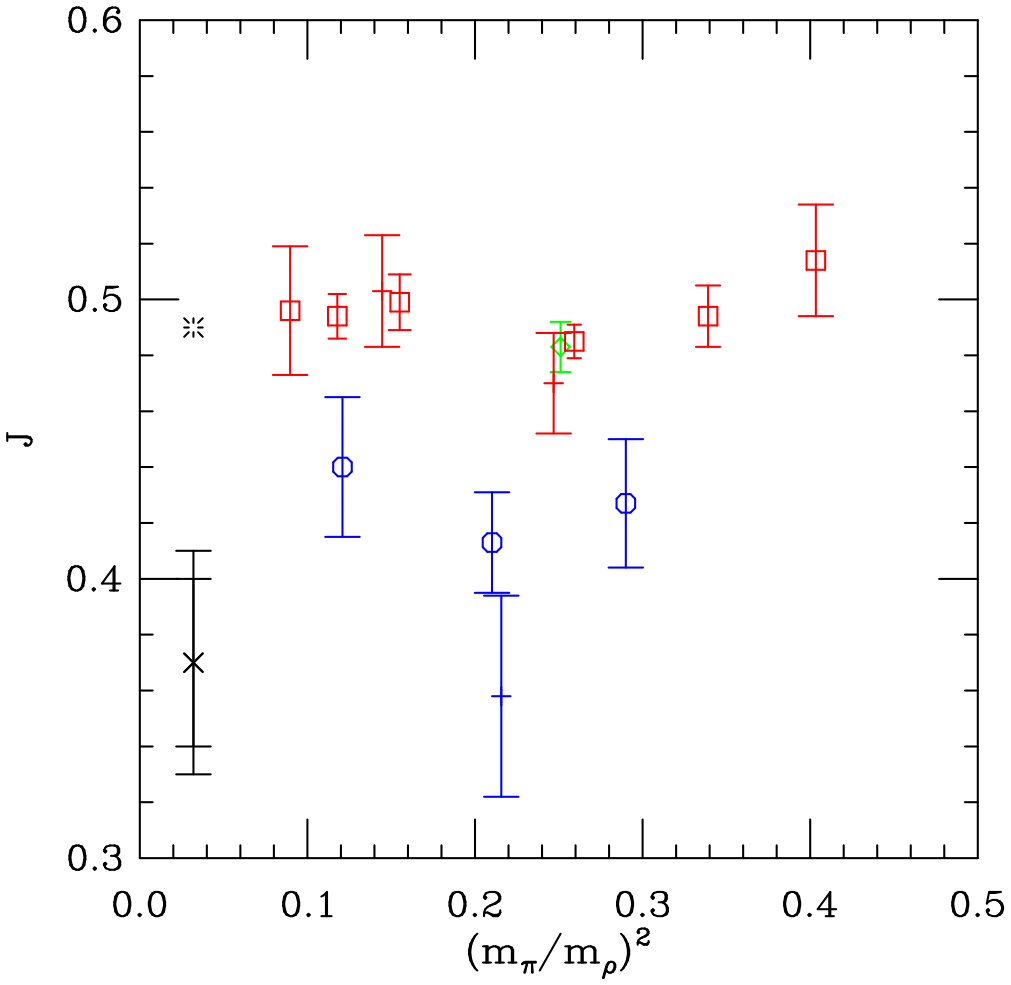

Figure 2: The mass ratio "J" in the quenched approximation and full QCD calculations. Red symbols are the three flavor results, and blue symbols are the quenched results. Octagons and squares are from the $a \approx 0.12$ fm runs, and the plusses from the $a \approx 0.09$ fm runs. The diamond is the two flavor run, using a non-dynamical strange quark with mass equal to its physical value. The burst is the real world value, and the cross is the UKQCD quenched value. The smaller error bar on the cross is the statistical error, and the larger the quoted systematic error.

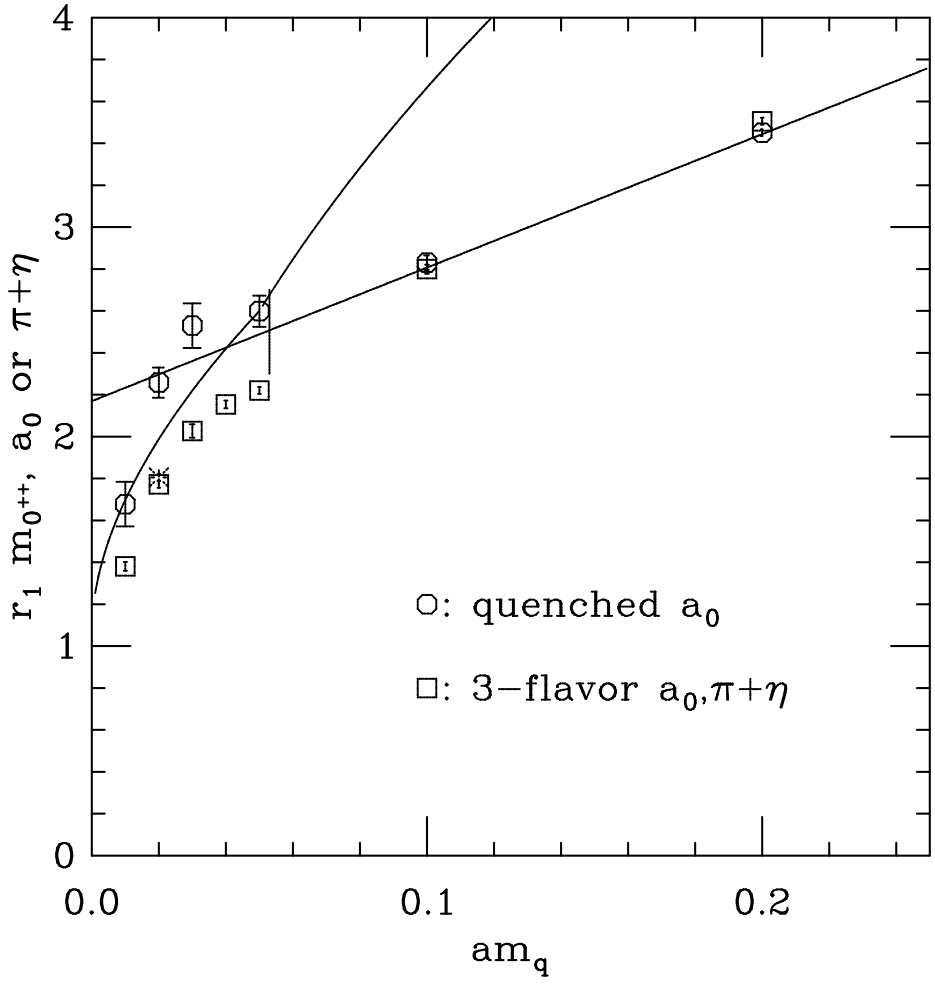

Figure 3: 0^{++} masses versus quark mass. The lighest fitted energy in the scalar channel. Octagons are quenched results, squares are three flavor results, and the burst is the two flavor run. The straight line is a crude extrapolation of the heavy quark points. The lower curved line is the $\pi+\eta$ mass estimate, as discussed in the text, and the upper line is a $\pi+\eta'$ mass estimate.

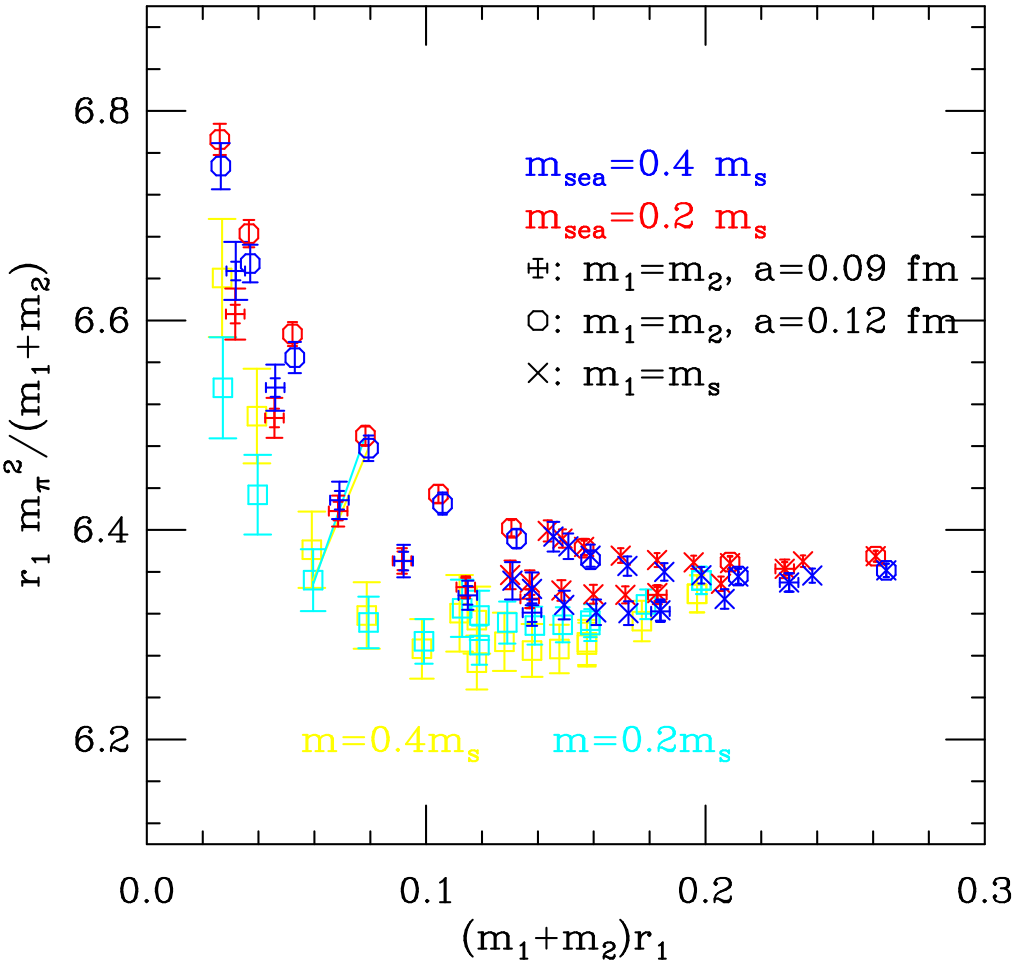

Figure 4: Pseudoscalar masses with $m_l \approx 0.3 m_s$ and $m_l \approx 0.2 m_s$ at $a \approx 0.12\,fm$ and $a \approx 0.09$ fm. A "point by point" extrapolation to $a = 0$ is also included.

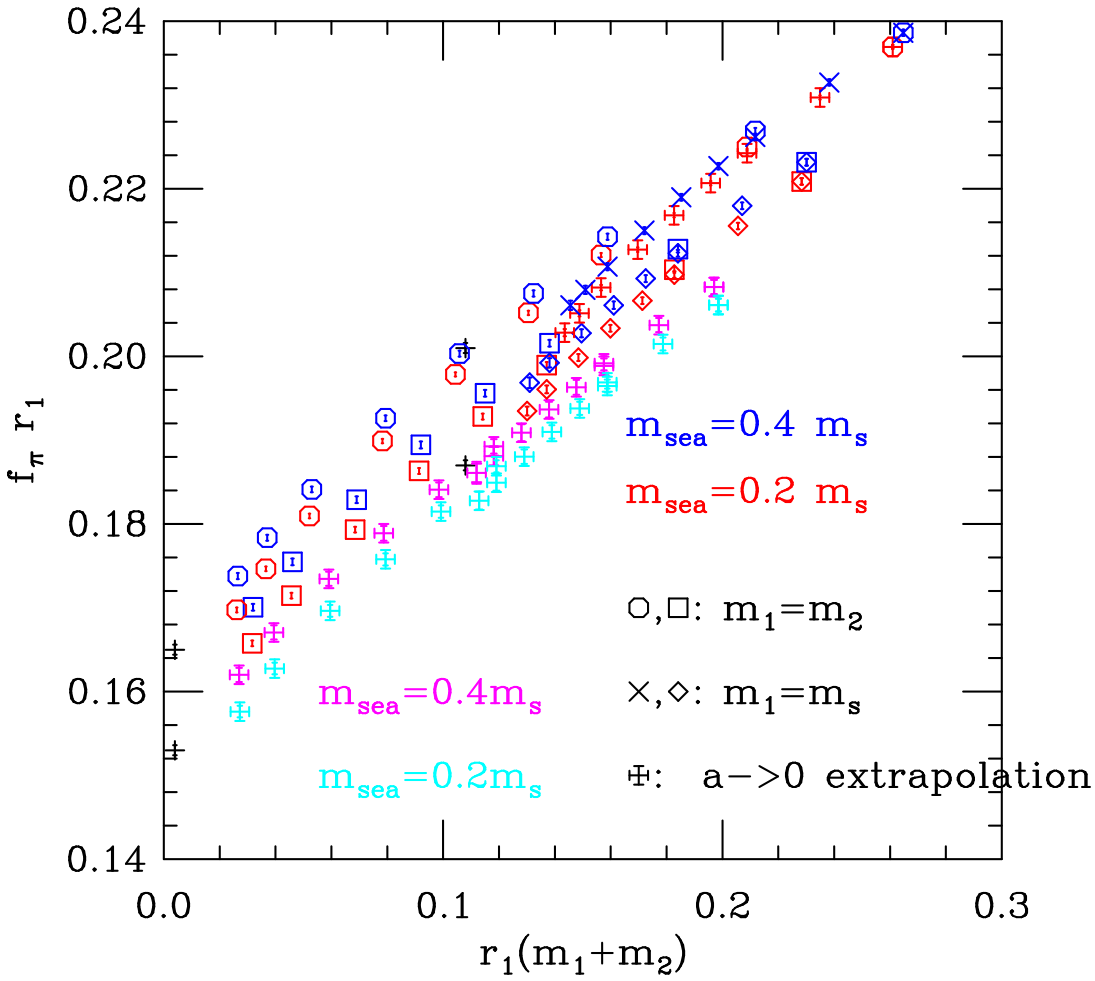

Figure 5: Decay constants with $m_l \approx 0.4m_s$ and $m_l \approx 0.2m_s$ at $a \approx 0.12\,fm$ and $a \approx 0.09$ fm. A "point by point" extrapolation to $a = 0$ is also included. Octagons are for $a \approx 0.12$ fm and squares for $a \approx 0.09$ fm. Magenta fancy plusses are an extrapolation to $a = 0$ at $m_{u,d} = 0.4m_s$ and cyan fancy plusses an extrapolation to $a = 0$ at $m_{u,d} = 0.2m_s$.

either the wrong number of dynamical (sea) quarks or no sea quarks at all — is absent for us, since we simulate with the physical number of light dynamical quarks.

Using the above method, we can presently compute the leptonic decay constants of the π and K mesons, f_π and f_K, to a total error of about 3%. The results agree with experiment at that level, providing good evidence that we understand and can control our errors. We can then use the same computational method to extract quark masses (the mass of the strange quark, m_s, and the average mass of the u and d quarks, $\hat{m}$) and several of the so-called Gasser-Leutwyler parameters [4], L_i. One of these in particular, the combination $2L_8 - L_5$, has very important phenomenological implications because its value determines whether a vanishing u quark mass is possible — which would be a solution of the strong CP problem [5]. Some current (preliminary) results for the quark masses and L_i have been presented at the Lattice-03 conference.

As an example, figures 4 and 5 show the effect of changing the lattice spacing on the pion mass and decay constant. For lattice spacings $a \approx 0.12$ fm and $a \approx 0.09$ fm we show results with light sea quark mass equal to 0.4 and 0.2 times the strange quark mass, again in units of r_1. Again, the horizontal axis is the sum of the valence quark masses in the meson. These figures also show a crude extrapolation to $a = 0$, made by taking a linear extrapolation in a^2g^2 using pairs of points with the same m_1/m_s. In Fig. 4 one pair of extrapolated points has diagonal lines showing the data points that were extrapolated to produce this point. In hindsight, the "strange quark mass" used in the $a \approx 0.09$ fm runs was smaller than that used in the $a \approx 0.12$ fm runs, as indicated by the fact that the finer lattice points fall slightly to the left of the corresponding coarse lattice points.

Hybrid meson masses and mixings

The fact that gluons carry color charge implies that they, like quarks, could be "valence" constituents of hadrons. In other words, we expect that the spectrum of QCD should contain glueballs and hybrids, or particles with both quarks and gluons as valence constituents. Hybrid mesons can have exotic quantum numbers, or J^{PC} combinations not possible with a quark-antiquark state. The lightest exotic hybrid meson is expected to have $J^{PC} = 1^{-+}$, and candidates for this meson have been found in recent experiments[6]. With staggered quarks we are able to work at smaller quark masses than with Wilson or Wilson-clover quarks, and in a multi-year project completed this year we have used this formulation to compute the mass of the lightest exotic hybrid meson[7, 8]. Figure 6 shows the mass of the exotic 1^{-+} hybrid meson in the quenched approximation in units of the string tension, along with the results of previous Wilson quark studies by the MILC collaboration [9], the UKQCD collaboration [10], the SESAM collaboration [11], as well as recent results from the Zhongshan University group [12] using Wilson quarks on an anisotropic lattice. We use the string tension σ to establish the lattice length scale and plot $M_{1^{-+}}/\sqrt{\sigma}$. Our results are consistent with the earlier results at heavier quark masses, but we are able to work at a quark mass half as large as previously used. In Fig. 6 we include the 1^{-+} experimental candidates $\pi_1(1400)$ and $\pi_1(1600)$ at the physical value of $(m_{\rm PS}/m_V)^2 = (m_\pi/m_\rho)^2 = 0.033$. These particles are represented by magenta and cyan vertical bars, offset slightly to the left or right for clarity, representing the range of values for the quenched string tension from 380 to 440 MeV.

We have also calculated hybrid meson propagators including the effects of three flavors of dynamical quarks, with light sea quark masses down to 0.4 times the strange quark mass. Here the

propagators show dramatic effects from the mixing of the hybrid state with two meson states — the states into which it might decay[8].

QCD Thermodynamics with Staggered fermions

At very high temperatures one expects to observe a phase transition or crossover from ordinary strongly interacting matter to a plasma of quarks and gluons. A primary physics goal of the Relativistic Heavy Ion Collider (RHIC), which recently began operation at the Brookhaven National Laboratory is the discovery and characterization of the quark-gluon plasma, a dominant state of matter in the early development of the universe, and a possible central component of neutron stars. In order to make such an observation, it is important to determine the nature of the transition, the properties of the plasma, including strange quark content, and the equation of state. Lattice gauge theory has proven to be the only source of *a priori* predictions about this form of matter in the vicinity of the phase transition, with our collaboration playing a major role in the worldwide effort. We are using our improved quark action to carry out a detailed study of these issues.

We have been doing thermodynamic studies at $N_t = 4$, 6, and 8, or lattice spacings of $1/4T$, $1/6T$ and $1/8T$ respectively. We are considering two cases: 1) all three quarks have the same mass, m_q; and 2) the two lightest quarks have equal mass, $m_{u,d}$, and the third quark has a mass equal to at that of the strange quark, m_s. We refer to these cases as $N_f = 3$ and $N_f = 2+1$, respectively. The $N_f = 3$ studies are being carried out on lattices with 4, 6 and 8 time slices, while the $N_f = 2+1$ studies are on lattices with 6 and 8 time slices. We have attempted to keep the physics unchanged as we vary the temperature by working along lines for which the ratio of the pseudoscalar to vector mass is constant. We have completed work with light quark masses $m_q = 0.6m_s$, $0.4m_s$, and $0.2m_s$ and are well underway at $0.1m_s$. These quark masses correspond to $m_pi/m_rho = 0.582$, 0.509, 0.392 and 0.298 respectively. For the quark masses studied to date we have found rapid crossovers, rather than bona fide phase transitions. We illustrate this fact in Fig. 7, where we show the triplet and strange quark number susceptibilities as a function of temperature for $N_f = 2+1$ with $m_q = 0.2m_s$. The sharp rise signals the crossover from confined behavior at low temperature to deconfined behavior at high temperature. The close agreement between the $N_t = 6$ and 8 results illustrates the excellent scaling properties of the Asqtad action, and indicates that our results are already close to those of the continuum. The quark number susceptibilities are of considerable experimental interest because they are related to event by event fluctuations in heavy ion collisions.

Portable Parallel code for QCD simulations

We have developed a family of codes for the study of QCD with Kogut-Susskind dynamical quarks, Wilson dynamical quarks, and in the quenched approximation. Our code runs on a wide variety of scalable parallel computers including the SP2 and SP3, Origin 2000, Exemplar, Compaq cluster at PSC, and Networks of workstations. It also runs on single processor workstations, which we use for much of our code development. The code can be obtained at `http://www.physics.utah.edu/~detar`. It has been our policy for some time to make our code and the large lattices we generate with it available to other lattice gauge theorists, and several other researchers have made use of the code.

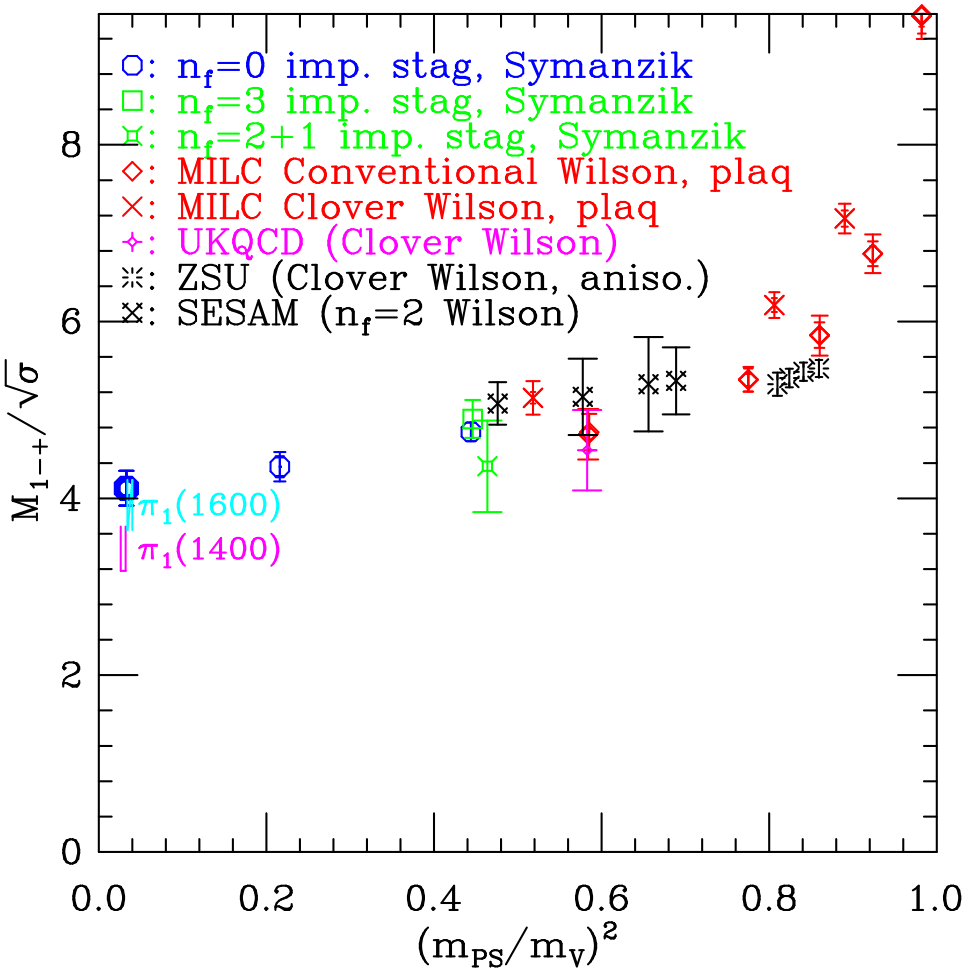

Figure 6: Summary of 1^{-+} hybrid meson mass predictions as a function of $(m_{\rm PS}/m_V)^2$. The bold octagon represents the linear extrapolation of $n_f = 0$ data to $(m_{\rm PS}/m_V)^2 = 0.033$. The improved staggered points are from this work, while the earlier data is from Refs [9, 10, 12, 11]

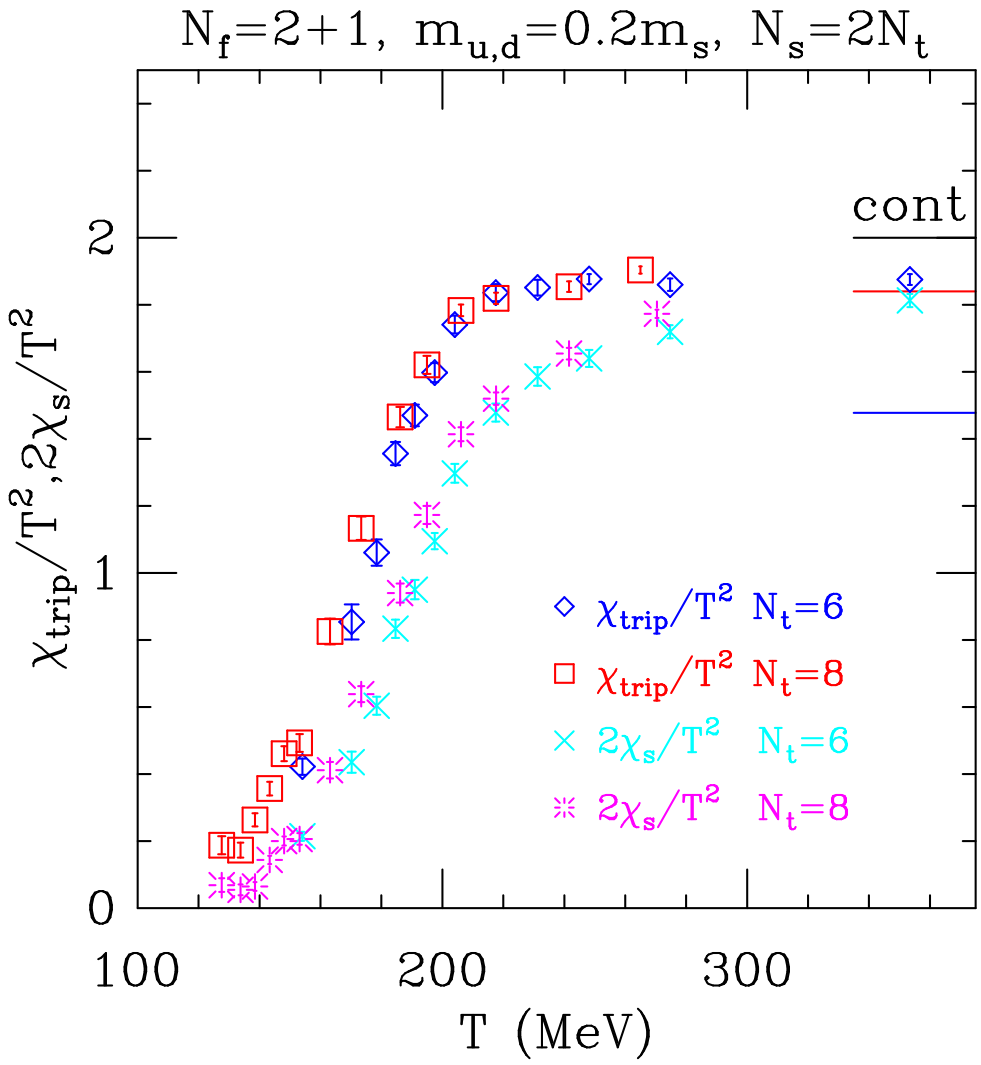

Figure 7: The triplet quark number susceptibility as a function of temperature for $N_f = 2+1$ with $m_q = 0.2m_s$ (red and blue points). We also plot twice the strange quark susceptibility (cyan and magenta points). The sharp rise signals the crossover from confined behavior at low temperature to deconfined behavior at high temperature. The close agreement between the $N_t = 6$ and 8 results illustrates the excellent scaling properties of the Asqtad action, and indicates that our results are already close those of the continuum.

The vanilla version of our code is written in C, and is highly portable. The only parts of the C code which are machine dependent are the communications routines. They are all stored in a single file. A version of this file exists for each machine on which our code runs. To move from one machine to another we simply link the appropriate communication file. Standard message passing libraries are especially interesting from the point of view of maintaining portable code, and we have implemented a version of the communications routines for both PVM and MPI.

In an effort spearheaded by Carleton DeTar, a revision of this code was completed in October 2002. Some improvements in algorithms were made, and many sections of the code were streamlined. Also, the compiling and linking of the codes on different machines is now done in a consistent way, so that a user can expect to download the code and run it successfully on a parallel machine.

Developments in the past grant period include a revision of the time-intensive conjugate gradient code to improve cache utilization by copying the required data into contiguous memory areas before beginning the inversion. A recent development is a variant of the conjugate gradient code which coalesces the two global reductions normally required in each iteration into a single global reduction of a three element array. This helps reduce the time lost to global reduction operations on large numbers of processors, which is a serious problem on the IBM SP machines.

Nonrelativistic hybrid mesons

Hybrid mesons with non-exotic quantum numbers will mix with $q\bar{q}$ mesons that have the same quantum numbers. When the quarks are heavy (b and maybe c), a non-relativistic approach (NRQCD) may be used to approximate the quark behavior. The Hamiltonian describing the evolution of the quark propagator is thus expanded in $1/m_q$:

$$H = \frac{-\vec{D}^2}{2m_q} + c_B \frac{-g}{2m_q} \vec{\sigma} \cdot \vec{B} + ..., \tag{1}$$

where $\vec{D}$ is the covariant derivative and $\vec{B}$ is the local chromo-magnetic field. Inclusion of the spin-dependent term allows the spin of the quark (or anti-quark) to flip with the emission (or absorption) of a gluonic excitation, thereby allowing a mixing of hybrid and quarkonium configurations with the same quantum numbers. We include the $\vec{\sigma} \cdot \vec{B}$ interaction at a single time slice ($t_{source} < t' < t_{sink}$) between a quarkonium source and hybrid sink. This provides us with a "perturbative" measurement of the off-diagonal matrix element of the Hamiltonian for the $q\bar{q}g$-$q\bar{q}$ two-state system on the lattice. Diagonalizing the two-state Hamiltonian, we thus find the amount of hybrid within the true ground state wavefunction[13]. In the past year we extended our earlier work on mixing of the 1^{--} bottomonium $b\bar{b}$ and $b\bar{b}g$ states, also looking at the 0^{+-} states[14]. The analysis was improved by using wall source operators as well as point sources and by using lattices with three different lattice spacings. We find that the mixing is fairly small, $\sin(\theta) \approx 0.06$, with the largest uncertainty being the renormalization of the coefficient of the $\vec{\sigma} \cdot \vec{B}$ term in the NRQCD hamiltonian. Eventually, experimental determination of the η_b mass will allow us to fix this coefficient and improve the accuracy.

Calibration of CCD detectors

As an interesting piece of cross disciplinary physics, it turns out that some of the simple techniques used in lattice physics can be applied to the problem of quickly calibrating charge coupled detectors for astromical applications[15]. (The CCD is a two dimensional lattice of pixels, with the logarithm of the pixel gain the scalar field.)

Topological susceptibility of the QCD vacuum

An important part of our understanding of QCD is the expected suppression of instantons by light sea quarks. MILC collaboration members together with Alistair Hart and Anna Hasenfratz have been studying this suppression on the three flavor lattices, and find results consistent with theoretical expectations in the continuum limit. Toussaint has only a minor part in this project.

Weak Matrix Elements in Quenched and Full QCD – MILC Collaboration

At the new B-factories at SLAC and KEK and at Fermilab and Cornell, a concerted experimental effort is underway to determine elements of the Cabibbo-Kobayashi-Maskawa (CKM) matrix through the mixings and decays of B mesons. Indeed one hopes that by tightly over-constrained these matrix elements, new physics beyond the Standard Model will be uncovered. However, the experimental results do not determine the CKM parameters without theoretical calculations of the effects of the strong interaction. At present, lattice QCD provides the only known approach to evaluate these effects from first-principles.

For the past several years, in an effort led by Claude Bernard, we have been involved in a study of the decays of pseudoscalar mesons with one light and one heavy quark[16]. The B with a heavy b quark and light u or d antiquark is such a meson, as is the B_s, in which the light quark is the strange quark. We are studying two types of decays: purely leptonic decays, e.g., $B \to l\nu_l$, and semileptonic decays, e.g., $B \to \rho l\nu_l$. Results of experimental measurements from these decays, combined with results from lattice calculations will provide crucial information about CKM matrix elements. As in the case of the decay constants, it is important to determine the effects of the dynamical quarks on the semileptonic form factors, and perform extrapolations to the physical mass of the up and down quarks. To this end, we are doing calculations of these form factors on both the quenched and three flavor lattices. Toussaint has only a minor role in this project.

References

[1] C.T.H. Davies *et al.*, hep-lat/0304004.

[2] C. Bernard and M. Golterman, Phys. Rev. D**49**, 486 (1994); S. Sharpe and N. Shoresh, Phys. Rev. D**62**, 094503 (2000).

[3] W. Lee and S. Sharpe, Phys. Rev. D 60, 114503 (1999); C. Bernard, Phys. Rev. D 65, 054031 (2001); C. Aubin *et al.*, Nucl. Phys. **B** (Proc. Suppl.) **119** (2003), 233 [hep-lat/0209066]; C. Aubin and C. Bernard, hep-lat/0304014 and hep-lat/0306026.

[4] See, for example, J. Gasser and H. Leutwyler, Nucl. Phys. **B250**, 465 (1985).

[5] D. B. Kaplan and A. V. Manohar, Phys. Rev. Lett. **56**, 2004 (1986); A. G. Cohen, D. B. Kaplan and A. E. Nelson, JHEP **9911**, 027 (1999) [arXiv:hep-lat/9909091].

[6] D. Alde *et al.*, Phys. Lett. B **205** (1988) 397; D. R. Thompson *et al.*, S.U. Chung *et al.*, Phys. Rev. D **60** (1999) 092001; A. Abele *et al.*, Phys. Lett. B **423** (1998) 175; A. Abele *et al.*, Phys. Lett. B **446** (1999) 349. G. S. Adams *et al.*, Phys. Rev. Lett. **81** (1998) 5760; E. I. Ivanov *et al.*, Phys. Rev. Lett. **86** (2001) 3977; Y. P. Gouz *et al.*, *In *Dallas 1992, Proc., HEP, vol. 1* 572-576.*

[7] C. Bernard *et al.*, hep-lat/0209097, to appear in Nucl. Phys. B(Proc. Suppl.).

[8] Lattice calculation of 1^{-+} hybrid mesons with improved Kogut-Susskind fermions, C. Bernard, T. Burch, C. DeTar, Steven Gottlieb, E.B. Gregory, U.M. Heller, J. Osborn, R. Sugar, D. Toussaint, hep-lat/0301024 , submitted to Phys. Rev. D.

[9] C. Bernard *et al.*, Phys. Rev. D **56** (1997) 7039; C. Bernard *et al.*, Nucl. Phys. (Proc. Suppl.) **60A** (1998) 61.

[10] P. Lacock, C. Michael, P. Boyle and P. Rowland, Phys. Lett. B **401** (1997) 308.

[11] P. Lacock and K. Schilling (SESAM collaboration), Nucl. Phys. (Proc. Suppl.) **73** (1999) 261.

[12] Z.H. Mei and X.Q. Luo, [arXiv:hep-lat/0206012]; to appear in Nucl. Phys. B (Proc. Suppl.)[hep-lat/0209049].

[13] Measurement of hybrid content of heavy quarkonia using lattice NRQCD T. Burch, K. Orginos and D. Toussaint, Phys. Rev. D **64** (2001) 074505.

[14] Hybrid configuration content of heavy S-wave mesons, T. Burch and D. Toussaint, hep-lat/0305008, submitted to Phys. Rev. D.

[15] R.M. Toussaint, J.W. Harvey and D. Toussaint, "Improved Convergence for CCD Gain Calibration Using SOR Techniques", to be published in Astronomical Journal.

[16] C. Bernard, P. Williams, S. Datta, Steven Gottlieb, C. DeTar, Urs M. Heller, C. McNeile, K. Orginos, R. Sugar and D. Toussaint, Phys. Rev. D **65** (2002) 014510. The MILC Collaboration: C. Bernard, S. Datta, T. DeGrand, C. DeTar, Steven Gottlieb, Urs M. Heller, C. McNeile, K. Orginos, R. Sugar and D. Toussaint, hep-lat/0206016, Phys. Rev. D **66**, 074505 (2002); C. Bernard, T. Burch, S. Datta, T. DeGrand, C. DeTar, S. Gottlieb, U.M. Heller, K. Orginos, R. Sugar and D. Toussaint, Nucl. Phys. (Proc.Suppl.) **106** (2002) 412.

[17] Y. Kuramashi *et al.*, Phys. Rev. Lett **72**, 3448 (1994).

[18] L. Venkataraman and G. Kilcup, hep-lat/9711006, Nucl. Phys. (Proc. Suppl.) **63** (1998) 826.

[19] C. Bernard *et al.* [MILC Collaboration], Phys. Rev. D **55**, 6861 (1997).

[20] F. Karsch, E. Laermann and A. Peikert, Phys. Lett. B **478**, 447 (2000)

II.2 PERTURBATION THEORY AND CONTINUUM LIMITS IN FIELD THEORIES - Adrian Patrascioiu

Before his death in March 2002, Adrian Patrascioiu carried out a program of nonperturbative studies of fundamental properties of QCD and of lower dimensional spin models that are generally considered to model features of QCD. This section of our report is taken from his progress description in our 2001 progress report.

Prof. Adrian Patrascioiu carried out a multi-year program to study certain properties of the most fundamental models employed by condensed matter and high energy physicists. The models range from Heisenberg ferromagnets, to Coulomb gases and Yang-Mills theories. The questions asked pertain to the true role of perturbation theory in such models, to their phase diagram and to the possible continuum limits which could be constructed. In a series of papers [1],[2] Patrascioiu pointed out that there are good reasons to suspect that the use of perturbation theory in such models can lead to false conclusions, such as the existence of the celebrated property of asymptotic freedom in QCD4. With regard to the phase structure of such models, Patrascioiu [3] argued that there should be no difference between the Abelian and non-Abelian models, contrary to common believes based on perturbative and/or topological differences.

These ideas were further developed in collaboration with Dr. E. Seiler, with whom Patrascioiu obtained several interesting results, which could have profound implications for particle physics. The important £ndings of the Patrascioiu-Seiler collaboration are the following: in 1991 they realized that for the 2D O(N) σ models, the existence of a massless phase might be proven rigorously. The basic idea followed from a new type of Monte Carlo updating proposed among others by Patrascioiu [4] to investigate this class models. It employs the Fortuin-Kasteleyn representation of the Ising model as a percolation process (a similar procedure was developed by U.Wolff) and it has proved remarkably successful in reducing critical slowing down. The important realization which occured in 1991 was that the same idea could be used to study rigourously the existence of a massless phase in all O(N) models in 2D. Namely the whole issue of the existence or absence of a mass gap could be reduced to the question whether the inverse image of a certain equatorial strip percolated or not. For the O(2) model and for certain discrete nonabelian models (the dodecahedron), Patrascioiu and Seiler proved rigorously the absence of exponential decay at low temperatures. These arguments were collected in a longer paper [5] which appeared in the Journal of Statistical Physics. A short version of the paper, containing the main results and tools used, appeared in Physical Review Letters [6]. The case of O(N) $N > 2$ was discussed by Patrascioiu in a separate paper [7] and it was concluded that although a rigorous proof could not be given at that time, it seemed rather impossible that the O(N) $N > 2$ models would exhibit exponential decay at low temperature. That those arguments were very sound is illustrated by the fact that they were and remain listed by the International Association of Mathematical Physics among the most important Open Problems in Mathematical Physics (www.iamp.org).

The next important £nding of Patrascioiu and Seiler was that in nonabelian models, even at short distances, perturbation theory produces ambiguos answers. More concretely, via concrete computations, they showed that in perturbation theory the expectation value of observables of compact lattice support (short distances in the continuum limit) depend upon the boundary condi-

tions used to reach the thermodynamic limit. This effect was shown to occur in both 2D nonlinear σ models and 4D gauge theories, but only in nonabelian models and starting at the one loop level. Since they could also show that expectation values of observables of compact support *must* be independent of the boundary conditions used to reach the thermodynamic limit, their result was a concrete demonstration that in nonabelian models perturbation theory may not be producing the correct asymptotic expansion. This result has direct physical consequences since, as Patrascioiu and Seiler showed, it affects the perturbative predictions regarding the running of the strong coupling constant $\alpha_s(Q)$. These important £ndings were reported in two papers which appeared in Physical Review Letters [8],[9].

In the same papers [8],[9] Patrascioiu and Seiler uncovered a new class of classical solutions, which they baptised superinstantons. They are 'super' in that in the in£nite volume limit their energy vanishes; and since they have as much entropy as the instantons, they dominate copiously the latter, whose energy is nonvanishing. These con£gurations were shown to exist in nonlinear σ models in $D \leq 2$ and in gauge theories in any D. In gauge theories superinstantons represent thin long loops carrying a magnetic ¤ux. The QCD vacuum at suf£ciently large β must be a gas of such loops, rather than the so called 'spaghetti vacuum'. In the 2D nonlinear models the existence of superinstantons renders obsolete the classic Kosterlitz-Thouless argument attributing the difference between the Abelian O(2) and the non-Abelian O(3) model to their different topological properties since both vortices and instantons are supressed with respect to superinstantons by energy considerations.

The next major development came in the spring of 2000, when, by combining rigorous results with some numerics Patrascioiu and Seiler showed that in 2D the O(3) nonlinear σ model must possess a massless phase for suf£ciently large β and that the existence of such a phase transition rules out rigorously the existence of asymptotic freedom in the massive continuum limit. They also provided a heuristic explanation for the mechanism which triggers the transition form a massive phase to a massless one: it is a change in the dominant con£gurations from a gas of instantons to a gas of super-instantons. The heuristic argument suggests the transition inverse temperature to be $\beta \approx \pi$, while the direct numerical identi£cation yields $\beta \approx 3.4$, in excellent agreement. These results were submitted for publication in Physical Review Letters [10] and will be described in more detail below under *Recent Results*.

The £ndings described above suggest that the beliefs that led to the Standard Model of particle physics may be wrong. Besides being of theoretical interest, these results have important experimental consequences, especially for particle physics. For instance if the 4D lattice QCD undergoes a decon£ning phase transition at zero temperature at nonzero lattice coupling, then, assuming the transition is of second order so that a massive continuum limit exists, that continuum limit would represent a QCD4 with a nontrivial £xed point. Consequently as one increased the energy Q, the strong coupling $\alpha_s(Q)$ would not go to zero as predicted by asymptotic freedom, but to some nonzero value. In February 1992, stimulated by a question raised by James Bjorken, Patrascioiu and Seiler used the best lattice data available at the time to estimate at what energy might the existence of such a nontrivial £xed point become experimentally detectable. To their surprise, the lattice numerics suggested 1 TeV or less. The implication was that already at LEP1, $\alpha_s(91)$ should be slightly larger than the value obtained by extrapolating low energy determinations (deep inelas-

tic) to the LEP1 energy via the perturbative formula. This prediction was published in February 1992 [11], before the £rst LEP1 results appeared in June 1992. In fact the measured value 0.124 was larger than the predicted value 0.113, but the difference was not considered statistically significant. Meanwhile, by changing the structure functions, the low energy prediction has been raised and the community is satis£ed that there is no discrepancy. In fact, as Bjorken emphasized, to test perturbation theory, one needs two accurate values of R (hadronic over leptonic cross-sections) because all other determinations of $\alpha_s(Q)$, such as event-shape, are in principle not calculable in perturbation theory and therefore polluted by uncontrolable nonperturbative effects.

Based partly on numerics, so far the results of Patrascioiu and Seiler can be considered only as indications that some fundamental ideas in particle physics, notably the validity of perturbation theory at short distances, may be wrong. However given the implications for particle physics of such a possibility, all efforts should be made to resolve this problem. A recent recognition of this impass is the offer by the Clay Mathematics Institute, headed by Alain Connes, Arthur Jaffe, Andrew Wiles and Edward Witten, of a prize of one million US dollars for a rigorous construction of the Yang-Mills theory in 4D. The understanding of the true properties of the 2D nonlinear σ models and in particular the validity of the perturbative predictions would represent an important step towards ellucidating the properties of the 4D Yang-Mills theories. The present research efforts of Patrascioiu are directed towards answering these questions.

1. Conformal properties of the critical theory.

One question raised by the scenario proposed by Patrascioiu and Seiler has to do with the conformal classi£cation of the proposed nonabelian critical theory. To understand this issue Patrascioiu and Seiler went back to the original arguments associating a conformal quantum £eld theory to a critical theory. In the process they discovered two gaps in the standard arguments. The £rst gap has to do with the problem of 'local cohomology': even though the divergence and curl of the current exist, the current itself may fail to exist as a bona£de operator. In two papers [12],[13] they provided a mathematically rigorous proof that in the 2D non-linear σ models that cannot happen; they also gave a concrete example of a model where this pitfall does arise. The second gap has to do with the possibility that in the continuum limit the current may become ultralocal. For the O(2) model Patrascioiu and Seiler ruled out this possibility by careful numerical studies. In the course of this investigation Patrascioiu and Seiler discovered a rigorous inequality which relates the current two point function to the lattice inverse coupling β. In particular it implies that if the massive phase terminates at a £nite β, then the massive continuum limit cannot be asymptotically free. This is a very important result as it relates the existence of asymptotic freedom in the massive continuum limit of the lattice model to the value of β_{crt}. Such a connection had never been made before and some people even wondered if in fact there was any contradiction between the existence of a massless phase in the O(N) $N \geq 3$ models and their being asymptotically free.

2. Is the 2D O(3) σ model asymptotically free?

One of the arguments usually given in favor of the standard scenario is the S-matrix prediction of Zamolodchikovs. That ansatz has been used by Hasenfratz, Maggiore and Niedermayer to pre-

dict the ratio Lambda/m and by Balog and Niedermaier to predict the continuum behavior of the spin and current 2-point functions as functions of p/m. Patrascioiu and Seiler decided to investigate numerically these predictions. They investigated the O(3) model on lattices ranging up to L=1200 and correlation lengths up to 167, their data representing the most accurate thermodynamic data available at the time for the O(3) model. The data showed a Λ/m lower by about 15% than the Hasenfratz et al prediction, however increasing steadily with the correlation length. Consequently they are also consistent with the Patrascioiu-Seiler scenario of a transition to a massless phase at £-nite β, which would require Λ/m to diverge. The data agreed very well with the Balog-Niedermaier prediction for the spin and current 2-point functions, however they agreed as well with the same quantities measured in another model Patrascioiu and Seiler studied, namely the dodecahedron spin model. But in the latter the massive high temperature phase must terminate at £nite β and hence the existence of asymptotic freedom seems unlikely. Therefore either the excellent numerical agreement of the continuum limits of the dodecahedron and O(3) models was accidental, or the O(3) model could not be asymptotically free. This very important observation was reported in Physics Letters B [14].

3. Deviations between the form factor prediction and the lattice model.

The excellent agreement between the lattice $O(3)$ data with both the form factor prediction and the dodecahedron spin model made no sense, since, as indicated above, the latter did not seem very likely to be asymptotically free. To resolve this apparent paradox, Patrascioiu and Seiler embarked on a very ambitious program of accumulating Monte Carlo data for the spin and current two point functions in both the $O(3)$ and dodecahedron spin models. To have a better chance of getting close to the continuum limit they investigated only the region $p/m < 13$ and studied thermodynamic lattices ($L/\xi \approx 14$ for ξ up to ≈ 65). They discovered small yet statistically signi£cant deviations between the continuum limit of the lattice $O(3)$ model and the form factor prediction. No such deviations were observed between the continuum limits of $O(3)$ and the dodecahedron models. These results, which at the time represented a benchmark in accuracy for the $O(3)$ model, were published in Physics Letters B [15].

4. Comparison of the form factor and lattice O(3) model.

Even though statistically signi£cant deviations in the current and spin two point functions (function of p/m) were observed, the agreement of the lattice continuum limit and the form factor prediction was impressively good. Thus a natural question to ask was whether this agreement was accidental and whether would persist for other quantities. An excellent observable to study was the renormalized coupling g_r. This quantity vanishes in a free £eld theory (it was studied by Kim and Patrascioiu [16] in their investigation of triviality of ϕ^4 in 4D) and thus it should really test whether the two approaches lead to the same S-matrix. Unfortunately there were no form factor predictions for g_r. Patrascioiu and Seiler convinced a few of their colleagues versed in the form factor approach that this was an important question and a large collaboration was formed (J.Balog, M.Niedermaier, F.Niedermayer, A.Patrascioiu, E.Seiler and P.Weisz). The collaboration decided to computed g_r analytically in the form factor approach, try to determine also its lattice continuum

value and compare the two values. Both projects turned out to be quite complicated. In the analytic computation not only was it hard to get some number, but since the result appeared as an in£nite sum, enough terms had to be computed to determine if the sum appeared to converge and how fast. On the other hand in the lattice model one had to be sure that both £nite cutoff and £nite volume effects are under control. The £rst set of results were published in 1999 [17] and revealed a very good agreement between the form factor value 6.770(17) and the lattice one 6.77(2).

5. Comparison of the form factor and lattice approach for other $O(N)$ models.

Although the agreement found was excellent, the last lattice value at $\xi \approx 122$ was a bit high. It was decided to reduce its error bar and also extend ξ to approximately 167. Moreover to test both the analytic techniques and the Monte Carlo programs, the collaboration decided to try to extend this comparison to the Ising and O(2) models. The analytic computations for the Ising model proved to be quite similar to those for $O(3)$ and a very accurate value could be obtained $g_r = 14.6975(1)$. The value obtained by the collaboration via the Monte Carlo study was also very accurate 14.69(2) and thus established the agreement of the two approaches beyond reasonable doubt. The main reason this feat could be accomplished for the Ising model was that it turned out that the cutoff effects were very small. On the contrary, re£ned data for the $O(3)$ data showed a value of g_r at $\xi \approx 167$ de£nitely above the original prediction of 6.77(2). That prediction was obtained via an adhoc extrapolation to the continuum limit, namely a £t linear in $1/\xi$ (the standard Symanzik £t did not accomodate the data). The trouble was that that £t worked quite well for $\xi \leq 65$ while the values at $\xi = 122$ and 167 were clearly above and suggesting a much larger continuum value. By analogy with the $O(2)$ model a £t involving $log(\xi)$ was tried, it worked well but it failed to predict a sharp continuum value for g_r. Thus it was no longer clear that in the $O(3)$ model the form factor value of g_r agreed with the continuum value of the lattice model. Those results, as well as preliminary form factor and lattice values for g_r in the $O(2)$ model were reported in Nuclear Physics B [18].

6. Nonabelian symmetry enhancement.

In an attempt to see again if some observable could be found where the apparent small differences between the form factor and lattice approach could be ampli£ed Patrascioiu investigated the renormalized spin two point function as a function of the physical distance. Given the dif£culty in £tting the lattice artefacts in g_r mentioned above, no attempt was made to extrapolate to the continuum limit via some £t. Instead very accurate (less that 0.3%) were produced for 6 values of ξ ranging from 11 to 167. The data suggested that for physical distances larger than 0.04 the continuum limit had been reached. It differed by about 2% from the 3 loop prediction with Λ/m £xed at the Hasenfratz-Maggiore-Niedermayer value and the overall normalization given by the Balog-Nidermaier form factor prediction. According to Balog and Niedermaier asymptotic scaling should not set in until $p/m \approx 10000$, hence from their point of view this discrepancy is not signi£cant. What should be signi£cant though is the comparison of these $O(3)$ data with the same quantity measured in the dodecahedron model. While at correlation length the renormalized spin 2 point function differs considerably (even in the sign of the lattice artefacts), by the time ξ reaches

≈ 121 the two sets of data agree within the estimated errors. It thus appears rather certain that the two models have the same continuum limit and that anonabelian discrete symmetry can be enhanced to a continuous one. While the enhancement of a discrete symmetry to a continuous one in abelian models (Z(N) to $O(2)$) has been known to occur for a long time, that something analogous can occur in nonabelian cases is a novel £nding. This result, which casts additional doubt on the existence of asymptotic freedom in the $O(3)$ model, has been submitted for publication in Physical Review Letters [19].

7. Absence of asymptotic freedom in the discrete nonabelian models.

The discrete nonabelian models undergo a freezing transition at nonzero temperature and hence should not be asymptotically free. Yet one would like to know for certain whether that is true or not. In the dodecahedron model that is hard to answer because the transition from the high temperature massive phase to the low temperature phase with long range order is not sharp - most likely an intermediate massless phase exists, as speculated long ago by Patrascioiu, Richard and Seiler [20]. The icosahedron model does not seem to possess such an extended massless phase and the phase transition from high to low temperature appears to be as sharp as in the Ising model. Patrascioiu and Seiler discovered this fact many years ago while numerically studying all regular polyhedra, but now, prompted by the question regarding existence of asymptotic freedom in such models, they returned to a detailed investigation of the icosahedron model. Firstly they veri£ed that its renormalized spin two point function agrees with that of $O(3)$ and the agreement at $\xi \approx 122$ is as good as that for the dodecahedron model. Secondly they determined the critical β by monitoring the apparent correlation length $\xi(L)$ versus the size of the lattice L. That resulted in a very sharp determination of $\beta_{crt} \approx 1.8094$. At the β_{crt} so determined they measured the Luescher-Weisz-Wolff coupling constant, which, in an asymptotically free theory, should vanish as the physical distance goes to 0. Clearly data taken right at β_{crt} correspond to 0 physical distance, hence if the continuum limit were asymptotically free, the Luescher-Weisz-Wolff coupling should vanish. The data show excellent scaling (indicating that the system is indeed critical), but that the continuum value of the coupling constant is nonzero. Thus, if both the dodecahedron and icosahedron models have the same continuum limit as the lattice $O(3)$ model, then the latter is clearly not asymptotically free. These result will be submitted for publication in Physical Review E [21].

8. Absence of asymptotic freedom in the 2D O(3) σ model.

As already indicated above, in the spring of 2000 Patrascioiu and Seiler combined rigorous mathematical results with some numerics to give conclusive proof that the 2D nonlinear σ model must possess a massless phase and that the existence of such a phase rules out the presence of asymptotic freedom in the massive continuum limit. The existence of a massless phase was demonstrated in the so called 'constrained' model: the ordinary nearest neighbour interaction is modi£ed so that for any two neighbouring spins at sites i and j, $s(i) \cdot s(j) < c$ for some c in [-1,1). The advantage of working with this model is that one can show rigorously that for any β, if at some c clusters of the set de£ned by the condition $s_z > \sqrt{(1-c^2)/2}$ have divergent mean size then the model must be massless. The Monte Carlo data produced by Patrascioiu and Seiler established

that fact beyond reasonable doubt since already at $\beta = c = 0$ (correlation length ≈ 52) clusters of the polar cap de£ned by $s_z > 0.95$ showed a mean size growing with the lattice size as $L^{2-\eta}$ for $\eta \approx 0.3$ (for L between 20 and 1280); moreover at £xed L the mean size of these clusters increased with c. While these studies could not determine precisely the value of c_{crt} it placed it between 0.5 and 0.7. The next step taken by Patrascioiu and Seiler was to verify that the continuum limit of this constrained model was the same as that of the standard action one. This was done by trying to match the L dependence of some continuum quantities in the two models (Luescher-Weisz-Wolff and renormalized coupling). It appears that the constrained model at $\beta = 0$ and $c = 0.61$ corresponds roughly to the standard model at $\beta = 3.4$, and this is the estimate of β_{crt} for the standard action O(3) model. As indicated in point (1) above, the rigorous inequality previously derived by Patrascioiu and Seiler rules out asymptotic freedom in the massive continuum limit if β_{crt} is £nite. Moreover the value 3.4 of β_{crt} also rules out the equivalence of the lattice continuum limit with the form factor approach (the latter requiring $\beta_{crt} > 5.5$). These results were submitted for publication in Physical Review Letters in ref.10. In that paper Patrascioiu and Seiler provided a heuristic explanation of the mechanism underlying this transition: a transition from an instanton to a superinstanton gas. Namely as they showed in their 1995 paper [8], the energy of a superinstanton vanishes as $1/log(L)$, while that of an instanton is a constant (4π). By choosing L to be the scale over which O(3) symmetry gets restored, one £nds that for $\beta > \pi$ superinstantons become dominant. Via the percolation argument, it is clear that a gas of superinstantons is massless, hence the change from a massive to a massless behavior.

9. Lattice artefacts and the running of the coupling constant.

A procedure to determine the nonperturbative running of the coupling constant was proposed by Lüscher, Weisz and Wolff in 1991. Their main idea was to use £nite size scaling to obtain informaation about the running of the coupling constant at smaller distances, not accessible by direct Monte Carlo measurements. They tried this procedure in the $2D$ $O(3)$ nonlinear σ model and claimed to have established the true running at physical distances as small as 0.0330(4). This feat was achieved by determining the *step scaling function*, the function describing how the coupling constant changes upon doubling the (linear) size of the lattice. To obtain this curve they investigated lattices of size L in the range $4 \leq L \leq 16$. Since what is really needed is the continuum value of the step scaling function, they extrapolated their values to the continuum limit using a Symanzik type of ansatz (quadratic polynomial in $\frac{1}{L^2}$). In this manner they showed that indeed at small distances the running agreed with the perturbative prediction. Intrigued by the apparent con¤ict between this £nding and the result mentioned in (7) above, indicating that the coupling constant did not go to zero at vanishing physical distance, Patrascioiu and Seiler decided to repeat the Lüscher, Weisz and Wolff study but on larger lattices. They investigated $20 \leq L \leq 160$ and found that the data did not corroborate the prediction made by Lüscher, Weisz and Wolff for the continuum value of the step scaling function. The data revealed a very complex (nonmonotonic) pattern for the cutoff effects, clearly violating the Symanzik ansatz. That is not really surprising because the Symanzik ansatz is inspired by perturbation theory and if in fact in the $O(3)$ model $\beta_{crt} < \infty$ perturbation theory should not be relevant for the critical behaviour of the model. The MC

data produced by Patrascioiu and Seiler suggest a running slower than predicted by perturbation theory. This is an important £nding since the Lüscher, Weisz and Wolff method has been applied also to *QCD*4, again taking data on small lattices and using a Symanzik ansatz to extrapolate to the continuum limit. There is good reason to expect that by going to larger lattices one may £nd a different running of $\alpha_s(Q)$. The results for the $O(3)$ model have been submitted for publication in Physical Review D [22].

10. Percolation and the existence of a soft phase in the classical Heisenberg model.

As already described in point (8) above, the combination of rigorous results with some unimpeachable numerics provided a very strong case that the standard lore about asymptotic freedom in nonabelian models must be wrong. Given the consequences of such a £nding, the paper reporting it was submitted for publication to Physical Review Letters [10]. In a typical display of unscienti£c behaviour, in spite of the fact that neither the referees nor anybody else could raise legitimate technical objections, the paper was temporarily rejected as being "too technical". A longer and more detailed presentation of the results was written and submitted for publication in Journal of Statistical Physics [23]. The agreement with the editor of Physical Review Letters is that once this technical paper is published, they will publish our letter.

11. Does the XY model have an integrable continuum limit?

The comparison of the form factor prediction with the continuum limit of the lattice models was extended to the $O(2)$ model by continuuing the collaboration with J.Balog, M.Niedermaier, F.Niedermayer, E.Seiler and P.Weisz. The $O(2)$ model is believed to be related to the Sine-Gordon model, which is integrable. By using the S-matrix of the latter model, the collaboration used the form factor approach to predict the value of several observables, namely the renomalized 4-point coupling at zero momentum, the renormalized spin and current 2-point functions at physical momenta p/m less than 50. The limitation in the range of the momentum comes from the fact that so far only the 1-3 and 2-4 form factors have been computed and the experience gained with $O(3)$ indicates that such an approximation can be valid only for suf£ciently small p/m. The project was very dif£cult because it also involved extensive numerics. Namely to control the continuum, thermodynamic limit, which is what the form factor predicts, one must control both £nite size effects and lattice artefcats. There exist no rigorous results regarding these issues, so the collaboration resorted to the accepted wisdom. For the £nite size effects, that came mostly from the 1/N expansion and for the lattice artefacts from the Kosterlitz prediction and its recent reinterpretation by Balog [24]. In confronting our Monte Carlo data with these theoretical expectations, we did not encounter a resounding success. For instance either because very accurate, our data were not accurate enough, or because the basic ansatz was wrong or because we were too far from the critical point (although our largest correlation length was 418) we could not really verify Balog's ansatz for the lattice artefacts. Modulo these uncertainties, we found general agreement between the form factor and the lattice continuum limit. These results were submitted for publication in Nuclear Physics B [25].

12. Testing asymptotic scaling and nonabelian symmetry enhancement.

A recent paper by Caracciolo et al [26] makes an interesting observation: if the standard perturbation scheme is correct, then the discrete nonabelian symmetry enhancement observed by Patrascioiu [19], by Patrascioiu and Seiler [21] and by Hasenfratz and Niedermayer [27] must be a temporary phenomenon and beyond correlation length ≈ 200 the agreement should start deteriorating. The autors reach this conclusion by pointing out that in perturbation theory, adding to the action an operator enjoying only a discrete symmetry constitutes a relevant perturbation. Hence either the stndard scenario regarding AF is incorrect and then a discrete nonabelian symmetry can be enhanced, or else there is no such enhancement. Patrascioiu and Seiler investigated this issue by studying the scaling curve of the correlation length itself in the $O(3)$ and icosaheron spin model. The £rst interesting thing they discovered was thati if one went to lattice sizes L as large as 640 in $O(3)$ the lattice artefacts were larger than originally reported [28] and did not obey the Symanzik ansatz. In fact they seem to obey the same law suggested by the investigation of the Lüscher-Weisz-Wolff coupling constant [22], that is a $\frac{1}{(log(L)+c)}$. The data suggested a continuum value of the scaling curve about 3Caracciolo et al [28]. In 1995, using this scaling curve, the latter claimed that one observed asymptotic scaling at correlation lengths of about 10^5. The new results of Patrascioiu and Seiler suggest that the correlation length is much larger than what AF predicts. In the regime investigated $20 \geq L \leq 640$, the data show an ever increasing agreement between the icosahedron and the $O(3)$ models and are consistent with the same continuum value for the two models. These important £ndings will be submitted for publication in Physical Review Letters [29].

References

[1] A.Patrascioiu, *Phys.Rev.Lett.* **54** (1985), 2292.

[2] A.Patrascioiu, *Phys.Rev.Lett.* **56** (1986), 1023.

[3] A.Patrascioiu, *Phys.Rev.Lett.* **58** (1987), 2286.

[4] A.Patrascioiu, *Nuovo Cim* **105B** (1990), 91.

[5] A.Patrascioiu and E.Seiler, *J.Stat.Phys.* **69** (1992), 573.

[6] A.Patrascioiu and E.Seiler, *Phys.Rev.Lett.* **68** (1992), 1395.

[7] A.Patrascioiu, *Existence of Algebraic Decay in Nonabelian Ferromagnets* **math-ph/0002028**.

[8] A.Patrascioiu and E.Seiler, *Phys.Rev.Lett.* **74** (1995), 1920.

[9] A.Patrascioiu and E.Seiler, *Phys.Rev.Lett.* **74** (1995), 1924.

[10] A.Patrascioiu and E.Seiler, *Absence of asymptotic freedom in nonabelian models.* **hep-th/0002153**.

[11] A.Patrascioiu and E.Seiler, *Expected Deviations from PQCD at 1 TeV or Less*, in **Results and Perspective in Particle Physics**, ed. M.Greco, Editions Frontiers 1992, p.125.

[12] A.Patrascioiu and E.Seiler, *Phys.Lett.* **B417** (1998), 123.

[13] A.Patrascioiu and E.Seiler, *Phys.Rev.* **E57** (1998), 111.

[14] A.Patrascioiu and E.Seiler, *Phys.Lett.* **B430** (1998), 314.

[15] A.Patrascioiu and E.Seiler, *Phys.Lett.* **B445** (1998), 160.

[16] J.-K.Kim and A.Patrascioiu, *Phys.Rev.* **D47** (1993), 2588.

[17] J.Balog, M.Niedermaier, F.Niedermayer, A.Patrascioiu, E.Seiler and P.Weisz, *Phys.Rev.* **D60:094508** (1999).

[18] J.Balog, M.Niedermaier, F.Niedermayer, A.Patrascioiu, E.Seiler and P.Weisz, *Nucl.Phys.* **B576** (2000), 517.

[19] A.Patrascioiu, *Quasi-asymptotic freedom in the two dimensional O(3) model.* **hep-lat/0002012**, to appear in *Euro Physics Letters*.

[20] A.Patrascioiu, J.-L.Richard and E.Seiler, *Phys.Lett.* **B254** (1991), 123.

[21] A.Patrascioiu and E.Seiler, *Discrete nonabelian enhancement and the absence of asymptotic freedom.* to appear in *Phys.Rev.* **D**

[22] A.Patrascioiu and E.Seiler, *Lattice artefacts and the running of the coupling constant.* submitted to *Phys.Rev.* **D**

[23] A.Patrascioiu and E.Seiler, *Percolation and the existence of a soft phase in the Heisenberg model*. submitted to *J.Stat.Phys.*

[24] J.Balog, *J.Phys.* **A34** (2001) 5237.

[25] J.Balog, M.Nierdermaier, F.Niedermayer, A.Patrascioiu, E.Seiler, P.Weisz, *Does the XY model have an integrable continuum limit?* , submitted to *Nucl. Phys.* **B**.

[26] S.Caracciolo, A.Montanari and A.Pelissetto, *Asymptotically free models and discrete nonabalian groups*, hep -lat/0103017

[27] P.Hasenfratz and F.Niedermayer, *Nucl.Phys.* **B596** (2001) 481.

[28] S.Caracciolo, R.G.Edwards, A.Pelissetto and A.D.Sokal, *Phys.Rev.Lett* **75** (1995) 1891.

[29] A.Patrascioiu and E.Seiler, *Testing asymptotic scaling and discrete nonabelian symmetry enhancement*, to be submitted to *Phys.Rev.Lett.*.

1 II. 3. Phenomenology of Strong and Weak Interactions at High Energies

The Phenomenology Group at the University of Arizona funded by the DOE grant DE-FG02-95ER40906 during the period of 1996-2004 consisted of Prof. Ina Sarcevic, postdoctoral fellows Hung-Jung Lu, Greg Mahlon (now faculty at Penn State) and Irina Mocioiu (now postdoc at Argonne/U of Chicago and faculty at Penn State), graduate students Peter Valerio (now faculty at Ravenscroft School), Sharada Iyer Dutta (now Research Assistant Professor at SUNY, Stony Brook) and Jeremy Jones, and undergraduate student Jeff Reifenberger (NASA/U of A Fellow, now graduate student at University of Illinois at Urbana-Champaign). In addition, the grant supported long-term visits of Prof. Sarcevic's former postdoc, Dr. Raj Gandhi (now permanent staff member at Harish-Chandra Research Institute). The projects over this eight year period ranged from ultrahigh neutrino interactions, neutrino oscillations in theories with large extra dimensions, black hole production at the LHC, ultrahigh energy tau neutrinos and their propagation, charm contribution to the "prompt" atmospheric muon and neutrino fluxes, propagation and energy loss of supersymmetric charged slepton produced in neutrino interactions as it traverses the Earth and ice, in the low-scale supersymmetric models, electroweak instanton-induced neutrino interactions, and interactions of relic supernova neutrinos with background neutrinos via new resonance interactions, as predicted in the low-scale models for neutrino masses.

PUBLICATIONS 1996-2004

1. "Domain Structure of a Disoriented Chiral Condensate from a Wavelet Prospective" (with Z. Huang, R. Thews and X. N. Wang), *Phys. Rev.* **D54**, 750 (1996).

2. "New Predictions for Neutrino Telescope Event Rates" (with R. Gandhi, C. Quigg and M.H. Reno), *Nucl. Phys.* **B78**, 475 (1996).

3. "Ultrahigh-Energy Neutrino Interactions", (with R. Gandhi, C. Quigg, and M.H. Reno), *Astropart. Phys.* **5**, 81 (1996).

4. "Wavelet View of a Disoriented Chiral Condensate", (with Z. Huang, R. Thews and X. N. Wang), in Proceedings of the *14th International Conference on Particles and Nuclei* (PANIC 96), pg 429.

5. "Ultrahigh-Energy Neutrino Interactions and Neutrino Telescope Event Rates", (with R. Gandhi, C. Quigg and M.H. Reno), in Proceedings of the *International Conference on Orbis Scientiae 1996: Neutrino Mass , Dark Matter, Gravitational Waves, Condensation of Atoms and Monopoles, Light-Cone Quantization*, eds. B. N. Kursunoglu, S. L. Mintz and A. Perlmutter (Plenum Pub.Co., New York, 1996) p. 115.

6. "Jet Quenching in the Opposite Direction of a Tagged Photon in High-Energy Ion Collisions", (with X. N. Wang and Z. Huang), *Phys. Rev. Lett.* **77**, 23 (1996).

7. "On the Nature of the EGRET Source at the Galactic Center", (with S. Markoff and F. Melia), *Astrophys. J. (Letters)* **489**, 47 (1997).

8. "What is the Brightest Source for Dilepton Emissions at RHIC?" (with D. Fein, Z. Huang and P. Valerio), *Phys. Rev.* **C56**, 1637 (1997).

9. "Detecting Neutrinos from AGNS and Topological Defects with Neutrino Telescope" (with R. Gandhi, C. Quigg and M.H. Reno), in Proceedings of the *1996 Annual Meeting of the American Physical Society, Division of Particles and Fields* (DPF'96), ed. K. Heller, J.K. Nelson and D. Reeder (World Scientific, Singapore, 1998), pg. 1240.

10. "Wavelet Perspective of a Disoriented Chiral Condensate", (with Z. Huang, R. Thews and X. N. Wang), in Proceedings of the *1996 Annual Meeting of the American Physical Society, Division of Particles and Fields* (DPF'96), ed. K. Heller, J.K. Nelson and D. Reeder (World Scientific, Singapore, 1998), pg. 1165.

11. "Wavelet Analysis of a Disoriented Chiral Condensate", (with Z. Huang, R. Thews and X. N. Wang), in Proceedings of the *Workshop on Multiparticle Correlations and Fluctuations*, eds. R.C. Hwa, W. Kittel, W.J. Metzger and D.J. Schotanus (World Scientific, 1997), p. 145.

12. "Physics at RHIC: the Search for the Quark Gluon Plasma", in Proceedings of the *XXVII International Symposium on Multiparticle Dynamics*, ed. G. Pancheri.

13. "Atmospheric Neutrinos from Charm", (with L. Pasquali and M.H. Reno) in Proceedings of the *Conference on Particle Physics and the Early Universe (COSMO 98)*, ed. D. Caldwell, Monterey, CA, November 15-20, 1998.

14. "Particle Cascades in Sgr A*: the Possibility of Observing their Gamma-Ray Signature", (with S. Markoff and F. Melia), in the Proceedings of the *184th Symposium of the International Astronomical Union: the Central Regions of Galaxy and Galaxies* (Kluwer Academic, Boston, 1998).

15. "Parton Distributions in Heavy Nuclei at small x", in the Proceedings of the Workshop on *Hard Parton Physics in High-Energy Nuclear Collisions*, Brookhaven National Laboratory, March 1-5, 1999.

16. "Neutrinos and Muons from Atmospheric Charm", (with L. Pasquali and M.H. Reno), in Proceedings of the *26th International Cosmic Ray Conference (ICRC 99)*, Vol. 2, pg. 244 (1999).

17. "Wavelet Analysis of a Disoriented Chiral Condensate", (with Z. Huang, R. Thews and X.N. Wang), in *The State of Physics at the End of the 20th Century*, eds. F. Cooper, I. Sarcevic, G. West and C.-I. Tan (World Scientific, Singapore, 1999), pg. 41.

18. "Parton Distributions in Nuclei at Small x", in the Proceedings of the *QCD and Multiparticle Dynamics*, XXIX International Symposium on Multiparticle Dynamics, eds. I. Sarcevic and C.-I. Tan (World Scientific, Singapore, 2000), pg. 255.

19. "Nuclear Parton Distributions in QCD", to appear in Proceeding of the *1999 Fall Meeting of the Division of Nuclear Physics of the American Physics Society*, Pacific Grove, CA, October 20-23, 1999.

20. "QCD Evolution of Gluon Density in a Nucleus", to appear in Proceeding of the *1999 Fall Meeting of the Division of Nuclear Physics of the American Physics Society*, Pacific Grove, CA, October 20-23, 1999.

21. "Partonic Picture of Nuclear Shadowing at Small x", (with Z. Huang and H.J. Lu), *Nucl. Phys.* **A63**, 79 (1998).

22. "Neutrino Interactions at Ultrahigh Energies", (with R. Gandhi, M.H. Reno and C. Quigg), *Phys. Rev.* **D58**, 093009 (1998).

23. "Secondary Decays in Atmospheric Charm Contributions to the Flux of Muon Neutrinos", (with L. Pasquali and M. H. Reno), *Astropart. Phys.* **9**, 193 (1998).

24. "Partonic Picture of Nuclear Shadowing at Small x", *Nucl. Phys.* **A638**, 531 (1998).

25. "Prompt Muons from Atmospheric Charm", (with L. Pasquali and M.H. Reno), *Phys. Rev.* **D59**, 034020 (1999).

26. "Muon and Muon Neutrino Fluxes from Atmospheric Charm", (with L. Pasquali and M. H. Reno), *Nucl. Phys.* **B70**, 361 (1999).

27. "High-Energy Emission from Relativistic Particles in Sgr A*", (with S. Markoff and F. Melia), *Astrophys. J.* **522**, 870 (1999).

28. "Searching for $\nu_\mu \to \nu_\tau$ Oscillations with Extragalactic Neutrinos", (with S. Iyer and M. H. Reno), *Phys. Rev.* **D61**, 053003 (2000).

29. "Tau Neutrinos Underground: Signals of $\nu_\mu \to \nu_\tau$ Oscillations with Extragalactic Neutrinos" (with S. Iyer Dutta and M. H. Reno), *Phys. Rev.* **D62**, 123001 (2000).

30. "Propagation of Muons and Taus at High Energies,", (with S. Iyer Dutta, M. H. Reno and D. Seckel), *Phys. Rev.* **D63**, 094020 (2001).

31. "High-Energy Neutrino Signals of Four Neutrino Mixing", (with S. Iyer Dutta and M.H. Reno), *Phys. Rev.* **D63**, 113001 (2001).

32. "Prompt Photons at RHIC", (with J. Jalilian-Marian and K. Orginos), *Phys. Rev.* **C63**, 041901 (Rapid Communications) (2001).

33. "Neutrino Flavor Oscillations without Flavor Mixing Angles", (with K. Dienes), *Phys. Lett.* **B500**, 133 (2001).

34. "Ultrahigh Energy Neutrinos, Small x and Unitarity", (with M.H. Reno, G. Sterman, M. Stratmann and W. Vogelsang), hep-ph/0110235, in APS/DPF/DPB Summer Study on the Future Particle Physics Snowmass 2001), eConf C010630:P508 (2001).

35. "Ultrahigh Energy Neutrinos in the Light of SNO and SuperK", (with S. Iyer Dutta and M.H. Reno), in the APS/DPF/DPB Summer Study on the Future Particle Physics Snowmass 2001 eConf C010630:P403 (2001).

36. "Working Group on QCD and Strong Interactions: Summary", E. L. Berger, S. Magill, I. Sarcevic, J. Jalilian-Marian, W. B. Kilgore, A. Kulesza, W. Vogelsang, R. V. Harlander, E. Kinney, R. Ball, B. Flaugher, W. Giele, P. Mackenzie, Z. Sullivan, C. Balazs, L. Reina, Wu-Ki Tung, N. Kidonakis, P. Nadolsky, F. Olness, G. Sterman, S. D. Ellis, Feb 2002. 34pp. in APS / DPF / DPB Summer Study on the Future of Particle Physics (Snowmass 2001), eConf C010630:P5001 (2001).

37. "Neutrinos in Theories of Large Extra Dimensions", in the Proceedings of the *XXXth Conference on High Energy Physics and Cosmology*, Coral Gables Conference 2001, December 12-16, 2001.

38. "Nuclear Effects in Prompt Photon Production at the LHC", (with J. Jalilian-Marian and K. Orginos), *Nucl. Phys.* **A700**, 523 (2002).

39. "On Black Hole Detection with OWL/AIRWATCH Telescope", (with Sharada Iyer Dutta and Mary Hall Reno), *Phys. Rev.* **D66**, 033002 (2002).

40. "Secondary Neutrinos from Tau Neutrino Interactions in Earth", (with Sharada Iyer Dutta and Mary Hall Reno), *Phys. Rev.* **D66**, 077328 (2002).

41. "High Energy Tau Neutrinos", (with S. Iyer Dutta and M.H. Reno), in AIP Conf. Proc. **624** 271 (2002).

42. " Impact of Extra Dimensions on the Standard Model", in the Proceedings of the *XXXVIth Recontres de Moriond, QCD and High Energy Hadronic Interactions*, ed. J. Tran Thanh Van (Editions Frontiers, 2002), pg. 357.

43. " Prompt Photons at RHIC and LHC", (with J. Jalilian and K. Orginos), in the Proceedings of the *XXXVIIth Recontres de Moriond, High Energy Hadronic Interactions*, ed. J. Tran Thanh Van (Editions Frontiers, 2002), pg. 401.

44. "Discovering New Physics with Ultrahigh Energy Neutrinos", to appear in the Proceedings of the *XXXIth Conference on High Energy Physics and Cosmology*, Coral Gables Conference 2002, December 10-15, 2002.

45. "Prompt Photon and Inclusive π^0 Production at RHIC and LHC", (with S.-Y. Jeon and J. Jalilian-Marian), *Nucl. Phys.* **A715**, 795 (2003).

46. "The Origin of Large p_T π^0 Suppression at RHIC", (with S.-Y. Jeon and J. Jalilian-Marian), *Phys. Lett.* **B562**, 45 (2003).

47. "Large p_T Inclusive π^0 Production in Heavy-Ion Collisions at RHIC and LHC", (with S. Y. Jeon and J. Jalilian-Marian), *Nucl. Phys.* **A723**, 467 (2003).

48. "Ultrahigh Energy Neutrinos", (with S. Iyer Dutta and M.H. Reno), *Int. J. Mod. Phys.* **A18**, 4085 (2003).

49. "Hadrons as Signature of Black Hole Production at the LHC", (with I. Mocioiu and Y. Nara), *Phys. Lett.* **B557**, 87 (2003).

50. "Neutrinos in Theories with Large Extra Dimensions", in *Cosmology and Elementary Particle Physics*, ed. B. N. Kursunoglu, S. L. Mintz and A. Perlmutter, AIP Conference Proceedings Vol 624 (Melville, New York 2002).

51. "Tau Neutrinos at EeV Energies", (with S. Iyer Dutta and M.H. Reno), in *Tsukuba 2003, Cosmic Ray*, (2003), pg. 1435.

52. "Photon Physics in Heavy Ion Collisions at the LHC", (with F. Arleo, P. Aurenche, F. Bopp, I. Dadic, G. David, H. Delagrange, D. d'Enterria, K.J. Eskola, F. Gelis, J.-Ph. Guillet, S. Jeon, Yu. Kharlov, O. Kodolova, P. Levai, J.H. Liu, I.P. Lokhtin, G.D. Moore, H. Niemi, A. Nikitenko,T. Peitzmann, P. Petreczky, J. Ranft, R. Rapp, P.V. Ruuskanen, K. Redlich, D.K. Srivastava, H. Takai, S. Tapprogge, M. Tokarev, I.N. Vardanyan, M. Werlen, P. Yepes), hep-ph/0311131, in *CERN Yellow Report on "Hard Probes in Heavy Ion Collisions at the LHC"*, 132 pages (2003).

53. "Ultrahigh Energy Neutrinos", (with S. Iyer Dutta and M.H. Reno, in the Proceedings of the *Neutrinos and Implications for Physics Beyond the Standard Model*, (World Scientific, Singapore, 2003), ed. R. Shrock, pg. 339.

54. "Tracing Very High Energy Neutrinos from Cosmological Distances in Ice", (with J. Jones, I. Mocioiu and M.H. Reno), *Phys. Rev.* **D69**, 033004 (2004).

55. "Tracing Very High Energy Neutrinos from Cosmological Distances in Ice", (with J. Jones, I. Mocioiu and M.H. Reno), to appear in the Proceedings of the *XXXII Conference on High Energy Physics and Cosmology*, eds. T. Curtright and S. Mintz, World Scientific, Singapore, 2004.

56. "Tracing Very High Energy Neutrinos from Cosmological Distances in Ice", (with J. Jones, I. Mocioiu and M.H. Reno), to appear in the Proceedings of the *XXVIIth International Symposium on Multiparticle Dynamics*, ed. W. Gary, World Scientific, Singapore, 2004.

57. "Tracing Very High Energy Neutrinos from Astrophysical Sources", (with J. Jones, I. Mocioiu and M.H. Reno), to appear in the Proceedings of the *Eighth Workshop on Non-perturbative QCD and Field Theory*, ed. B. Muller and C.-I. Tan, World Scientific, Singapore, 2004.

EDITTED VOLUMES (1996-2004)

1. Proceedings of the Workshop on the *State of Physics at the End of the 20th Century*, eds. F. Cooper, I. Sarcevic, G. West and C.I. Tan (World Scientific, Singapore, 1999) 255 pages.

2. Proceedings of the *XXIX International Symposium on Multiparticle Dynamics, QCD and Multiparticle Dynamics*, eds. I. Sarcevic and C.I. Tan (World Scientific, Singapore, 2000), 525 pages.

INVITED TALKS (1996-2004)

1. "Small-x Parton Densities from HERA and the Ultrahigh Energy Neutrino-Nucleon Cross Sections", presented at the *IVth International Workshop on Theoretical and Phenomenological Aspect of Underground Physics (TAUP '95)*, Toledo, Spain, September 1995.

2. "Ultrahigh Energy Neutrinos from Active Galactic Nuclei," presented at *XXIV Coral Gables Conference on Elementary Particle Physics and Cosmology*, Coral Gables, Florida, January 1996.

3. "Ultrahigh Energy Neutrino Interactions", presented at the Aspen Winter Conference on Particle Physics, Aspen, CO, January 1996.

4. "New Predictions for Neutrino Telescope Event Rates", presented at the Aspen Workshop on Neutrino Astrophysics, Aspen, Colorado, May 1996.

5. "Detecting Neutrinos from AGNS and Topological Defects with Neutrino Telescope", presented at the *1996 Annual Meeting of the American Physical Society, Division of Particles and Fields* (DPF'96), Minneapolis, MN, 10-15 Aug. 1996.

6. "Wavelet Perspective of a Disoriented Chiral Condensate", presented at the *1996 Annual Meeting of the American Physical Society, Division of Particles and Fields* (DPF'96), Minneapolis, MN, 10-15 Aug. 1996.

7. "Wavelet Analysis of a Disoriented Chiral Condensate", presented at the *Workshop on Multiparticle Correlations and Fluctuations*, Nijmegen, Netherlands, July 1-7, 1996.

8. "Neutrinos from Topological Defects Formed in the Early Universe", presented at the *Celebration of 25 Coral Gables Conferences and Their Impact on High Energy Physics and Cosmology Since 1964*, Miami Beach, Florida, January 23-26, 1997.

9. "Heavy-Ion Physics at RHIC", review talk, presented at the *Aspen Winter Conference on Particle Physics, Particle Physics Enters its Second Century*, January 19-25, 1997.

10. "Search for the Quark Gluon Plasma", review talk, presented at the *XXVII International Workshop on Multiparticle Dynamics*, Frascati, Italy, September 1997.

11. "Ultrahigh Energy Neutrino Interactions", presented at the *Workshop on Observing Giant Cosmic Ray Airshowers for $E > 10^{20} eV$ Particles from Space*, College Park, Maryland, November 1997.

12. "Partonic Picture of Nuclear Shadowing at Small x", presented at *Quark Matter '97*, Tsukuba, Japan, December 1997.

13. "Ultrahigh Energy Neutrinos", invited talk at *Dark Matter '98*, UCLA, February 1998, (had to cancel due to the knee injury).

14. "Ultrahigh Energy Neutrinos", invited talk at *Particles, Strings and Cosmology, PASCOS 98*, Boston, MA, March 21-28, 1998 (had to cancel due to the knee injury).

15. "Jet Quenching in High-Energy Heavy-Ion Collisions", presented at the *IVth Workshop on QCD*, Paris, June 1-8, 1998.

16. "Recent Progress in Multiparticle Dynamics", invited review at the *Vth Workshop on Nonlinear Correlations and Fluctuations '98*, Matrahaza, Hungary (June 1998).

17. "Interactions of Ultrahigh Energy Neutrinos", talk presented at the Workshop on *Neutrinos in Physics and Astrophysics: from Solar to Ultra-High Energy Neutrinos*, June 15-July 12, 1998, Aspen, CO.

18. "Ultrahigh Energy Neutrinos", talk selected for presentation at the *Xth International Symposium on Very High Cosmic Ray Interactions,* Laboratori Nazionali del Gran Sasso, Italy (July 1998). Conference, Rome, Italy (July 1998).

19. "Nuclear Shadowing Effect", invited talk at the *XXVII International Symposium on Multiparticle Dynamics*, Athens, Greece (September 1998), (cancelled due to visa problems).

20. "Can Neutrino Oscillations be Detected with Neutrino Telescope", invited talk at the *1998 Orbis Scientiae: Confluence of Cosmology, Massive Neutrinos, Elementary Particles and Gravitation (27th Coral Gables Conference on Particle Physics)*, Ft. Lauderdale, FL, December 17-20, 1998 (had to cancel due to knee injury).

21. "Ultrahigh Energy Neutrinos", invited talk at the *XVII th International Workshop Weak Interactions and Neutrinos (WIN99)*, Cape Town, South Africa, January 24-30, 1999 (had to cancel due to knee injury).

22. "Parton Distributions in Heavy Nuclei at small x", invited talk at the *Hard Parton Physics in High-Energy Nuclear Collisions*, RIKEN Workshop, Brookhaven National Laboratory, March 1-5, 1999.

23. "Parton Distributions in Nuclei at Small x", invited talk presented at the *XXIX International Symposium on Multiparticle Dynamics, QCD and Multiparticle Dynamics*, Providence, RI, August 9-13, 1999.

24. "Nuclear Parton Distributions in QCD", invited talk presented at the *1999 Fall Meeting of the Division of Nuclear Physics of the American Physics Society*, Pacific Grove, CA, October 20-23, 1999.

25. "QCD Evolution of Gluon Density in a Nucleus", presented at the *1999 Fall Meeting of the Division of Nuclear Physics of the American Physics Society*, Pacific Grove, CA, October 20-23, 1999.

26. "Searching for $\nu_\mu \to \nu_\tau$ Oscillations with Extragalactic Neutrinos", presented at the Aspen Winter Conference on *Way Beyond the Standard Models of Particle Physics and Cosmology*, Aspen Center for Physics, January 31-February 5, 2000.

27. "Tau Neutrino Appearance with Megaparsec Baseline", invited talk at the *Second Tropical Workshop on Particle Physics and Cosmology, Neutrino and Flavor Physics*, San Juan, Puerto Rico, May 1-6, 2000. (cancelled due to sickness)

28. "Neutrino Flavor Oscillations without Flavor Mixing", presented at the Aspen Workshop on *Neutrinos with Mass*, Aspen Center for Physics, June 26-July 16, 2000.

29. "Probing Extra Dimensions with Neutrinos", invited talk at the *XXIXth Coral Gables Conference on Particle Physics*, Fort Lauderdale, December 14-17, 2000 (cacelled due to sickness).

30. "Phenomenology of Extra Dimensions", invited talk to be presented at the *XXXVth Recontres de Moriond on QCD and High Energy Hadronic Interactions* Les Arcs, Savoie, France, March 17-24, 2001.

31. "Impact of Extra Dimensions on the Standard Model", invited talk presented at the *XXXVth Recontres de Moriond on QCD and High Energy Hadronic Interactions* Les Arcs, Savoie, France, March 17-24, 2001.

32. "Ultrahigh Energy Neutrinos in the Light of SNO and SuperK", invited talk presented at the *Snowmass 2001, Future of Particle Physics*, Snowmass, CO, July 1-21, 2001.

33. "Phenomenology of Hard Photon Production at RHIC and LHC", invited talk presented at the "LHC Workshop on Heavy-Ion Collisions", CERN, October 10-13, 2001.

34. "Neutrinos in Theories of Large Extra Dimensions", invited talk presented at the *XXXth Coral Gables Conference on Particle Physics*, Fort Lauderdale, December 11-16, 2001.

35. "Ultrahigh Energy Neutrinos in the Light of SNO and SuperK", invited talk presented at the 2002 Aspen Winter Conference on *Ultra High Energy Particles from Space*, Aspen Center for Physics, Aspen, CO, January 27- February 2, 2002.

36. "Neutrino Oscillations in Theories of Large Extra Dimensions", invited talk presented at the 2002 Aspen Winter Conference on *Ultra High Energy Particles from Space*, Aspen Center for Physics, Aspen, CO, January 27- February 2, 2002.

37. 'Inclusive π^0 Production at the LHC", talk presented at CERN Workshop on *Hard Probes in Heavy Ion Collisions at LHC*, March 11-15, 2002.

38. "Prompt Photon Production at RHIC and LHC", invited talk presented at the *XXXVI-Ith Recontres de Moriond, QCD and High Energy Hadronic Interactions*, Les Arcs, France, March 16-23, 2002.

39. "Neutrinos in Theories with Large Extra Dimensions", invited talk, Fifth European Meeting *From the Planck Scale to the Electroweak Scale, Supersymmetry and Brane Worlds*, Kazimierz, Poland, May 25 - 29, 2002.

40. "Solar Neutrino Mystery", invited talk, National Optical Astronomy Observatory, Tucson, Arizona, May 8, 2002.

41. "Production of Prompt Photons and Neutral Pions at RHIC and LHC", invited talk presented at Workshop on *QCD and Gauge Theory Dynamics in the RHIC Era*, ITP, Santa Barbara, June 26, 2002.

42. "Prompt Photon and Inclusive π^0 Production at RHIC and LHC", invited talk presented at *Quark Matter 2002*, Nantes, France, July 17-23, 2002.

43. "Hard QCD Processes at RHIC and LHC", invited talk to be presented at International Workshop on *Coherent Effects at RHIC and LHC: Initial Conditions and Hard Probes*, ECT, Trento, Italy, October 14-25, 2002.

44. "Black Hole Production in Neutrino Interactions", invited talk presented at the XXXI Coral Gables Conference on Cosmology and Elementary Particle Physics, Ft. Lauderdale, Florida, December 11-15, 2002.

45. "Discovering New Physics with Ultrahigh Energy Neutrinos", invited talk presented at Aspen Winter Conference on Particle Physics, *At the Frontiers of Particle Physics*, Aspen Center for Physics, Aspen, Colorado, Jan. 19 - 25, 2003.

46. "Photon and Pion Production at the LHC", invited talk to be presented at the *19th Winter Workshop on Nuclear Dynamics*, Breckenridge, CO, February 9-13, 2003.

47. "Tau Neutrinos in km^3 Detector", invited talk presented at *Neutrinos: Data, Cosmos and Planck Scale* Conference, KITP, Santa Barbara, March 3-8, 2003.

48. "Ultrahigh Energy Neutrinos as Probes of New Physics", invited talk presented at the Workshop on *Trends in Neutrino Physics*, Argonne National Laboratory, Argonne, IL, May 12-16, 2003.

49. "Prompt Photon and Inclusive Pion Production at RHIC and LHC", invited talk presented at the Workshop on *The First Three Years of Heavy Ion Physics at RHIC*, Institute for Nuclear Theory, University of Washington, Seattle, June 9-20, 2003.

50. "Black Hole Production in High Energy $p-p$ and Neutrino Collisions", invited talk, *10th Marcel Grossmann Meeting on General Relativity*, Rio de Janeiro, Brazil, July 20-26, 2003.

51. "Tracing Very High Energy Neutrinos from Cosmological Sources", invited talk presented at the *XXXII Coral Gables Conference on Cosmology and Elementary Particle Physics*, Ft. Lauderdale, Florida, December 17-21, 2003.

52. "Tracing Very High Energy Tau Neutrinos from Cosmological Sources", invited talk presented at the *Eighth Workshop on Non-perturbative QCD and Field Theory*, l'Institut Astrophysique de Paris, France, June 7-11, 2004.

53. "Tracing Very High Energy Neutrinos from Cosmological Sources", invited talk presented at the *XXXIVth International Symposium on Multiparticle Production (ISMD2004)*, Sonoma State University, Sonoma, California, July 26-August 1, 2004.

54. "Ultra High Energy Neutrinos", invited talk presented at the High Energy Conference *Celebrating 40 Years of Quarks, Cosmology and CP Violation*, Miami, Florida, December 15-20, 2004.

INVITED SEMINARS AND COLLOQUIA (1996-2004)

55. "The Ultrahigh Energy Neutrino Interactions: Implications for AGN Neutrino Searches", Astronomy Department, UCLA, Los Angelos, June 1995.

56. "Ultrahigh Energy Neutrino Interactions", LPTHE Universite Paris XI, Orsay, France, June 1995.

57. "On Detection of Neutrinos from AGNs and Topological Defects Formed in the Early Universe", Colloquium, Aspen Center for Physics, June 1996.

58. "Physics at RHIC", Physics Department, University of Arizona, January 1997.

59. "Prospects of Physics at RHIC: The Search for the Quark-Gluon Plasma", CEBAF, Virginia, January 1997.

60. "Prospects for Detection of Ultrahigh Energy Neutrinos from AGNs and from Topological Defects formed in the Early Universe", Colloquium, College of William and Mary, Virginia, February 1997.

61. "Prospects for the Detection of Extragalactic Neutrinos", Department of Physics and Astronomy and Bartol Institute, University of Delaware, May 1997.

62. "Prospects of Physics at RHIC and LHC: the Search for the Quark Gluon Plasma", LPTHE Universite Paris XI, Orsay, France, September 1997.

63. "High Energy Neutrino Astrophysics", colloquium, Auburn University, Auburn, Alabama, October, 1997.

64. "Ultrahigh Energy Neutrinos", Physics Department, Brown University, Providence, RI, April, 1998.

65. "Prospects of Physics at RHIC: the Search for the Quark-Gluon Plasma", Physics Department, SUNY Stony Brook, March 1999.

66. "A Novel Concept for Detecting $\nu_\mu \to \nu_\tau$ Oscillations with Extragalactic Neutrinos", seminar, UCLA, March 2000.

67. "A Novel Concept for Detecting $\nu_\mu \to \nu_\tau$ Oscillations with Extragalactic Neutrinos", seminar, Fermilab, May 2001.

68. "Particle Astrophysics with High Energy Neutrinos", invited colloquium, Physics Department, Utah State University, December 4, 2001.

69. "Solar Neutrino Mystery", invited talk, National Optical Astronomy Observatory, Tucson, Arizona, May 8, 2002.

70. "Ultrahigh Energy Neutrinos as Probes of New Physics", invited joint Particle Physics/Astrophysics seminar, University of California, Irvine, March 12, 2003.

71. "Ultrahigh Energy Neutrinos as Probes of Physics Beyond the Standard Model", seminar, High Energy Theory Group, Physics Department, Brookhaven National Laboratory, Upton, NY, May 16, 2003.

CONFERENCES AND WORKSHOPS ORGANIZED (1996-2004)

1. "Interface of Soft and Hard Processes in QCD", Aspen Center for Physics, June 2-23, 1996 (organizers: I. Sarcevic, L. Durand and Chung-I Tan).

2. "The State of Physics at the End of the 20th Century", Santa Fe, NM, October 23-26, 1996 (organizers: F. Cooper, I. Sarcevic and G. West).

3. "Frontiers in Particle Physics", Aspen Winter Conference on Particle Physics, January 25-31, 1998 (organizers: I. Sarcevic and W. C. Louis).

4. "XXIX International Symposium on Multiparticle Dynamics, *QCD and Multiparticle Dynamics*", Providence, RI, August 9-13, 1999 (organizers: I. Sarcevic and Chung-I Tan).

5. "Neutrinos with Mass", Aspen Center for Physics, Aspen, CO, June 26-July 16, 2000 (organizers: M. Goodman, J. Learned, M.H. Reno and I. Sarcevic)

6. American Physical Society, Division of Nuclear Physics, DNP 2003 Meeting October 23-27, 2003 (organizers: B. Barrett, I. Sarcevic and B. Van Kolck).

7. "QCD, Confinement and Heavy-Ion Collisions", Workshop preceding the American Physical Society, Division of Nuclear Physics, DNP 2003 Meeting October 22, 2003 (organizers: I. Sarcevic and R.L. Thews).

PHENOMENOLOGY AT HIGH ENERGIES

Ina Sarcevic

Ultrahigh-Energy Neutrino Interactions

(with R. Gandhi, C. Quigg and M.H. Reno), *Astropart. Phys.* **5**, 81 (1996); *Nucl. Phys.* **B78**, 475 (1996)

The Active Galactic Nuclei (AGN) are potentially the most powerful sources of high-energy neutrinos. With typical luminosities in the range 10^{42} to 10^{48} erg/s, AGNs are believed to be the most powerful individual sources of radiation in the Universe. These extragalactic point sources are also considered as prodigious particle accelerators presumably powered by the gravitational energy of matter spiraling in to a supermassive black hole, though the mechanism responsible for the conversion of gravitational energy to luminous energy is not presently understood. Recent detection of energetic photons ($E_\gamma \sim 100$ MeV) from about 40 AGNs by the EGRET collaboration [2] and of TeV photons from Mkn 421, Mkn 501 [3] and most recently from 1ES2344+514 by the Whipple collaboration [4] have created new excitement in the field of high-energy gamma-ray physics. If the observed photons are decay products of π^0s produced in hadronic interactions in the disk surrounding the AGN, then AGNs are also powerful sources of ultrahigh-energy (UHE) neutrinos [2]. Unlike photons, which are absorbed by a few hundred gm/cm^2 of material, TeV neutrinos have interaction lengths on the order of 250 kt/cm^2 and thus can provide a direct window to the most energetic processes in the universe.

The advantage of the long interaction length translates to a challenge in the detection of neutrinos. Interaction rates increase with energy, but the fluxes of UHE neutrinos are steeply falling functions of neutrino energy. Cerenkov detection of muons from interactions of muon neutrinos in the rock or ice surrounding the detector is feasible[3]. More difficult is the detection of charged-current interactions of electron neutrinos. Large-area air shower arrays or large volume underground detectors may be adequate for the detection of electron neutrinos, especially near the W-boson resonance in $\bar{\nu}_e e$ collisions. Theoretical calculations of the neutrino-nucleon and neutrino-electron cross sections are instrumental in evaluating event rates for neutrino telescopes.

Recently we have completed calculation of charged current and neutral current cross sections for energies up to 10^{21} eV [4] obtained using new parton distributions measured in ep collisions at HERA [5]. Detection of UHE neutrinos depends on these cross sections and on the neutrino fluxes from UHE neutrino sources. We have compared event rates for muon neutrino conversions to muons with earlier results based on older parton distribution functions [8]. We have also obtained results for contained events with higher threshold energies.

A variety of sources may contribute to the neutrino flux at the surface of the Earth. Three types of sources are discussed here: atmospheric neutrinos from cosmic-ray interactions in the atmosphere, neutrinos from active galactic nuclei, and cosmic neutrinos from extragalactic cosmic ray interactions with the microwave background radiation. Model predictions for neutrino fluxes from these three types of sources are shown in Figure 1 [4]. Atmospheric

neutrinos[15] (ATM), while interesting in their own right, mask extraterrestrial sources for $E_\nu < 1$ TeV. Consequently, we restrict our discussion to neutrino energies above 1 TeV.

The TeV photons observed by Whipple collaboration[3] may be byproducts of hadronic cascades initiated by the protons generated within the AGN accretion disk of gas, or in the jets, which interact with matter or radiation in the AGN disk, to produce pions whose decay products include both photons and neutrinos. The structure of the corresponding hadronic cascade is:

$$\begin{aligned} pp &\rightarrow \pi + X \\ p\gamma &\rightarrow \pi + X \\ np &\rightarrow \pi + X \\ \pi^0 &\rightarrow \gamma + \gamma \\ \pi^\pm &\rightarrow \nu_\mu + \mu \\ \mu &\rightarrow \nu_\mu + \nu_e + e \end{aligned}$$

If charged and neutral pions are produced in equal proportions and photons originate in hadronic cascades, simple counting leads to equal fluxes of photons and $\nu_\mu + \bar{\nu}_\mu$. The flux of $\nu_e + \bar{\nu}_e$ equals half of the flux of $\nu_\mu + \bar{\nu}_\mu$. The observed photon energy spectrum is a power-law with[3]

$$\frac{dN_\gamma}{dE_\gamma} \sim E_\gamma^{-2}$$

for 100 MeV $\leq E_\gamma \leq 2$ TeV, and the same for neutrinos. We have chosen three representative fluxes of neutrinos from AGN, each corresponding to the diffuse flux integrated over all AGNs. These fluxes are shown in Figure 1 [4]. The Nellen, Mannheim and Biermann flux[10] (AGN-NMB), which comes from assuming that pp collisions are the dominant neutrino source, is parameterized by:

$$\frac{dN_{\nu_\mu+\bar{\nu}_\mu}}{dE_\nu} = 1.13 \times 10^{-12} (E_\nu/\mathrm{TeV})^{-2} \mathrm{cm}^{-2}\mathrm{s}^{-1}\mathrm{sr}^{-1}\mathrm{GeV}^{-1}$$

with the $\nu_e + \bar{\nu}_e$ spectrum assumed to be 1/2 of $\nu_\mu + \bar{\nu}_\mu$. The neutrino luminosity of a source is normalized to the observed diffuse x-rays and γ-rays. The NMB parameterization is valid for $E_\nu \leq 4 \times 10^4$ GeV. In our calculations described in the next section, we have used this parameterization up to $E_\nu = 10^8$ GeV. A somewhat different assumption of the luminosity is used by Szabo and Protheroe[11] (AGN-SP) in their extended model of neutrino sources, yielding a higher normalization of dN/dE_ν at 1 TeV. Above $E_\nu > 10^6$ GeV, the AGN-SP follows a steeper power law,

$$dN/dE_\nu \sim E^{-3.5}$$

which accounts for the lack of protons at even higher energies required to produce neutrinos. The Stecker and Salamon flux[8] (AGN-SS) contains contributions from both pp and $p\gamma$ interactions in the accretion disk and has a nearly constant value of dN/dE_ν up to $E_\nu \sim 10^5$ GeV.

Two models of neutrino fluxes from cosmic ray interactions with the microwave background[13] are labeled CR-2 and CR-4 in Figure 1 in Ref. 6. The fluxes depend on the redshift of the cosmic ray sources. Maximum redshifts contributing are $z_{max} = 2$ and $z_{max} = 4$, respectively.

The electron neutrino plus antineutrino fluxes, to a good approximation, are equal to half of the muon neutrino fluxes.

a) Detection of UHE neutrinos

The primary means of detection of muon neutrinos and antineutrinos is by charged-current conversion into muons and antimuons. The long range of the muon means that the effective volume of an underground detector can be significantly larger than the instrumented volume. For example, a 10 TeV muon produced by a charged-current interaction in rock will propagate several kilometers in water-equivalent distance units before its energy is degraded to 1 TeV.

Backgrounds to AGN sources of $\nu_\mu + \bar{\nu}_\mu$ include atmospheric neutrinos and atmospheric muons. Muons produced by cosmic ray interactions in the atmosphere mask astrophysical signals unless detectors are very deep underground, muon energy thresholds are set very high, or one observes upward-going muons. We evaluate here event rates for upward-going muons produced in the rock surrounding the detector, for muon energy thresholds above 1 TeV and 10 TeV.

The neutrino-nucleon cross section comes into the calculation of the event rate in two ways. The probability of conversion $\nu_\mu \to \mu$ is proportional to the νN charged current cross section. In addition, the neutrino flux is attenuated by passage through the Earth. In the next section we describe our calculation of the neutrino-isoscalar nucleon (νN) cross section. The νN charged-current reaction is the dominant source of neutrino interactions except in a very narrow energy window at the W-boson resonance.

b) Small-x Parton Distribution Functions and $\sigma(\nu N)$

The inclusive cross section for $\nu_\mu + N \to \mu^- + X$ is given by

$$\frac{d^2\sigma}{dxdy} = \frac{2G_F^2 M E_\nu}{\pi} \frac{M_W^4}{\left(Q^2 + M_W^2\right)^2} [xq(x,Q^2) + x(1-y)^2 \bar{q}(x,Q^2)], \tag{1}$$

where $x = Q^2/2M\nu$, $y = \nu/E_\nu$, with $-Q^2$ the momentum transfer between the neutrino and muon, and ν the lepton energy loss in the lab frame, $\nu = E_\nu - E_\mu$. M is the mass of the nucleon and M_W is the mass of the W-boson, while the Fermi constant is $G_F = 1.16 \times 10^{-5}$ GeV^{-2}. Taking the target as isoscalar nucleons, in terms of the parton distribution functions for the proton,

$$q(x,Q^2) = \frac{u_v + d_v}{2} + \frac{u_s + d_s}{2} + s_s + b_s \tag{2}$$

$$\bar{q}(x,Q^2) = \frac{u_s + d_s}{2} + c_s + t_s \tag{3}$$

where we have written explicitly valence (v) and sea (s) distributions.

The general form of the cross section shows that at low energies, where the four-Fermi approximation is valid, $\sigma \sim E$. At higher energies, the W-boson propagator plays an important role. The value of $\langle Q^2 \rangle$ saturates at $\sim M_W^2$, and $x \sim M_W^2/(2ME_\nu y)$ decreases. For neutrino energies above 10^5 GeV, the small-x ($x \leq 3 \times 10^{-2}$) behavior of the parton distribution functions becomes important for the evaluation of the cross section.

Neutrino charged-current interactions have been measured directly in laboratory experiments for neutrino energies up to $E_\nu = 300$ GeV[16]. Charged-current ep scattering at HERA, equivalent to $E_\nu = 47.4$ TeV, can be translated to a value of $\sigma(\nu N)$[17]. Recent ZEUS and H1 measurements at HERA[5] of F_2^{ep} at small-x ($10^{-4} \leq x \leq 10^{-2}$) and for a large range of Q^2, 4 GeV$^2 \leq Q^2 \leq 1600$ GeV^2 have provided valuable information about parton densities at small-x and low-Q^2. To evaluate the neutrino-nucleon cross section at ultrahigh energies, extrapolations beyond the measured regime in x and Q^2 are required.

There are two main theoretical approaches in the evolution in Q^2 of parton densities: Gribov-Lipatov-Altarelli-Parisi[8] (GLAP) evolution and Balitskii-Fadin-Kuraev-Lipatov[9] (BFKL) evolution. In the GLAP approach, parton distribution functions are extracted at modest values of Q^2 and evolved to higher scales. The BFKL approach involves a leading $\alpha_s \ln(1/x)$ resummation of soft gluon emissions, which generates a singular behavior in x at an initial scale Q_0,

$$xq_s(x, Q_0^2) \sim x^{-0.5} \tag{4}$$

for small x, which persists at higher values of Q. In our extrapolation of the parton distribution functions outside the measured region, we use GLAP evolution with input at $Q_0 = 1.6$ GeV,

$$xq_s(x, Q_0^2) \sim x^{-\lambda}. \tag{5}$$

The value of λ is determined by fits to deep-inelastic scattering and hadron-hadron data by the MRS[10] and CTEQ[11] Collaborations. The MRS set A' has $\lambda = 0.17$, the MRS set G has $\lambda = 0.07$ while the MRS set D_ has $\lambda = 0.5$. All of the MRS distribution function are fitted using the $\overline{\rm MS}$ factorization scheme. The CTEQ-DIS, using the deep-inelastic scattering factorization scheme, has $\lambda = 0.33$. These distribution functions are extrapolated using the power law fit to the distribution functions at $x = 10^{-5}$ and $Q = M_W$. We have also extrapolated the leading-order CTEQ distributions using the double-log approximation[12]. For reference, the Eichten *et al.*[23] parton distribution functions, extrapolated using the double-log approximation, are also shown. The spread in values for the parton distribution functions is an indication of the uncertainty in evaluating the νN cross section.

For each of these sets of distribution functions, we have evaluated the neutrino-nucleon cross section. Figure 3 in Ref. 6 illustrates the range of predictions as a function of neutrino energy. Also shown is the average of H1 and ZEUS effective neutrino nucleon cross sections[17]. There is excellent agreement among the predictions of the MRS D_, G, and A' distributions and the CTEQ3 distributions up to $E_\nu \approx 10^7$ GeV. Above that energy, our DLA modification of the CTEQ3 distributions gives a lower cross section than the full CTEQ3 distributions (CTEQ-DIS), as expected from its less singular behavior as $x \to 0$. At the highest energy displayed, the most singular (MRS D_) distribution predicts a significantly higher cross section than the others. Above about 10^6 GeV, the EHLQ-DLA distributions yield noticeably smaller cross sections than the modern distributions. Plots similar to Figure 3 in Ref. 6 for antineutrino-nucleon charged current interactions, as well as neutral current interactions, can be found in Ref. 6. For charged current and neutral current interactions, for 10^{15} eV $\leq E_\nu \leq 10^{21}$ eV, the cross sections follow a simple power law, for example

$$\sigma_{CC}(\nu N) = 2.69 \times 10^{-36} \mathrm{cm}^2 \left(\frac{\mathrm{E}_\nu}{1 \text{ GeV}} \right)^{0.402}.$$

Table 1: Number of upward $\mu + \bar{\mu}$ per year per steradian for $A = 0.1$ km^2 and $E_\mu^{\rm min} = 1$ TeV.

Fluxes	EHLQ-DLA	CTEQ-DIS
AGN-SS [8]	82	92
AGN-NMB [10]	100	111
AGN-SP [11]	2660	2960
ATM [15]	126	141

c) New Prediction for the Neutrino Telescope Event Rates

In order to calculate the number of upward-moving muons that can be detected with neutrino detectors such as AMANDA, BAIKAL, DUMAND II and NESTOR [3], we fold in the neutrino flux and its attenuation in the Earth with the probability that a neutrino passing on a detector trajectory creates a muon in the rock that traverses the detector.

The attenuation of neutrinos in the Earth is described by a shadow factor $S(E_\nu)$, equivalent to the effective solid angle for upward muons, normalized to 2π:

$$\frac{dS(E_\nu)}{d\Omega} = \frac{1}{2\pi} \exp\Big(-z(\theta) N_A \sigma_{\nu N}(E_\nu)\Big), \tag{6}$$

where $N_A = 6.022 \times 10^{23}$ mol^{-1} $= 6.022 \times 10^{23}$ cm^{-3} (water equivalent) is Avogadro's number, and $z(\theta)$ is the column depth of the earth, in water-equivalent units, which depends on zenith angle [13]. The probability that the neutrino with energy E_ν converts to a muon is proportional to the cross section and depends on the threshold energy for the muon $E_\mu^{\rm min}$:

$$P_\mu(E_\nu, E_\mu^{\rm min}) = \sigma_{\rm CC}(E_\nu) N_A \langle R(E_\nu, E_\mu^{\rm min}) \rangle, \tag{7}$$

where the average muon range in rock is $\langle R \rangle$ [14]. A more detailed discussion appears in Ref. 6.

The diffuse flux of AGN neutrinos, summed over all AGN sources, is isotropic, so the event rate is

$$\text{Rate} = A \int dE_\nu P_\mu(E_\nu, E_\mu^{\rm min}) S(E_\nu) \frac{dN_\nu}{dE_\nu}, \tag{8}$$

given a neutrino spectrum dN_ν/dE_ν and detector area A. As the cross section increases, P_μ increases, but the effective solid angle decreases.

Event rates for upward muons and antimuons for a detector with $A = 0.1$ km^2 for $E_\mu^{\rm min} = 1$ TeV and $E_\mu^{\rm min} = 10$ TeV are shown in Tables 1 and 2. The CTEQ-DIS distribution functions are taken as representative of the modern parton distribution function sets, and compared with the EHLQ-DLA event rate predictions. The muon range is that of Ref. 26.

The theoretical predictions for ultrahigh-energy neutrinos from AGNs yield event rates comparable to, or in excess of, the background rate of atmospheric neutrinos for $E_\mu^{\rm min} =$ 1 TeV. The AGN-SP rate is large compared to the AGN-NMB rate because additional mechanisms are included. Flux limits from the Fréjus experiment are inconsistent with

Table 2: As in Table 1, but for $E_\mu^{\rm min} = 10$ TeV.

Fluxes	EHLQ-DLA	CTEQ-DIS
AGN-SS [8]	46	51
AGN-NMB [10]	31	34
AGN-SP [11]	760	843
ATM [15]	3	3

the SP flux for 1 TeV$< E_\nu <$ 10 TeV [15]. The atmospheric neutrino background is greatly reduced by requiring a 10 TeV muon threshold, though AGN induced event rates are reduced as well. The flatter neutrino spectra have larger contributions to the event rate for muon energies away from the threshold muon energy than the steep atmospheric flux.

We have evaluated the event rates using the other parton distribution functions shown in Figure 2. Event rate predictions are unchanged with the other modern parton distributions because all these distributions are in agreement in the energy range $E_\nu \sim 1 - 100$ TeV. However, our results for event rates are about 15% larger than for the EHLQ structure functions. This is due to the fact that EHLQ parton distributions were based on the CERN-Dortmund-Heidelberg-Saclay measurements of neutrino-nucleon structure functions [16] which had low normalization of about 15%.

d) W-resonance and PeV Neutrino Detectors

Finally we consider event rates from electron neutrino and antineutrino interactions. For $\nu_e N$ (and $\bar{\nu}_e N$) interactions, the cross sections are identical to the muon neutrino (antineutrino) nucleon cross sections. Because of the rapid energy loss or annihilation of electrons and positrons, it is generally true that only contained-vertex events can be observed. Since electron neutrino fluxes are small, an extremely large effective volume is needed to get measurable event rates. There is one exceptional case: resonant formation of W^- in $\bar{\nu}_e e$ interactions at $E_\nu = 6.3$ PeV. The resonant cross section is larger than the νN cross section at any energy up to 10^{21} eV. In Fig. 4 we present neutrino-electron cross sections.

We note that, at the resonance energy, upward-moving electron antineutrinos do not survive passage through the Earth. However, the contained events have better prospects for detection. The contained event rate for resonant W production is

$$\text{Rate} = \frac{10}{18} V_{\rm eff} N_A \int dE_{\bar{\nu}_e}\, \sigma_{\bar{\nu}_e e}(E_{\bar{\nu}_e}) S(E_{\bar{\nu}_e}) \frac{dN_{\bar{\nu}_e}}{dE_{\bar{\nu}_e}}. \tag{9}$$

We show event rates for resonant W-boson production in Table 3. The background is for events with $E_\nu > 3$ PeV.

¿From Table 3 we note that a 1 km^3 detector with energy threshold in the PeV range would be suitable for detecting resonant $\bar{\nu}_e e \to W$ events. However, the $\nu_\mu N$ background may be difficult to overcome. By placing the detector a few km underground, one can reduce atmospheric-muon background, which is 5 events per year per steradian at the surface of the Earth for $E_\mu > 3$ PeV.

Table 3: Downward resonance $\bar{\nu}_e e \to W^-$ events per year per steradian for a detector with effective volume $V_{\rm eff} = 1$ km^3 together with the potential downward (upward) background from ν_μ and $\bar{\nu}_\mu$ interactions above 3 PeV.

Mode	AGN-SS [8]	AGN-SP [11]
$W \to \bar{\nu}_\mu \mu$	6	3
$W \to$ hadrons	41	19
$(\nu_\mu, \bar{\nu}_\mu) N$ CC	33 (7)	19 (4)
$(\nu_\mu, \bar{\nu}_\mu) N$ NC	13 (3)	7 (1)

We find that detectors such as DUMAND II, AMANDA, BAIKAL and NESTOR have a very good chance of being able to test different models for neutrino production in the AGNs [1]. For $E_\mu^{\rm min} = 1$ TeV, we find that the range of theoretical fluxes leads to event rates of 900-29,600 upward-moving muons/yr/km^2/sr originating from the diffuse AGN neutrinos, with the atmospheric background of 1400 events/yr /km^2/sr. For $E_\mu^{\rm min} = 10$ TeV, signal to background ratio becomes even better, with signals being on the order of 500-8,400 events/yr/km^2/sr, a factor $\sim$20-300 higher than the background rate. For neutrino energies above 3 PeV there is significant contribution to the muon rate due to the $\bar{\nu}_e$ interaction with electrons, due to the W-resonance contribution. We find that acoustic detectors with 3 PeV threshold and with effective volume of 0.2 km^3, such as DUMAND, would detect 48 hadronic cascades per year from $W \to$ hadrons, 7 events from $W \to \mu \bar{\nu}_\mu$ and 36 events from ν_μ and $\bar{\nu}_\mu$ interactions with virtually no background from ATM neutrinos.

References

[1] C. E. Fichtel, *et al.*, *Astrophys. J. Suppl.* 94:551 (1994).

[2] M. Punch, *et al.* (Whipple Observatory Gamma Ray Collaboration) *Nature (London)* 160:477 (1992); A.D. Kerrick *et al.*, *Astrophys. J.* 438:L59 (1995); J. Quinn, *et al.* (Whipple Observatory Gamma Ray Collaboration) *IAU Circular* 6169 (June 16, 1995).

[3] T. C. Weekes, private communication.

[4] See T. Gaisser, F. Halzen and T. Stanev, *Physics Reports* 258:173 (1995) for a review of neutrino astronomy and sources of UHE neutrinos.

[5] J. Babson *et al.*, (DUMAND Collaboration), *Phys. Rev.* D42:3613 (1990); *Proceedings of the NESTOR workshop at Pylos, Greece*, ed. L. K. Resvanis (University of Athens, 1993); D. Lowder *et. al.*, *Nature* 353:331 (1991).

[6] R. Gandhi, C. Quigg, M.H. Reno and I. Sarcevic, hep-ph/9512364, to appear in *Astroparticle Physics* (Sep. 1996); ibid, Nucl. Phys. **B48** (1996) 475c.

[7] ZEUS Collaboration, M. Derrick *et al.*, *Phys. Lett.* B316:412 (1993); H1 Collaboration, I. Abt *et al.*, *Nucl. Phys.* B407:515 (1993).

[8] C. Quigg, M. H. Reno and T. Walker, *Phys. Rev. Lett.* 57:774 (1986); M. H. Reno and C. Quigg, *Phys. Rev.* D37:657 (1988).

[9] L. V. Volkova, *Yad. Fiz.* 31:1510 (1980) (*Sov. J. Nucl. Phys.* 31:784 (1980)).

[10] L. Nellen, K. Mannheim and P. L. Biermann, *Phys. Rev.* D47:5270 (1993).

[11] A. P. Szabo and R. J. Protheroe, *Astropart. Phys.* 2:375 (1994).

[12] F. W. Stecker, C. Done, M. H. Salamon and P. Sommers, *Phys. Rev. Lett.* 66:2697 (1991); Errat.: *Phys. Rev. Lett.* 69:2738 (1992). Revised estimates of the neutrino flux appear in F. W. Stecker and M. H. Salamon, astro-ph/9501064, submitted to *Space Sci. Rev.*

[13] S. Yoshida and M. Teshima, *Prog. Theoret. Phys.* (Kyoto) 89:833 (1993).

[14] W. H. Rhode *et al.* (Fréjus Collaboration), Wuppertal preprint WUB-95-26, to appear in *Astropart. Phys.*

[15] P. Gondolo, G. Ingelman and M. Thunman, Uppsala preprint TSL/ISV-95-0120, hep-ph/9505417.

[16] S. R. Mishra, *et al.* (CCFR Collaboration), Nevis Laboratory Report Nevis–1465 (1992), and in *Lepton–Hadron Scattering*, Proceedings of the Nineteenth SLAC Summer Institute on Particle Physics, edited by Jane Hawthorne, SLAC–REPORT–398 (1992), p. 407.

[17] Rolf Beyer, 1995 *Workshop on Weak Interactions and Neutrinos*, Talloires, France.

[18] V.N. Gribov and L.N. Lipatov, *Sov. J. Nucl. Phys.* 15:438 (1972); L.N. Lipatov, *Sov. J. Nucl. Phys.* 20:181 (1974); Yu.L. Dokshitser, *Sov. Phys. JETP* 46:641 (1977); G. Altarelli and G. Parisi, *Nucl. Phys.* B126:298 (1977).

[19] E.A. Kuraev, L.N. Lipatov and V.S. Fadin, *Sov. Phys. JETP* 44:443 (1976); 45:199 (1977); Ya.Ya. Balitskii and L.N. Lipatov, *Sov. J. Nucl. Phys.* 28:822 (1978).

[20] A.D. Martin, W.J. Stirling and R.G. Roberts, *Phys. Rev.* D47:867 (1993); *Phys. Lett.* 354B:155 (1995).

[21] H. Lai *et al.*, *Phys. Rev.* D51:4763 (1995).

[22] L. V. Gribov, E. M. Levin and M. G. Ryskin, *Phys. Rep.* 100:1 (1983). See also D. W. McKay and J. P. Ralston, *Phys. Lett.* 167B:103 (1986).

[23] E. Eichten, I. Hinchliffe, K. Lane and C. Quigg, *Rev. Mod. Phys.* 56:579 (1984); ibid. 58:1065E (1986).

[24] See §7 of T. K. Gaisser, F. Halzen and T. Stanev, Ref. 4, for a review of several models in addition to the models presented here.

[25] A. Dziewonski, "Earth Structure, Global," in *The Encyclopedia of Solid Earth Geophysics*, ed. D. E. James (Van Nostrand Reinhold, New York, 1989), p. 331.

[26] P. Lipari and T. Stanev, *Phys. Rev.* D44:3543 (1991).

e) Neutrinos from Topological Defects

A variety of topological defects, including monopoles, cosmic strings, domain walls, and superconducting cosmic strings, might have been formed in symmetry-breaking phase transitions in the early Universe. When topological defects are destroyed by collapse or annihilation, the energy stored in them is released in the form of massive quanta denoted X of the fields that generated the defects. The X particles can then decay into quarks, gluons, leptons, and such, that eventually materialize into energetic neutrinos and other particles. Topological defects formed in phase transitions around the unification scale could therefore constitute a "nonacceleration" source of ultrahigh-energy neutrinos.

Topological defects are a more speculative source of the highest-energy neutrinos than the interaction of cosmic rays with the cosmic microwave background, but they might produce much higher fluxes. Some examples of these fluxes have been given by Bhattacharjee, Hill, and Schramm [1]. Dimensional arguments yield a master equation for the rate of release of X particles through the collapse of topological structures in terms of the mass scale M_X and the Hubble time t,

$$\frac{dN_X(t)}{dt} = \kappa M_X^p t^{-4+p}, \tag{10}$$

where the dimensionless constants κ and p depend on the characteristics of the topological defect. For example, $p = 1$ corresponds to the collapse of cosmic string loops or to the collapse of monopole-antimonopole bound states, while $p = 1$ is appropriate to a process involving saturated superconducting cosmic string loops.

Using their model assumptions, Bhattacharjee, et al. have produced example neutrino spectra for $p = 1.5$, 1.0, 0.5, and 0. The largest flux, corresponding to $p = 1.5$, is in conflict with the Frejus limit [2] at energies around a few TeV. The next largest case, for $p = 1.0$, lies comfortably below the Frejus bound, but is considerably larger than the CR-2 and CR-4 fluxes calculated by Yoshida and Teshima[3]. We take this flux as a plausible example to consider the sensitivity of a km^3 detector to the fossil neutrinos from the collapse of topological defects.

The $BHS_{p=1.0}$ flux emerges from the AGN fluxes shown in Figure 18 of GQRS [4] at about 10^7 GeV. In the regime 10^7 GeV $\leq E_\nu \leq 10^{10}$ GeV, we can parametrize the $BHS_{p=1.0}$ flux as

$$\frac{dN_{\nu_\mu+\bar{\nu}_\mu}}{dE\nu} = 4.84 \times 10^{-10} \left(\frac{E_\nu}{1 \text{ GeV}}\right)^{-1.554} \text{cm}^{-2}\text{s}^{-1}\text{sr}^{-1}\text{GeV}^{-1} \tag{11}$$

We show in Table 1 the rates for charged-current events with vertices contained in a detector with an effective volume of 1 km^3, for muon energy thresholds of $E_\mu^{min} = 10^7$ and 10^8 GeV. As a practical matter, we have taken the upper limit of the neutrino energy to be $E_\nu^{max} = 10^{10}$ GeV. Upward rates for uncontained events are smaller by a factor of three or four. Both upward and downward rates are about two and a half orders of magnitude larger than the corresponding CR-4 rates in Table 6 of GQRS.

For our nominal set (CTEQ-DIS) of parton distributions, the $BHS_{p=1.0}$ flus leads to 10 events per steradian per year with $E_{mu} > 10^7$ GeV, equally divided between μ^+ and μ^-. This

is an attractive target for a $1km^3$ detector, and raises the possibility that even a $0.1 - km^3$ detector could see hints of the collapse of topological defects.

Table 1: Downward $\mu^+ + \mu^-$ event rates per steradian per year arising from $\nu_\mu N$ and $\bar{\nu}_\mu N$ interactions that occur within a detector with effective volume $V_{eff} = 1\ km^3$, for the $BHS_{p=1.0}$ neutrino flux.

Parton Distributions	E_μ^{min}	
	10^7 GeV	10^8 GeV
CTEQ-DIS	10	6
CTEQ-DLA	8	4
MRS D_	12	8
EHLQ-DLA	6	3

References

[1] P. Bhattacharjee, C. T. Hill, and D. N. Schramm, *Phys. Rev. Lett* **69** (1992) 567.

[2] W. Rhode, *et.al* (Frejus Collaboration), "Limits on the flux of very high energy neutrinos with the Frejus Detector," Wuppertal preprint WUB-95-26, to appear in *Astroparticle Physics*. This paper contains extensive comparisons with models of the very-high-energy neutrino flux.

[3] S. Yoshida and M. Teshima, *Prog. Theoret. Phys. (Kyoto)* **89** (1993) 833.

[4] R. Gandhi, C. Quigg, M. H. Reno, and I. Sarcevic, "Ultrahigh-Energy Neutrino Interactions," *Astropart. Phys.* (1995).

Neutrino Interactions and Detection of Extragalactic Neutrinos

(R. Gandhi, C. Quigg, M.H. Reno and I. Sarcevic, *Phys. Rev.* **D58** (1998) 093009

Neutrino flux at the surface of the Earth has contributions from the atmospheric neutrinos from cosmic-ray interactions in the atmosphere, neutrinos from Active Galactic Nuclei, cosmic neutrinos from extragalactic cosmic ray interactions with the microwave background radiation, neutrinos from the topological defects formed in the early Universe, neutrinos from gamma-ray bursts and cosmological neutrinos from cosmic ray interactions with the microwave background. The "conventional" atmospheric neutrino flux comes from the decay of charged pions and kaons produced by cosmic ray interactions in the atmosphere. The atmospheric neutrino flux is large at $E_\nu = 1$ TeV, but the spectrum falls rapidly as a function of energy. An additional "prompt" contribution to the atmospheric flux arises from charm production and decay. Atmospheric neutrinos and muons constitute a background to the detection of extraterrestrial neutrino sources, such as Active Galactic Nuclei, topological defects formed in the Early Universe and Gamma-Ray Bursts.

The Active Galactic Nuclei (AGN) might be the most powerful sources of high-energy neutrinos. With typical luminosities in the range 10^{42} to 10^{48} erg/s, AGNs are believed to be the most powerful individual sources of radiation in the Universe. If the observed photons are decay products of π^0s produced in hadronic interactions in the disk surrounding the AGN, then AGNs are also powerful sources of ultrahigh-energy (UHE) neutrinos [2]. Unlike photons, which are absorbed by a few hundred gm/cm^2 of material, TeV neutrinos have interaction lengths on the order of 250 kt/cm^2 and thus can provide a direct window to the

most energetic processes in the universe.

The advantage of the long interaction length translates to a challenge in the detection of neutrinos. Interaction rates increase with energy, but the fluxes of UHE neutrinos are steeply falling functions of neutrino energy. Cerenkov detection of muons from interactions of muon neutrinos in the rock or ice surrounding the detector is feasible[3]. More difficult is the detection of charged-current interactions of electron neutrinos. Large-area air shower arrays or large volume underground detectors may be adequate for the detection of electron neutrinos, especially near the W-boson resonance in $\bar{\nu}_e e$ collisions. Theoretical calculations of the neutrino-nucleon and neutrino-electron cross sections are instrumental in evaluating event rates for neutrino telescopes. At very high energies, these cross sections are strongly dependent on the behavior of the parton distribution at small x and large Q^2 ($Q^2 \sim M_W^2$).

Recently we have completed calculation of charged-current and neutral-current cross sections for energies up to 10^{21} eV [4] obtained using new parton distributions measured in ep collisions at HERA in the wide kinematic range from $10^{-5} < x < 0.1$ and 0.05 GeV^2 < $Q^2 < 100$ GeV^2 [5] and with the assumption that the evolution to higher values of Q^2 can be obtained using Altarelli-Parisi evolution equations. Detection of UHE neutrinos depends on these cross sections and on the neutrino fluxes from UHE neutrino sources.

We have considered several model predictions for neutrino fluxes from atmospheric neutrinos from cosmic-ray interactions in the atmosphere, neutrinos from active galactic nuclei, and cosmic neutrinos from extragalactic cosmic ray interactions with the microwave background radiation. Recent observation of the short time variability of EGRET sources have put stringent constraints on AGN models. Mannheim and Protheroe have revised their AGN neutrino fluxes to accommodate EGRET data, and the new neutrino fluxes are peaked in the PeV energy range, due to the dominance of $p\gamma$ interactions[6, 7].

The primary means of detection of muon neutrinos and antineutrinos is by charged-current conversion into muons and antimuons. The long range of the muon means that the effective volume of an underground detector can be significantly larger than the instrumented volume. For example, a 10 TeV muon produced by a charged-current interaction in rock will propagate several kilometers in water-equivalent distance units before its energy is degraded to 1 TeV. Backgrounds to AGN sources of $\nu_\mu + \bar{\nu}_\mu$ include atmospheric neutrinos and atmospheric muons. Muons produced by cosmic ray interactions in the atmosphere mask astrophysical signals unless detectors are very deep underground, muon energy thresholds are set very high, or one observes upward-going muons. We have evaluated event rates for upward-going muons produced in the rock surrounding the detector, for muon energy thresholds above 1 TeV and 10 TeV.

The neutrino-nucleon cross section comes into the calculation of the event rate in two ways. The probability of conversion $\nu_\mu \to \mu$ is proportional to the νN charged-current cross section. In addition, the neutrino flux is attenuated by passage through the Earth. Below we describe our calculation of the neutrino-isoscalar nucleon (νN) cross section. The νN charged-current reaction is the dominant source of neutrino interactions except in a very narrow energy window at the W-boson resonance.

At high energies, the inclusive cross section for $\nu_\mu + N \to \mu^- + X$ depends on the small-x behavior of the parton distributions. Recent ZEUS and H1 measurements at HERA[5] of F_2^{ep} at small-x ($10^{-4} \le x \le 10^{-2}$) and for a large range of Q^2, 4 GeV^2 $\le Q^2 \le$ 1600 GeV^2 have provided valuable information about parton densities at small-x and low-Q^2. To

evaluate the neutrino-nucleon cross section at ultrahigh energies, extrapolations beyond the measured regime in x and Q^2 are required. There are two main theoretical approaches in the evolution in Q^2 of parton densities: Gribov-Lipatov-Altarelli-Parisi[8] (GLAP) evolution and Balitskii-Fadin-Kuraev-Lipatov[9] (BFKL) evolution. In the GLAP approach, parton distribution functions are extracted at modest values of Q^2 and evolved to higher scales. The BFKL approach involves a leading $\alpha_s \ln(1/x)$ resummation of soft gluon emissions, which generates a singular behavior in x at an initial scale Q_0, $xq_s(x, Q_0^2) \sim x^{-0.5}$ for small x, which persists at higher values of Q. In our extrapolation of the parton distribution functions outside the measured region, we use GLAP evolution with input at $Q_0 = 1.6$ GeV, $xq_s(x, Q_0^2) \sim x^{-\lambda}$. The value of λ is determined by fits to deep-inelastic scattering and hadron-hadron data by the MRS[10] and CTEQ[11] Collaborations. The MRS set A' has $\lambda = 0.17$, the MRS set G has $\lambda = 0.07$ while the MRS set D_ has $\lambda = 0.5$. All of the MRS distribution function are fitted using the $\overline{\rm MS}$ factorization scheme. The CTEQ4-DIS, using the deep-inelastic scattering factorization scheme, has $\lambda = 0.227$. These distribution functions are extrapolated using the power law fit to the distribution functions at $x = 10^{-5}$ and $Q = M_W$. We have also extrapolated the leading-order CTEQ distributions using the double-log approximation[12]. The spread in values for the parton distribution functions is an indication of the uncertainty in evaluating the νN cross section.

For each of these sets of distribution functions, we have evaluated the neutrino-nucleon cross section. There is excellent agreement among the predictions of the MRS D_, G, and A' distributions and the CTEQ4 distributions up to $E_\nu \approx 10^7$ GeV. Above that energy, our DLA modification of the CTEQ4 distributions gives a lower cross section than the full CTEQ4 distributions (CTEQ-DIS), as expected from its less singular behavior as $x \to 0$. At the highest energy displayed, the most singular (MRS D_) distribution predicts a significantly higher cross section than the others. Above about 10^6 GeV, the EHLQ-DLA distributions yield noticeably smaller cross sections than the modern distributions. For charged-current and neutral-current interactions, for 10^{16} eV $\leq E_\nu \leq 10^{21}$ eV, the cross sections follow a simple power law, for example

$$\sigma_{CC}(\nu N) = 5.53 \times 10^{-36} \mathrm{cm}^2 \left(\frac{\mathrm{E}_\nu}{1\ \mathrm{GeV}} \right)^{0.363} .$$

In order to calculate the number of upward-moving muons that can be detected with neutrino detectors such as AMANDA II, ANTARES, RICE and NESTOR [3], we fold in the neutrino flux and its attenuation in the Earth with the probability that a neutrino passing on a detector trajectory creates a muon in the rock that traverses the detector.

The attenuation of neutrinos in the Earth is described by a shadowing factor $S(E_\nu)$, equivalent to the effective solid angle for upward muons, normalized to 2π:

$$\frac{dS(E_\nu)}{d\Omega} = \frac{1}{2\pi} \exp\Big(-z(\theta) N_A \sigma_{\nu N}(E_\nu)\Big), \tag{12}$$

where $N_A = 6.022 \times 10^{23}$ mol^{-1} $= 6.022 \times 10^{23}$ cm^{-3} (water equivalent) is Avogadro's number, and $z(\theta)$ is the column depth of the earth, in water-equivalent units, which depends on zenith angle [13]. The probability that the neutrino with energy E_ν converts to a muon

is proportional to the cross section and depends on the threshold energy for the muon $E_\mu^{\rm min}$:

$$P_\mu(E_\nu, E_\mu^{\rm min}) = \sigma_{\rm CC}(E_\nu) N_A \langle R(E_\nu, E_\mu^{\rm min})\rangle, \tag{13}$$

where the average muon range in rock is $\langle R\rangle$ [14].

The diffuse flux of AGN neutrinos, summed over all AGN sources, is isotropic, so the event rate is

$$\text{Rate} = A \int dE_\nu P_\mu(E_\nu, E_\mu^{\rm min}) S(E_\nu) \frac{dN_\nu}{dE_\nu}, \tag{14}$$

given a neutrino spectrum dN_ν/dE_ν and detector area A. As the cross section increases, P_μ increases, but the effective solid angle decreases.

Event rates for upward muons and antimuons for a detector with $A = 0.1$ km^2 for $E_\mu^{\rm min} = 1$ TeV and $E_\mu^{\rm min} = 10$ TeV for nearly horizontal nadir angles and for all angles are shown in Tables 3 and 4 in Ref. 1.

The theoretical predictions for ultrahigh-energy neutrinos from AGNs yield event rates comparable to the background rate of atmospheric neutrinos for $E_\mu^{\rm min} = 10$ TeV. The AGN-SP rate is large compared to the AGN-NMB rate because additional mechanisms are included. Flux limits from the Fréjus experiment are inconsistent with the SP flux for 1 TeV$< E_\nu <$ 10 TeV [15]. The atmospheric neutrino background is greatly reduced by requiring a 10 TeV muon threshold, though AGN induced event rates are reduced as well. The flatter neutrino spectra have larger contributions to the event rate for muon energies away from the threshold muon energy than the steep atmospheric flux.

We have also considered event rates from electron neutrino and antineutrino interactions. For $\nu_e N$ (and $\bar\nu_e N$) interactions, the cross sections are identical to the muon neutrino (antineutrino) nucleon cross sections. Because of the rapid energy loss or annihilation of electrons and positrons, it is generally true that only contained-vertex events can be observed. Since electron neutrino fluxes are small, an extremely large effective volume is needed to get measurable event rates. There is one exceptional case: resonant formation of W^- in $\bar\nu_e e$ interactions at $E_\nu = 6.3$ PeV. The resonant cross section is larger than the νN cross section at any energy up to 10^{21} eV.

We note that, at the resonance energy, upward-moving electron antineutrinos do not survive passage through the Earth. However, the contained events have better prospects for detection. The contained event rate for resonant W production is

$$\text{Rate} = \frac{10}{18} V_{\rm eff} N_A \int dE_{\bar\nu_e}\, \sigma_{\bar\nu_e e}(E_{\bar\nu_e}) S(E_{\bar\nu_e}) \frac{dN_{\bar\nu_e}}{dE_{\bar\nu_e}}. \tag{15}$$

The event rates for resonant W-boson production are presented in Ref. 1.

In summary, our new calculations of the cross sections for neutrino-nucleon charged-current and neutral-current interactions are at most 25% smaller than those of GQRS96[4], with the deviation largest at the highest energy considered here, 10^{21}eV. By varying the extrapolations of the small-x behavior of the parton distribution functions, we find that the uncertainty in the νN cross section is at most a factor of $2^{\pm 1}$ at the highest energies. All modern sets of parton distribution functions give comparable cross sections for energies up to 10^{16}eV.

Table 4: Downward $\mu^+ + \mu^-$ events per year arising from $\nu_\mu N$ and $\bar{\nu}_\mu N$ interactions in $1km^3$ of water.

	Muon-energy threshold, $E_\mu^{\rm min}$		
Flux	100TeV	1PeV	3PeV
ATM [16]	0.85	0.0054	0.00047
ATM [16] + charm [17]	2.6	0.050	0.0076
AGN-SS91 [8]	520.	120.	42.
AGN-M95 ($p\gamma$) [6]	16.	11.	8.7
AGN-P96 ($p\gamma$) [7]	100.	50.	31.
GRB-WB [19]	7.7	1.9	0.93
TD-SLSC [20]	0.037	0.032	0.029
TD-WMB12 [21]	1.1	0.74	0.58
TD-WMB16 [21]	0.00087	0.00050	0.00035

Table 5: Annual neutral-current (ν_e, $\bar{\nu}_e$)N and charged-current (ν_μ, $\bar{\nu}_\mu$)N event rates for the Pierre Auger Cosmic Ray Observatory.

Flux	$E_{\rm sh} > 10^8$GeV		$E_{\rm sh} > 10^9$GeV	
	(ν_e, $\bar{\nu}_e$)N NC	(ν_μ, $\bar{\nu}_\mu$)N CC	(ν_e, $\bar{\nu}_e$)N NC	(ν_μ, $\bar{\nu}_\mu$)N CC
AGN-SS91 [8]	0.0045	0.019	0.000006	0.000024
AGN-M95 ($p\gamma$) [6]	0.65	2.7	0.26	1.1
AGN-P96 ($p\gamma$) [7]	0.74	3.1	0.13	0.53
GRB-WB [19]	0.038	0.16	0.020	0.085
TD-SLSC [20]	0.013	0.052	0.010	0.042
TD-WMB12 [21]	0.15	0.59	0.11	0.44
TD-WMB16 [21]	0.000026	0.00011	0.000011	0.000046

We have estimated event rates for several energy thresholds and detection methods, using a variety of models for the neutrino fluxes from AGNs, gamma-ray bursters, topological defects, and cosmic-ray interactions in the atmosphere. In $\nu_\mu N \to \mu X$ interactions, requiring a muon energy above 10 TeV reduces the atmospheric background enough to permit the observation of upward-going muons for the AGN-SS91 and AGN-P96 fluxes. These models yield tens to hundreds of events per year for detectors of $0.1km^2$ effective area. The GRB-WB flux emerges at a higher threshold, but suffers from a small event rate.

Event rates for downward muons above 100TeV from neutrinos are substantial in $1km^3$, except for the TD models. Resonant W boson production will be difficult to distinguish from the νN interaction background. For the Pierre Auger Cosmic Ray Observatory, the most promising rates arise from (ν_e, $\bar{\nu}_e$)N charged-current interactions in the AGN-M95 and AGN-P96 models. By combining measurements of the upward-going muon rate at lower energies with air-shower studies at the highest energies, it may be possible to distinguish among alternative high-energy extrapolations of the νN cross section.

The origins of the highest energy cosmic rays are not well understood, but cosmic rays should be accompanied by very high energy neutrinos in all models. The absolute normalization and energy dependence of the fluxes vary from model to model. Neutrino telescopes ultimately will probe extraterrestrial accelerator sources. We expect that detectors with effective areas on the order of $0.1km^2$ will yield significant clues to aid in our understanding of physics to the 10^{20}eV energy scale.

References

[1] R. Gandhi, C. Quigg, M.H. Reno and I. Sarcevic, *Phys. Rev.* **D58** (1998) 093009.

[2] See T. Gaisser, F. Halzen and T. Stanev, *Physics Reports* 258:173 (1995) for a review of neutrino astronomy and sources of UHE neutrinos.

[3] J. Babson *et al.*, (DUMAND Collaboration), *Phys. Rev.* D42:3613 (1990); *Proceedings of the NESTOR workshop at Pylos, Greece*, ed. L. K. Resvanis (University of Athens, 1993); D. Lowder *et. al.*, *Nature* 353:331 (1991).

[4] R. Gandhi, C. Quigg, M.H. Reno and I. Sarcevic, *Astroparticle Physics* **5**, 81 (1997); ibid, Nucl. Phys. **B48** (1996) 475c.

[5] ZEUS Collaboration, M. Derrick *et al.*, *Phys. Lett.* B316:412 (1993); H1 Collaboration, I. Abt *et al.*, *Nucl. Phys.* B407:515 (1993).

[6] K. Mannheim, *Astropart. Phys* **3** 295 (1995)

[7] R. J. Protheroe, astro-ph/9697165, in Proceedings of IUA Colloquium 163, Accretion Phenomena and Related Outflows, edited by D. Wickramasinghe et al., 1996, in press.

[8] V.N. Gribov and L.N. Lipatov, *Sov. J. Nucl. Phys.* 15:438 (1972); L.N. Lipatov, *Sov. J. Nucl. Phys.* 20:181 (1974); Yu.L. Dokshitser, *Sov. Phys. JETP* 46:641 (1977); G. Altarelli and G. Parisi, *Nucl. Phys.* B126:298 (1977).

[9] E.A. Kuraev, L.N. Lipatov and V.S. Fadin, *Sov. Phys. JETP* 44:443 (1976); 45:199 (1977); Ya.Ya. Balitskii and L.N. Lipatov, *Sov. J. Nucl. Phys.* 28:822 (1978).

[10] A.D. Martin, W.J. Stirling and R.G. Roberts, *Phys. Rev.* D47:867 (1993); *Phys. Lett.* 354B:155 (1995).

[11] H. Lai *et al.*, *Phys. Rev.* D51:4763 (1995).

[12] L. V. Gribov, E. M. Levin and M. G. Ryskin, *Phys. Rep.* 100:1 (1983).

[13] A. Dziewonski, "Earth Structure, Global," in *The Encyclopedia of Solid Earth Geophysics*, ed. D. E. James (Van Nostrand Reinhold, New York, 1989), p. 331.

[14] P. Lipari and T. Stanev, *Phys. Rev.* D44:3543 (1991).

[15] W. H. Rhode *et al.* (Fréjus Collaboration), Wuppertal preprint WUB-95-26, to appear in *Astropart. Phys.*

[16] L. V. Volkova, *Yad. Fiz.* 31:1510 (1980) (*Sov. J. Nucl. Phys.* 31:784 (1980)).

[17] L. Pasquali, M. H. Reno, and I. Sarcevic, "Lepton fluxes from atmospheric charm", hep-ph/9806428, submitted to *Phys. Rev.* **D**.

[18] F. W. Stecker, C. Done, M. H. Salamon and P. Sommers, *Phys. Rev. Lett.* 66:2697 (1991); Errat.: *Phys. Rev. Lett.* 69:2738 (1992). Revised estimates of the neutrino flux appear in F. W. Stecker and M. H. Salamon, astro-ph/9501064, submitted to *Space Sci. Rev.*

[19] E. Waxman and J. Bahcall, *Phys. Rev. Lett.* **78**, 2292 (1997).

[20] G. Sigl, S. Lee, D. N. Schramm and P. Coppi, *Phys. Lett.* **B392**, 129 (1997).

[21] U. F. Wichoski, J. H. MacGibbon, and R. H. Brandenberger, "High Energy Neutrinos, Photons and Cosmic Rays from Non-Scaling Cosmic Strings," BROWN–HET–1115 hep-ph/9805419.

Charm Production and High-Energy Atmospheric Muon and Neutrino Fluxes

(L. Pasquali, M.H. Reno and I. Sarcevic, *Astropart. Phys.* **9** (1998) 259; *Phys. Rev.* **D59**, 034020 (1999); *Nucl. Phys.* **B70**, 361 (1999).

We have re-examined the charm contribution to atmospheric lepton fluxes in the context of perturbative QCD. We have included next-to-leading order corrections and discuss theoretical uncertainties due to the extrapolations of the gluon distributions at small-x. We have shown that the charm contribution to the atmospheric muon flux becomes dominant over the conventional contribution from π and K decays at the energies of about 10^5 GeV.

Neutrino and muon fluxes from cosmic ray interactions with the Earth's atmosphere have been topics of considerable experimental and theoretical interest [1]. At energies near 1 GeV, the IMB [2], Kamiokande [3] and Soudan [4] experiments detect an excess of ν_e relative to ν_μ in the atmospheric neutrinos. Recent results from SuperKamiokande [2] appear to confirm this observation. At these energies, leptonic decays of charged pions and leptonic and semileptonic decays of kaons are responsible for the lepton fluxes, the so-called "conventional" lepton flux. Currently, it is believed that the conventional flux dominates until energies of about 10^3 TeV, when the effects of atmospheric charm production and decay become important contributions to the lepton fluxes. The issue of where the charm contributions dominate is of interest, in part, because this is an energy regime accessible to large underground experiments [6]. Recent results from Fréjus [7], Baksan [8] and other experiments [9] show an excess relative to the conventional muon flux in the 10 TeV energy range. This may be an indication of a charm contribution at lower energies that expected. One of the main goals of the neutrino experiments such as AMANDA [10], Antares [11], Nestor [12] and at Lake Baikal [13] are searches for muon neutrinos from extragalactic neutrino sources for which atmospheric neutrinos and muons present the main background.

Lepton fluxes from atmospheric charm have been calculated previously [14, 15] for specific models of charm particle production. We calculate the leptonic flux from charm in the context of perturbative QCD. We include next-to-leading order radiative corrections and we study the importance of small-x behavior of the parton distribution functions. We

emphasize the uncertainties inherent in the necessary extrapolation of cross sections and energy distributions beyond the experimentally measured regime. We use the comparison with low-energy charm production data to constraint some of the theoretical uncertainties, such as the charm quark mass and the factorization and renormalization scale dependence. We compare our results to the earlier work on the prompt muons from charm including a recent calculation [14] calculated using PYTHIA Monte Carlo program [16].

Particle fluxes are determined by solving the coupled differential equations that account for production, decays and interactions of the particles. The general form of the cascade equations describing the propagation of particle j through column depth X is given by[17, 18]

$$\frac{\mathrm{d}\phi_j}{\mathrm{d}X} = -\frac{\phi_j}{\lambda_j} - \frac{\phi_j}{\lambda_j^{(dec)}} + \sum_k S(k \to j) \tag{16}$$

where λ_j is the interaction length, $\lambda_j^{(dec)} \simeq \gamma c \tau_j \rho(X)$ is the decay length, accounting for time dilation factor γ and expressed in terms of g/cm^2 units. The density of the atmosphere is $\rho(X)$ and

$$S(k \to j) = \int_E^\infty \mathrm{d}\, E_k \frac{\phi_k(E_k, X)}{\lambda_k(E_k)} \frac{\mathrm{d}n_{k\to j}(E; E_k)}{\mathrm{d}E} \ . \tag{17}$$

In Eq. (6), $\mathrm{d}n/\mathrm{d}E$ refers to either the production distribution $1/\sigma_k \cdot \mathrm{d}\sigma_{k\to j}\ /\mathrm{d}E$ or decay distribution $1/\Gamma_k \cdot \mathrm{d}\Gamma_{k\to j}/\mathrm{d}E$.

It is possible to solve these equations numerically, however, it has been shown [14] that the same results can be obtained with an analytic solution which was derived by noticing that the energy dependence of the fluxes approximately factorizes from the X dependence. Consequently, one can rewrite

$$\begin{aligned} S(k \to j) &\simeq \frac{\phi_k(E, X)}{\lambda_k(E)} \int_E^\infty \mathrm{d}\, E_k \frac{\phi_k(E_k, 0)}{\phi_k(E, 0)} \frac{\lambda_k(E)}{\lambda_k(E_k)} \frac{\mathrm{d}n_{k\to j}(E; E_k)}{\mathrm{d}E} \\ &\equiv \frac{\phi_k(E, X)}{\lambda_k(E)} Z_{kj}(E) \ . \end{aligned} \tag{18}$$

It is often convenient to write Z_{kj} in terms of an integral over $x_E \equiv E/E_k$, so

$$Z_{kj}(E) = \int_0^1 \frac{\mathrm{d}x_E}{x_E} \frac{\phi_k(E/x_E, 0)}{\phi_k(E, 0)} \frac{\lambda_k(E)}{\lambda_k(E/x_E)} \frac{\mathrm{d}n_{k\to j}(E/x_E)}{\mathrm{d}x_E} \ . \tag{19}$$

In the limits where the flux has a single power law energy behavior, the interaction lengths are energy independent and the differential distribution is scaling (energy independent), the Z-moment $Z_{kj}(E)$ is independent of energy. In practice, the Z-moments have a weak energy dependence because $\mathrm{d}n/\mathrm{d}x_E$ depends on E_k, the interaction lengths λ are not energy independent, and in general, $\phi_k(E)$ is not a constant power law in energy over the full energy range. The cosmic ray flux can be represented by the following flux of primary nucleons at $X = 0$:

$$\phi_p(E, X = 0)[\mathrm{cm}^{-2}\mathrm{s}^{-1}\mathrm{sr}^{-1}\mathrm{GeV}^{-1}] = \begin{array}{ll} 1.7\ (E/\mathrm{GeV})^{-2.7} & E < E_0 \\ 174\ (E/\mathrm{GeV})^{-3} & E \geq E_0 \ , \end{array} \tag{20}$$

where $E_0 = 5 \cdot 10^6$ GeV [19, 20]. At these energies, we assume isotropy of the flux [21].

Following Ref. [14], we assume that the incident cosmic ray flux can be represented by protons. The flux results, in high energy and low energy regimes for lepton flavor $\ell = \nu_\mu,\ \nu_e$ or μ due to proton production of hadron j followed by j decay into ℓ are

$$\phi_\ell^{j,high} = \frac{Z_{pj}(E) Z_{j\ell}(E)}{1 - Z_{pp}(E)} \frac{\ln(\Lambda_j/\Lambda_p)}{1 - \Lambda_p/\Lambda_j} \frac{m_j\, c\, h_0}{E\, \tau_j}\ f(\theta) \phi_p(E, 0), \tag{21}$$

$$\phi_\ell^{j,low} = \frac{Z_{pj}(E) Z_{j\ell}(E)}{1 - Z_{pp}(E)} \phi_p(E, 0)\ , \tag{22}$$

where an isothermal model for the atmosphere, in which $\rho(h) = \rho_0 \exp(-h/h_0)$ describes the density profile as a function of altitude h. The parameters are $h_0 = 6.4$ km and $\rho_0 = 2.03 \times 10^{-3}$ g/cm^3 [22]. When the cascade involves charmed hadrons, the low energy behavior dominates and the flux is called "prompt". Critical energies, below which the decay length is less than the vertical depth of the atmosphere, range from $3.7 - 9.5 \times 10^7$ GeV [14].

Eqs. (10) and (11) show that the bases for the calculation of the prompt lepton fluxes are production and decay Z-moments involving charm. The main uncertainties in the calculation of the lepton flux from atmospheric charm are the production Z-moments: Z_{pD} and $Z_{p\Lambda_c}$. The production moments are given by

$$Z_{pc} = 2 \int_0^1 \frac{dx_E}{x_E} \frac{\phi_p(E/x_E)}{\phi_p(E)} \frac{1}{\sigma_{pA}(E)} \frac{d\sigma_{pA\to c\bar{c}}(E/x_E)}{dx_E}\ . \tag{23}$$

The differential cross section is evaluated here using perturbative QCD. The factor of two accounts for the multiplicity of charmed (or anticharmed) particles. The charm Z-moments can be converted to hadronic moments by

$$Z_{pj}(E) = f_j\, Z_{pc}(E)\ , \tag{24}$$

where f_j is the fraction of charmed particles which emerges as hadron j, where $j = D^0,\ D^+,\ D_s^+$ and Λ_c. We implicitly sum over particles and antiparticles.

The inelastic proton-air cross section $\sigma_{pA}(E)$ is parameterized by [23]

$$\sigma_{pA}(E) = 280 - 8.7 \ln(E/\text{GeV}) + 1.14 \ln^2(E/\text{GeV})\ \text{mb}\ . \tag{25}$$

The total cross sections are parameterized using the particle data book values [24] based on Regge theory [25]. The prompt lepton flux below 10^8 GeV is insensitive to the detailed values of Λ_j because essentially all of the charmed hadrons decay before reaching the surface of the earth. Therefore, for most of the energy range considered here, the charmed particles are "low energy" and Eq. (11) describes the lepton fluxes.

The charm production cross section and energy distribution are the largest uncertainties in the calculation of the prompt lepton fluxes. Since the charm quark mass is of the order of 1.3 GeV, the treatment of the charm quark as a heavy quark may be questionable. Theoretical uncertainties, due to the possible range of charm quark masses, as well as the usual factorization and renormalization scale dependence need to be studied. Theoretical predictions based on perturbative QCD calculation fit the available data reasonably well in

the energy range up to 800 GeV beam energy [26]. However, atmospheric lepton flux calculations require beam energies up to and beyond 10^8 GeV. The parton distribution functions are needed at very small parton momentum fraction x, outside of the measured regime [27].

We have addressed the following theoretical issues:

- the effect of next-to-leading order corrections on the cross section and charmed particle energy distribution,
- charmed quark mass dependence,
- factorization and renormalization scale dependence,
- the consequences of the small-x behavior of the parton distribution functions on the interaction Z_{pc} moment, and
- the A dependence of the proton-air charm production cross section.

The next-to-leading order (NLO) total charm cross section has been calculated by Nason, Dawson and Ellis [28] and by van Neerven and collaborators [29]. The NLO cross section is a factor of between 2 and 2.5 larger than the leading order cross section. Gluon fusion dominates the production process. We show the importance of the charm quark mass in the NLO cross section. We compare the NLO $\sigma(pN \to c\bar{c}X)$ as a function of the beam energy E obtained with the renormalization scale μ equal to the factorization scale M equal to the charm quark mass m_c with $m_c = 1.3$ GeV and $m_c = 1.5$ GeV. The cross sections are evaluated using the CTEQ3 parton distribution functions [30]. The corresponding value of $\Lambda_4^{\overline{MS}}$ is 239 MeV. We note that the fixed target data from a summary by Frixione *et al.* [31] seem to prefer $m_c = 1.3$ GeV. The CTEQ3 parton distribution functions will be our canonical set, in part because they incorporate global fits to HERA data, and while their validity is not claimed for parton fraction x below $x_{min} = 10^{-5}$ and $Q_0 = 1.6$ GeV, the program nevertheless provides smooth parton distribution functions below these values.

We study dependence of the total cross section on the scale and parton distribution. We plot the NLO cross section for different values of μ and M: using the CTEQ3 structure functions, we set $\mu = M = m_c$ (dot-dashed) and $\mu = m_c$, $M = 2m_c$ (solid) with $m_c = 1.3$ GeV. The dashed line is the cross section obtained with the MRSD- parton distribution functions [32] and scales $\mu = m_c$, $M = 2m_c$ with $m_c = 1.3$ GeV. We compare those with the data.

The MRSD- distribution functions have a small-x behavior that is suggested by the BFKL approach [33]. In the small-x limit, the parameterization of the gluon (and sea quark) distribution functions at reference scale Q_0 is

$$xg(x, Q_0) \sim x^{-\lambda} \ . \tag{26}$$

The D- distributions have $\lambda = 0.5$. Typically, global fits such as the MRSA [34], MRSG[35] and CTEQ3 distributions have $\lambda \simeq 0.3$. By using the D- distributions, we are effectively setting an upper limit on the perturbative charm cross section, given our choices of m_c, μ and M. We note that, generally, parton distribution functions begin evolution at Q_0 larger than 1.3 GeV. Consequently, our default factorization scale is $M = 2m_c$ so that we can use more than the CTEQ3 parameterizations.

We find that at low energies, the total cross section has weak dependence on the choice of the scale and the parton distribution function. At high energies, $E \geq 10^6$ GeV, there is a factor of 1.7-2.1 increase from $M = m_c$ to $M = 2m_c$. The D- cross section is a factor of 1.3 larger than the CTEQ3 cross section at $E = 10^6$ GeV, both with $M = 2m_c$. The D- cross section increases more rapidly because of the steeper small-x behavior of the parton distribution function and is enhanced by a factor of 2.6 at 10^8 GeV. This gives an overall uncertainty of factor of 5.5 at the highest energy of 10^8 GeV. The MRSA and MRSG cross sections for $M = 2m_c$ lie between the upper and lower curves.

The total charm cross section in p-Air collisions, $\sigma_{pA\to c\bar{c}}(E)$, can be written as

$$\sigma_{pA\to c\bar{c}} = A^{\gamma}\sigma_{pN\to c\bar{c}} \tag{27}$$

We have evaluated the A dependence for charm pair production using a Glauber-Gribov model of nuclear shadowing [36]. We find that over an energy range of $10^2 - 10^6$ GeV, $\gamma = 1.0 - 0.8$. Since $A = 14.5$, the shadowing effect is small, so we set $\gamma = 1$. This is consistent with recent measurements at $E = 800$ GeV [37]. Low energy measurements at larger x_E [38] indicate smaller γ values ($\gamma \simeq 0.75$), which would reduce our flux predictions by an overall factor of 0.5.

We have used a comparison between data and theory for the total cross section to show that $m_c = 1.3$ GeV is a reasonable choice, and to estimate the range of cross sections, related to the approximate uncertainty in the flux. To evaluate Z_{pc}, we need the energy distribution of the charmed particle. We discuss the energy distribution of charm quarks in NLO QCD.

NLO single differential distributions in charm quark production have been evaluated Nason, Dawson and Ellis [39] and incorporated into a computer program, which also calculates double differential distributions, by Mangano, Nason and Ridolfi [40]. The program is time consuming, so we have incorporated NLO corrections to $d\sigma/dx_E$ by rescaling the leading order distribution. The x_E distributions at next-to-leading order are well fit by a K-factor rescaling which is a function of x_E, where K is defined by

$$K \equiv \frac{d\sigma(NLO)/dx_E}{d\sigma(\text{"}LO\text{"})/dx_E} \tag{28}$$

where "LO" means taking the leading order matrix element squared, but using the two-loop $\alpha_s(\mu^2)$ and the NLO parton distribution functions. K defined this way shows the effects of the NLO matrix element corrections.

Using the NLO computer program with the CTEQ3 parton distribution functions, we evaluate $K(E, x_E)$ for $E = 10^3$ and $2K(E, x_E)$ for $E = 10^6$ GeV. K can be parameterized as

$$\begin{aligned} K(E, x_E) &= 1.36 + 0.42\ln(\ln(E/\text{GeV})) \\ &\quad + \Big(3.40 + 18.7(E/\text{GeV})^{-0.43} - 0.079\ln(E/\text{GeV})\Big)\cdot x_E^{1.5} \end{aligned} \tag{29}$$

for $\mu = m_c$ and $M = 2m_c$.

Using the x_E and energy dependent K-factor, we find the charm quark x_E distribution for $E = 10^3$ GeV, 10^6 GeV and 10^9 GeV. The distributions fall rapidly with x_E. The convolution of the differential distribution with the ratio of proton fluxes and interaction

lengths, integrated over x_E at fixed outgoing charm quark energy, is what is required for the Z-moment.

In the context of perturbative hard scattering production of charm pairs, the average x_E value in the evaluation of Z_{pc} is 0.15-0.2. More than 80% of the cross section comes from charm transverse momenta below a value of $2m_c$. In the low transverse momentum limit, $x_E \simeq x_F$. Fixed target experiments measure $d\sigma/dx_F$. The measured charmed meson x_F distributions are consistent with the perturbative NLO QCD calculations for charm quark production, without any fragmentation corrections that would soften the x_F distributions [41]. Fragmentation calculations are applicable at large transverse momentum. For the calculation of Z_{pc}, we are in the low transverse momentum regime, so we do not need fragmentation.

The proton flux falls like $E^{-2.7} - E^{-3}$. The charm production Z-moments increase with energy. We put in the low energy D^+ meson flux and evaluate the $Z_{D^+\ell}$ moment. All of the other low energy decay moments can be obtained by branching fraction rescaling. For the high energy moments, we take $Z_{pk} \sim E^{0.42}$ for the D- distributions and $Z_{pk} \sim E^{0.23}$ for CTEQ3, with $\phi_k \sim Z_{pk}(E)\phi_p(E)$.

We present our results for the prompt atmospheric flux scaled by E^3 for two parton distributions and factorization scale choices. The highest flux at $E = 10^8$ GeV is with the D- distribution and $M = 2\mu = 2m_c$ (dashed). The CTEQ3 distributions with the same choice of scale are represented by the solid line, while the dot-dashed line shows the result when $M = \mu = m_c$. For reference, we show the vertical conventional and prompt flux calculated and parameterized by TIG in Ref. [14]. The fluxes directly reflect the interaction Z-moments. We emphasize that the prompt flux is isotropic except at the highest energies, while the conventional flux is not.

We have also estimated the flux due to pion-air interactions creating charm pairs. The effect is to increase the prompt flux by $\sim 30\%$ at 10^2 GeV and by $\sim 15\%$ at 10^6 GeV. This is a small effect, so we neglect pion contributions to charm production.

The prompt lepton flux evaluated using perturbative QCD can be parameterized as

$$\log_{10}\Big(E^3\phi_\ell(E)/(\mathrm{GeV}^2/\mathrm{cm}^2\,\mathrm{s}\,\mathrm{sr})\Big) = -A + B\,x + C\,x^2 - D\,x^3 \tag{30}$$

where $x \equiv \log_{10}(E/\mathrm{GeV})$.

Several experiments show an excess in muon flux above ~ 10 TeV [7, 8, 9]. Following Rhode in Ref. [7], we consider the quantity $E^{3.65}\phi_\mu(E)$, where ϕ_μ represents the sum of the prompt and vertical conventional flux. Also shown are the data from Ref. [7]. The energy scale factor mostly accounts for the rapidly falling conventional flux [43]. When we add the prompt fluxes to the TIG vertical conventional flux, one sees an enhancement at muon energies above 10^5 GeV, at a higher energy than the experimental excess shown by data points.

In Ref. [44], we have shown that it is possible to enhance the prompt flux sufficiently to account for some of the observed muon excess at a few TeV. This is accomplished by extrapolating the charm cross section at 1 TeV with a faster growth in energy than predicted by perturbative QCD. The x_E dependence was taken as $d\sigma/dx_E \sim (1 - x_E)^4$. The inputs are consistent with fixed target data below 1 TeV beam energies. We found that the predicted prompt flux made significant contributions in the region of the observed excess of muons,

but it does not fully describe the Fréjus data [7]. These inputs are not consistent with perturbative QCD. The experimental excess of muons cannot be accounted for by perturbative QCD production of charm.

We find that the perturbative charm contributions to lepton fluxes are significantly larger than the recent TIG calculation. The prompt muon flux becomes larger than the conventional muon flux from pion and kaon decays at energies above $\sim 10^5$ GeV. We set values of the charmed quark mass, renormalization scale and factorization scale by fitting the charm production cross section to low-energy data, then we extrapolate to higher energies. We find that the NLO corrections give a correction of more than a factor of two which is weakly energy and x_E dependent. Nuclear shadowing corrections are small for all energies, due to the air nucleus being relatively light. The main uncertainty in the perturbative calculation of the prompt flux, given fixed charm mass, factorization scale and renormalization scale, is the small-x behavior of the parton distribution functions. Different choices of scales and distribution functions, extrapolated to low x with the same power law dependence as for $x > 10^{-5}$, yield as much as a factor of ~ 10 discrepancy in the prompt flux at $E = 10^8$ GeV.

We conclude that the prompt muon flux calculated in the context of perturbative QCD cannot explain the observed excess of muons in the TeV region [7, 8, 9], independent of the theoretical uncertainties associated with small parton x. However, prompt fluxes calculated using non-perturbative models of charm production such as discussed in Refs. [44] could provide a muon excess in that energy range. Measurements of the atmospheric flux in the 100 TeV range would help pin down the charm cross section at energies above those currently accessible using accelerators and would provide valuable information about the small-x behavior of the gluon distribution function.

Even though the prompt contributions to the lepton fluxes change the energy behavior of the differential fluxes by a factor of E, the atmospheric neutrino fluxes do not compete with neutrino fluxes from extragalactic sources above 10 TeV [45]. Possible oscillations of muon neutrinos as indicated by the Super-Kamiokande experiment [2] do not affect our results due to the extremely small oscillation probability for the energies of interest.

References

[1] For a review, see T.K. Gaisser, in *Neutrino '96, Proceedings of the 17th International Conference on Neutrino Physics and Astrophysics*, ed. K. Enquist, K. Huitu and J. Maalampi (World Scientific, Singapore, 1997), p. 211 and references therein.

[2] R. Becker-Szendy *et al.*, Phys. Rev. D **46**, 3720 (1992).

[3] Kamiokande Collaboration, H. S. Hirata *et al.*, Phys. Lett. **B205**, 416 (1988); ibid, Phys. Lett. **B280**, 146 (1992); Y. Fukuda *et al*, Phys. Lett. **B335**, 237 (1994).

[4] Soudan Collaboration, W. W. Allison, *et al.*, Phys. Lett. **B391**, 491 (1997); M. C. Goodman, in *Proceedings of the 25th International Cosmic Ray Conference*, eds. M.S. Potieger, B.C. Raubenheimer and D. J. van der Walt, **7**, 77 (1997).

[5] J.G. Learned (SuperKamiokande Collaboration) in *Proceedings of the 25th International Cosmic Ray Conference*, eds. M.S. Potieger, B.C. Raubenheimer and D. J. van der Walt, **7**, 73 (1997).

[6] T. K. Gaisser, F. Halzen and T. Stanev, Phys. Rep. **258**, 173 (1995).

[7] W. Rhode, Nucl. Phys. (Proc. Suppl.) **B35**, 250 (1994).

[8] V. N. Bakatanov *et al.*, Sov. J. Nucl. Phys. **55**, 1169 (1992).

[9] For a summary of experimental results, see E. V. Bugaev *et al.*, eprint archive hep-ph/9803488, and references therein.

[10] See, for example, F. Halzen, eprint archive astro-ph/9707289. The experiment homepage is http://amanda.berkeley.edu/.

[11] Homepage http://infodan.in2p3.fr/antares/saclay/home.html.

[12] E. G. Anassontzis *et al.*, presented at the XVI Int. Workshop on Weak Interactions and Neutrino 97 Conference (Capri). Article available at the experiment homepage http://www.rama1.infn.it/nestor/nestor.html.

[13] I. Sokalski (for the Baikal Collaboration), submitted to the Proceedings of the International Workshop XXXIInd Rencontres de Moriond - Very High Energy Phenomena (Les Arcs, Savoie, France, January 18-25, 1997). Homepage http://www.ifh.de/baikal/baikalhome.html.

[14] M. Thunman, P. Gondolo and G. Ingelman, Astropart. Phys. **5**, 309 (1996).

[15] L. V. Volkova, Yad. Fiz. **31**, 1510 (1980) [English translation: Sov. J. Nucl. Phys. **31**, 784 (1980)]; L. V. Volkova and G. T. Zatsepin, Yad. Fiz. **37**, 353 (1983); H. Inazawa and K. Kobayakawa, Prog. Theor. Phys. **69**, 1195 (1983); L. V. Volkova, W. Fulgione, P. Galeotti and O. Saavedra, Nuo. Cim. C **10**, 465 (1987).

[16] T. Sjöstrand, Comput. Phys. Commun. **82**, 74 (1994).

[17] T. K. Gaisser, *Cosmic Rays and Particle Physics*, (Cambridge University Press, New York, 1990).

[18] P. Lipari, Astropart. Phys. **1**, 195 (1993).

[19] P. Pal and D. P. Bhattarcharyya, Nuo. Cim. **C15**, 401 (1992).

[20] T. H. Burnett et al., (JACEE Collaboration), Ap. J. **349**, L25 (1990).

[21] A. Gregory and R. W. Clay, in *CRC Handbook of Chemistry and Physics* (CRC Press Inc., Boca Raton, Florida, 1982-1983) p. F-175.

[22] K. Maeda, Fortschr. Phys. **21**, 113 (1973).

[23] H. H. Mielke, M. Foller, J. Engler and J. Knapp, J. Phys. G **20**, 637 (1994).

[24] See Table 36.2 in R. M. Barnett et al. (Particle Data Group), Phys. Rev. D **54**, 1 (1996).

[25] A. Donnachie and P. V. Landshoff, Phys. Lett. **B296**, 227 (1992).

[26] The data were taken from a summary by S. Frixione et al., e-print archive hep-ph/9702287, to be published in *Heavy Flavors II*, edited by A. J. Buras and M. Lindner, World Scientific, Singapore.

[27] C. Adeloff *et al.* (H1 Collaboration), Nucl. Phys. **B497**, 3 (1997); M. Derrick *et al.* (ZEUS Collaboration), Z. Phys. **C72**, 399 (1996).

[28] P. Nason, S. Dawson and R. K. Ellis, Nucl. Phys. **B303**, 607 (1988).

[29] W. Beenakker, H. Kuijf, W. L. van Neerven and J. Smith, Phys. Rev. D **40**, 54 (1989); T. Matsuura, S. C. van der Marck and W. L. van Neerven, Nucl. Phys. **B319**, 570 (1989).

[30] H. Lai *et al.* (CTEQ Collaboration), Phys. Rev. D **51**, 4763 (1995).

[31] S. Frixione, M. L. Mangano, P. Nason and G. Ridolfi, Nucl. Phys. **B431**, 453 (1994). See also the review by S. Frixione *et al.*, Ref. [28].

[32] A. D. Martin, W. J. Stirling and R. G. Roberts, Phys. Lett. **B306**, 145 (1993).

[33] E. A. Kuraev, L. N. Lipatov and V. S. Fadin, Zh. Eksp. Teor. Fiz. **71**, 840 (1976) [Sov. Phys.-JETP **44**, 443 (1976)].

[34] A. D. Martin, W. J. Stirling and R. G. Roberts, Phys. Rev. D **50**, 6734 (1994).

[35] A. D. Martin, W. J. Stirling and R. G. Roberts, Phys. Lett. **B354**, 155 (1995).

[36] I. Sarcevic and P. Valerio, Phys. Rev. C **51**, 1433 (1995).

[37] M. J. Leitch *et al.* (E789 Collaboration), Phys. Rev. Lett. **72**, 2542 (1994).

[38] M. E. Duffy *et al.*, Phys. Rev. Lett. **55**, 1806 (1985).

[39] P. Nason, S. Dawson and R. K. Ellis, Nucl. Phys. **B327**, 49 (1989); *ibid.* **B335**, 260 (1990).

[40] M. Mangano, P. Nason and G. Ridolfi, Nucl. Phys. **B373**, 295 (1992).

[41] See, for example, G. Alves et al. (E769 Collaboration), Phys. Rev. Lett. **77**, 2392 (1996).

[42] T. Sjöstrand, Comput. Phys. Commun. **27**, 243 (1982).

[43] A better choice of rescaling given our assumed cosmic ray flux would be $E^{3.7}\phi_\mu$.

[44] L. Pasquali, M. H. Reno and I. Sarcevic, eprint archive hep-ph/9710363, *Astropart. Phys.* **9** (1998).

[45] For a discussion of recent models and event rates, see R. Gandhi, C. Quigg, M. H. Reno and I. Sarcevic, Astropart. Phys. **5**, 81 (1996) and Fermilab preprint FERMILAB-PUB-98/087-T (eprint archive hep-ph/9807264).

Particle Production in Galactic and Extragalactic Astrophysical Sources

(S. Markoff, F. Melia and I. Sarcevic, *Astrophys. J. (Letters)* **47**, 489 (1997); *Astrophys. J.* **522**, 870 (1999).

Recent detection of a γ-ray flux from the direction of the Galactic center by EGRET on the Compton GRO raises the question of whether this is a point source or whether the emitter is diffuse. Using the latest experimental particle physics data and theoretical hadronic cross-sections, we have examined in detail the γ-ray spectrum produced by synchrotron, inverse Compton scattering and mesonic decay resulting from the interaction of relativistic protons with hydrogen accreting onto a point-like object. Such a population of high-energy baryons may be expected to form within an accretion shock as the inflowing gas becomes supersonic. This scenario is motivated by hydrodynamic studies of Bondi-Hoyle accretion onto Sgr A*, which indicate that many of its radiative characteristics may ultimately be associated with energy liberated as this plasma descends down into the deep potential well. Earlier attempts at analyzing this process concluded that the EGRET data are inconsistent with a massive point-like object. We demonstrate that a more careful treatment of the physics of p-p scattering suggests that a $\sim 10^6\ M_\odot$ black hole may indeed be contributing to this high-energy emission.

Several high-energy instruments have detected X-ray and γ-ray emission from the direction of the Galactic Center. The implications for the radio point source Sgr A* are rather interesting, since the X-ray luminosity is not as large as what is expected based on X-ray observations of other, smaller black hole candidates. Of critical importance to our understanding of the high-energy emissivity of this source, in conjunction with the global high-energy properties of the inner 50 pc region of the Galaxy, is the more recent detection by EGRET on board the Compton GRO of a central ($< 1^o$) $\sim$ 30 MeV - 30 GeV continuum source with luminosity $\approx 5 \times 10^{36}$ ergs s^{-1}). The Sgr* spectrum observed appears to be well represented by a hard power-law with a cut-off at tens of GeV, which is significantly different from that of the Galactic diffuse emission, but may resemble the spectra of γ-ray pulsars. At lower energies, COMPTEL's limited angular resolution does not permit us to distinguish between a point source and a continuum emission from the Galactic center molecular arm, but the COMPTEL data do provide useful upper limits. The compiled data set yields a photon spectral index $\alpha = -1.74 \pm 0.09$ ($S = S_0\, e^\alpha$).

These γ-rays may originate either (1) close to the massive black hole, possibly from the action of relativistic particles accelerated by a shock within the accreting plasma, or (2) in more extended features where relativistic particles are known to be present, including the Galactic center Arc. Recombination lines detected from the Sickle, which is a component of the Arc, suggest the existence of thermal material there, while the detection of polarized emission from the straight filaments of the Arc and the absence of recombination lines show the dominance of synchrotron radiation from this component.

In the case of shock acceleration of protons in the vicinity of the black hole, who in addition considered a thermal distribution of hot protons), the γ-rays may result from the decay of pions produced via p-p collisions by relativistic protons energized at an accretion shock. Although the multiplicity of pion production (i.e., the number of pions produced per collision) is a strong function of energy, in all previous calculations it was approximated with

a constant value of 3. The fact that it can change by orders of magnitude at higher energy clearly has an impact on the ensuing photon distribution. In addition, ignoring the role of cascading protons (as was done earlier) is not a valid approximation when the energy carried away by the exiting channel products is as high as 0.5 of the incoming proton energy. Our goal was to examine the hypothesis of a black hole origin for the γ-rays employing the most up-to-date data for the energy-dependent cross-sections, inelasticity, and pion multiplicity, together with a self-consistent treatment of the particle cascade.

It is not unreasonable to suppose that a fraction of the particles (mostly electrons and protons for cosmic abundance) are accelerated to very high energy by the shock. However, the greater synchrotron and inverse Compton efficiency of the electrons compared to that of the protons limits the maximum attainable Lorentz factor of the former by several orders of magnitude compared to that of the latter, and so for reasons we discuss more fully below, the (accelerated) electron contribution to the radiation field is negligible. The relativistic protons are injected through the shock region with a rate $\dot{\rho}_p(E_p) = \rho_o E_p^{-x}$ cm^{-3} s^{-1} GeV^{-1}. In steady state, this generally leads to a power-law distribution with proton index z typically in the range $2.0 - 2.4$. In our case, the value of z is determined in part by the proton cooling processes and the particle cascade, and as we shall see, $z \sim x$.

These relativistic particles interact with the ambient particles and the magnetic field, producing photons via synchrotron, inverse Compton scatterings and the decay of mesons created during p-p collisions. Because the injected protons are ultrarelativistic, the leading order nucleons produced in the scattering events also contribute to the spectrum via multiple collisions in an ensuing cascade, until they lose most of their energy and rejoin the ambient plasma. The main products in these collisions are pions, which then decay either to photons ($\pi^0 \rightarrow \gamma\gamma$) or leptons ($\pi^{\pm} \rightarrow \mu^{\pm}\nu_{\mu}$, with $\mu^{\pm} \rightarrow e^{\pm}\nu_e\nu_{\mu}$). The latter also provides an influx of relativistic cascade electrons.

Particle Cascade

The relativistic protons undergo a series of interactions that we may summarize as $pN \rightarrow pN\, M_{\pi}\, M_{N\bar{N}}$, where N is either a proton or a neutron, M_{π} represents the multiplicity of pions, and $M_{N\bar{N}}$ is the multiplicity of nucleon/anti-nucleon pairs (both increasing functions of energy). The other possible interactions are $p\gamma \rightarrow p\pi^0\gamma$, $p\gamma \rightarrow n\pi^+\gamma$, $p\gamma \rightarrow e^+e^-p$ and $pe \rightarrow NM_{\pi}$.

The high-energy cutoff for the injected proton distribution is set by determining the Lorentz factor above which the combined energy loss rate due to synchrotron emission, inverse Compton scattering and hadronic collisions exceeds the rate of energy gain due to shock acceleration. This transition energy depends in large measure on the functional form of the inelasticity and the fraction of power transferred to the pions during the p-p collisions. In our calculations, the proton synchrotron and inverse Compton spectra are determined from the steady state proton distribution with the imposition of this high-energy cutoff.

Using the energy-dependent pion multiplicity measured at several center-of-momentum (CM) energies, it is straightforward to determine the pion injection rate from the proton distribution and the physical characteristics of the ambient medium. From here the particle cascade continues with the emission of γ-rays and leptonic decays. The electrons and positrons produced in this fashion themselves constitute an energetic population and one must assess their contribution to the overall spectrum via synchrotron emission and inverse Compton scattering.

For the conditions in Sgr A*, the p-p collisions dominate over all other pion production modes. The relevant energy (E_p) range is bounded at the low end by the pion production threshold and at the high end by the maximum attainable Lorentz factor, as discussed above. Using logarithmic bins, and assuming time independence, we first calculate the steady state proton distribution $\rho_p(E_p)$ using the space independent diffusion loss equation. In the p-p CM frame, we use inelasticity, $K_{pp} = 1.35\, s^{-0.12}$ for $\sqrt{s} \geq 62$GeV, and $K_{pp} = 0.5$ for $\sqrt{s} \leq 62$GeV, where the higher energy slope is from Alner et al. (1986), normalized to match the approximately constant low energy value. In this frame, then, $\sqrt{s} = (1 - K_{pp})\sqrt{s}$, with $s = 2m_p(E_p + m_p)$.

The cross section σ_{pp} is taken as a function of energy from the most current particle physics data . Unfortunately, the highest energy achieved in modern colliders is orders of magnitude below the values attained in our system. However, the data for $s > 100$ GeV have a log-linear form which makes it possible to extrapolate up to much higher E_p. For the entire range, this is within the Froissart upper bound, which states that at extremely high energy, $\sigma_{pp\,\infty} \propto (\ln s)^2$.

From our steady state relativistic proton distribution we calculate the synchrotron and inverse Compton scattering spectra, following Rybicki & Lightman (1979). This distribution can also be used to determine the rate, $R_{pp} = n_p\, \sigma_{pp}(E_p)\, c\, \rho_p(E_p)\ \ cm^{-3}s^{-1}GeV^{-1}$, of p-p collisions. For each of these collisions, a multiplicity M_π of pions is produced, with a ratio of charged to neutral particles of roughly 2:1. These have a distribution in transverse (to the beam in experiments, in our case to the direction of the boost back to the lab frame) momentum $dN_\pi/dp_\perp$, which is measured as a function of $\sqrt{s}$ at collider experiments. In order to find the energy of the pions in the CM frame, we also need the parallel component of the momentum, $p_\parallel$, which we extract from the pion distribution as a function of the rapidity, y. In the CM frame, $y = (1/2)\ln[(E^*_\pi + p_\parallel)/(E^*_\pi - p_\parallel)]$, and $y \approx -\ln[\tan(\theta/2)]$ for relativistic energies, where $\cos\theta = p_\parallel / \mid p \mid$. At lower energy ($\sqrt{s} > 200$ GeV), dN_π/dy is Gaussian in shape, the top of which widens gradually into a plateau with increasing energy. The width and the height of this plateau can be fit to functional forms in s.

The charged pions decay to leptons, which can themselves be a source of radiation from synchrotron and Compton processes. We follow a procedure for the $e^\pm$ completely analogous to that developed above. As with the protons, we use the diffusion loss equation to find the steady state $e^\pm$ distribution.

In all, there are five spectral components resulting from the interaction of relativistic protons with the ambient medium near Sgr A* that may be contributing to the EGRET γ-ray source 2EGJ1746-2852. These are: proton synchrotron, proton inverse Compton scattering, $e^\pm$ synchrotron, $e^\pm$ inverse Compton scattering, and pion decay. In attempting to fit the EGRET data we find that, for a reasonable efficiency (i.e., $\eta \sim 10\%$), the proton synchrotron spectrum dominates over that of the photons from π^0 decay as long as the proton injection index $x \sim 2.2$. We consider all five of these components for the case when $r_{sh} = 40r_g$, and $x = 2.0$ with an efficiency of 1%. The proton synchrotron seems to fit the data reasonably well, but clearly misses the apparent low energy turnover in the EGRET data, and the upper limits for the highest energy COMPTEL points. This could be due to the simplified geometry we have adopted in this paper, but this seems unlikely to us since the synchrotron spectrum depends primarily on the particle physics rather than the geometry. It is also evident that Compton scattering is not important for this source, and that the cascade $e^\pm$ are relatively

ineffective. For these parameters, the photons produced by pion decay are also insignificant. Placing the shock at $120r_g$ instead of $40r_g$ increases the emission area while decreasing B, and the proton synchrotron spectrum misses several data points at both the low and high energy ends of the EGRET spectrum.

With the shock at $40r_g$, the π^0 decay spectral component begins to dominate over synchrotron when $x > 2.2$. We find the three proton spectral contributions for the case $x = 2.4$, which leads to a steady state proton distribution with index $z = 2.46$. Here, the efficiency η needs to be $\approx 9\%$ in order for the pion decay photons to match the data. It should be noted that the fit is rather good.

The shape of the π^0-induced γ-ray spectrum can be understood as follows. The center of the curve is set by the energy ($\epsilon_\gamma = 67.5$ MeV) of the decay photons in the π^0 rest frame, and the width is determined by Doppler broadening. The slope of the sides, and hence the index of the EGRET spectrum, is due to the falloff in the number of decaying pions at higher energy. Each pion decay produces a flat photon spectrum whose width increases with E_π. So the cumulative effect of all the decays makes the biggest contribution near $\epsilon_\gamma = 67.5$ MeV since all pions contribute at this energy. The relative contribution to the spectrum at lower or higher ϵ_γ then depends on the overall pion distribution, which in turn is a function of both the pion multiplicity and the relativistic proton energy profile.

The flattened top, and hence the turnover in the pion decay spectrum at the low energy boundary of the EGRET window is due to the cutoff in pion production near the threshold. It is important to emphasize that the pion decay spectrum cannot be translated laterally. As such, a simultaneous match of both this turnover and the spectral slope is significant.

Our detailed study shows that a population of relativistic protons energized within an accretion shock near a super-massive black hole at the Galactic center may be contributing to the ~ 30 MeV–30 GeV emission from this region. Depending on the value of the injected proton index (i.e., $x \sim 2.2$ or $x > 2.2$), this contribution may come either from proton synchrotron or π^0 decay. However, the synchrotron emissivity cannot account for the turnover in the EGRET spectrum and some of the COMPTEL upper limits at $\epsilon_\gamma \sim 100$ MeV, whereas the pion-induced photon distribution has a natural flattening there due to the threshold for pion production in p-p scatterings.

Neutrino Interactions and Oscillations in the Standard Model and Beyond

Together with her graduate student S. Iyer Dutta and with M. H. Reno, Sarcevic had proposed a novel concept for detecting $\nu_\mu \rightarrow \nu_\tau$ oscillations with extragalactic neutrinos. They have shown that by comparing event rates for upward hadronic/electromagnetic showers with the rates for the upward-going muons, the tau neutrino signature is unambiguous, providing the unique opportunity for future kilometer-size neutrino detectors to search for neutrino oscillations testing Δm^2 down to $10^{-17} eV^2$, far beyond current accelerator experiments. In collaboration with M. H. Reno and L. Pasquali, Sarcevic has also studied the origin of recently reported by Frejus Collaboration enhanced muon flux in TeV energy range, indicating that perhaps prompt muon flux from charm decay is larger than expected in the "standard" atmospheric neutrino and muon calculation. They have evaluated the prompt muon and neutrino production in cosmic ray interactions with nuclei in the atmosphere which arise

through semi-leptonic decays of hadrons containing heavy quarks, mostly charm, including next-to-leading order radiative corrections and improved small-x parton distributions. They have also studied contribution from the secondary decays of charmed particles. The results for cosmic ray energies are significantly different than what is currently part of the "standard" atmospheric neutrino flux, but not sufficiently large in TeV energy range to explain the Frejus anomalous muon flux. In collaboration with Raj Gandhi, C. Quigg and M. H. Reno, Sarcevic had shown that planned kilometer-size neutrino detectors have a very good chance of testing different theoretical models of particle production in Active Galactic Nuclei (AGN), the gamma-ray bursts models recently proposed by Bahcall and Waxman and the models of topological defects formed in the early Universe. In particular, due to a singular behavior of the parton distributions at small x, the angular dependence of the muon event rates from different sources is shown to be the optimal way for the detection of neutrinos from point sources. Sarcevic, together with S. Iyer Dutta, M. H. Reno and D. Seckel, is currently working on muon and tau energy losses as they pass through the Earth. Their preliminary results indicate that photonuclear reactions of τ leptons are the dominant energy loss at energies greater than 10^{17}eV, thus enabling the detection of ν_τ by observing and identifying τ lepton in the energy range where the "double-bang" technique is inefficient due to the increasing tau decay length. Together with K. Dienes, Sarcevic has started to investigate the possibility of probing extra dimensions with neutrino oscillations. They have constructed a model with large extra dimensions that has no flavor mixing on the brane and the bulk-brane couplings are flavor-blind, but still induces neutrino flavor oscillations through the Kaluza-Klein modes. They are currently working on explaining all the neutrino oscillation data, atmospheric, LSND and solar, with this simple model, and they are expecting to be able to put stringent constraints on the size of the extra dimension.

Studying $\nu_\mu \to \nu_\tau$ Oscillations with Extragalactic Neutrinos

Recently we have proposed a novel approach for studying $\nu_\mu \to \nu_\tau$ oscillations with extragalactic neutrinos [1]. Recent Super-Kamiokande (SuperK) measurements of the low atmospheric ν_μ/ν_e ratio and the strong zenith angle dependence of the ν_μ events suggest oscillations of ν_μ into ν_τ with the parameters $\sin^2 2\theta > 0.7$ and $1.5\times10^{-3} < \Delta m^2 < 1.5\times10^{-2}$ eV^2 [2]. This is in agreement with previously reported results on the atmospheric anomaly by Kamiokande [3] and MACRO [4] and is consistent with limits from other experiments, e.g., CHOOZ [5]. Confirmation of $\nu_\mu \to \nu_\tau$ oscillations and determination of neutrino mixing angles would be a crucial indication of the nature of physics beyond the Standard Model. The firmest confirmation of this hypothesis would be via detection of τ leptons produced by charged current interactions of ν_τ's resulting from oscillations of ν_μ's, which is extremely difficult with current neutrino experiments.

Sources of extragalactic neutrinos are Active Galactic Nuclei and Gamma Ray Bursts. With distances of 100 Mpc or more, they provide an unusually long baseline for possible detection of $\nu_\mu \to \nu_\tau$ with mixing parameters Δm^2 down to 10^{-17}eV^2 [6], many orders of magnitude below the current accelerator experiments. Over such long baselines, half of the neutrinos arriving at the earth would be ν_τ's in oscillation scenarios, the other half being ν_μ's. By observing both ν_μ and ν_τ from extragalatic sources such as Gamma Ray Bursts (GRBs) [7] and Active Galactic Nuclei (AGN) [8], neutrino oscillation hypothesis would be confirmed and models of these sources would be tested.

The effect of attenuation of the neutrino flux due to interactions of neutrinos in the Earth is qualitatively different for ν_μ and ν_τ. Muon neutrinos are absorbed by charged current interactions, while tau neutrinos are regenerated by tau decays. The Earth never becomes opaque to ν_τ, though the effect of $\nu_\tau \to \tau \to \nu_\tau$ interaction and decay processes is to degrade the energy of the incident ν_τ. The identical spectra of ν_μ and ν_τ incident on the Earth emerge after passage through the Earth with distinctly different spectra. The preferential penetration of ν_τ through the Earth is of great importance for high energy neutrino telescopes such as AMANDA, NESTOR and ANTARES.

We have shown that the energy spectrum of the ν_τ becomes enhanced at low energy, providing a distinctive signature for its detection. The degree of enhancement depends on the initial neutrino flux. We consider initial fluxes $F_\nu^0 \sim E^{-n}$ for $n = 1, 2, 3.6$, a GRB flux and an AGN flux. We solve the coupled transport equations for lepton and neutrino fluxes as indicated below.

Let $F_{\nu_\tau}(E, X)$ and $F_\tau(E, X)$ be the differential energy spectrum of tau neutrinos and tau respectively at a column depth X in the medium. Then, one can derive the following cascade equation for neutrinos as,

$$\frac{\partial F_{\nu_\tau}(E,X)}{\partial X} = -\frac{F_{\nu_\tau}(E,X)}{\lambda_{\nu_\tau}(E)} + \int_E^\infty dE_y \left[\frac{F_{\nu_\tau}(E_y,X)}{\lambda_{\nu_\tau}(E_y)}\right] \frac{dn}{dE}(\nu_\tau N \to \nu_\tau X; E_y, E) +$$

$$+ \int_E^\infty dE_y \left[\frac{F_\tau(E_y,X)}{\rho_\tau^{dec}(E_y)}\right] \frac{dn}{dE}(\tau \to \nu_\tau X; E_y, E) + \int_E^\infty dE_y \left[\frac{F_\tau(E_y,X)}{\lambda_\tau(E_y)}\right] \frac{dn}{dE}(\tau N \to \nu_\tau X; E_y, E)$$

and for taus as,

$$\frac{\partial F_\tau(E,X)}{\partial X} = -\frac{F_\tau(E,X)}{\lambda_\tau(E)} - \frac{F_\tau(E,X)}{\rho_\tau^{dec}(E,X,\theta)} + \int_E^\infty dE_y \left[\frac{F_{\nu_\tau}(E_y,X)}{\lambda_{\nu_\tau}(E_y)}\right] \frac{dn}{dE}(\nu_\tau N \to \tau X; E_y, E).$$

The first term in Eq. (1) is a loss due to the neutrino interactions, the second is the regeneration term due to the neutral current, the third term is a contribution due to the tau decay and the last term is the contribution due to tau interactions.

In Eq. (2), the first term is a loss due to tau interactions, the second term is a loss due to the tau decay, while the last term is a contribution from neutrino charged current interactions. Tau decays are more important than tau interactions at the energies below 10^6GeV. Tau charged current interaction length and the photonuclear interaction length both become comparible to the tau decay length at $E > 10^8$GeV. The tau energy loss, in principle, affects the shape of the tau neutrino energy spectrum by enhancing the lower energy part [9]. We are currently studying this effect.

To demonstrate the importance of regeneration of tau neutrinos from tau decays, we evaluate the tau neutrino flux for several input neutrino spectra and compare to the attenuated ν_μ flux. For the incoming neutrino spectrum we use $F_\nu^0(E) \sim E^{-n}$. We solve coupled transport equations for the fluxes by introducing Z-moments and solving them iteratively. Details can be found in Ref. [1].

For an incoming flux, $n = 1$, we find that the ν_τ flux is enhanced (relative to the incoming ν_τ flux) for all nadir angles for $E_{\nu_\tau} = 10^4$ GeV and 10^5 GeV, and for $\theta > 50^\circ$ for $E_{\nu_\tau} = 10^6$

GeV. The peak of the enhancement gets shifted toward the higher nadir angles as the energy increases. This is due to the fact that high energy ν_τ can remain high energy if the column depth is small, i.e. for large nadir angles. In case of the steeper incoming flux, $n = 2$, we find that ν_τ's are less attenuated than the ν_μ's, and the expected enhancement at low energy is not evident due to the steepness of the flux. For even steeper flux, $n = 3.6$, the difference between ν_τ and ν_μ flux is very small. For small nadir angles, $\theta = 0$ and 30° and $F^0_\nu(E) \sim E^{-1}$ we find that enhancement of tau neutrinos is in the energy range of 10^2 GeV and 10^5 GeV, while for $\theta = 60^\circ$, the enhancement extends up to 10^6 GeV. In contrast the ν_μ flux is attenuated for all the nadir angles. When the incoming flux is steeper, $n = 2$, the ν_τ flux appears to be attenuated at high energies, although less than the ν_μ flux. For $n = 3.6$, the energy dependence of these two fluxes is very similar, they are both reduced at high energies, and the effect is stronger for smaller nadir angle, since in this case the column depth is larger and there are more charged current interactions possible.

In case of the GRB fireball model [7] we find that due to the steepness of the input flux for $E_{\nu_\tau} > 100$ TeV, the ν_τ flux is enhanced only by about $10 - 27\%$, depending on the energy and nadir angle. However, for the AGN quasar model [8], we find that the ν_τ flux is a factor of 2 to 2.5 times larger than the input flux, for nadir angle, $\theta = 0$. We find that for larger angles, the effect is smaller. Detection of AGN neutrinos would be optimal for small nadir angles and for ν_τ with energy of 10^2 GeV to 10^4 GeV.

References

[1] S. Iyer, M. H. Reno, I. Sarcevic, *Phys. Rev.* **D61**, 053003 (2000).

[2] Super-Kamiokande Collaboration (Y. Fukuda et al.) *Phys. Rev. Lett.* **82**, 2430 (1999); ibid, hep-ex/9908049; *Phys. Lett.* **B433**, 9 (1998); *Phys. Lett.* **B436**, 33 (1998); ibid, *Phys. Rev. Lett.* **81**, 1562 (1998).

[3] Kamiokande Collaboration, S. Hatakeyama *et al.*, *Phys. Rev. Lett.* **81**, 2016 (1998).

[4] MACRO Collaboration, M. Ambrosio *et al.*, *Phys. Lett.* **B434**, 451 (1998).

[5] CHOOZ Collaboration, M. Apollonio *et al.*, *Phys. Lett.* **B420**, 397 (1998).

[6] F. Halzen and D. Saltzberg, *Phys. Rev. Lett.* **81**, 4305 (1998)

[7] E.Waxman and J.N.Bahcall, *Phys. Rev. Lett.* **78**, 2292 (1997).

[8] F. W. Stecker and M. Salomon, *Space Sci. Rev.* **75**, 341 (1995).

[9] S. Iyer Dutta, M. H. Reno, I. Sarcevic and D. Seckel, in preparation.

Tau Neutrino Appearance with a 1000 Megaparsec Baseline

We have recently proposed the best way to detect the appearance of high energy tau neutrinos due to $\nu_\mu \to \nu_\tau$ oscillations of extragalactic neutrinos by measuring the neutrino

induced upward hadronic and electromagnetic showers and upward muons [1]. Charged-current interactions of the upward tau neutrinos below and in the detector, and the subsequent tau decay create muons or hadronic and electromagnetic showers. The background for these events are muon neutrino and electron neutrino charged-current and neutral-current interactions, where in addition to extragalactic neutrinos, we consider atmospheric neutrinos. We find significant signal to background ratios for the hadronic/electromagnetic showers with energies above 10 TeV to 100 TeV initiated by the extragalactic neutrinos and show that the tau neutrinos from point sources also have the potential for discovery above a 1 TeV threshold. A kilometer-size neutrino telescope has a very good chance of detecting the appearance of tau neutrinos when both muon and hadronic/electromagnetic showers are detected.

Direct detection of ν_τ appearance is extremely difficult because at low energies, the charged-current cross section for producing a tau is small and the tau has a very short lifetime. Furthermore, the enhancement of the tau neutrino flux does not necessarily translate to dramatic modifications of the standard model (no-oscillation) rates for upward-going muons, especially in view of uncertainties in the normalization of the extragalactic fluxes. However, by comparing rates for upward-going muons with rates for upward hadronic/electromagnetic (EM) showers, we find that the signature of tau neutrino interactions is unambiguous for a number of neutrino flux predictions.

We have studied several extragalactic sources for ultra-high energy neutrinos: Active Galactic Nuclei, Gamma Ray Bursts and topological defects formed in the early Universe. AGN are the most luminous objects in the Universe. Most of this radiation comes from their central region, indicating that the energy radiation most likely comes from accretion of matter into a superheavy black hole. Protons within the AGN get accelerated via first order Fermi acceleration to very high energies. They interact with protons and photons in the infalling gas, or in the jets along the rotation axis. Photoproduction takes place in the optically thick photon field around the core, producing pions, which decay into charged leptons, neutrinos and photons. The recent detections of energetic photons ($E_\gamma \sim 100$ MeV) from about 40 AGN by the EGRET collaboration [2] and especially of TeV photons from Mkn 421, Mkn 501 [3] and 1ES2344+514 by the Whipple collaboration [4] support the hadronic mechanism as origin of high energy AGN photons. If the observed photons are decay products of π^0's produced in hadronic interactions in the disk surrounding the AGN, then AGN are also powerful sources of ultrahigh-energy (UHE) neutrinos [5, 6]. Several hadronic models have been proposed, in particular, a blazar model for the AGN with jets [7] and a quasar model for an AGN disk with no jets [8].

Another extragalactic source with powerful radiation and possibly associated high energy neutrino flux are the gamma ray bursts (GRB). Several models have been proposed in order to explain the origin of GRB's. In the fireball model [9], the gamma ray bursts are produced by the dissipation of the kinetic energy of the relativistic expanding fireball with a large fraction, $> 10\%$, of the fireball energy being converted by photopion production to high energy neutrinos. Photomeson production takes place when extremely energetic protons accelerated at high energies in the ultra-relativistic shocks interact with synchrotron photons surrounding the fireball. The decay of these charged pions and subsequently produced muons then produce electron and muon neutrinos. The gamma ray burst model of Waxman and Bahcall (GRB_WB) is parameterized by $F^s_{\nu+\bar{\nu}}(E) = 4.0 \times 10^{-\alpha} E^{-n}$, where $\alpha = 13$ and

$n = 1$ for $E < 10^5$ GeV and $\alpha = 8$ and $n = 2$ for $E > 10^5$ GeV. Cosmic topological defects (TD) such as magnetic monopoles, cosmic strings and domain walls are predicted to be formed in the Early Universe as a result of symmetry breaking and phase transition in Grand Unified Theories (GUTs) of particle interactions. In the TD models, γ-rays, electrons (positrons), and neutrinos are produced directly at ultra-high energies via cascades initiated by the decay of a supermassive elementary "X" particle associated with some Grand Unified Theory, rather than being produced in high energy hadronic interactions. The X particle is usually thought to be released from topological monopoles left over from GUT phase transition. It decays into quarks, gluons, leptons. We have considered neutrino fluxes from topological defects models of Sigl-Lee-Schramm-Coppi (TD_SLSC) [10] and the model of Wichoski-MacGibbon-Brandenberger (TD_WMB) [11]. The main difference between these two models is the main channel for energy loss of the string network, in the former it is the gravitational radiation, while in the later it is the particle production.

We have evaluated the attenuated tau neutrino plus antineutrino flux and attenuated muon neutrino plus antineutrino flux assuming the equal fluxes of tau neutrinos and muon neutrinos incident on the surface of the Earth at a nadir angle of 0° for $F^o_{\nu+\bar{\nu}}(E_\nu) = 0.5 \times 10^{-13} E^{-1}$, $F^o_{\nu+\bar{\nu}}(E_\nu) = 0.5 \times 10^{-7} E^{-2}$, the Stecker-Salamon AGN model, the Mannheim AGN model, the two topological defects models, the Waxman-Bahcall GRB model and the atmospheric ν_e and ν_μ flux. We find that the enhancement of the tau neutrino flux relative to the initial flux and also to the muon neutrino flux, is prominent for the flat fluxes, such as $F^o_\nu(E_\nu) \sim E^{-1}$ [12], the Stecker-Salamon AGN model and the topological defects model of Sigl *et al*. In case of the atmospheric flux, which represents the background, the enhancement is very small due to the steepness of the initial neutrino flux. The angular dependence of the upward ν_τ flux is also distinct.

Detection of muon neutrinos, in general, is via their charged-current interactions. Produced muons have very large average range making the effective volume of an underground detector significantly larger than the instrumented volume. On the other hand, tau neutrino charged-current interactions produce tau, which has a very short lifetime, making its detection extremely difficult. Tau neutrinos will interact via neutral currents, producing a hadronic signal as well. Therefore, the signals of tau neutrino interactions below the double-bang threshold are muons from tau decay, or hadronic/EM showers from the tau production and/or decay. In the first case the background to tau production of high energy muons is ν_μ charged-current interactions. In the latter case, the backgrounds are ν_μ neutral current and ν_e charged-current and neutral current interactions. The background rates are obtained with the assumption that the electromagnetic shower from $\nu_e \to e$ charged current interactions cannot be distinguished from hadronic showers. As a consequence, we evaluate the hadronic/electromagnetic (EM) shower rates.

The standard evaluation of the muon event rate per solid angle for neutrino interactions with isoscalar nucleons N ($\nu_\mu N \to \mu X$) follows from the formula [5]

$$\begin{aligned} \text{Rate} \quad &= A N_A \int_{E_\mu^{\min}}^{\infty} dE_\nu \int dy \langle R_\mu(E_\nu(1-y), E_\mu^{\min}) \rangle \frac{d\sigma_{cc}(E_\nu, y)}{dy} \\ &\times F_\nu(E_\nu, X) \Theta(E_\nu(1-y) - E_\mu^{\min}), \end{aligned} \tag{31}$$

where y is the neutrino energy loss, and $d\sigma_{cc}/dy$ is the charged current differential cross section. $F_\nu(E_\nu, X)$ is the upward neutrino or antineutrino flux which depends on angle

implicitly through the pathlength X. The fluxes of neutrinos and antineutrinos at the detector are different because of the difference in charged and neutral current cross sections below energies of 10^6 GeV [5, 6]. The average range of a muon, $\langle R_\mu(E_\mu, E_\mu^{\rm min})\rangle$, is the range of a muon produced in a charged-current interaction with energy E_μ which, as it passes through the medium, looses its energy via bremsstrahlung, ionization, pair production and photonuclear interaction and arrives in a detector with an energy above $E_\mu^{\rm min}$. Avogadro's number is N_A and A is the effective area of the detector.

The rate for muons produced by the tau neutrino charged current interactions followed by the tau leptonic decays is given by a modified equation, taking into account the branching fraction for $\tau \to \nu_\tau \nu_\mu \mu$ and the decay distribution of the muon via $dn(E_\tau)/dz$ [13], where $z = E_\mu/E_\tau$. The differential event rate is

$$\begin{aligned} \text{Rate} \quad &= AN_A \int_{E_\mu^{\rm min}}^{\infty} dE_\nu \int dy \int dz \langle R_\mu(E_\nu(1-y)z, E_\mu^{\rm min})\rangle \frac{dn(E_\nu(1-y)z)}{dz} \\ &\times \frac{d\sigma_{cc}(E_\nu, y)}{dy} F_\nu(E_\nu, X)\Theta(E_\nu(1-y)z - E_\mu^{\rm min}). \end{aligned} \tag{32}$$

We find that with the exception of the E^{-1} and TD_SLSC fluxes, the observed muon rate is about half of what one would expect in the absence of oscillations. Given the uncertainties in the normalizations of the predicted fluxes, this factor would not unambiguously signal the presence of tau neutrinos from oscillations. The situation with the E^{-1} and TD_SLSC fluxes is only slightly better. There, in the oscillation scenario, the measured muon event rate is about 80% of the no oscillation prediction at $\theta = 0^\circ$, but less than 70% of the prediction for horizontal events. Testing the oscillation hypothesis by measuring upward muons only will be very difficult.

The relatively small contribution to the muon rate from ν_τ's, despite the fact that the attenuated flux of tau neutrinos is larger than that of the muon neutrinos, is due to the fact that the muon carries a small fraction of the initial tau neutrino energy. Even with some "pileup", the tau neutrino fluxes are decreasing fast enough that the muon energy fraction results in sampling a much smaller tau neutrino flux than the corresponding muon neutrino flux. Thus we consider signals that carry a much larger fraction of the incident tau neutrino energy, such as the hadronic/EM shower signal of ν_τ interactions. The next generation of neutrino telescopes may not be able to distinguish between hadronic and electromagnetic showers, so we include in the signal and in the background, processes that include hadrons and electron.

The processes that go into our evaluation of $\nu_\tau \to$ hadrons are

$$\begin{aligned} &\nu_\tau N \to \tau + \text{hadrons},\ \tau \to \nu_\tau + \text{hadrons}\ , \\ &\nu_\tau N \to \tau + \text{hadrons}, \tau \to \nu_\tau + e + \nu_e\ , \\ &\nu_\tau N \to \nu_\tau + \text{hadrons}\ . \end{aligned}$$

For the charged-current interactions, the hadronic/electromagnetic energy is the sum of the energy carried by the hadrons in tau production, as well as the tau decay hadronic energy or tau decay electron energy.

The background for the hadronic/electromagnetic showers is due to the ν_μ and ν_e neutral current interactions, and ν_e charged-current interactions are

$$\nu_{\mu,e} + N \rightarrow \nu_{\mu,e} + \text{hadrons} \ ,$$
$$\nu_e + N \rightarrow e + \text{hadrons} \ .$$

The tau neutrino shower event rate per unit solid angle from charged-current interactions followed by the tau hadronic decay is given by

$$\begin{aligned} \text{Rate} \quad &= VN_A \int_{E_{\rm shr}^{\rm min}}^{\infty} dE_\nu \int dy \int dz \frac{dn(E_\tau)}{dz} \frac{d\sigma_{cc}(E_{\nu_\tau}, y)}{dy} F_{\nu_\tau}(E_{\nu_\tau}, X) \\ &\times \Theta(E_{\nu_\tau}(y + (1-y)(1-z)) - E_{\rm shr}^{\rm min}). \end{aligned} \tag{33}$$

The hadronic energy from the broken nucleon $E_{\rm shr}^{int} = E_\nu y$ and the hadronic energy from the decay $E_{\rm shr}^{\rm decay} = E_\nu (1-y)(1-z)$ are added to get the total shower energy. The neutral (charged) current background event rate is given by

$$\text{Rate} = VN_A \int_{E_{\rm shr}^{\rm min}}^{\infty} dE_\nu \int dy \frac{d\sigma_{nc/cc}(E_\nu, y)}{dy} F_\nu(E_\nu, X) \Theta(E_\nu y - E_{\rm shr}^{\rm min}) \ . \tag{34}$$

We have calculated the upward hadronic/EM shower event rates as a function of the nadir angle for $E_{\rm shr} > E_{\rm shr}^{\rm min}$ where $E_{\rm shr}^{\rm min} = 1$ TeV, 10 TeV and 100 TeV for input fluxes: $F_{\nu+\bar{\nu}}^0 \sim E^{-1}$, $F_{\nu+\bar{\nu}}^0 \sim E^{-2}$ AGN_SS, AGN_M95, TD_WMB, TD_SLSC and GRB_WB, all assuming that $V = 1$ km^3.

We find that in the case of the E^{-1} flux, the contributions from tau neutrinos are large, a factor of 4 times larger than the muon neutrino plus electron neutrino contribution at zero nadir angle. For horizontal showers, the enhancement factor is smaller, about 2. For E^{-2} flux, the tau neutrino contribution is a factor of 1.7 times larger than the muon neutrino plus electron neutrino contributions for upward showers. The AGN_SS rates at zero nadir angle are comprised of 60% tau neutrino induced, decreasing to about 40% tau neutrino induced for horizontal showers. AGN_SS flux gives 25-80 shower events for $E_{\rm shr}^{\rm min} = 10$ TeV and 6-45 events for $E_{\rm shr}^{\rm min} = 100$ TeV with negligible atmospheric background. For AGN_M95 model we find 3-6 shower events per year per steradian for $E_{\rm shr}^{\rm min} = 10$ TeV, with atmospheric background of 2-16 events.

The TD_WMB model shows an enhancement of between 2.1-2.3 for zero nadir angle, and a factor of 1.7 for almost horizontal showers. The more striking enhancement in the TD_SLSC model, where the enhancement is a factor of between 3.7 to 6.2 at zero nadir angle, to a factor of 2 for large nadir angles. However, due to the particularly low normalization of the TD_SLSC flux, the kilometer-size detector would not be sufficient for its detection. For the GRB_WB model in which the enhancement factor is between 1.5 to 2, depending on energy threshold and angle. The event rates for showers with energies above 10 TeV are comparable with the background, but higher energy threshold of 100 TeV would still give a few events per year for large nadir angle with negligible background.

For atmospheric $\nu_\mu + \bar{\nu}_\mu + \nu_e + \bar{\nu}_e$ and $\nu_\tau + \bar{\nu}_\tau$ showers with energies above 10 TeV, the event rates are twice as large as for the E^{-1} flux at small nadir angle. For $E_{\rm shr}^{\rm min} = 10$ TeV, we find the event rates for the showers to be about 8-18 per km^3 per year per steradian for the E^{-2} flux, compared with the atmospheric background of 2-16.

The AGN rates will stand out above the atmospheric background for $E_{\rm shr}^{\rm min} \sim 10$ TeV. The GRB_WB rates are more than half of the atmospheric neutrino rates at the 10 TeV shower threshold at small nadir angles. The TD rates are all quite low overall, and in comparison to the atmospheric background rates.

Since one does not measure separately the tau neutrino induced shower rates and the muon and electron induced shower rates, an effective test of the oscillation hypothesis is to compare the rates with the oscillation hypothesis to the predicted rates without oscillations. To illustrate the effect of oscillations we evaluate the ratio of the shower event rates from ν_τ, ν_μ and ν_e in the oscillation scenario to the shower rates from ν_μ and ν_e in the standard model, with no oscillations. We note that for the E^{-1} flux, the upwrad shower event rates in the oscillation scenario are a factor of 3 larger than in the no oscillation case for $E_{\rm shr}^{\rm min} = 1 - 100$ TeV. For the E^{-2} flux, the enhancement is a factor of 1.5 relative to the no oscillation case. In the case of AGN models, if one assumes oscillations, the shower event rates are factor of 2 to 3 times larger. We show this for AGN_SS model in Fig. 2. For AGN_M95, the ratio ranges between 1.4-1.9, and the shower event rates for TD_WMB are factor of 1.5- 2 enhanced for energy thresholds of 1-100 TeV. In the TD_SLSC model, the shower event rate is a factor of 3-3.6 enhanced at small nadir angles, and a factor of 1.6 enhanced for horizontal showers. In the case of GRB_WB model, there is an enhancement of 1.4-1.7 for $E_{\rm shr}^{\rm min} = 1 - 100$ TeV. We evaluate the ratio of the shower and muon event rates in the case of the oscillation and no oscillation scenario for AGN_SS model and we find that in case of the oscillation scenario this ratio is a factor of 3 times larger than in no oscillation case. We also find the same ratio for all extragalactic sources of neutrinos with energy thresholds of 1TeV, 10TeV and 100TeV. We find that the ratio in the oscillation case is a factor of 2 to 5 larger than in no oscillation case, thus providing clear signal for the oscillations, independent of the specific extragalactic neutrino source.

As concluded in earlier work [5, 6], in general, an energy threshold of between 10 TeV and 100 TeV for upward muons and showers is needed in order to reduce the background from atmospheric neutrinos. We find that diffuse AGN neutrino fluxes, as described by the Stecker-Salamon and Mannheim models, as well as neutrinos from GRBs can be used to detect tau appearance. By measuring upward showers with energy threshold of 10 TeV, and upward muons, the event rates exceed the atmospheric background and are about a factor of 1.5-2 larger than in the no-oscillation scenario.

The detection of $\nu_\mu \to \nu_\tau$ oscillations with a point source might also be possible. With the resolution for the planned neutrino telescopes of 2°, the atmospheric background is reduced by 3.8×10^{-3}. For upward showers, this gives less than 1 event per year for $E_{\rm shr}^{\rm min} = 1$ TeV, and even less for higher energy thresholds. Thus, if the point source has a flat spectrum, for example $F_{\nu+\bar{\nu}} = 10^{-16} E^{-1}$, then one would be able to detect tau neutrinos by measuring upward showers with $E_{\rm shr}^{\rm min} = 1$ TeV. In the more realistic case, when the point source has a steeper spectrum (E^{-2}), such as Sgr A* [14], a normalization of $10^{-7}/{\rm cm}^2/{\rm s}/{\rm sr}/{\rm GeV}$ would be sufficient for the detection of tau neutrinos with threshold of 1 TeV.

References

[1] S. Iyer, M. H. Reno, I. Sarcevic, hep-ph/0005310, to appear in *Phys. Rev.* **D**.

[2] C. E. Fichtel, *et al.*, *Astrophys. J. Suppl.* **94**, 551 (1994).

[3] M. Punch, *et al.* (Whipple Observatory Gamma Ray Collaboration) *Nature (London)* **160**, 477 (1992); A.D. Kerrick *et al.*, *Astrophys. J.* **438**, L59 (1995); J. Quinn, *et al.* (Whipple Observatory Gamma Ray Collaboration) *IAU Circular* 6169 (June 16, 1995).

[4] T. C. Weekes, private communication.

[5] R.Gandhi, C.Quigg, M.H.Reno and I.Sarcevic, *Astropart. Phys.* **5**, 81 (1996).

[6] R.Gandhi, C.Quigg, M.H.Reno and I.Sarcevic, *Phys. Rev.* **D58**, 093009 (1998).

[7] K. Mannheim, *Astropart. Phys.* **3**, 295 (1995).

[8] F. W. Stecker and M. H. Salamon, *Space Sci. Rev.* **75**, 341 (1995).

[9] E.Waxman and J.N.Bahcall, *Phys. Rev. Lett.* **78**, 2292 (1997).

[10] G. Sigl, S. Lee, D. N. Schramm, and P. Coppi, *Phys. Rev. Lett.* **B392**, 129 (1997).

[11] U. F. Wichoski, J. H. Macgibbon, and R. H. Brandenberger, 'High Energy Neutrinos, Photons and Cosmic Rays from Non-Scaling Cosmic Strings,' BROWN-HET-1115, hep-ph/9607165.

[12] S. Iyer, M. H. Reno, I. Sarcevic, *Phys. Rev.* **D61**, 053003 (2000).

[13] L. Pasquali and M. H. Reno, *Phys. Rev.* **D59**, 093003 (1998).

[14] S. Markoff, F. Melia and I. Sarcevic, *Astrophys. J.* **522**, 870 (1999).

[15] T. K. Gaisser, *Cosmic Rays and Particle Physics*, (Cambridge University Press, Cambridge, 1990).

[16] P. Lipari, *Astropart. Phys.* **1**, 195 (1993).

Ultrahigh Energy Neutrino Interactions and Detection of Extragalactic Neutrinos

Neutrino observatories hold great promise for probing the deepest reaches of stars and galaxies. Unlike charged particles, neutrinos arrive on a direct line from their source, undeflected by magnetic fields. Unlike photons, neutrinos interact weakly, so they can penetrate thick columns of matter. For example, the interaction length of a 1-TeV neutrino is about 2.5 million kilometers of water, or 250 kilotonnes/cm^2, whereas high-energy photons are blocked by a few hundred grams/cm^2.

Ultrahigh-energy neutrinos can be detected by observing long-range muons produced in charged-current neutrino-nucleon interactions. To reduce the background from muons produced in the atmosphere, it is advantageous to site a neutrino telescope at a depth of several kilometers (water equivalent) or to observe upward-going muons. The reactions $(\nu_\ell, \bar{\nu}_\ell)N \to (\ell^-, \ell^+) + \text{anything}$ and $(\nu_\ell, \bar{\nu}_\ell)N \to (\nu_\ell, \bar{\nu}_\ell) + \text{anything}$ are the major sources of both the desired signal and the attenuation of the neutrino "beam" as it passes through the

Earth *en route* to the detector. We have recently studied detection of extragalactic neutrinos taking into account the improved knowledge of the partonic structure of the nucleon that has made possible a series of increasingly refined predictions for the interaction cross sections [1]. Plans for neutrino observatories that will detect neutrinos that originate beyond Earth have matured to the point that it is now reasonable to contemplate instrumenting a volume of water or ice as large as 1km^3. The ground array of the proposed Pierre Auger Cosmic Ray Observatory would have an acceptance exceeding 1km^3 of water for neutrino energies greater than 10^{17}ev. The Orbiting Wide-angle Light collectors project (OWL) would place in Earth orbit a lens to study air showers initiated by $> 10^{20}$-eV particles, including neutrinos.

We have evaluated the cross sections for charged-current and neutral current interactions of neutrinos with nucleons, to take account of new information about the parton distributions within the nucleon [1]. At higher energies, the predictions rely on incompletely tested assumptions about the behavior of parton distributions at very small values of the momentum fraction x. We consider the diffuse flux of neutrinos from AGNs and the flux of neutrinos that may accompany gamma-ray bursts, as well as neutrinos from cosmological sources such as the decay of topological defects formed in the early universe. We evaluate rates for upward-going muons produced in or beneath large underwater and ice detectors, and we compute rates for contained neutrino interactions in a km^3 volume. We have also estimated rates for the proposed ground array of the Pierre Auger Cosmic Ray Observatory.

The detection of upward-going muons from AGNs looks feasible in the next generation of underground experiments with effective areas on the order of $0.1km^2$. As the muon energy threshold increases above a few TeV, atmospheric neutrinos and muons become less important backgrounds. Downward and air-shower event rates look promising for km^3 detectors, for a variety of models.

At low energies the charged-current cross section $\sigma_{\rm CC}$ rises linearly with E_ν, but for energies exceeding about 10^4GeV, the cross section is damped by the W-boson propagator. For the range of neutrino energies of interest here, the charged-current results apply equally to the reaction $\nu_e N \to e^- + \text{anything}$.

The CTEQ4–DIS parton distributions are somewhat less singular as $x \to 0$ than the CTEQ3–DIS parton distributions we adopted as our nominal set in our previous work [2]. Specifically, the sea-quark distributions of the CTEQ4 set behave as

$$x q_s^{[\rm CTEQ4]}(x) \propto x^{-0.227} \tag{35}$$

near $x = 0$, whereas those of the CTEQ3 set behave as

$$x q_s^{[\rm CTEQ3]}(x) \propto x^{-0.332} \ . \tag{36}$$

The gentler singularity of the CTEQ4 distributions implies a smaller cross section at the highest energies, where the predominant contributions to the cross section come from very small values of x.

How well is it possible to predict the charged and neutral current cross section? For $E_\nu < 10^{16}$eV, all the standard sets of parton distributions, by which we mean those fitted to a vast universe of data, yield very similar cross sections, within the standard electroweak theory. For $E_\nu > 10^{16}$eV, cross sections are sensitive to the behavior of parton distributions

at very small x, where there are no direct experimental constraints. At these high energies, different *assumptions* about $x \to 0$ behavior then lead to different cross sections.

We have focused on the production of upward-going muons in the charged-current reactions $(\nu_\mu, \bar{\nu}_\mu)N \to (\mu^-, \mu^+) + \text{anything}$. Upward-going muons are free of background from the flux of muons produced by cosmic-ray interactions in the atmosphere. It is in any case advantageous to site a detector beneath several kmwe to shield it from the (downward) rain of atmospheric muons. Even at 3 kmwe underground, a detector still sees more than 200 vertical muons, though most of these muons are quite soft. If we impose the requirement that $E_\mu^{\min} > (10^3, 10^4, 10^5)\text{GeV}$, the flux is $(7, 3 \times 10^{-2}, 6 \times 10^{-5})$ muons. As the incident zenith angle of the atmospheric muons increases, the background flux decreases. For horizontal incidence and below, the muon rate observed underground should be largely background-free. There is another important reason for looking down: The few-km range of UHE muons means that large-volume detectors can observe charged-current events that occur not only within the instrumented volume, but also in the rock or water underlying the detector. Accordingly, the effective volume of a detector may be considerably larger than the instrumented volume, for upward-going muons. For energies above 40TeV, the Earth's diameter exceeds the interaction length of neutrinos. At these energies it is beneficial to look for events induced by downward and horizontal neutrino conversions to muons.

We have also considered the observability of neutrino interactions in the atmosphere. A neutrino normally incident on a surface detector passes through a column of density of 1 033 cmwe, while a neutrino arriving along the horizon encounters a column of about 36 000 cmwe. Both amounts of matter are orders of magnitude smaller than the neutrino interaction lengths for Earth, so the atmosphere is essentially transparent to neutrinos. However, the horizontal path length low in the atmosphere is not tiny compared with the depth available for the production of contained events in a water or ice Cerenkov detector, so it is worth asking what capabilities a large-area air-shower array might have for the study of UHE neutrino interactions. The proposed Pierre Auger Cosmic Ray Observatory, which would consist of an array of water Čerenkov tanks dispersed over a large land area, is designed to detect showers of particles produced in the atmosphere. Proton- and photon-induced showers are typically produced high in the atmosphere. Nearly horizontal events with shower maxima near the surface array are more likely to arise from neutrino interactions than from p-Air or γ-Air collisions.

The acceptance $\mathcal{A}$ of the Auger ground array, which has dimensions of volume times solid angle, has been evaluated by several authors. We adopt the Billoir's estimate to compute the event rate

$$\text{Rate} = N_{\text{A}}\, \rho_{\text{air}} \int_{E_{\text{th}}}^{E^{\max}} dE_{\text{sh}} \int_0^1 dy \frac{dN_\nu}{dE_\nu} \frac{d\sigma_{\nu N}}{dy}(E_\nu, y) \mathcal{A}(E_{\text{sh}}) \ . \tag{37}$$

The $(\nu_\mu + \bar{\nu}_\mu)N$ neutral-current rates are twice those for the $(\nu_e + \bar{\nu}_e)N$ case. We also evaluate the $(\nu_e + \bar{\nu}_e)N$ charged-current rates for three different sets of parton distributions.

The largest rates for neutrino-induced horizontal air showers arise from $(\nu_e + \bar{\nu}_e)N$ charged-current interactions, for which $E_{\text{sh}} \approx E_\nu$. In one year, a few to tens of horizontal $(\nu_e + \bar{\nu}_e)N \to e^\mp + \text{anything}$ events may be observed in the Auger detectors, assuming the modern estimates of AGN neutrino fluxes.

Given the high thresholds that must be set for detection, the expected event rates are dependent on the choice of parton distribution functions. The D_′ rates are approximately

a factor of two larger than the CTEQ3-DLA rates. If the absolute normalization and energy behavior of the AGN fluxes could be established in underground experiments at lower energies, the Auger experiment might suggest distinctions among the various high-energy extrapolations of the cross sections [1].

We have estimated event rates for several energy thresholds and detection methods, using a variety of models for the neutrino fluxes from AGNs, gamma-ray bursters, topological defects, and cosmic-ray interactions in the atmosphere. In $\nu_\mu N \to \mu X$ interactions, requiring a muon energy above 10 TeV reduces the atmospheric background enough to permit the observation of upward-going muons for the AGN-SS91 and AGN-P96 fluxes. These models yield tens to hundreds of events per year for detectors of $0.1 km^2$ effective area. The GRB-WB flux emerges at a higher threshold, but suffers from a small event rate.

Event rates for downward muons above 100TeV from neutrinos are substantial in $1 km^3$, except for the TD models [1]. Resonant W boson production will be difficult to distinguish from the νN interaction background. For the Pierre Auger Cosmic Ray Observatory, the most promising rates arise from $(\nu_e,\ \bar{\nu}_e)N$ charged-current interactions in the AGN-M95 and AGN-P96 models. By combining measurements of the upward-going muon rate at lower energies with air-shower studies at the highest energies, it may be possible to distinguish among alternative high-energy extrapolations of the νN cross section. The origins of the highest energy cosmic rays are not well understood, but cosmic rays should be accompanied by very high energy neutrinos in all models. The absolute normalization and energy dependence of the fluxes vary from model to model. Neutrino telescopes ultimately will probe extraterrestrial accelerator sources. We expect that detectors with effective areas on the order of $0.1 km^2$ will yield significant clues to aid in our understanding of physics to the 10^{20}-eV energy scale.

References

[1] R.Gandhi, C.Quigg, M.H.Reno and I.Sarcevic, *Phys. Rev.* **D58**, 093009 (1998).

[2] R.Gandhi, C.Quigg, M.H.Reno and I.Sarcevic, *Astropart. Phys.* **5**, 81 (1996).

[3] P. Jain, D. McKay, S. Panda and J.P. Ralston, *Phys. Lett.* **B484**, 267 (2000); C. Tyler, A. Olinto and G. Sigl, hep-ph/0002257.

[4] L. Dixon, private communications.

Charm Contribution to the High-Energy Atmospheric Muon and Neutrino Fluxes

Recently we have evaluated the charm contribution to the atmospheric muon and neutrino fluxes [1]. Neutrinos and muons are produced in the atmosphere from primary cosmic ray interactions with air nuclei. The range of energies of the neutrinos and muons determines their source: at energies below 10-100 TeV, muons come from pion and kaon decays. Muon neutrinos and electron neutrinos come from those same decays as well as from muon decay,

depending on the energy. These lepton fluxes are termed 'conventional', in contrast to muons and neutrinos that come from the decays of charmed particles, denoted 'prompt'.

Current interest has been focused on the observations of atmospheric muon neutrinos and electron neutrinos by the Super-Kamiokande experiment. Interpretations of these data rely on the conventional neutrino flux calculations. One interpretation of the measured deficit of muon neutrinos is that muon neutrinos are massive and oscillate into tau neutrinos, which are not detected in the Super-K experiment. A test of this hypothesis would be evidence of tau neutrino appearance through detection of $\nu_\tau \to \tau$. A background flux of tau neutrinos comes from tau neutrinos produced directly in the atmosphere by charm particle decays, namely, $D_s \to \tau\nu_\tau$, followed by the decay of the tau itself.

Charmed particle contributions to the high energy muon flux may be the explanation of underground measurements which appear to be larger than conventional flux calculations predict. The deviation appears in the TeV energy region for muons.

We have calculated muon and neutrino fluxes using next-to-leading order (NLO) perturbative QCD [1]. We focused on the muon fluxes above 100 GeV, where we examine the energy at which the crossover from conventional dominated to prompt dominated flux occurs. The calculation of the prompt lepton fluxes relies on the semi-analytic method using approximate cascade equations. Details of the method can be found in Ref. 1. The lepton fluxes depend on the incident cosmic ray flux. Initially, we assume that the incident cosmic ray flux is comprised of protons, and that at the top of the atmosphere, the proton flux $\phi_p(E) = 1.7\ (E/\mathrm{GeV})^{-2.7}$ for $E < 5 \cdot 10^6$ GeV and scales as $174\ (E/\mathrm{GeV})^{-3}$ for $E \geq 5 \cdot 10^6$ GeV, in units of (GeV cm^2 s sr)$^{-1}$.

Of particular importance for charm production is the Z-moment,

$$Z_{pj} = 2 f_j \int_0^1 \frac{dx_E}{x_E} \frac{\phi_p(E/x_E)}{\phi_p(E)} \frac{1}{\sigma_{pA}(E)} \frac{d\sigma_{pA\to c\bar{c}}(E/x_E)}{dx_E}, \tag{38}$$

where $x_E = E/E_p$, the energy of the outgoing charmed hadron divided by the incident nucleon energy, and f_j is the fraction of charmed particles which emerge as hadron j, as outlined in Ref. 2. To evaluate the differential cross section for charm production, we chose a charmed quark mass $m_c = 1.3$ GeV as it yields the best consistency with the experimental data. Our default parton distribution functions are CTEQ3, however, for comparison, we also used the MRSD$_-$ set. Our factorization scale (M) and renormalization scale (μ) were chosen as either m_c or $2m_c$. To include NLO corrections, we have parameterized in energy and x_E the ratio of the NLO to leading order distribution $d\sigma/dx_E$.

Our results for the vertical prompt atmospheric flux at sea level, scaled by E^3, are shown in Fig. 4 by the solid, dashed and dot-dashed lines. All fluxes shown are the sum of particle plus antiparticle. The dotted lines show the Thunman, Gondolo and Ingelman (1996) vertical prompt and conventional muon fluxes. The prompt flux is isotropic below $\sim 10^7$ GeV due to the fact that essentially all charmed particles decay below that energy. At higher energies, the turnover in the flux curve indicates that some charmed particles are not decaying in the region between where they are produced and sea level.

The dashed curve based on the MRSD$_-$ distributions should be considered as an upper limit, as the parton distribution functions are larger at small parton x than the results reported by HERA experiments. The CTEQ3 distribution functions are a better fit. The

solid line in Fig. 4 can be parameterized by

$$\log_{10}[E^3\phi_\mu/(\mathrm{GeV}^2/\mathrm{cm}^2\mathrm{s\,sr})] = -5.79 + 0.345x + 0.105x^2 - 0.0127x^3, \tag{39}$$

where $x = \log_{10}(E/\mathrm{GeV})$. The crossover from conventional to prompt flux occurs at $E \sim 200 - 600$ TeV according to Fig. 4, so perturbative QCD production of charm in the atmosphere cannot explain the deviation of the muon flux from the conventional flux predictions. The electron neutrino and muon neutrino fluxes from charm are essentially identical to the prompt muon flux shown in Fig. 4. The conventional muon neutrino flux is on the order of 1/5 of the conventional muon flux, while the conventional electron neutrino flux is $\sim 1/150$ of the conventional muon flux.

We have evaluated the contributions of charmed particle decays to the atmospheric lepton fluxes. For ν_τ fluxes, the D_s decays are the dominant source. To reduce uncertainties, the charmed mass was chosen to fit accelerator data on charm production, however, we have extrapolated our differential cross sections well beyond the measured regime. In particular, the parton distribution functions below parton $x = 10^{-5}$ are assumed to have the form, e.g., $xg(x) \sim x^{-\lambda}$. For x below some critical value x_c, this extrapolation should be invalid due to shadowing effects.

In an effort to estimate the effect of shadowing, we have considered $x_c = 10^{-6} - 10^{-4}$, below which we have set $\lambda = 0.08$. This shadowing affects the prompt fluxes at $E \sim 10^4 - 10^6$ GeV, with the lower onset due to $x_c = 10^{-4}$. It is unlikely that $x_c = 10^{-4}$ is realistic in view of the data from HERA, including recent measurements at scales above ~ 1 GeV. At $E = 10^8$ GeV, for $x_c = 10^{-4}$ the solid line in Fig. 4 dips to almost $4 \cdot 10^{-4}$, while for $x_c = 10^{-6}$, the flux is 2/3 of the solid curve. The flattening of the small-x parton distribution functions doesn't change our qualitative conclusions about the crossover between conventional and prompt, however, it does indicate that our fluxes above $E \sim 10^6$ GeV have significant theoretical uncertainties [3].

The atmospheric lepton fluxes are directly proportional to the primary cosmic ray flux at the top of the atmosphere, as well as weakly dependent on the primary flux through the Z-moments, e.g., as in Eq. (1). Since the atmospheric lepton fluxes come from averages of many interactions, the use of the superposition model, in which a nucleus of mass A is equivalent to A nucleons, is a good approximation. We have used two power laws for the flux ($E^{-2.7}$ and E^{-3}), with a critical energy of $5 \cdot 10^6$ GeV for the transition between powers. If we use the same powers, but move the critical energy to 10^5 GeV, the new fluxes begins to deviate from the fluxes in Fig. 4 at $E \sim 10^4$ GeV. The solid curve drops by a factor of $\sim 1/3$ at $E = 10^8$ GeV for this choice of critical energy. The transition from conventional to prompt muons occurs at a higher energy, on the order of $E \sim 10^6$ GeV.

We find that due to the charm contribution the upward-going muon event rates increase by about factor of 2 for $E_\mu^{min} = 100$TeV. For lower energy threshold, the charm contribution is about 10%. Thus, by measuring upward-going atmospheric muons with kilometer-size neutrino telescope and with the high energy threshold, there is a possibility of determining the small x behavior of the parton distributions in the (x, Q^2) range inaccessible to the current accelerator experiments.

References

[1] L. Pasquali, M.H. Reno and I. Sarcevic, *Phys. Rev.* **D59**, 034020 (1999).

[2] L. Pasquali, M.H. Reno and I. Sarcevic, *Astropart. Phys.* **9** (1998) 193.

[3] L. Pasquali, M.H. Reno and I. Sarcevic, *Nucl. Phys.* **B70**, 361 (1999).

Probing Extra Dimensions with Neutrino Oscillations

In collaboration with K. Dienes, Sarcevic has recently proposed a model with large extra dimensions which gives flavor oscillations even though the Standard Model on the brane is flavor-diagonal, the bulk neutrino theory is flavor-neutral, and the brane/bulk couplings are flavor-blind [1]. In such a scenario, all neutrino flavor oscillations are induced indirectly through Kaluza-Klein states, and no mixing angles are required for the Standard-Model sector.

Experimental evidence that neutrinos have mass and undergo oscillations has the potential to radically alter our understanding of the lepton sector of the Standard Model, and in many ways introduce a parallel structure between the lepton sector and the corresponding quark sector. There is, however, one important difference between the lepton and quark sectors of the Standard Model. Whereas right-handed quarks carry both color and electromagnetic charge, right-handed neutrinos are neutral under all Standard-Model gauge symmetries, indicating that the right-handed neutrinos might have completely different properties than their quark counterparts.

This observation becomes particularly compelling within the context of Type I string theory. If one seeks to derive the Standard Model as the low-energy limit of a Type I theory consisting of both open and closed strings, the fact that right-handed quarks carry both color and electromagnetic charge implies that they must necessarily be realized as open strings, with the color and electromagnetic quantum numbers residing at the string endpoints. By contrast, the absence of non-trivial Standard-Model charges for right-handed neutrinos implies that these states can be realized either as open strings or as closed strings. If the right-handed neutrinos are realizable as components of a *closed*-string state, then such neutrinos are no longer restricted to lie on the same four-dimensional brane that contains the Standard Model. This is because it is only the endpoints of strings that bind strings to branes, and closed strings have no endpoints. Therefore, such closed strings may propagate off the brane, and live in a higher-dimensional "bulk". From a four-dimensional field-theoretic perspective, this implies that we would effectively have not only a single right-handed neutrino, but also an infinite tower of corresponding Kaluza-Klein excitations. When the extra spacetime dimensions are large, then the corresponding Kaluza-Klein states are relatively light. Therefore, we can expect their effects to be significant, leading to an entirely new approach to neutrino physics.

We have constructed a model with extra dimensions in which only one bulk neutrino is introduced. Namely, we consider flavor to be a property internal to the Standard Model, one which is restricted to the brane and which therefore does not extend into the bulk.

We assume flavor-blind couplings between our brane and bulk fields. Thus, only the brane physics is flavor-sensitive.

On the brane, we introduce three left-handed neutrinos ν_i ($i = 1, 2, 3$); these are our flavor eigenstates. We assume that these left-handed neutrinos have corresponding Majorana masses m_i on the brane, but in order to make the model simple we do not introduce any explicit flavor mixings between these left-handed neutrinos on the brane. We consider these Majorana masses to be input parameters. These masses do not arise as a result of any of the higher-dimensional physics perpendicular to the brane. The important point, however, is that these Majorana masses are unequal, since through these Majorana masses our model will distinguish between the different flavors on the brane. Since we do not introduce any flavor mixings on the brane, the brane sector of our model is completely flavor-diagonal.

In higher dimensions, we consider a single Dirac fermion Ψ, which in the Weyl basis can be decomposed into two two-component spinors: $\Psi = (\psi_1, \bar{\psi}_2)^T$. This Dirac fermion does not carry any flavor indices, and is therefore completely flavor-neutral. We impose the orbifold relations $\psi_{1,2}(-y) = \pm\psi_{1,2}(y)$ where y is the coordinate of the fifth dimension. For convenience, we also define the linear combinations $N^{(n)} \equiv (\psi_1^{(n)} + \psi_2^{(n)})/\sqrt{2}$ and $M^{(n)} \equiv (\psi_1^{(n)} - \psi_2^{(n)})/\sqrt{2}$ for all $n > 0$. Use of these linear combinations will ensure a diagonal mass matrix.

We specify coupling between the brane neutrinos and the bulk neutrinos. Assuming that the brane is located at the orbifold fixed point $y = 0$, ψ_2 vanishes on the brane. The most natural brane/bulk coupling is therefore simply between ν_i and ψ_1. Although in principle each left-handed neutrino ν_i on the brane can have a different coupling to ψ_1, we consider a simple model in which this brane/bulk coupling is completely flavor-blind, labeled by $\hat{m}$.

Our Lagrangian has the form

$$\begin{aligned}
\mathcal{L}_{\mathbf{brane}} &= \int d^4x \sum_{i=1}^{3} \left\{ \bar{\nu}_i i\bar{\sigma}^\mu D_\mu \nu_i + m_i(\nu_i\nu_i + \text{h.c.}) \right\} \\
\mathcal{L}_{\mathbf{bulk}} &= \int d^4x\, dy\; M_s \left\{ \bar{\psi}_1 i\bar{\sigma}^\mu \partial_\mu \psi_1 + \bar{\psi}_2 i\bar{\sigma}^\mu \partial_\mu \psi_2 \right. \\
\mathcal{L}_{\mathbf{coupling}} &= \int d^4x \sum_{i=1}^{3} (\hat{m}\nu_i\psi_1|_{y=0} + \text{h.c.}) \; . \qquad (40)
\end{aligned}$$

Here M_s is the mass scale of the higher-dimensional fundamental theory. After we compactify the Lagrangian (40) down to four dimensions by expanding the five-dimensional Ψ field in Kaluza-Klein modes, we obtain

$$\begin{aligned}
\mathcal{L} &= \int d^4x \left\{ \sum_{i=1}^{3} \bar{\nu}_i i\bar{\sigma}^\mu D_\mu \nu_i + \bar{\psi}_1^{(0)} i\bar{\sigma}^\mu \partial_\mu \psi_1^{(0)} + \sum_{n=1}^{\infty} \left(\bar{N}^{(n)} i\bar{\sigma}^\mu \partial_\mu N^{(n)} + \bar{M}^{(n)} i\bar{\sigma}^\mu \partial_\mu M^{(n)} \right) \right. \\
&\quad + \sum_{i=1}^{3} m_i\nu_i\nu_i \; + \; \tfrac{1}{2} \sum_{n=1}^{\infty} \left[\left(\frac{n}{R}\right) N^{(n)} N^{(n)} - \left(\frac{n}{R}\right) M^{(n)} M^{(n)} \right] \\
&\quad \left. + \; m \sum_{i=1}^{3} \nu_i \left(\psi_1^{(0)} + \sum_{n=1}^{\infty} N^{(n)} + \sum_{n=1}^{\infty} M^{(n)} \right) \; + \; \text{h.c.} \right\} \qquad (41)
\end{aligned}$$

where $m \equiv \hat{m}/\sqrt{2\pi M_s R}$ is the volume-suppressed brane/bulk coupling resulting from the rescaling of the individual $\psi_1^{(0)}$, $N^{(n)}$, and $M^{(n)}$ Kaluza-Klein modes.

Given the Lagrangian (41), we see that the Standard-Model flavor-eigenstate neutrinos ν_i will mix with the entire tower of Kaluza-Klein states of the higher-dimensional Ψ field, even though they do not mix directly with each other. Defining

$$\mathcal{N}^T \;\equiv\; (\nu_1, \nu_2, \nu_3, \psi_1^{(0)}, N^{(1)}, M^{(1)}, N^{(2)}, M^{(2)}, ...) \;, \tag{42}$$

we see that the mass terms in the Lagrangian (41) take the form $\frac{1}{2}(\mathcal{N}^T\mathcal{M}\mathcal{N} + \text{h.c.})$ where $\mathcal{M}$ takes the symmetric form

$$\mathcal{M} \;=\; \begin{pmatrix} m_1 & 0 & 0 & m & m & m & m & m & \dots \\ 0 & m_2 & 0 & m & m & m & m & m & \dots \\ 0 & 0 & m_3 & m & m & m & m & m & \dots \\ m & m & m & 0 & 0 & 0 & 0 & 0 & \dots \\ m & m & m & 0 & 1/R & 0 & 0 & 0 & \dots \\ m & m & m & 0 & 0 & -1/R & 0 & 0 & \dots \\ m & m & m & 0 & 0 & 0 & 2/R & 0 & \dots \\ m & m & m & 0 & 0 & 0 & 0 & -2/R & \dots \\ \vdots & \vdots & \vdots & \vdots & \vdots & \vdots & \vdots & \vdots & \ddots \end{pmatrix} . \tag{43}$$

Majorana masses m_i merely serve to distinguish the different flavors. Three brane neutrinos will nevertheless undergo flavor oscillations as a result of their indirect mixings with the bulk Kaluza-Klein neutrinos. In order to demonstrate this explicitly, we have solved the eigenvalues and eigenvectors of this mass matrix. The eigenvalues λ of the matrix (43) are the solutions to the transcendental equation

$$\tan\pi(\lambda)R \;=\; \pi m^2 R \sum_{i=1}^{3} \frac{1}{\lambda - m_i} \;. \tag{44}$$

For each solution λ to (44), the corresponding mass eigenstate $\tilde{\nu}_\lambda$ is given by

$$\begin{aligned} |\tilde{\nu}_\lambda\rangle \;=\; & \frac{1}{\sqrt{N_\lambda}}\left[\left(\sum_{j=1}^{3}\frac{m}{\lambda - m_j}\right)^{-1} \sum_{i=1}^{3}\frac{\lambda}{\lambda - m_i}\,|\nu_i\rangle \;+\; |\psi_1^{(0)}\rangle \right. \\ & \left. +\; \sum_{k=1}^{\infty}\frac{\lambda}{\lambda - k/R}\,|N^{(k)}\rangle \;+\; \sum_{k=1}^{\infty}\frac{\lambda}{\lambda + k/R}\,|M^{(k)}\rangle\right] \end{aligned} \tag{45}$$

where N_λ is the normalization constant. We note that different mass eigenstates $|\tilde{\nu}_\lambda\rangle$ contain different proportions of the flavor eigenstates $|\nu_i\rangle$ for each λ and the flavor eigenstates correspond to different linear combinations of the mass eigenstates, and hence oscillate into each other (as well as into all of the Kaluza-Klein states). We rescale all of our remaining mass variables (λ, m_i, m) by R so that these variables shall henceforth correspond to dimensionless quantities. The fact that this rescaling removes all radii R from the above expressions illustrates that the radius R merely serves to set a single overall mass scale for the parameters that govern neutrino oscillations in extra dimensions.

We have explored some phenomenological properties of bulk-mediated neutrino oscillations. In particular, we have considered the probability $P_{i\to j}(t)$ that a given flavor eigenstate

brane neutrino $|\nu_i\rangle$ will oscillate into a given brane flavor eigenstate $|\nu_j\rangle$ as a function of time t. For $i = j$, this refers to a preservation probability, while for $i \neq j$ this refers to a flavor conversion probability. In general, this probability is given by

$$\begin{aligned} P_{i\to j}(t) &= |\langle\nu_j|\nu_i(t)\rangle|^2 \\ &= \left|\sum_\lambda \langle\nu_j|\lambda\rangle e^{-iE_\lambda t}\langle\lambda|\nu_i\rangle\right|^2 \\ &= \sum_\lambda |\langle\nu_i|\lambda\rangle|^2 |\langle\nu_j|\lambda\rangle|^2 \\ &\qquad + \ 2\sum_{\lambda>\lambda'} \langle\nu_i|\lambda\rangle\langle\nu_i|\lambda'\rangle\langle\nu_j|\lambda\rangle\langle\nu_j|\lambda'\rangle \ \cos\left\{[\lambda^2-(\lambda')^2]\tilde{t}\right\} \end{aligned} \tag{46}$$

where we have made the ultra-relativistic approximation $E_\lambda \approx p + \lambda^2/2pR^2$ in passing from the second to the third line, where p is the neutrino momentum. We have also defined a dimensionless time variable

$$\tilde{t} \ \equiv \ \frac{t}{2pR^2} \ \approx \ \frac{1}{2R^2}\frac{L}{E} \ , \tag{47}$$

where $L \approx ct$ is the spatial distance between the locations of neutrino production and neutrino detection, and $E \approx pc$ is the neutrino energy. Finally, the overlaps $\langle i|\lambda\rangle$ can be determined from (45).

In general, the first term in the last line of (46) is the time-independent (time-averaged) probability $\overline{P_{i\to j}}$, while the second term gives rise to the time-dependence of the oscillation probability. However, in the special cases for which two of the m_i are equal and opposite while the third vanishes, the spectrum of solutions of (44) has a reflection symmetry $\lambda \to -\lambda$. In such cases, the second term in (46) will also contain additional time-independent contributions when $\lambda' = -\lambda$.

The main feature of our model is that large neutrino flavor oscillations can arise in higher dimensions even when all neutrino flavor Standard-Model mixing angles on the brane are zero. To this end, we have investigated this feature in a variety of special cases. Because of their phenomenological relevance, we shall mostly concentrate on the probabilities $P_{1\to1}(t)$, $P_{2\to2}(t)$, and $P_{2\to1}(t)$ where the subscripts $(1,2,3)$ signify (ν_e,ν_μ,ν_τ) respectively. These are ultimately the three probabilities which are relevant for addressing constraints from solar, atmospheric, and long-baseline neutrino experiments.

In the case when the brane/bulk coupling is extremely small, *i.e.*, $m \ll 1$. the mass matrix (43) is nearly diagonal, and there is relatively little mixing between the brane neutrinos and the bulk neutrinos. One might suspect, therefore, that there is correspondingly little chance that one can have a large indirect flavor oscillation via the Kaluza-Klein states.

This is not the case, however, since a large flavor oscillation can still be achieved when $m_1 \approx m_2 \approx k$ for $k \in \mathbb{Z}$. As an explicit example, let us consider the case $m = 0.01$, $m_{1,2} = 1 \mp \delta m/2$, and $m_3 = 5$, with $\delta m = m_2 - m_1$ free to vary. What is happening is that we are exploiting a resonance between the brane neutrinos $|\nu_1\rangle$, $|\nu_2\rangle$, and the first excited Kaluza-Klein bulk neutrino $|N^{(1)}\rangle$, so that large effective flavor oscillations between the brane neutrinos are mediated indirectly through their oscillations with the bulk neutrino. Note that for sufficiently precise resonance conditions (*i.e.*, for δm sufficiently small), the

resulting oscillation pattern effectively resembles a simple two-flavor oscillation with maximal mixing angle.

We stress that even though this flavor mixing appears to resemble a simple two-state oscillation in the limit $\delta m \ll 1$, the time-averaged probabilities for each flavor are not 1/2, but 3/8. This reflects the fact that we are dealing with a three-state oscillation in which 1/4 of the total neutrino probability has been lost to the bulk neutrino $|N^{(1)}\rangle$, and is hence unobservable on the brane. As $\delta m \to 0$ for small, fixed $m > 0$, the neutrino mass eigenstates $|\tilde{\nu}_i\rangle, |\tilde{N}^{(1)}\rangle$ are related to the flavor eigenstates $|\nu_i\rangle, |N^{(1)}\rangle$ via

$$\begin{aligned} |\tilde{\nu}_{1,2}\rangle &= \frac{1}{2}\left(|\nu_1\rangle + |\nu_2\rangle\right) \pm \frac{1}{\sqrt{2}}|N^{(1)}\rangle \\ |\tilde{N}^{(1)}\rangle &= \frac{1}{\sqrt{2}}\left(|\nu_1\rangle - |\nu_2\rangle\right) \ . \end{aligned} \tag{48}$$

Of course, strictly speaking, we cannot take the full $\delta m = 0$ limit, since in this limit we obtain a degeneracy in which $|\nu_1\rangle$ and $|\nu_2\rangle$ become indistinguishable, with one linear combination of these states decoupling from the oscillation pattern. This mirrors the case of a simple two-state oscillation. However, we see that even for relatively small values of δm, we have achieved a significant indirect flavor oscillation.

Given that this is effectively a three-state nearly-degenerate oscillation, it may appear that the underlying higher-dimensional nature of the theory plays no role; indeed, the resulting oscillation could equally well be achieved with a single additional degenerate neutrino on the brane to mediate the oscillation. However, the higher-dimensional nature of the theory ensures that such an extra neutrino will always exist which can be in resonance with the degenerate brane neutrinos. As long as $m_i R \gg 1$, the level spacing of the Kaluza-Klein states will be much smaller than the mass of the brane neutrinos. This implies is that as long as two of the m_i are nearly equal, there will essentially always be a nearby bulk Kaluza-Klein state which is in resonance with these neutrinos and which can therefore mediate the desired flavor oscillation between them. Thus, because of the higher-dimensional nature of the underlying theory, no additional fine-tuning is necessary in order to achieve this flavor oscillation.

We observe that certain features of the resulting bulk-mediated oscillation are independent of which Kaluza-Klein state serves as the mediator. To see this, we consider the general case where $m_{1,2} = k \mp \delta m/2$, where $k \in \mathbb{Z}$. In this case, it is the Kaluza-Klein mode $|N^{(k)}\rangle$ which mediates the flavor oscillation between $|\nu_1\rangle$ and $|\nu_2\rangle$. Nevertheless, the amplitude of the resulting oscillation depends on only the ratio $r \equiv \delta m/m$, and is independent of k. Likewise, the time-averaged oscillation probabilities are also fixed uniquely by r, and do not depend on k.

On the other hand, in the $\delta m \to 0$ limit, the period of the resulting oscillations depends strongly on both k and m. This is because all three of these parameters determine the relevant mass eigenvalues λ whose differences enter into the expression for the probability amplitudes in (46). It might initially seem that for fixed k one can arrange arbitrarily large oscillation frequencies simply by taking $\delta m \to 0$. This is not the case because the minimum splitting between the eigenvalues $\lambda_{1,2}$ associated with $|\tilde{\nu}_{1,2}\rangle$ in (48) is set not by δm as $\delta m \to 0$, but rather by the brane/bulk coupling m. This observation follows directly from the eigenvalue equation (44). This is why the period of oscillations does not vary when

δm is taken from 10^{-2} to 10^{-3}; one instead finds $\Delta\lambda \equiv \lambda_2 - \lambda_1 \approx 3 \times 10^{-2}$ in each case. Of course, even for a fixed $\Delta\lambda$, the period of the resulting oscillation scales inversely with k for small splittings because

$$\lambda_2^2 - \lambda_1^2 \;\approx\; (k + \Delta\lambda/2)^2 - (k - \Delta\lambda/2)^2 \;=\; 2k\Delta\lambda \;. \tag{49}$$

Thus, while the minimum difference in the eigenvalues is fixed by m, the minimum difference in their squares depends linearly on k as well.

We have also considered the long-time behavior of the flavor oscillations. We have seen that for relatively short times, the flavor mixing resembles a maximal two-state oscillation in which one effectively has complete flavor conversion at periodic intervals, with one flavor depleted as the other is generated. At longer times, by contrast, two effects come into play simultaneously. First, although the time-averaged probabilities remain fixed at 3/8, the amplitudes of the oscillations around this value themselves experience an oscillation, with the first node occurring at $\tilde{t} \approx 9000$. This reflects the presence of a secondary "beat" frequency corresponding to a "beat" oscillation between the brane neutrinos and the bulk neutrino. Second, the relative phase between the two brane flavors is shifted, so that by the time the first node is reached, both flavors are depleted and generated simultaneously. Both of these characteristics indicate the presence of the third component to the oscillation, with the bulk in some sense acting as a "reservoir" for neutrino probability.

We have also considered the situation in which all three of the brane neutrino flavors are approximately degenerate, so that $m_1 \approx m_2 \approx m_3$. We take $m \ll 1$, and will furthermore assume $m_i \approx k \in \mathbb{Z}$ so that these neutrinos are in resonance with a bulk Kaluza-Klein neutrino. In this case, the bulk neutrino mediates an effective four-state flavor oscillation which closely resembles a three-state oscillation on the brane. For concreteness, let us imagine a symmetric arrangement in which $m_2 = k \in \mathbb{Z}$ and $m_{1,3} = k \mp \delta m/2$. In the limit $\delta m \to 0$, our four mass eigenstates $|\tilde{\nu}_i\rangle$, $|\tilde{N}^{(k)}\rangle$ are effectively given in terms of the corresponding flavor eigenstates as

$$\begin{aligned} |\tilde{\nu}_{1,3}\rangle &= \frac{1}{\sqrt{6}}\left(|\nu_1\rangle + |\nu_2\rangle + |\nu_3\rangle\right) \;\pm\; \frac{1}{\sqrt{2}}|N^{(k)}\rangle \\ |\tilde{\nu}_2, \tilde{N}^{(k)}\rangle &= \pm\frac{1}{2}\left(|\nu_1\rangle - |\nu_3\rangle\right) - \frac{1}{\sqrt{12}}\left(|\nu_1\rangle + |\nu_3\rangle\right) + \frac{1}{\sqrt{3}}|\nu_2\rangle \;, \end{aligned} \tag{50}$$

implying the time-averaged probabilities

$$\begin{aligned} \overline{P_{1\to1}} &= 4/9 \;, & \overline{P_{2\to1}} &= 5/18 \;, & \overline{P_{3\to1}} &= 1/9 \\ \overline{P_{1\to2}} &= 5/18 \;, & \overline{P_{2\to2}} &= 5/18 \;, & \overline{P_{3\to2}} &= 5/18 \\ \overline{P_{1\to3}} &= 1/9 \;, & \overline{P_{2\to3}} &= 5/18 \;, & \overline{P_{3\to3}} &= 4/9 \;. \end{aligned} \tag{51}$$

Thus, if we start with ν_2, we are equally likely to have conversion into each flavor, whereas if we start with ν_1 or ν_3, we are more likely to preserve the initial flavor, with declining probabilities for conversion into nearby flavors. In all cases, independent on the initial flavor of brane neutrino, exactly 1/6 of the initial probability is ultimately lost into the bulk.

Remarkably, for early times, all preservation probabilities $P_{i\to j}$ with $i = j$ coincide with each other, while all conversion probabilities with $i \neq j$ also coincide with each other. It

may seem that this is in conflict with (51), which indicates a strong sensitivity to the flavor of the initial neutrino. However, at later times, these probabilities deviate from each other in a flavor-dependent way, and asymptotically take time-averaged values in accordance with (51). We also stress that unlike the previous case with two degenerate flavors on the brane, the effective mixing angle in this three-degenerate case is not maximal (in the sense that we never have complete conversion from one flavor to another).

If both m_1 and m_2 are near different integers, then the time-averaged preservation probability for each flavor is simply $\overline{P_{1\to 1}} = \overline{P_{2\to 2}} = 1/2$. A natural guess would then be that this reflects a two-state oscillation between ν_1 and ν_2 rather than a set of independent oscillations between each ν_i and the bulk. This fact illustrates that it is imperative to actually see flavor conversion before concluding the presence of a flavor oscillation. This observation becomes particularly relevant in light of the current experimental evidence for neutrino oscillations. From studies of solar and atmospheric neutrino fluxes, ample evidence exists of individual flavor deficits. However, only one experiment, namely LSND, actually claims to see flavor conversion. We remark that for $m \ll 1$, the amplitude of the resulting neutrino oscillations depends critically on the fact that our brane neutrinos are relatively close to a bulk Kaluza-Klein resonance. However, for situations in which $m_i R \gg 1$, this is natural and does not require fine-tuning.

We have also considered the case when the brane/bulk coupling parameter m is not small. In such cases, a larger population of bulk Kaluza-Klein neutrino states participates in the neutrino mixings, and it is no longer necessary (or possible) to exploit a single Kaluza-Klein resonance in order to achieve sizable flavor oscillations on the brane. In other words, we no longer are required to have a flavor degeneracy on the brane in order to achieve sizable flavor oscillations. Moreover, the masses of the resulting physical neutrinos begin to deviate substantially from the bare Majorana masses m_i that serve as inputs to our model, reflecting the fact that our mass matrix (43) is no longer as nearly diagonal as had been previously. These two features ultimately reflect the truly higher-dimensional nature of the model, and result in significantly richer neutrino oscillation patterns than can be achieved when m is small. Because the resulting oscillations are much more complex, we plan to explore a few generic cases first.

The model we have constructed provides a compact set of parameters with which one can attempt a detailed comparison with experimental data. Even though our model contains only five free parameters, it yields a surprising richness in resulting neutrino oscillation phenomenology, and exploits the higher-dimensional nature of the recent theories of reduced quantum-gravity scale in an essential way. Thus, this model might be profitably used as the basis of a detailed experimental investigation of the viability of the higher-dimensional neutrino oscillation mechanism.

References

[1] K. Dienes and I. Sarcevic, *Phys. Lett.* **B500**, 133 (2001).

[2] K.S. Babu, J.C. Pati, and F. Wilczek, *Phys. Lett.* **B359** (1995) 351.

Ultrahigh Energy Neutrinos as Probes of New Physics
(S. Iyer Dutta, M. H. Reno and I. Sarcevic, Phys. Rev. **D66**, 033002 (2002).)

In the past three years we have made significant contributions to the understanding of high energy neutrino interactions. One of our goals was to explore the possibility that ultrahigh energy neutrinos could be used as a probe of physics beyond the Standard Model. Recently, Arkani-Hamed, Dimopoulos and Dvali have proposed a solution to the hierarchy problem by bringing quantum gravity down to the TeV scale, as a profound implication of the possibility that we live in $4+n$ spacetime dimensions. One of the most striking consequences of a low fundamental Planck scale is the possibility of producing black holes and observing them in future colliders or in cosmic rays/neutrino interactions. If gravity propagates in $d = 4 + n$ dimensions while the other fields are confined to a 3-brane, the 4-dimensional Planck scale is given by $M_{Pl}^2 = M_P^{n+2} V_n = G_{n+4}^{-1} V_n$, where M_P is the fundamental Planck scale in $4 + n$ dimensions and $V_n = (2\pi R)^n$ is the volume of the n-torus that describes the compact space. For large size of the extra dimensions R, the fundamental scale M_P can be as low as in the TeV range. The existence of large compact dimensions leads to deviations from Newtonian gravity at distances of the order of R, as well as strong effects of Kaluza-Klein excitations of the graviton on various processes at high energies. These effects impose constraints on the scale M_P, depending on the number of extra dimensions. Scales much lower than 1 TeV would be manifest in collider experiments by additional contributions from virtual graviton exchange, requiring $M_P > 1$ TeV. Direct graviton emission is already constrained by collider data, and astrophysical limits exclude $n = 2$ and $n = 3$ for M_P in TeV range.

Ultra-high energy galactic and extragalactic neutrinos ($E_\nu > 10^3$ TeV) hold great potential for the discovery of new physics. UHE neutrinos are produced by high energy cosmic rays interacting with the microwave background radiation (photoproduction followed by pion decay). Cosmic rays of energies up to 10^9 TeV have been observed. The "cosmogenic" neutrinos are more or less guaranteed to exist among ultrahigh energy cosmic neutrinos predicted from various sources. In addition, extragalactis sources, such as Active Galactic Nuclei and Gamma Ray Bursts are also believed to be sources of ultra-high energy neutrinos, as well as more speculative sources, such as topological defects formed in the Early Universe. We have studied black hole production in scattering of ultrahigh energy ($E_\nu > 10^3$TeV) cosmic or extragalactic neutrinos off nuclei in air or in ice and their detection by neutrino telescopes such as IceCube or with the satellite experiments, such as the Orbiting Wide-angle Light-collectors Experiment (OWL) and the Extreme Universe Space Observatory (EUSO). Detection of the black hole formation in neutrino interactions has potential of revealing the structure of the extra dimensions on scales large as compared to the Planck scale.

We find that the standard model cross section is exceeded by the black hole production cross section in the energy range of $\sim 10^8 - 10^{10}$ GeV, depending on n, M_P, and $M_{BH}^{\min}$. With these cross sections, we have evaluated the contained event rates for black hole production in a km^3 detector like IceCube and for the satellite experiments, such as EUSO and OWL/Airwatch. We have considered black hole decay into hadrons as a dominant process. We find the OWL rates to be factor of 20 times higher than the IceCube rates for threshold energy of 10^5 TeV. Lowering the energy threshold for IceCube increases the event rates for steep fluxes, such as the Waxman-Bahcall flux bound, but decreases the signal to background

ratio. The cosmogenic neutrino flux is less sensitive to the energy threshold because it does not fall $\sim E_\nu^{-2}$ for $E_\nu < 10^5$ TeV. We find that IceCube should be able to detect black hole events (showers and muons) with $E_{th} \sim 10^2$ TeV if $M_P \leq 2$ TeV and $n \geq 6$, however, at higher energies OWL will have more sensitivity. The non-observation of an excess of shower events at the AGASA air shower array lead to limits on the black hole production parameters and require $M_P \geq 1.3 - 1.8$ TeV. The OWL standard model rates are at the 1.5-3 events per year level, depending on the flux, when one includes all flavors of neutrinos. The rates for OWL are ten to hundreds of events per year for $M_P = 1$ TeV for $M_{BH}^{\rm min} = 1 - 10$, even in the case of the conservative evolution of the cosmogenic flux. Similar results are found for the Waxman-Bahcall flux, which represents the upper bound for optically thin sources. For $M_{BH}^{min} = 5\,(1)\,M_P$, $M_P = 3$ TeV, $n = 6$, the annual signal event rates are of the order of 4.4 (24) for the strong evolution cosmogenic flux model and 2.4 (12) for the standard evolution. This is a much larger reach in parameter space that the terrestrial experiments. One year of data taking would be sufficient for OWL to have unique opportunity to detect black holes, or to probe fundamental Planck scale up to $M_P = 3$ TeV for $n \geq 4$. OWL is planned for possible implementation after 2007. EUSO is scheduled to go on the International Space Station in 2006. EUSO, with a projected event rate on the order of 1/5 of the OWL rate, will be able to probe regions of parameter space intermediate between IceCube and OWL.

High Energy Neutrino Cross Sections and Perturbative Unitarity

(M.H. Reno, I. Sarcevic, G. Sterman, M. Stratmann and W. Vogelsang, in APS/DPF/DPB Summer Study on the Future of Particle Physics (Snowmass 2001), eConf C010630:P508 (2001).)

Recently Dicus, Kretzer, Repko, and Schmidt (2001) have criticaly addressed the issue of perturbative unitarity in the context of neutrino-nucleon cross section at high energies. We have investigated this very important question of unitarity constraints in the ultrahigh energy cross section for neutrino interactions with nucleons. We have examined to what extent the cross section may be sensitive to the presence of saturation effects in the evolution of the parton distributions and studied what can and cannot be learned by relating the neutrino-nucleon forward scattering amplitude to the total neutrino-nucleon cross section.

Dicus *et al.* have brought unitarity considerations to the fore. A restatement of the optical theorem relates the total neutrino-nucleon cross section to the neutrino-nucleon forward elastic scattering amplitude. The latter can be written in terms of the differential elastic cross section, evaluated at Mandelstam variable $t = 0$, which, with some approximations, yields:

$$\left.\frac{d\sigma_{\rm el}}{dt}\right|_{t=0} \geq \frac{1}{16\pi}\sigma_{\rm tot}^2 \ . \tag{52}$$

One can view this as a lower bound on the forward scattering elastic cross section, or as an upper bound on the total cross section. Dicus *et al.* observe that the inequality is saturated at a relatively low energy by using the lowest order, G_F^2, contribution for the elastic cross section on the left, and the G_F^4 contribution that comes from the inclusive cross section expression on the right. Specifically, using the leading term in G_F for the elastic differential cross section, they conclude that $\sigma_{\rm tot} < 9.3 \times 10^{-33}\,{\rm cm}^2$, which already is violated

for $E > 2\times10^8$ GeV. From this they deduce that at yet higher energies, where the right-hand side of Eq. (52) increases, while the left is constant (at $\mathcal{O}(G_F^2)$), previously neglected terms that are higher order in the weak coupling g, in particular, g^6 or g^8 terms, *must* become important. They go on to suggest that this signals a breakdown in perturbation theory in the weak coupling, g. This would be a striking implication indeed, especially given the small size of the cross section.

We have shown more natural interpretation of the equality when $E > 2\times10^8$ GeV. First, we observe that the forward elastic cross section receives two qualitatively different and quantum mechanically incoherent contributions. The first of these describes the coherent elastic scattering of the entire nucleon through weak vector boson exchange, which begins at tree level, that is, at G_F^2 in the cross section. The second is the contribution of high-Q^2 virtual states that results from the *incoherent* scattering of partons. The latter, not the former, is related independently by the optical theorem to the inelastic cross section on the right-hand side of Eq. (52), and will saturate that inequality identically at order G_F^4, regardless of its size, just as at order G_F^2 the forward cross section is identically equal to the corresponding contribution from the square of the real part. One may still ask whether the dominance of the partonic part of the cross section, higher-order by g^2 compared to the elastic part, might not be a sign of large contributions from yet higher orders in the weak coupling. Integrating the factorized form of charged-current cross section, over x and Q^2, however, shows that at very high energy the square of the total cross section behaves as G_F^2 times $[g^2(S/M_W^2)^\lambda]^2$. This is to be compared to G_F^2 on the left-hand side of Eq. (52). The factor g^2 is the default size of a higher-order electroweak correction. The factor $(S/M_W^2)^\lambda$ is due to the large number of partons of size $1/M_W$ at $x \sim M_W^2/S$. For higher orders in g^2 to contribute at a similar level, they would have to come accompanied by a similar large counting factor. At the leading power in $1/M_W$, this cannot happen, simply because $q(x)$ and $\bar{q}(x)$ already count the partons.

The forgoing arguments, of course, assume that the unaided QCD extrapolations described above are equal to the task of so many orders of magnitude. We have shown above the self-consistency of these extrapolations, and that they do not, by themselves, lead to problems with unitarity, or give evidence of a breakdown in perturbation theory in the weak coupling. The very fact of the self-consistency of the QCD extrapolations shows that ultra high energy neutrinos offer an exploration of the strong interactions, as well as of cosmic dynamics, into unprecedented length scales.

Hadrons as Signature of Black Hole Production at the LHC
(I. Mocioiu, Y. Nara and I. Sarcevic, Phys. Lett. **B557**, 87 (2003))

If the fundamental Planck scale is of order of a TeV, as in some extradimensional scenarios, LHC is expected to be black hole factory. Recently we have proposed a novel way to look for a black hole production at the LHC. In pp collisions at the LHC, when the high energy partons with energies above TeV approach each other at the impact parameter which is less than the Schwarzschild radius in $4+n$ dimensions, they can form the $4+n$ dimensional black hole. Black hole production and evaporation can be described semiclassically and statistically when the mass of the black hole is very large compared to the fundamental Planck mass. When the mass of the black hole approaches M_P one expects quantum gravity effects

to become important. We have explored only the parameter space where the semi-classical treatment is justified. The black holes decay very rapidly and decay occurs in several stages. For the purpose of detecting black hole events, the most important phase is the semi-classical Hawking evaporation, since it provides a large multiplicity of particles and a characteristic black-body type spectrum. Most of this Hawking radiation is on the brane, producing all Standard Model particles. Because most of the Standard Model degrees of freedom come from strongly interacting particles (quarks and gluons), hadrons will be the dominant signal for the events where black holes are formed.

Recently, we have proposed that the shape of the transverse momentum distributions of charged hadrons at large p_T could be used as a signal for the black hole production. We have evaluated the transverse momentum distributions of charged hadrons at mid-rapidity obtained from the evaporation of black holes produced in pp collisions at LHC energies. We find that in pp collisions the black hole events produce a large number of hadrons and dominate over the QCD background at transverse momenta above around 30-100 GeV/c, where they can be clearly measured. The results have a weak dependence on the number of large extra dimensions, but depend quite strongly on M_P. We find the signal to be big enough to detect even for $M_P \sim 5$ TeV.

We find that the cross section for inclusive charged hadron production from black holes for several values of M_P ranging from 1 to 5 TeV in pp collision at LHC, compared to the expected spectrum of hadrons from QCD. LHC will be sensitive enough to detect the QCD hadrons up to p_T around 400 GeV/c. The black hole signal is much bigger than the QCD one starting at $p_T \sim 50 - 200$ GeV/c, depending on the Planck scale. It can be seen that even for M_P as high as 5 TeV there is a considerable signal above background at $p_T \approx 200$ GeV/c. At higher p_T the background is practically inexistent, while the black hole signal is still very large.

We evaluate the cross-section for inclusive charged hadron production from black hole decay for $M_P = 2$ TeV, compared with the QCD background. We find the results for $M_{BH}^{min} = 10$ TeV and $M_{BH}^{min} = 12$ TeV. It can be seen that including lower mass black holes gives considerably higher rates. Consequently, we consider our approach to be a 'conservative' one: our results are an underestimate of the actual signal and our qualitative conclusions always hold, while the actual quantitative results could be much higher than our estimates, making the signal easier to detect. Even for high mass black holes the signal clearly dominates over the QCD background in the region above 100 GeV/c, where it can be easily seen in the experiments. Including lower mass black holes gives a bigger signal for all momenta and also drives the signal above the background even for lower momenta, of the order of tens of GeV.

We also study the dependence of the results on the number of extra dimensions and show that it is very small. The QCD background is shown for different choices of the scale used in the structure and fragmentation functions (we use $p_T, p_T/2, 2p_T$). The dependence on this scale is very weak in the high transverse momentum region. For the black hole signal, the same change in Q_f leads to differences of up to a factor of 2 in the results, which does not change any of our conclusions.

We notice that even though there are significant changes in the overall rate of hadrons produced, the transverse momentum dependence of the hadrons does not change much when changing M_P or M_{BH}^{min}. This is not the case at the parton level. Changing M_P or M_{BH}^{min} the temperature of the black hole is modified and consequently the spectrum of the emitted

particles is different. Even though we can still see this for partons, the hadronization washes out most of the effect. We conclude that we cannot get a direct determination of the temperature of the black holes from the hadron spectrum. One could attempt to do that by looking at the spectrum of photons and electrons in the black hole event, which preserves the black body radiation type of spectrum, but is considerably lower than the hadron signal because photons and electrons are only a small fraction of the particles produced in the black hole evaporation. In that case, one would be forced to consider black holes with lower masses in order to obtain a detectable signal.

We have shown that the hadrons from black holes are detectable and dominate the background for p_T above about 100 GeV for fundamental Planck scales up to 5 TeV for any number of extra dimensions. Our results are conservative, as they only take into account very high mass black holes. Including black holes with lower masses gives even stronger signals. The value of p_T at which the signal becomes bigger than the background is determined by M_P and M_{BH} considered. We note that the QCD background shown in the graphs is computed at $y = 0$. For high rapidity this background is actually much smaller, while the black hole signal is the same for all rapidities. This would indicate that by looking in the high rapidity region one would enhance the signal to background ratio even further.

Our work on black hole production has attracted a lot of attention and several experimentalists have approaches us to pursue this work.

High energy neutrino signals of four neutrino mixing
(S. Iyer Dutta, M. H. Reno and I. Sarcevic, Phys. Rev. **D64**, 113015 (2001))

The combined results of solar, atmospheric and laboratory experiments with neutrinos, taken at face value, require a fourth neutrino species. This follows from the observation that the results of the three categories of experiments require at least three mass-squared differences δm^2. The mass-squared difference for solar neutrino experiments is limited to $\delta m^2_{solar} \approx 10^{-3}$ eV^2. The SuperKamiokande results for atmospheric neutrinos require $\delta m^2_{atm} \sim 3 \times 10^{-3}$ eV^2, and the laboratory LSND experiment limits $\delta m^2_{LSND} > 0.2$ eV^2. Combined fits to all of the experimental data do require a sterile neutrino species.

Given source ratios of fluxes $\nu_s^S : \nu_e^S : \nu_\mu^S : \nu_\tau^S = 0 : 1 : 2 : 0$ yield different ratios of neutrino fluxes at the detector, depending on whether the 2+2 or 1+3 scenario describes four-neutrino mixing. In the $1 + 3$ case with small ϵ and δ, the detector ratios are approximately $0 : 1 : 1 : 1$, while for the $2 + 2$ case, sterile neutrinos make an important component of the flux at the Earth, with $\nu_s^D : \nu_e^D : \nu_\mu^D : \nu_\tau^D \simeq 0.5 : 0.5 : 1 : 1$. With three neutrino species and bi-maximal mixing, one finds $\nu_e^D : \nu_\mu^D : \ \nu_\tau^D \simeq 1 : 1 : 1$. Without mixing, the source fluxes and detector fluxes have the same flavor ratios of $1 : 2 : 0$. As a result, the $1 + 3$ scenarios essentially reproduce the three-flavor bi-maximal mixing scenario, while the $2 + 2$ scenarios lie between the 3-flavor bi-maximal mixing model and the no-mixing model.

We have studied the upward shower and muon event rates for two characteristic four neutrino mixing models for extragalactic neutrinos, as well as for the atmospheric neutrinos, with energy thresholds of 1 TeV, 10 TeV and 100 TeV. We have shown that by comparing the shower to muon event rates, one can distinguish between oscillation and no-oscillation models. By measuring shower and muon event rates for energy thresholds of 10 TeV and 100 TeV, and by considering their ratio, it is possible to use extragalactic neutrino sources

to determine the type of four-flavor mixing pattern. Backgrounds from atmospheric muons make downward event rates difficult to extract, so our focus is on upward events. Two types of events will be produced: muon events and shower events. The muon events come from upward muons from $\nu_\mu \to \mu$ charged current events and from $\nu_\tau \to \tau \to \mu X$ from charged current production of taus followed by a muonic decay. In spite of the pile-up in the tau neutrino flux, the net effect of oscillations is to reduce the muonic event rate by approximately a factor of two relative to the no-oscillation rate, whether in the $1+3$ or $2+2$ mixing scenario.

Probing Extra Dimensions with Neutrino Oscillations
(K. Dienes and I. Sarcevic, Phys. Lett. **B500**, 133 (2001))

We have proposed a simple model for the neutrino mass matrix with no flavor mixing on the brane (only diagonal, mass elements are assumed to be non zero), only one bulk neutrino, and the couplings between our brane and the bulk are flavor blind. We find that it is possible to obtain flavor oscillations between our left-handed neutrinos in such a scenario even if the brane theory is itself flavor-diagonal. In such a scenario, all neutrino flavor oscillations are mediated indirectly through Kaluza-Klein states, and no mixing angles are required for the Standard-Model sector.

In the case when the brane/bulk coupling, m, is extremely small and the brane theory is flavor-diagonal, the brane/bulk oscillations are triggered when any of the m_i (diagonal elements on the brane) take values that are near integers (in units of R^{-1}). Sizable flavor oscillations (and actual flavor conversion) require approximate flavor degeneracies on the brane when m is small. In the case of large brane/bulk coupling, such cases, larger numbers of Kaluza-Klein states begin to participate in the neutrino oscillations. This increases the probabilities for oscillations into bulk neutrinos. Asymptotic probabilities are non-zero implying that even when an infinite number of bulk Kaluza-Klein states contribute to the neutrino oscillations, we do not lose all of our initial neutrino probability into the bulk states. Instead, as $m \to \infty$, we lose only $1/3$ of the initial probability into bulk neutrinos. This result generalizes to an arbitrary number of flavors. In general, we may take n_f flavors of neutrinos ν_i on the brane, where $i = 1, ..., n_f$. We find that $1/n_f$ of the initial probability is ultimately lost into bulk neutrinos, whereas $(n_f - 1)/n_f$ of the initial probability remains on the brane. If there were only one flavor of neutrino, we would therefore find that *all* probability is ultimately lost into the bulk. The different flavors in our model thus play a significant role in keeping a non-zero neutrino probability on the brane as $m \to \infty$. In our model we continue to have n_f brane neutrinos, but we only have one bulk neutrino. Therefore, as $m \to \infty$, we expect that this bulk neutrino will continue to take only $1/n_f$ of the initial brane probability. This is thus a key difference between our model and all other models in which one bulk neutrino is introduced for each brane neutrino, and indicates that our model has a very different behavior for large brane/bulk coupling than all other models which have been explored.

Our model provides a compact set of parameters with which one can attempt a detailed comparison with experimental data. Even though our model contains only five free parameters, it yields a surprising richness in resulting neutrino oscillation phenomenology, and exploits the higher-dimensional nature of the recent theories of reduced quantum-gravity

scale in an essential way. Thus, this model might be profitably used as the basis of a detailed experimental investigation of the viability of the higher-dimensional neutrino oscilliation mechanism. In 2001, after I have given seminar at Aspen Center for Physics on this work, several members of SuperK Collaboration expressed interest in testing our model with their data. Dr. J. Wilkes (U of Washington) and his graduate student had started to perform this analysis, but the recent SNO and KamLand data seem to leave very little room for models with sterile neutrino.

Secondary Neutrinos from Tau Interactions in the Earth
(S. Iyer Dutta, M. H. Reno and I. Sarcevic, Phys. Rev. **D66**, 077328 (2002))

In a recent paper, Beacom, Crotty and Kolb have suggested that in addition to a pile-up of tau neutrinos, the signal of astrophysical tau neutrinos will be enhanced by the appearance of "secondary" neutrinos. These secondary neutrinos come from purely leptonic decays of τ's. The idea is that while ν_ℓ ($\ell = e, \mu$) fluxes starting, for example, at nadir angle 0 are extinguished for sufficiently high energies, they will be regenerated by the $B = 0.18$ branching fraction for $\tau \to \nu_\tau \ell \bar{\nu}_\ell$, the τ being produced by $\nu_\tau \to \tau$ CC interactions. The flux of $\bar{\nu}_\ell$ is less likely to be extinguished due to the shorter path-length through the Earth (the ν_τ already had to travel its "interaction distance,") and its lower energy due to the combined energy loss in the CC process and the decay of the τ. Beacom *et al.* have considered mono-energetic neutrinos. We have explored realistic neutrino fluxes as well as generic power-law fluxes. We have evaluated the ratio of the attenuated flux to the incident flux at nadir angle $\theta = 0,\ 30$ and 60 degrees for $1/E$ and $1/E^2$. Except for the smallest nadir angles for the E_ν^{-1} spectrum, the secondary antineutrino flux is a small correction to the primary attenuated electron neutrino or muon neutrino flux. Even at nadir angle zero, the secondary flux is negligible compared to the transmitted primary flux for the $1/E_\nu^2$ spectrum. One should note that even though the ν_τ flux dominates the primary and secondary ν_μ fluxes, it does not dominate the contributions to the muon event rate because of the branching fraction $B = 0.18$ of $\tau \to \mu$ together with the effect of energy loss as the ν_τ converts to a τ which then decays to a μ.

In our event rates for IceCube, we have included the contributions from $\nu_\mu \to \mu$ and $\nu_\tau \to \tau \to \mu$ and in addition, the corresponding antineutrino induced antimuons from $\nu_\tau \to \tau \to \bar{\nu}_\mu \to \bar{\mu}$. We find that the secondary neutrino contribution to the muon event rate has its largest relative contribution at nadir angle zero, with an enhancement over the $\nu_\mu \to \mu$ plus $\nu_\tau \to \tau \to \mu$ rate of 50-60% for the $1/E_\nu$ flux. At this angle, the ratio of rates of the secondary contribution to the muon event rate relative to the event rate of muons from tau decays is quite large, about 1.5 for $E_\mu > 10^4$ GeV and 2.6 for $E_\mu > 10^5$ GeV. Unfortunately, this is where the event rate is smallest and statistics are low. By a nadir angle of $\sim 60^\circ$ (1 rad), where the event rate is roughly a factor of 10-20 larger, depending on the minimum muon energy, the enhancement in the overall muon rate is about 25%. At this nadir angle, the secondary ν produced muons are equal to the tau decay muon rate for $E_\mu > 10^5$ GeV. The crossover occurs at $\theta \sim 0.7$ rad for $E_\mu > 10^4$ GeV. At the larger nadir angles, the $\nu_\mu \to \mu$ contribution to the muon event rate is dominant.

The energy dependence of the incident tau neutrino flux is crucial in evaluations of the implications of ν_τ interactions to regenerate ν_τ and secondary $\bar{\nu}_\mu$ and $\bar{\nu}_e$. Neutrino fluxes

are attenuated due to their passage through the Earth, even the tau neutrinos, thus moderating tau neutrino contributions to secondary neutrino fluxes. With our current theoretical expectations for flux normalizations, the secondary neutrinos coming from τ decays will be difficult to observe experimentally, as they contribute significantly to a muon excess only at small nadir angles where the fluxes are already strongly attenuated.

Propagation of Muons and Taus at High Energies
(S. Iyer Dutta, M. H. Reno, I. Sarcevic and D. Seckel, Phys. Rev. **D63**, 094020 (2001))

We have studied the photonuclear contribution to charged lepton energy loss by taking into account HERA results on real and virtual photon interactions with nucleons. We have calculated the tau energy loss for energies up to 10^9 GeV taking into consideration the decay of tau. We have also re-evaluated the muon energy loss due to photonuclear interactions using the recent HERA results for the real and virtual photon-nucleon scattering. We have used the ALLM parameterization of the electromagnetic structure function $F_2(x, Q^2)$ to evaluate the photonuclear cross section including the $Q^2 \gg 0$ region. Our Monte Carlo evaluation of tau survival probability and range show that at energies below $10^7 - 10^8$ GeV, depending on the material, only tau decays are important. At higher energies the tau energy losses are significant, reducing the survival probability of the tau. We show that the average range for tau is shorter than its decay length and reduces to 17 km in water for an incident tau energy of 10^9 GeV, as compared with its decay length of 49 km at that energy. In iron, the average tau range is 4.7 km for the same incident energy.

At low energies, continuous energy loss by ionization dominates muon propagation, but at higher energies (above $\sim 10^3$ GeV), losses through pair production, bremsstrahlung and photonuclear interactions dominate. In the case of the muon, pair production is the most important mechanism, but for taus, the photonuclear process is at least as important as pair production. The high energy extrapolation of the photonuclear cross section has the largest theoretical uncertainty in the contributions to energy loss.

We have evaluated the pair production, bremsstrahlung and ionization energy loss for tau leptons, and we have evaluated the tau photonuclear differential cross section. We find that the photonuclear contribution dominates above $E \sim 10^5$ GeV.

The tau charged-current interaction length is comparable to its decay length at energies above 10^{10} GeV in water. Already at 10^8 GeV taus lose energy in water due to electromagnetic interactions. For tau energies above 10^{10} GeV in water, it will be an interplay of electromagnetic energy loss, decay and charged-current weak interaction disappearance of taus that will dictate tau effective ranges. Even in lead, which has a density of 11.35 g/cm^3, the decay length is shorter than the charged-current interaction length for energies below a few times 10^9 GeV, so our neglect of weak interactions below $E = 10^9$ GeV is a good approximation.

At energies above $\sim 10^8$ GeV, tau interactions become important in water and the range becomes significantly shorter. The effect appears at lower energies for more dense materials, for example, at tau energies less than 10^7 GeV for iron. We thus expect a decrease in the observed tau flux and tau neutrino energy relative to that expected if these effects had be ignored. The effect is most important for high energy taus arriving from directions just below the horizon. For directions subtending a significant portion of the Earth, energies will

be degraded to less than 10^6 GeV by repeated neutrino conversion to tau and tau decay. Near the horizon, the interaction length for charged current conversion becomes comparable to the length of the chord through the Earth, and the produced taus may arrive directly in the detector depending on their range. For $E > 10^8$ GeV, the tau range is decreased in water and such taus will either not arrive or arrive at lower energies. Correspondingly, for taus produced in a detector, measured dE/dX would be higher than expected without the revised photonuclear effects that we have calculated.

Tracing Ultrahigh Energy Neutrinos from Cosmological Distances in Ice

(*Jeremy Jones, Irina Mocioiu, Mary Hall Reno and Ina Sarcevic*)

Astrophysical sources of ultrahigh energy neutrinos yield tau neutrino fluxes due to neutrino oscillations. We have studied in detail the propagation of all flavors of neutrinos with very high energy ($E \geq 10^6$ GeV) as they traverse the Earth. We were particularly interested in the contribution from tau neutrinos, produced in oscillations of extragalactic muon neutrinos as they travel large astrophysical distances. After propagation over very long distances, neutrino oscillations change the initial (source) flavor ratio $1:2:0$ to $1:1:1$ because of the maximal $\nu_\mu \leftrightarrow \nu_\tau$ mixing. However, for GZK neutrinos, we have found that the flavor ratio at Earth deviates from 1:1:1 because the incident fluxes are different. In our propagation through the Earth, we have focused on kilometer size neutrino detectors, such as ICECUBE and RICE and on a detector with much larger effective area which uses Antarctic ice as a converter, the ANITA. We have found that ν_τ flux above 10^8 GeV resembles ν_μ flux, due to the tau energy loss. However, at lower energies, $E \leq 10^8$ GeV, regeneration of ν_τ becomes important for trajectories where the other flavors of neutrinos are strongly attenuated, but the ν_τ regeneration is very effective. The regeneration effect depends strongly on the shape of the initial flux and it is larger for flatter fluxes. The enhancement due to regeneration also depends on the amount of material traversed by neutrinos and leptons, i.e. on nadir angle. We have considered the signals of ν_τ in the kilometer size (ice) detectors, as well as in ANITA, such as electromagnetic and hadronic showers. Results are shown in Fig. 1. We have studied dependence of the enhancements on the shape of the initial flux. We have included contribution from secondary neutrinos, which we find to be relatively small for both GZK and 1/E flux. We find that large detectors with energy threshold below 10^8 GeV and with very good angular resolution are needed for distinguishing between diffrerent neutrino flavors.

Recently, it was proposed to use rock salt formations as large scale neutrino detectors. Salt has a higher density than ice, so it is possible to achieve an effective detection volume of several hundred km^3 water equivalent in salt. The threshold for detecting the radio signal from showers in salt is of the order of $\sim 10^7$ GeV. Also proposed is LOFAR, a digital telescope array designed to detect radio Cherenkov emission in air showers with sensitivity in an energy range of $\sim 10^5 - 10^{11}$ GeV. LOFAR will likely be configured to detect horizontal showers from skimming neutrinos as well. With its low energy threshold, LOFAR has an excellent opportunity to observe the shower enhancement at lower energies due to ν_τ regeneration and tau pileup, which is not easily accessible in ANITA. We plan to study signals for neutrino oscillations and flavor composition in SALSA and LOFAR.

Signals of Electroweak Instantons in Neutrino Telescopes

(*Sharada Iyer Dutta, Jeremy Jones and Ina Sarcevic*)

Instantons are non-perturbative gauge field fluctuations that describe tunnelling transitions between different topological configurations in non-abelian gauge theories like electroweak theory pr QCD. Instanton induced processes are beleived to be at the origin of baryon and lepton number violations in electroweak theory. In semi-classical approximation, the collision process can be well described by solutions to the equations of motion that interpolate between the intial and final states. There exists a static unstable solution, so-called "sphaleron" (of energy $E \sim 8$ TeV), to the equations of motion that lies at the top of the potential barrier. The energies at which trasition rate is not too small are not currently accessible to the colliders. Thus, ultrahigh energy cosmic neutrinos provide unique probe of electroweak instantons.

Recently we have calculated instanton-induced neutrino-nucleon cross section. From Fig. 2 we note that this cross section becomes dominant over the charged-current cross section at energies above 10^6 GeV. We also show our results for the cross section for producing microscopic black hole, predicted in theories of large extra dimensions, in neutrino interactions. These cross sections have strong dependence on scale of extra dimensions and the number of extra dimensions.

In effect, this causes an enhancement in the neutrino-nucleon cross section relative to the standard model cross section at parton center-of-mass energies $E \geq 30$ TeV.

High Energy Neutrino Propagation and Small x Parton Distributions

(*Irina Mocioiu, Mary Hall Reno, Ina Sarcevic and Anna Stasto*)

Ultrahigh energy neutrino cross section depends on parton distributions at very small x, values that are beyond currently accesible range in the colliders. In order to obtain charged-current and neutral-current neutrino cross sections at energies above 10^6GeV, we need to extrapolate parton distribution into the low x region. We consider three approaches to the extrapolation:

- extrapolation of the standard DGLAP evolution
- unifed BFKL/DGLAP evolution equations
- inclusion of saturation effects, via nonlinear terms in BFKL/DGLAP equations

The most straightforward approach is to use the standard gluon distribution obtained within the DGLAPframework from the global fit, such as MRS or CTEQ, and extend it to lower values of x using the power-law extrapolation. Another approach is to use the BFKL framework which resums the leading terms $\alpha_s \ln 1/x$. This approach has the advantage of treating both the BFKL and DGLAP evolution schemes on equal footing and it also resums the major part of the NLO corrections to the BFKL equation. In this framework one is using the high energy factorisation theorem together with the unintegrated parton distribution function. In the region of high energies, where the parton densities become high, the parton recombination effects can become important. These effects lead to the slower increase of the parton density with energy and in consequence to the damping of the cross section. This

is called perturbative parton saturation. These effects are included via nonlinear terms in BFKL/DGLAP evolution equation.

We have found results for charged-current neutrino cross sections obtained with these three approaches. We note that the cross section differs by a factor of 2 at energy 10^{12} GeV. We have studied the effect of this difference on neutrino flux as it propagates thorugh rock and ice, with DGLAP parton distribution and with nonlinear BFKL/DGLAP. We note that the nonlinear effects are large for energies above 10^8 GeV.

Propagation of Supersymmetric Charged Leptons at High Energies: Probing Low Scale Supersymmetry with Neutrinos

(*Mary Hall Reno, Ina Sarcevic, Shufang Su*)

In low scale supersymmetric models, such as gauge mediated supersymmetry breaking, the lightest supersymmetric particle is the gravitino. The next to lightest supersymmetric particle is typically a long lived charged slepton. Collisions of high energy neutrinos with nucleons in the earth can result in the production of sleptons. Their very high boost means they travel very long distances before decaying. However, as sleptons traverse the earth they also lose energy via photonuclear inetractions, pair production and bremsstrahlung. Energy dependence of the energy loss results in in very different energy spectrum of the staus that reach the detector where they decay. We are currenyly investigating the energy loss of sleptons. We have found that photonuclear interactions dominate at high energies. We also find that they are energy dependent. We have compared slepton energy loss with their standard model partners, muon and tau.

Detection of Low-Scale Models of Neutrinos Masses with Supernova Neutrinos

(*Haim Goldberg, Lawrence Hall, Gilad Perez and Ina Sarcevic*)

Models with low-scale breaking of global symmetries in the neutrino sector provide an alternative to the seesaw mechanism for understanding why neutrinos are light. Such models can easily incorporate light sterile neutrinos required by the LSND experiment. Furthermore, the constraints on the sterile neutrino properties from nucleosynthesis and large scale structure can be removed due to the non-conventional cosmological evolution of neutrino masses and densities. We have studied explicit, fully realistic supersymmetric models, and discussed the characteristic signatures predicted in the angular distributions of the cosmic microwave background.

III.1.1 DØ Physics Program – Overview

Brief History

In Run I, much of the University of Arizona effort on DØ was led by Ken Johns who, along with a group composed typically of two postdocs and two to three graduate students, led substantial initiatives in building the experiment (Level 1.5 Muon Trigger) and producing interesting physics output (b-quark cross section and correlations using dimuons). This group produced six Ph.D. dissertations during this period (David Fein, Eric James, Alex Smith, Ajay Narayanan, David Vititoe, and Kevin Davis), and its members were primary authors on many DØ publications.

In the years of transition between Run I and Run II, Ken Johns received teaching relief from the Department of Physics to go to Fermilab for two years as co-head of the Muon Detector Upgrade for Run II. In this capacity he oversaw the complete replacement of all DØ forward region detector subsystems, and refurbishment of the wide-angle detector Proportional Drift Tubes (the WAMUS PDT's). In the forward region, PDT's were replaced by planes of fast response scintillators (PIXEL counters), organized into stations with Miniature Drift Tube planes (MDT's). The scale of this effort was approximately the same as that required for the fabrication of the Run I muon system, and subsequent data taking has shown this major upgrade to be a great success.

Arizona's muon trigger fabrication commitments continued in Run II, where Ken Johns and his group led the construction and commissioning of the Level 1 Muon Trigger (L1MU), a critical piece of the DØ detector upgrade. He and his group are now exploiting the L1MU trigger to produce top quark physics in the muon decay channels. This is one of several instances where this group has taken a project from the "A" of hardware design to the "Z" of final physics analysis.

Approximately one year ago, the University of Arizona effort on DØ was dramatically increased when faculty members Elliott Cheu and Erich Varnes joined the collaboration. On a very short time scale, each began making significant contributions to a variety of physics analyses and service tasks.

The Arizona group also has a long record of accomplishment in calorimetry and QCD related physics. Andrew Milder (advised by John Rutherfoord), made the first efforts to understand the jet energy scale of DØ (basing the jet response on the single particle response from testbeam work). He also did considerable work on understanding the jet trigger response. Andy's thesis was on the dijet mass distribution, and its use to set limits on quark compositeness. Brent May (advised by Geoff Forden, no longer at Arizona), did his thesis on rapidity gaps in multijet events, which reflect the underlying kinematics and color flow of QCD events – a topic dear to the heart of theorists such as James Bjorken. And Levan Baboukhadia (advised by Michael Shupe) did the `final' DØ Run I thesis on the inclusive jet P_T spectrum – the other primary measurement in collider detectors sensitive to quark substructure. Levan's contribution was to extend the jet analysis into the endcap calorimeters, exploiting DØ's full acceptance, and to participate with other QCD collaborators in establishing the final Run I jet energy scale for DØ

in 1999. Levan confirmed earlier DØ results that there was no excess of events at high P_T, which would have signaled possible quark substructure. To this day, we remain a bit at odds with the CDF experiment, which tends to favor the view that an excess has been detected. We are looking forward to the opportunity in Run II to revisit this problem and see whether the DØ or CDF conclusions change. However, the QCD related effort in Run II is of small scale compared to that in top quark, B physics, and muon physics, so the remainder of this DØ progress report and the DØ proposal focus on these major Run II efforts.

Group Members

Current members of the University of Arizona DØ group are listed in Table III.1.1. Also included is a few word description of the physics and service groups to which each member has contributed. This is meant only as a brief summary. We've made an effort to identify people with specific achievements below. Note that Elliott Cheu, Erich Varnes, Stefan Anderson, Peter Tamburello, and Bryan Gmyrek are just now reaching their one-year anniversary on DØ.

Some details of the group members listed in Table III.1.1 follow:

Elliott Cheu joined the DØ effort in April 2002 after a very productive collaboration on KTEV. One measure of his KTEV success was his promotion to Associate Professor in 2002. On joining DØ, Elliott made an immediate impact by playing a leading role in commissioning the Global Monitor (GM) examine for which he wrote and tested a number of ROOT macros. The GM examine is the online monitor of the physics performance of the experiment. Most recently, he has been leading a physics analysis effort to search for $B_s \rightarrow \mu\mu$.

Ken Johns has been a DØ collaborator since 1991. He has held a variety of important leadership roles on the experiment including B Physics co-convener (Run I) and co-head of the Muon Detector Upgrade (Run II). He also led the design, development, installation, commissioning, and certification of the L1MU trigger for Run II, which in general has been a big success. He is working with Stefan Anderson and Jeff Temple on the measurement of the top quark production cross section and mass in the dimuon channel and with Erich Varnes and Bryan Gmyrek on the measurement of the W polarization in top quark decays using the muon plus jets channel. Finally, he is leading the L1CalTrack trigger project, a Run II trigger upgrade.

Mike Shupe, having recently finished a long series of radiation background simulations for ATLAS, is returning to DØ to pursue QCD physics in Run II. He will also collaborate with others at Arizona in top quark physics. His service contribution will initially be to help in the move of the DØ luminosity database from the current flat files to the Oracle database.

Erich Varnes joined the University of Arizona in July 2002 and is presently supported by his start-up funds. He is an important addition to our request for a new DOE contract. Erich's postdoctoral work was done on BABAR (Princeton). However he is an experienced DØ collaborator, having measured the top quark mass for his thesis dissertation (LBL). Since rejoining DØ, Erich has been very active in evaluating the performance of the tracking algorithms, initiating analysis work on the measurement of the W polarization in top quark decays, and collaborating with Ken Johns on the L1CalTrack trigger.

Name	Position	Present Funding	Physics/Service
Elliott Cheu	Faculty	Arizona/DOE	Higgs, B/L3
Ken Johns	Faculty	Arizona/DOE	Top/L1MU, L1CalTrack
Mike Shupe	Faculty	Arizona/DOE	/Luminosity DB
Erich Varnes	Faculty	Arizona	Top/Tracking, L1CalTrack
Stefan Anderson	Postdoc	DOE	Top/L1MU
Peter Tamburello	Postdoc	DOE	Higgs, B/L3
Susan Burke	Grad Student	DOE	Top/
Bryan Gmyrek	Grad Student	DOE	Top/L1CalTrack
Rob McCroskey	Grad Student	DOE	B/L1MU
Jeff Temple	Grad Student	DOE	Top/L1MU
Vernon Miller	Grad Student	DOE	/L1CalTrack
Semra Bekele	Undergraduate Technician	NSF	L1CalTrack
Chris Leeman	Undergraduate Technician	DOE/Fermilab	/L1MU, L1CalTrack
Joel Steinberg	Elec. Engineer	Arizona/Fermilab/ DOE	/L1MU, L1CalTrack
Dan Tompkins	Elec. Engineer	Arizona/ATLAS	/L1MU, L1CalTrack

Table III.1.1 Current Arizona personnel working on the DØ experiment.

Stefan Anderson joined DØ after earning his thesis on the CLEO experiment (Minnesota). He is leading our day-to-day effort on the top quark production cross section and mass measurement in the dimuon decay channel. He has also become one of the experts who monitors and trouble-shoots the L1MU trigger hardware.

Peter Tamburello is a senior postdoc who previously worked on CDF in the Exotics physics group. Like Erich Varnes, he is also a seasoned DØ collaborator, having written his thesis on the measurement of the top quark production cross section in the electron plus jets decay channel (Maryland). Peter is focusing primarily on data analysis. He is searching for the Higgs particle in associated W production and collaborating with Elliott Cheu in the search for $B_s \rightarrow \mu\mu$

Noah Wallace was a senior postdoc with Arizona from December 2002 until July 2003 when he left for more lucrative employment in industry. Noah's most important contribution during this period was to the online software for the L1MU trigger. Given the high priority placed on data-taking efficiency, Noah's creativity in writing sophisticated GUIs that allowed us (as well as the shifters) to control many of the most important L1MU options with a few keystrokes was invaluable. He also simplified a number of the L1MU trigger algorithms in the trigger simulator, tsim_l1muo.

Susan Burke joined our DØ group in January 2003. During the spring she finished her classes and this summer she is primarily preparing for the written and oral exams required at the University of Arizona. However she also performed some important data versus Monte Carlo comparisons in missing E_T (MET). Her thesis topic is still TBA but will either be in top quark physics or in non-Standard Model Higgs searches involving tau decays.

Bryan Gymrek joined our DØ group in June 2002 but was not a full-time researcher until he successfully passed the required written and oral exams at the University of Arizona. He is our local expert in b-jet tagging and his tentative thesis topic is the measurement of the W polarization in top decay using the muon plus jets decay channel.

Rob McCroskey is a senior graduate student who leads L1MU trigger operations at Fermilab. He has been involved in nearly every aspect of the L1MU trigger beginning with prototype testing and his knowledge of the L1MU trigger electronics is complete. The fact that the L1MU trigger operates so smoothly during data taking now is the result of a tremendous amount of debugging and problem solving by Rob before first collisions. He has also made important contributions to L1MU trigger simulation, tsim_l1muo. His thesis topic is the measurement of the rapidity dependence of the J/ψ cross section. He will likely defend this thesis at the end of 2003.

Vernon Miller joined our DØ group in June 2003. He is working with Erich Varnes on simulations of the L1CalTrack trigger.

Jeff Temple is a senior graduate student who has also made a number of important contributions to the L1MU trigger, especially to online software and monitoring. He created a sophisticated L1MU web page that posts L1MU trigger rates and certification plots every hour. Certification means comparison of the L1MU trigger hardware results in data with those from the L1MU trigger simulator using detector front-end data as input. Jeff's thesis topic is the measurement of the top quark mass in the dimuon decay channel.

Chris Leeman is an electrical engineering student who has worked with us as an electronics technician since June 2000. Unfortunately for us, she will graduate next year. Chris has played an important role in testing and debugging all L1MU trigger cards in the lab. At times she has also assembled boards, terminated and tested cables, and simulated L1MU trigger algorithms using Altera's MAXPLUS II and QUARTUS. She is presently helping with various design checks of the L1CalTrack trigger.

Joel Steinberg is an outstanding senior electronics engineer who designed and oversaw fabrication of the L1MU trigger. He also designed the Gb/s serial links (SLDB's) that are used by the L1MU trigger as well as by other detector systems on DØ including the Trigger Framework. The SLDBs have performed flawlessly. Joel is presently working on the design and fabrication of the L1CalTrack trigger system.

Status of DØ

A thumbnail summary of the status of DØ is provided here. Run II collisions began in June 2001 and serious data-recording began in August 2001. The running period from August 2001 until August 2002 was effectively dominated by commissioning of the experiment. The CFT tracker was fully instrumented in April 2002 and the CFT Level 1 Tracking Trigger (CTT) was commissioned by December 2002 . Most physics analyses use data beginning with August 2002. Since that date DØ has recorded approximately 150 pb^{-1} of data from the 200 pb^{-1} delivered by the accelerator. Currently the ratio of recorded/delivered luminosity on DØ is typically 90% / store. The peak luminosity during the above period was $45x10^{30}/cm^2/s$. Current physics analyses in progress typically use data sets of 90-110 pb^{-1}.

Longer term, our understanding is that the Tevatron hopes to deliver 1.5 fb^{-1} by the end of CY 2004 and 3.5-4.5 fb^{-1} by the end of CY 2007. While these goals are smaller than originally envisioned, the physics program at DØ still represents the best opportunity for new discovery in the field of particle physics before the turn-on of the LHC.

Summary

As noted above, a majority of the Arizona DØ group has been working on the experiment for only one year. In the following section, we detail our physics analyses in top, B, and Higgs physics. Postdoc Stefan Anderson, Ken Johns, and graduate student Jeff Temple are measuring the $t\bar{t}$ production cross section and top quark mass in the dimuon decay channel. Erich Varnes, Ken Johns, and graduate student Bryan Gmyrek are just beginning an analysis to measure the *W*-boson polarization in the muon plus jets decay channel. Elliott Cheu and postdoc Peter Tamburello are searching for $B_s \rightarrow \mu\mu$. Peter Tamburello is also searching for the Higgs in the $l\nu b\bar{b}$ decay mode.

Arizona has traditionally carried a heavy service load on DØ. Our most significant service contribution was the delivery of the Level 1 Muon Trigger (L1MU) to the DØ experiment. We continue to provide extensive support described below for the L1MU trigger hardware and software. Ken Johns leads this effort with substantial support from postdoc Stefan Anderson and graduate students Rob McCroskey and Jeff Temple. Erich Varnes' service contributions are in the important area of track reconstruction. Elliott Cheu and postdoc Peter Tamburello are involved with several aspects of the Level 3 (L3) trigger, including holding primary responsibility for the L3 online trigger examine. Many of us run data-taking shifts each month.

Taking the attitude of exploiting every chance for new discoveries at the Tevatron before the turn-on of the LHC, we are supporting Run II detector upgrades through our leadership and efforts on the L1CalTrack trigger. Ken Johns is leading this project in collaboration with Erich Varnes and graduate students Bryan Gmyrek and Vernon Miller. This project is briefly summarized at the end.

III.1.2 DØ Physics Program - Top Quark Physics

For the next ten years, top quark physics will be aggressively pursued by experiments at both the Fermilab Tevatron and CERN Large Hadron Collider. There are many reasons why this physics is compelling. Radiative corrections to the W boson mass link the W boson, Higgs boson, and top quark masses, meaning that precise measurements of the top quark mass and W boson mass provide an indirect measurement of the Standard Model (SM) Higgs boson mass. If, or when, the Higgs boson is discovered, comparison of the measured Higgs boson mass with this indirect measurement will be a crucial test for the Standard Model.

Top quark physics is compelling for other reasons as well. The heavy mass of the top quark implies a Yukawa coupling to the Standard Model Higgs boson of order unity, making it somewhat unique among the fundamental particles. This suggests that the top quark could play some special role in electroweak symmetry breaking. In addition, the top quark lifetime is less than a yoctosecond, which is shorter than the hadronization time of QCD. Thus the top quark can be studied free of confinement effects. An example of such a study is the measurement of the W-boson helicity in top quark decays. Finally, in Run I of the Tevatron, DØ and CDF measured the top quark mass and $\sigma(t\bar{t})$, but little else with much precision. Run II of the Tevatron provides an exciting opportunity to study top quark production and decay properties with reasonable statistics.

Top Quark Physics – Production Cross Section in the Dimuon Decay Channel

Given a Run II data set nearly equal in size to that of Run I, an important milestone for DØ is the measurement of the $t\bar{t}$ production cross section and top quark mass in all decay channels. While the dimuon decay channel has a small branching ratio (1/81) it benefits from the fact that there are few background processes with two muons and two jets each with high transverse momentum (P_T) along with substantial missing E_T. Additionally, there is an intrinsically low rate of falsely identified muons in the DØ detector.

Postdoc Stefan Anderson is leading the Arizona effort to measure the $t\bar{t}$ production cross section in the dimuon decay channel. Others doing substantial work on this analysis are Ken Johns and graduate students Jeff Temple and Susan Burke.

The experimental signature for the $t\bar{t}$ dimuon decay channel is two high-P_T, isolated muons, two high-E_T jets from the *b*-quarks, and large missing E_T from the neutrinos. The trigger used to select $t\bar{t}$ events in the dimuon decay channel is based on hits in the muon detector. The Level 1 trigger requires that at least two muons be found where each is identified from scintillator hits inside and outside the toroid magnet iron. Some additional rejection at Level 1 is achieved by requiring that luminosity monitors on either side of the interaction region fire in coincidence. The Level 2 trigger requires at least one reconstructed muon using scintillator and wire chamber hits inside and outside the iron.

As the delivered luminosity increased, it became necessary to add additional rejection of backgrounds to reduce the rate to tape from the above trigger. Two separate Level 3 trigger requirements were added as a logical OR. The first required a reconstructed muon at Level 3 with $P_T > 15$ GeV/*c*. The second required a central track with $P_T > 10$ GeV/*c*.

The cross section analysis uses DØ's standard particle identification criteria for muons, jets, and missing E_T. Muon identification involves both the muon system and central tracker. Muons reconstructed with the muon detector system are required to have both wire chamber and scintillator hits inside and outside of the toroid magnet iron. Central tracks are reconstructed from hits in the silicon tracker and central fiber tracker and then combined with the muon system track in a global fit. Candidate muons are required to have a matching central track. Isolated muons are selected by requiring little calorimeter energy and total track P_T in a cone about the muon track.

Jets are found using the well-established cone algorithm. Noise is suppressed by additional requirements such as limiting the fraction of energy that can be deposited in the coarse hadronic layer of the calorimeter. The missing E_T is constructed as the vector sum of the transverse components of all calorimeter cells having energy greater than 100 MeV. To account for the fact that muons are nearly minimum ionizing, the measured P_T of muons is added to missing E_T and the expected dE/dX calorimeter energy deposition is subtracted from the missing E_T.

The data used for this measurement were collected from August 15, 2002 through June 30, 2003. After runs having detector problems are removed, the integrated luminosity of the sample is approximately 90 pb^{-1}. The reconstructed *Z*-boson mass using selection criteria appropriate for *Z*-bosons (essentially two reconstructed, isolated muons with opposite sign) is shown in Figure III.1.1. The fit function is a Gaussian plus an exponential background. The width of the Gaussian is approximately 9 GeV/c^2.

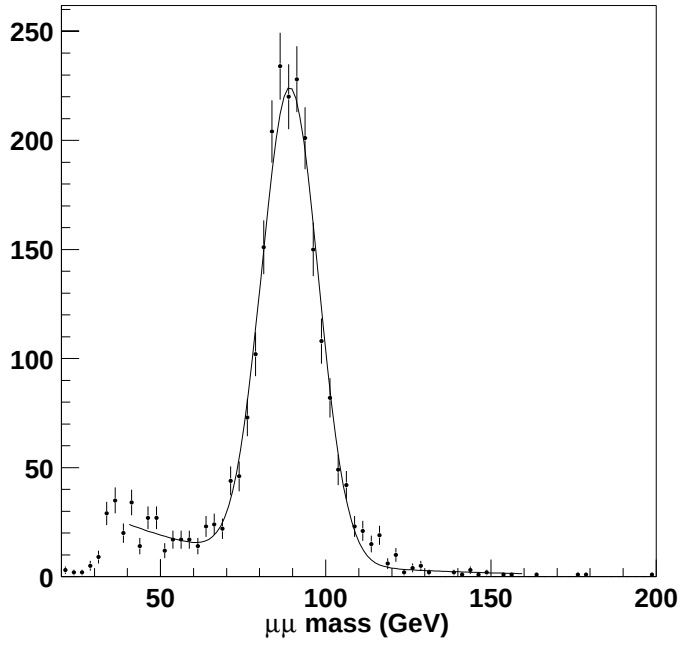

Figure III.1.1. The dimuon invariant mass for two isolated muons with $P_T > 15$ GeV/*c*. The fit to the data uses a Gaussian for the signal plus an exponential for the background. The width of the Gaussian is approximately 9 GeV/c^2.

Event passes the dimuon trigger at Level 1, 2, and 3
At least 3 tracks used in fitting the primary vertex
|Primary vertex z position| < 60 cm
Two reconstructed, isolated muons with opposite sign
Two muons with P_T > 15 GeV/c
Difference in the z vertex position of the two muons < 5 cm
Distance-of-closest approach (DCA) significance < 3 for both muons
At least 2 jets with E_T > 20 GeV
M(μμ) < 70 GeV/c^2 or M(μμ) > 110 GeV/c^2
Missing E_T > 25 GeV
H_T > 100 GeV

Table III.1.2. Selection criteria for $t\bar{t} \rightarrow \mu\mu$ events.

Measured Quantity	Value (GeV)
P_T of Muon 1	188.1
P_T of Muon 2	20.0
E_T of Jet 1	80.6
E_T of Jet 2	26.5
E_T of Jet 3	17.3
M(μμ)	137.2
Missing E_T	89.4
H_T	124.4

Table III.1.3. Observables for the $t\bar{t}$ to dimuons candidate event.

The selection criteria optimized to accept signal and reject backgrounds for this analysis are listed in Table III.1.2. The variable H_T is the sum of the E_T of all jets with E_T > 15 GeV within $|\eta| < 2.5$.

One event survives all selection criteria. The observed quantities for this event are given in Table III.1.3. Different views of the event display are shown in Figures III.1.2-III.1.4.

The trigger and event selection criteria efficiencies are summarized in Table III.1.4. The efficiencies are derived using both data and signal Monte Carlo events. The errors are only statistical at this time. For signal Monte Carlo we used Pythia $t\bar{t} \rightarrow \mu\mu$ events generated with a top mass of 175 GeV/c^2. Correction factors to Monte Carlo efficiencies based on appropriate data samples were calculated and are also listed in Table III.1.4.

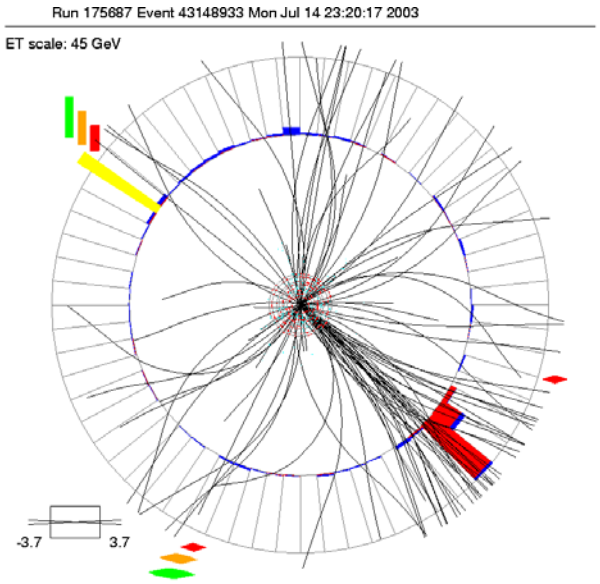

Figure III.1.2. R- φ view of the $t\bar{t}$ to dimuons candidate event

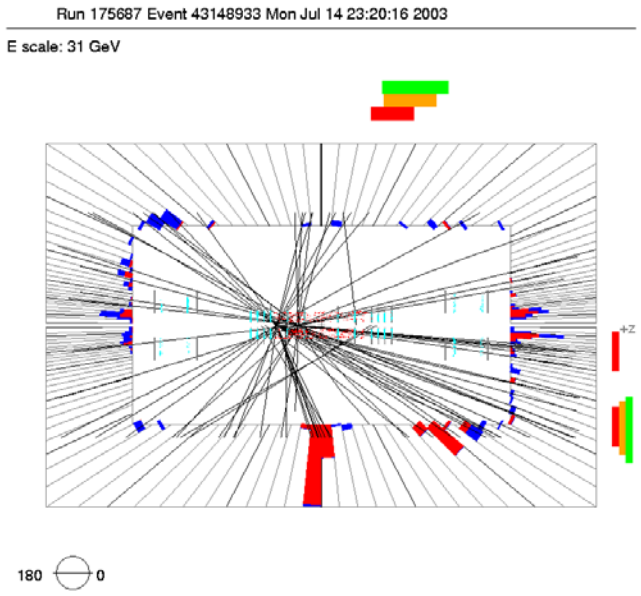

Figure III.1.3. R-z view of the $t\bar{t}$ to dimuons candidate event.

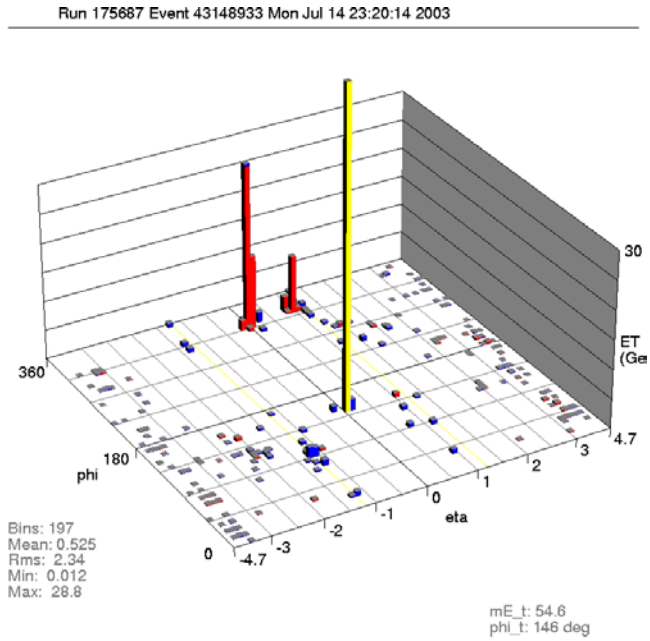

Figure III.1.4. Lego plot of the $t\bar{t}$ to dimuons candidate event.

Category	Cut	Efficiency	Source
Vertex quality	$\|z\| < 60$ cm, $N_{vertex} > 3$	0.974 ± 0.002	Signal Monte Carlo
Muon ID	≥ two muons	0.438 ± 0.004	Signal Monte Carlo
Muon ID	Isolation	0.609 ± 0.008	Signal Monte Carlo
Muon ID	DCA significance < 3	0.933 ± 0005	Signal Monte Carlo
Muon ID	Data/MC muon ID per muon	1.083 ± 0.013	*Z*'s from data
Muon ID	Data/MC track match	0.611 ± 0.010	*Z*'s from data
Muon ID	Data/MC isolation per muon	0.989 ± 0.046	*Z*+2 jets from data
Trigger	Level 1	0.937 ± 0.005	Jet triggered data
Trigger	Level 2	0.995 ± 0.002	Jet triggered data
Trigger	Level 3	0.99 ± 0.01	High mass dimuon data
Jet ID	≥ two jets	0.892 ± 0.007	Signal Monte Carlo
Kinematic	Two muons with $P_T >$ 15 GeV/c	0.867 ± 0.006	Signal Monte Carlo
Kinematic	Two muons with $E_T >$ 20 GeV	0.916 ± 0.006	Signal Monte Carlo
Kinematic	Missing $E_T > 20$ GeV and M(μμ)	0.627 ± 0.007	Signal Monte Carlo
Kinematic	$H_T > 100$ GeV	0.843 ± 0.010	Signal Monte Carlo
Total	All	0.06 ± 0.01	

Table III.1.4. Efficiencies for the selection criteria for $t\bar{t} \rightarrow \mu\mu$.

The $t\bar{t} \rightarrow \mu\mu$ efficiency for all selection criteria is $\varepsilon_{total} = 0.06 \pm 0.01$. The expected signal event yield is given by

$$N_{exp} = \varepsilon_{total} \times BR \times \sigma \times \int L dt.$$

Inserting values for these variables gives $N_{exp} = 0.06 \times 0.012 \times 7$ pb $\times 90$ pb$^{-1} = 0.5$ events. We thus expect to observe 0.5 signal $t\bar{t} \rightarrow \mu\mu$ events in our data sample with the above selection criteria applied.

The primary background for this decay channel with the above selection criteria is Drell-Yan/$Z \rightarrow \mu\mu$. This background has a large cross section with two high P_T muons, but has no significant missing E_T, and the Z-boson mass can be resolved. Secondary backgrounds include $Z \rightarrow \tau\tau \rightarrow \mu\mu$, $WW \rightarrow \mu\mu$, and QCD heavy flavor production. The $Z \rightarrow \tau\tau$ background has a small branching ratio to dimuons and the muon P_T and missing E_T are moderate. The $WW \rightarrow \mu\mu$ background has a small cross section but the final state resembles that for the $t\bar{t}$ signal, though it tends to have less hadronic energy. The QCD background has a large cross section but the muons are soft and non-isolated and there is rarely large missing E_T.

For many of the background estimates we currently rely on Monte Carlo samples generated using Pythia and Alpgen. Graduate student Susan Burke performed comparisons of measurable quantities in data and Monte Carlo in order to check the reasonableness of this method. To correct for the difference in momentum resolution between data and Monte Carlo, we smear the muon P_T in Monte Carlo. The functions are chosen to give good agreement between data and Monte Carlo in the mean and standard deviation of the inverse muon momentum distribution.

Using Pythia samples of Z-bosons and Alpgen samples of Z + 1 jet, data/Monte Carlo comparisons were made for the following observables: muon P_T, dimuon invariant mass, and missing E_T. After smearing the muon P_T in Monte Carlo, we find good agreement in these observables.

For example, we select events from Alpgen Z + 1 jet Monte Carlo and from data with two isolated muons having $P_T > 15$ GeV/c and at least one jet with $E_T > 20$ GeV. To preserve statistics, no H_T cut is employed. Figure III.1.5 shows the missing E_T distribution from data and Monte Carlo overlaid. While the statistics are low, the agreement is reasonable.

Another data/Monte Carlo cross check is performed by comparing the number of Z-boson plus two jet events for $75 < M(\mu\mu) < 105$ GeV/c^2. We observe 11 events in the data while the Monte Carlo predicts 15.9 ± 1.6, where we assigned a 10% systematic uncertainty due to the luminosity uncertainty. The much smaller $Z \rightarrow \tau\tau \rightarrow \mu\mu$ and $WW \rightarrow \mu\mu$ backgrounds were estimated using Alpgen and Pythia Monte Carlo samples respectively.

The background from QCD and W–boson plus jets heavy flavor production is estimated using the missing E_T distribution for events having isolated muons. The ratio of the missing E_T distribution for events with one isolated muon to the missing E_T distribution for all muons is shown in Figure III.1.6. The events were also required to have two jets and $H_T > 100$ Gev. Though the statistics are low, we interpret the rise in the ratio above missing $E_T > 40$ GeV to be an indication of the presence of truly isolated muons from W-boson and Z-boson decays. We

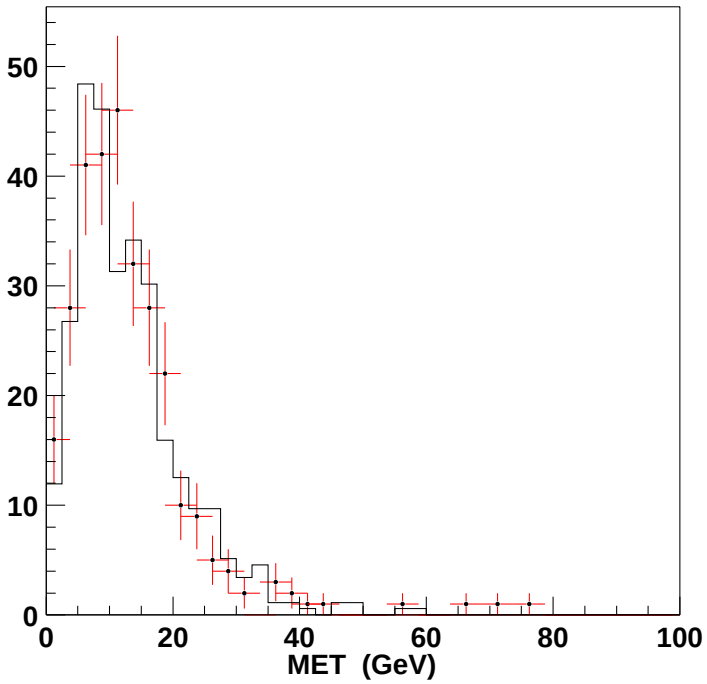

Figure III.1.5. Comparison of the missing E_T distribution between data and Alpgen Z + 2 jet Monte Carlo. The events were required to have two high P_T muons and two high E_T jets.

extract the fake isolation rate using the ratio of isolated/all dimuons, which is conservative. This ratio is found to be $f_{iso} = 0.032 \pm 0.002 \pm 0.032$, where a 100% systematic error is assumed.

To estimate the background from QCD and W–boson plus jets heavy flavor production, events are selected with all selection criteria applied except that only one isolated muon is required instead of two. The number of events that pass times f_{iso} above gives the estimate for this background.

The expected background contributions from all sources is summarized in Table III.1.5.

Background	Yield	Statistical Error	Systematic Error
Z/DY	1.302	0.272	0.130
WW	0.007	0.001	0.001
QCD and W+jet heavy flavor	0.256	0.092	0.256
Total	1.6	0.3	0.3

Table III.1.5. Summary of background contributions to the $t\bar{t} \rightarrow \mu\mu$ signal.

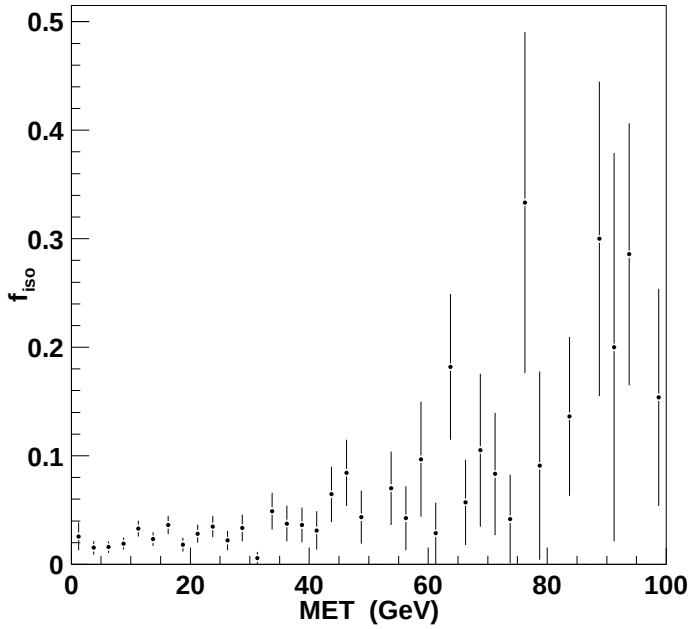

Figure III.1.6. The ratio of the MET distribution for events that have one isolated muon to the MET distribution for all muons. Events were also required to have two jets and $H_T > 100$ GeV.

In summary, we observe one candidate $t\bar{t} \rightarrow \mu\mu$ event that passes all selection criteria. With those criteria we expect to observe 0.5 $t\bar{t} \rightarrow \mu\mu$ events and 1.6 events from background. Thus our present observation of one event is consistent with the expected background yield. While we have presented a relatively complete analysis, there is much additional work that needs to be done. This work includes fine-tuning the event selection criteria, estimating background using appropriate data samples, and performing studies to estimate systematic errors. Our goal is to publish this measurement in the coming year.

Top Quark Physics - Mass Measurement in the Dimuon Decay Channel

Measurement of the top quark mass in the $t\bar{t} \rightarrow \mu\mu$ channel is graduate student Jeff Temple's thesis topic and one of Arizona's early Run II physics goals. Ken Johns and postdoc Stefan Anderson are also working on this analysis. We are also collaborating with Harry Weerts, postdoc Bob Kehoe, and graduate student Joe Kozminski of Michigan State to develop general methods to measure the top quark mass in the $t\bar{t}$ to dileptons decay channel. To date, most of our effort has gone into measuring the production cross section in the dimuon decay channel, so only a brief summary of the mass measurement work is given here. To start out, we are using a method developed by Erich Varnes and used in Run I to measure the top quark mass in the dilepton decay channel [1].

The $t\bar{t}$ to dilepton decay channel is kinematically underconstrained due to the presence of two final state neutrinos. However, the system can be made solvable if the value of the top mass is assumed a priori. In general, there is a range of top masses over which the system is solvable. Thus, solutions over this entire range must be considered, and a probability for each solution being correct must be assigned.

This is done by first assuming a rapidity for each of the two neutrinos, where the rapidity distribution is taken to be a Gaussian whose width depends on the initial choice of the top mass. Given the rapidities, we can then solve for the momenta of the neutrinos. Weights are assigned to each solution based on the difference of the net transverse momentum of the neutrinos and the measured missing transverse energy of the event. This procedure is repeated for multiple rapidities, and the resulting weights for each rapidity are summed to form an overall event weight for the chosen top mass. Event weights are generated for a range of top masses and the mass with the largest event weight is taken as the "measured" mass for that event.

Analysis code was written to implement the above procedure and it has been tested using Pythia $t\bar{t} \rightarrow \mu\mu$ Monte Carlo events. Event weights are calculated for 20 different top quark masses, ranging from 140 GeV/c^2 to 240 GeV/c^2. The weight distribution for a $t\bar{t} \rightarrow \mu\mu$ Monte Carlo event with m_t = 175 GeV/c^2 is shown in Figure III.1.7. The peak for this event is at 140 GeV/c^2. The distributions for ee events show a similar behavior, which we are investigating.

Erich Varnes suggested to us that choosing the peak of the event weight distribution as the top mass may not be optimal, since some weight distributions may have several narrow local peaks. Thus we are currently exploring the possibility of using the shape of the event weight distribution, rather than merely the largest event weight, to determine the top quark mass for each event. In addition, muon and jet smearing are being added to the analysis code in order to mimic detector resolution effects.

Future plans for this analysis method include investigating the effects of initial and final state gluon radiation on the mass measurement. We are also implementing a multi-dimensional maximum-likelihood analysis for the distribution of event weights (rather than a one-dimensional maximum-likelihood analysis for the peak of the weights). A longer-term goal is to

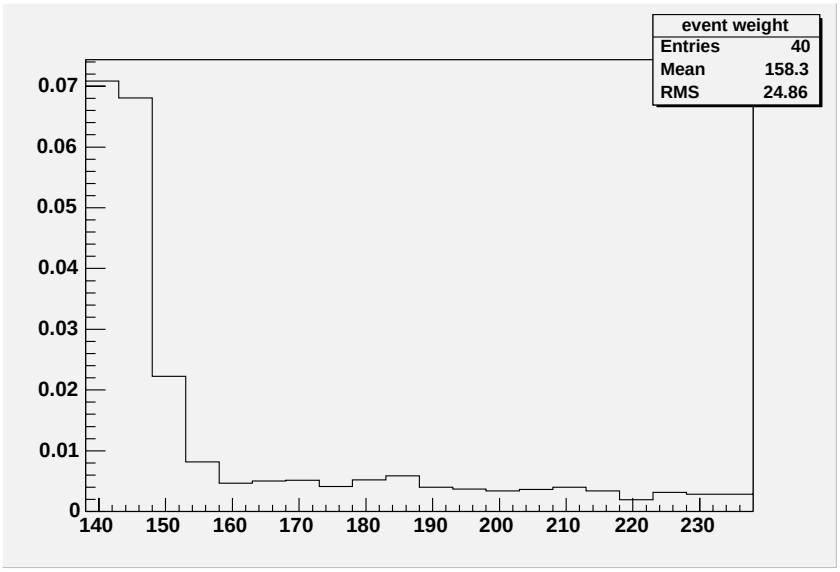

Figure III.1.7. Distribution of event weights for a single $t\bar{t} \rightarrow \mu\mu$ Monte Carlo event with a top quark mass of 175 GeV/c^2.

use the leading-order $q\bar{q} \rightarrow t\bar{t} \rightarrow \mu\mu$ matrix element in our maximum-likelihood analysis, as was recently done for the Run I top quark mass measurement using leptons plus jets data.

Top Quark Physics – W Helicity Measurement in the Muon Plus Jets Decay Channel

Several years ago Ken Johns and graduate student Rob McCroskey performed studies on the Run II physics reach in the measurement of W polarization in top decays using the muon plus jets decay channel. Recently Erich Varnes in collaboration with Ken Johns and graduate student Bryan Gmyrek began a more formal analysis to make this measurement. A brief summary of the previous work and a description of the newer studies are given here. Also described are related studies in the background model for the muon plus jets decay channel (Varnes) and b-jet tagging (Gmyrek).

The Standard Model (SM) predicts that about 70% of the *W*-bosons produced in top quark decay (with m_t = 175 GeV/c^2) will be polarized longitudinally, with nearly all of the remaining 30% having a left-handed polarization. Because longitudinal *W*-bosons play an important role in electroweak symmetry breaking, physics beyond the SM may show up as a departure from the above prediction. CDF published a result in Run I of 0.91 ± 0.37 (sys.) ± 0.13 (stat.) for the fraction of longitudinal *W*-bosons using the lepton P_T spectrum [2]. Our previous studies showed that with a sample of 1000 *b*-tagged leptons plus jets events (roughly the sample size expected in Run II) one could measure Br($t \rightarrow b\, W_{long}$) to about 10%.

The *W*-boson helicity can be determined by analyzing the angular distribution of the daughter lepton in the *W* rest frame (with respect to the direction of the top quark in the *W* rest frame). The lepton helicity angle can be conveniently written in terms of invariants:

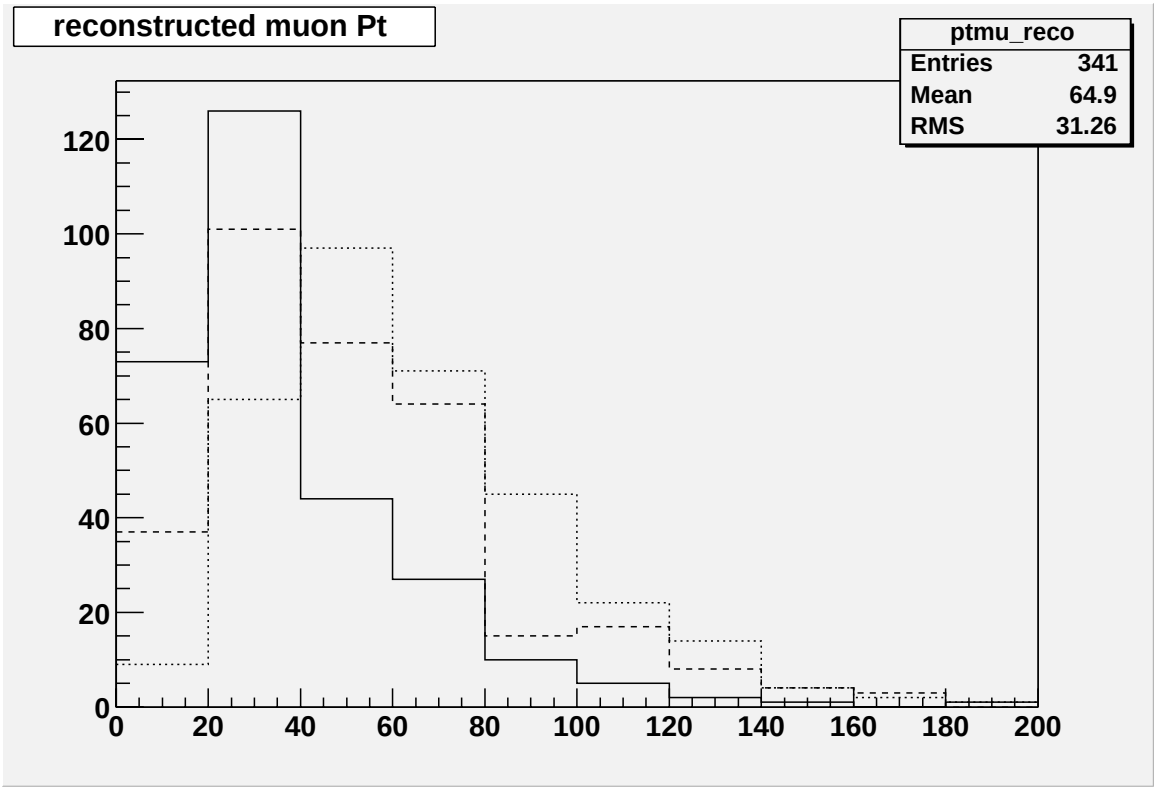

Figure III.1.8. Distribution of lepton transverse momenta (in GeV/*c*) for the three *W*-boson helicity states. The solid histogram represents helicity –1, the dashed histogram helicity 0, and the dotted histogram helicity +1.

$$\cos\theta^* \approx \{2m_{lb}^2 / (m_{lbv}^2 - m_W^2)\} - 1.$$

The Standard Model prediction for cosθ* at the parton level is simple: (½ ($\sin^2\theta^*$) and ¼ (1 - $\cos\theta^*$)^2 for longitudinal and left-handed *W*-bosons respectively).

These ideal shapes are modified by a number of factors including QCD radiation of the top decay products, associating the wrong jet with the muon in calculating m_{lb} and m_{lbv}, detector resolution, event selection criteria, and backgrounds. In our Run II reach studies we used a log-likelihood fit to an approximate, but fast, Monte Carlo distribution of these modified shapes, containing signal plus background, to determine Br($t \to b\ W_{long}$). A similar study was performed using the lepton P_T distributions, which are correlated with the *W* helicity as shown in Fig. III.1.8 . Using several trial samples of the expected Run II data size, we found the statistical error on Br($t \to b\ W_{long}$) to be approximately 10%, with the sensitivity being about the same regardless of whether $\cos\theta^*$ or lepton P_T was used in the measurement.

Now that much of the DØ Run II Monte Carlo, detector simulation, and reconstruction machineries are in place, more realistic studies can be carried out. To do this, one needs to generate samples for each *W*-boson helicity, pass them through a detailed simulation of the detector, process them with the standard reconstruction software, and apply the selection criteria

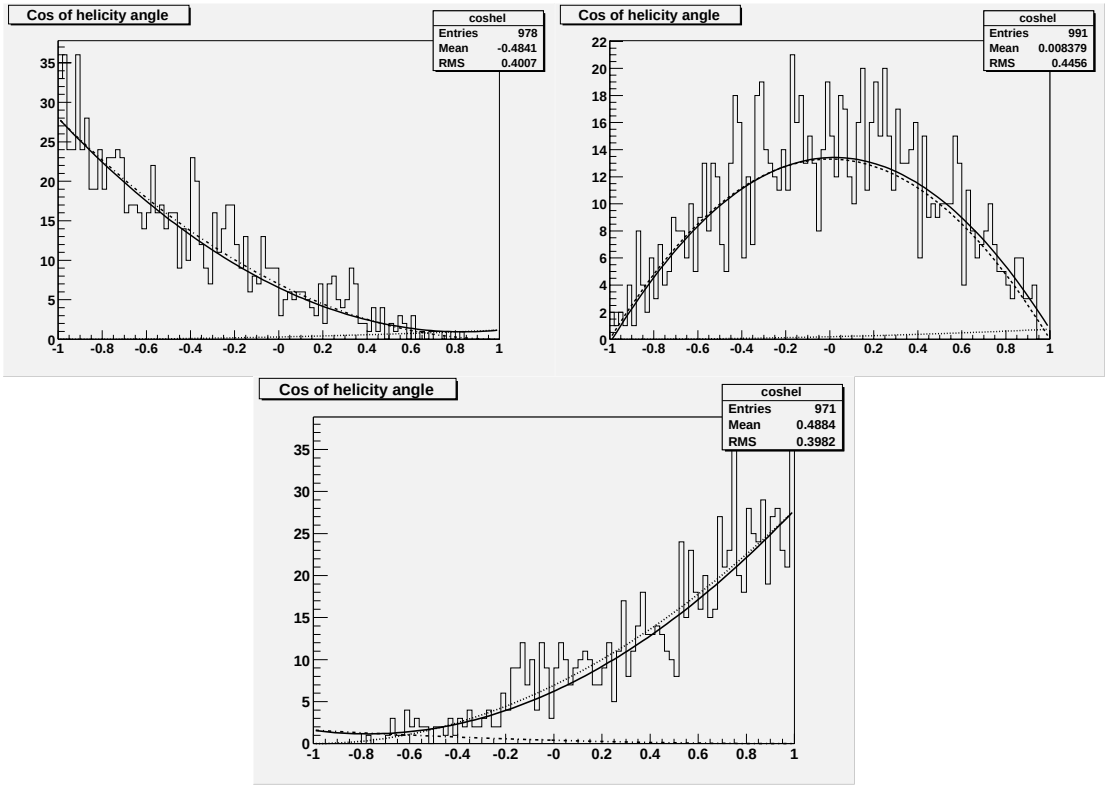

Figure III.1.9. Distribution of the cosine of the lepton helicity angle in top quark decays in specially-prepared Pythia samples. The plot at upper left shows a sample of pure negative helicity, upper right shows pure longitudinal helicity, and the lower plot show pure positive helicity.

used for $t\bar{t}$ events. The standard Monte Carlo event generators, however, do not allow the user to generate a particular helicity state.

To prepare the needed samples, a set of Pythia $t\bar{t}$ events that decay into muon plus jets was generated. The angular dependence of the matrix element turned off, thus producing a flat distribution in the muon helicity angle $\cos\theta^*$. Events from this parent sample were then selected with the probability for a given *W*-boson helicity to produce the event's $\cos\theta^*$. The result is a set of statistically independent samples that model each of the *W*-boson helicity states, as shown in Figure III.1.9.

The CDF measurement of the *W*-boson helicity was based on the lepton P_T distribution. We are now revisiting the issue of whether this is the optimal variable for this analysis. In particular, we are exploring in more detail whether one can benefit from reconstructing $\cos\theta^*$.

The critical step in this reconstruction is identifying the *b*-quark jet that originated from the same top quark decay as the muon. Here we have an advantage over previous measurements in

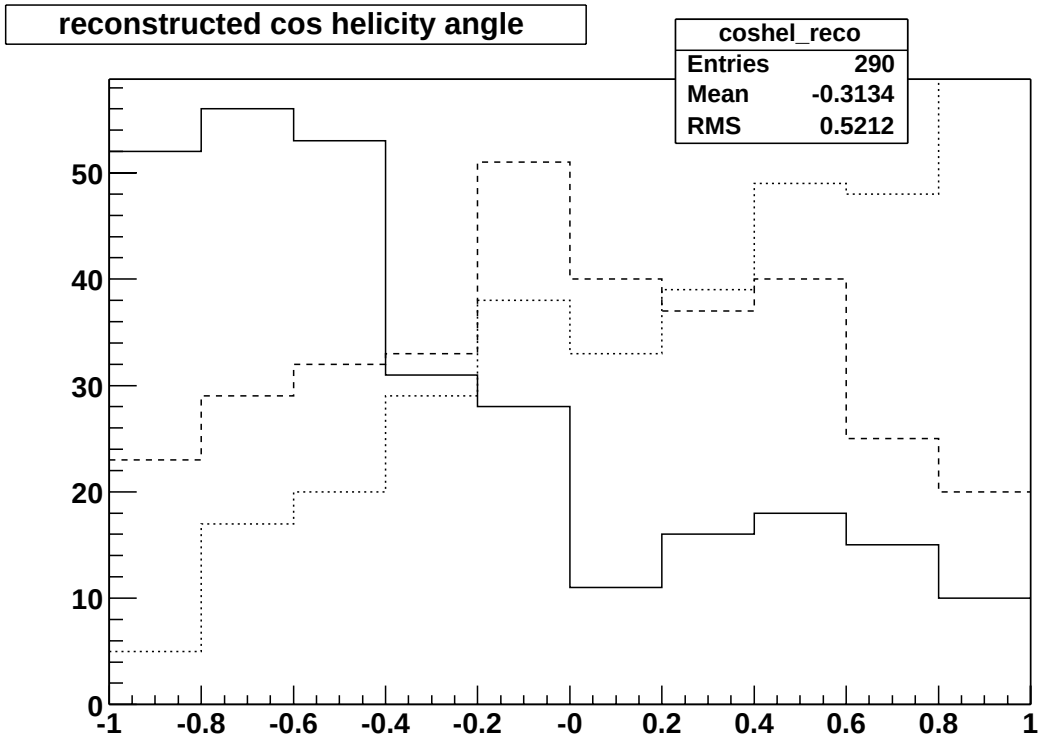

Figure III.1.10: Reconstructed $\cos\theta^*$ in simulated $t\bar{t}$ events for the three W-boson helicity states. The solid histogram represents helicity –1, the dashed histogram helicity 0, and the dotted histogram helicity +1.

that the top quark mass is well known. This allows one to form a χ^2 to estimate the likelihood that an

assignment of jets is the correct one. Considering only the four highest E_T jets in the event, each of which can be assigned to be either the b-quark jet from the same top quark that produced the muon (b_μ), the b-quark jet form the top quark that decayed to hadrons (b_h), or a jet from the decay of a W (j_i), the χ^2 has the form:

$$\chi^2 = \frac{\left(m_{\mu\nu b_\mu} - m_{\text{top}}\right)^2}{\sigma_{\text{top}}^2} + \frac{\left(m_{j_1 j_2 b_h} - m_{\text{top}}\right)^2}{\sigma_{\text{top}}^2} + \frac{\left(m_{j_1 j_2} - m_W\right)^2}{\sigma_W^2}$$

We set m_{top} to 174 GeV/c^2, σ_{top} to 10 GeV/c^2, and σ_W to 5 GeV/c^2. To form the measured mass of the top quark that decayed leptonically we need to assign a value to the longitudinal momentum of the neutrino. This is done by requiring that $m_{\mu\nu}$ equals the W mass. If no solution exists, the neutrino is assigned a longitudinal momentum of zero.

Choosing the jet assignment that minimizes this χ^2 selects the correct jet as b_μ slightly more than half the time in simulated $t\bar{t}$ events. This leads to the reconstructed $\cos\theta^*$ distributions seen in

Figure III.1.10. Substantial separation is achieved between the three helicity states. Currently, it appears that cosθ∗ is a slightly more powerful variable than lepton P_T when one fixes the fraction of right-handed W's to zero. However, when all three helicity fractions are allowed to float, using cosθ* is much more powerful.

We are now attempting to reduce the fraction of wrong b-jet assignments in the reconstruction of $\cos\theta^*$. Three examples of our ongoing effort are a) taking advantage of *b*-quark jet tagging information by eliminating combinations where a *b*-tagged jet is assigned to *W*-boson decay, b) properly calculating the χ^2 by performing a constrained kinematic fit to the event, and c) including initial- and final-state radiation assignments for events with more than four reconstructed jets.

Work on selecting muon plus jets events from the Run II data and estimating the background contributions is in progress. To model the kinematics of the QCD multijet background, we take events from the data sample where muons are found within a hadronic jet. The *W*-boson plus jets background is generated using the Alpgen *W*jjj process, passed through Pythia, which models the parton shower and approximates higher-order jet production. The complete model of the data is then formed by summing the QCD and *W*-boson plus jets models in the expected ratio using the measured efficiency for a muon from each source to be isolated from hadronic energy. The resulting model is composed of 58% *W*+jets and 42% QCD events. If our understanding is complete, this model will exactly reproduce the kinematics of the isolated muon plus three or more jet sample.

Currently the comparison shows good agreement in muon P_T (Figure III.1.11). However, discrepancies appear in the jet E_T spectrum, where the Monte Carlo predicts more energetic jets than are observed in the data (Figure III.1.12). Investigation continues to determine the source of this discrepancy.

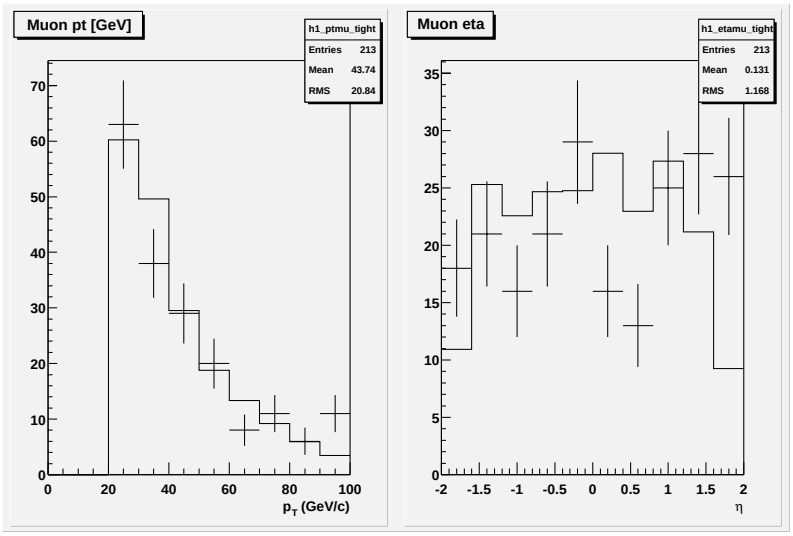

Figure III.1.11. Distribution of muon P_T (left) and η (right) for isolated muon plus three or more jet data (points with error bars) and the model of QCD plus *W* +jets events (histogram).

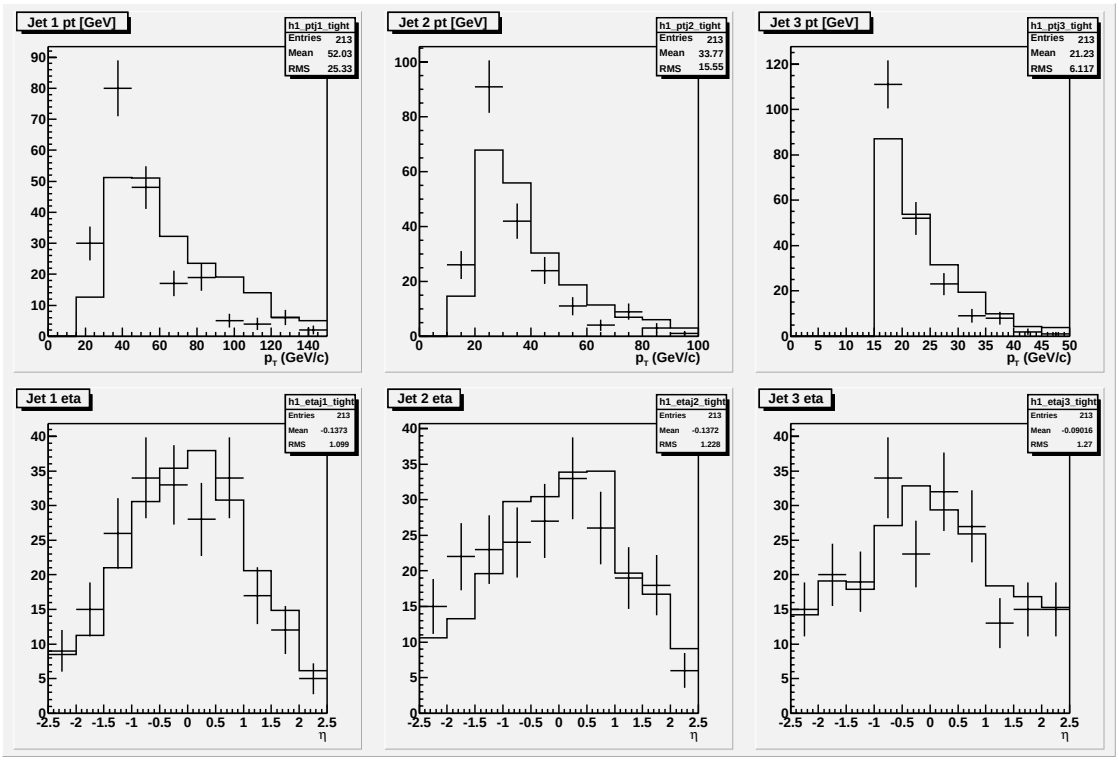

Figure III.1.12. Distribution of jet E_T (top) and η (bottom) for the three highest E_T jets in the isolated muon plus three or more jet data (points with error bars) and the model of QCD plus *W* + jets events (histogram).

One method of separating $t\bar{t}$ events from W+jets and QCD multijet events is through *b*-jet tagging. While we were not involved in the development of *b*-jet tagging algorithms themselves we did perform studies on both data and Monte Carlo in order to understand and eventually exploit one of them. The method we chose to study was the CSIP (Counting Signed Impact Parameter) method developed by Flera Ritzadinova of Kansas State. We first incorporated the CSIP macro into our dimuon analysis code. For data we use the same dimuon skims used in the $t\bar{t} \rightarrow \mu\mu$ decay channel cross section analysis. For Monte Carlo we used Pythia $t\bar{t} \rightarrow \mu\mu$ events.

In order to produce a sample rich in *b*-quark jets, we applied the following selection criteria to the data: two jets with $E_T > 15$ GeV and two muons with $P_T > 15$ GeV/*c*, with each muon required to be within $\Delta R < 0.5$ of one of the jet axes. We then use the P_T of the muon relative to the jet axis (P_T^{rel}) to further increase the fraction of *b*-quark jet events.

In order to calculate the *b*-quark jet tagging efficiency we use events that have either two CSIP tags (DT) or one CSIP tag (ST). The efficiency is then given by $e = 2DT/(DT + ST)$ where DT and ST are the number of double and single CSIP-tagged events respectively. Results on the efficiency as a function of P_T^{rel} are given in Table III.1.6.

For $t\bar{t} \rightarrow \mu\mu$ Monte Carlo, we simply used events with exactly two jets and calculated the efficiency as above. (An improved method that first tags *b*-quark jets at the parton level is in progress.) This result is also given in Table III.1.6. Both *b*-quark jet tagging efficiencies from

Sample	*b*-quark jet tagging efficiency (2DT/(DT + ST))
Pythia tt dimuon Monte Carlo	0.53 ± 0.008
Dimuon plus dijet data (P_T^{rel} > 0.0 GeV/c)	0.21 ± 0.015
Dimuon plus dijet data (P_T^{rel} > 0.5 GeV/c)	0.23 ± 0.02
Dimuon plus dijet data (P_T^{rel} > 1.0 GeV/c)	0.27 ± 0.03
Dimuon plus dijet data (P_T^{rel} > 1.5 GeV/c)	0.31 ± 0.06

Table III.1.6. *b*-quark tagging efficiency in data and Monte Carlo.

data and Monte Carlo agree well with those found by the top *b*-tagging subgroup [3]. Work in progress includes evaluating the jet lifetime probability (JLIP) method and integrating *b*-quark jet tagging in general into our dimuon and muon plus jets physics analyses.

References

[1] "*Measurement of the Top Quark Mass in the Dilepton Channel",*
DØ Collaboration, V.M. Abazov *et al*., Phys. Rev. **D60**, 52001 (1999).

[2] "*Measurement of the Helicity of W-Bosons in Top Quark Decays",*
CDF Collaboration, F. Abe *et al*., Phys. Rev. Lett. **84**, 216 (2002).

[3] "*Measurement of the $t\bar{t}$ Cross Section at $\sqrt{s}$ = 1.96 TeV Using Lifetime Tagging*",
R. Demina *et al*., DØNote 4141.

III.1.3 DØ Physics Program - B Physics and Higgs Searches

Search for $B_s \to \mu^+\mu^-$

The decay $B_s \to \mu^+\mu^-$ is a distinctive signature of some popular classes of SUSY models [1]. In particular, flavor-changing neutral currents, while suppressed in the Standard Model, can be large in SUSY models due to flavor-changing couplings of the neutral Higgs bosons. The current experimental bound on the branching fraction is BR($B_s \to \mu^+\mu^-$) $< 2.6\times10^{-6}$, a Run I result from CDF [2]. In the Standard Model, the branching fraction is predicted to be only $(3.7\pm1.2)\times10^{-9}$ [3], so this decay mode presents one of the best ways to search for SUSY at the Tevatron. Elliott Cheu and postdoc Peter Tamburello are searching for $B_s \to \mu^+\mu^-$ in the present Run II data. With the total Run II data set, we expect to be able to achieve a limit on BR($B_s \to \mu^+\mu^-$) better than 10^{-7}. The current analysis uses an integrated luminosity of approximately 100 pb^{-1}.

We start by selecting events with two good muons. Candidate muons are required to have hits in both the muon system wire chambers and scintillator, and to match to tracks in the central tracker. The mass distribution of muon pairs is shown in Figure III.1.13. Note that the figure is plotted on a log scale. As can be seen, the backgrounds to $B_s \to \mu^+\mu^-$ are appreciable, with the expected signal being many orders of magnitude smaller than the current level of background. A peak from $B_s \to \mu^+\mu^-$ would have a width of approximately 100 MeV.

To reduce the backgrounds, the following selection criteria are applied: we require that L_{xy}, the distance from the primary vertex to the muon pair vertex projected onto the muon pair direction, be at least 550 μm, and that the uncertainty on L_{xy} be less than 150 μm. This removes prompt tracks while retaining decay products of long-lived *B* hadrons. The direction transverse to the displacement of the muon pair vertex from the primary vertex (T_{xy}) is required to be less the two standard deviations. This removes muon pairs that do not point back to the primary vertex. Further reduction of the background is achieved by requiring the transverse momentum (P_T) of the muon pair to be at least 4 GeV/*c*. Finally, we require the isolation to be less than 0.39 GeV/*c*. The isolation is defined as the scalar sum of the P_T of all tracks, excluding the two muons, within a cone of $\Delta R = 1.0$ around the muon pair direction. Figure III.1.14 shows the distributions of these quantities for signal and background. Each variable provides good discrimination between the signal and the dimuon backgrounds.

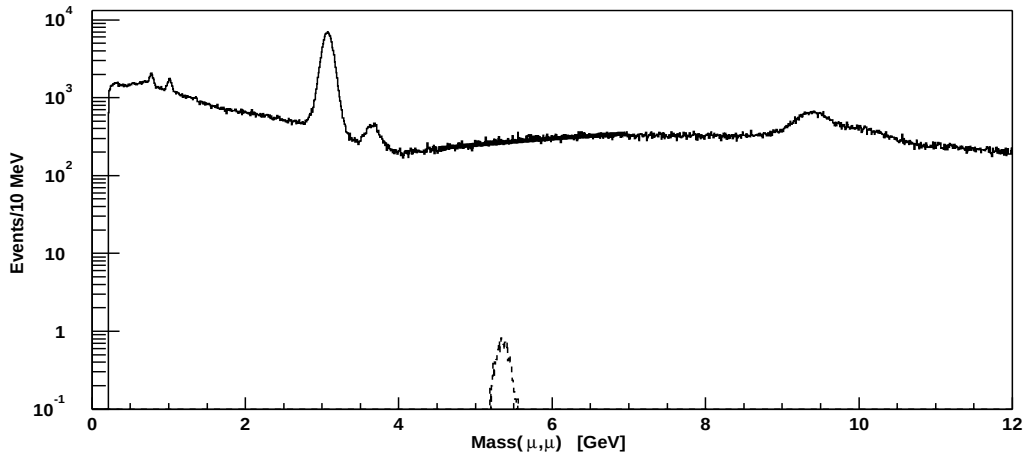

Figure III.1.13. Muon pair mass distribution for data (solid) and $B_s \to \mu^+\mu^-$ Monte Carlo (dashed). The Monte Carlo normalization represents BR($B_s \to \mu^+\mu^-$) = 1×10^{-6}.

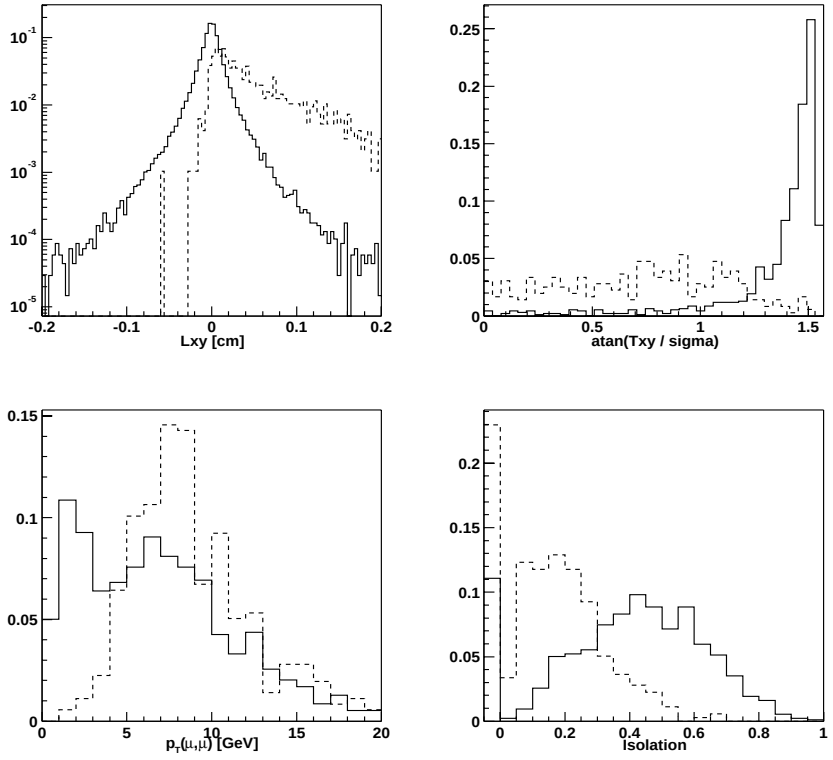

Figure III.1.14. Quantities used to separate signal from background. The background distributions (solid) are from data with a muon pair mass between 4.5 and 7.0 GeV. The signal distributions (dashed) are from $B_s \to \mu^+\mu^-$ Monte Carlo. T_{xy}, P_T, and isolation are shown after the cut on L_{xy}.

After all cuts, the muon pair masses are distributed as shown in the top left and the bottom of Figure III.1.15. As can be seen, there is no appreciable signal for $B_s \to \mu^+\mu^-$, so we set an upper limit on the branching fraction. In the signal region, 5.22 GeV $< m_{\mu^+\mu^-} <$ 5.51 GeV/c^2, there are three candidates with an estimated background of 3.42 ± 0.79. The background is determined from a straight line fit to the sidebands around the signal region.

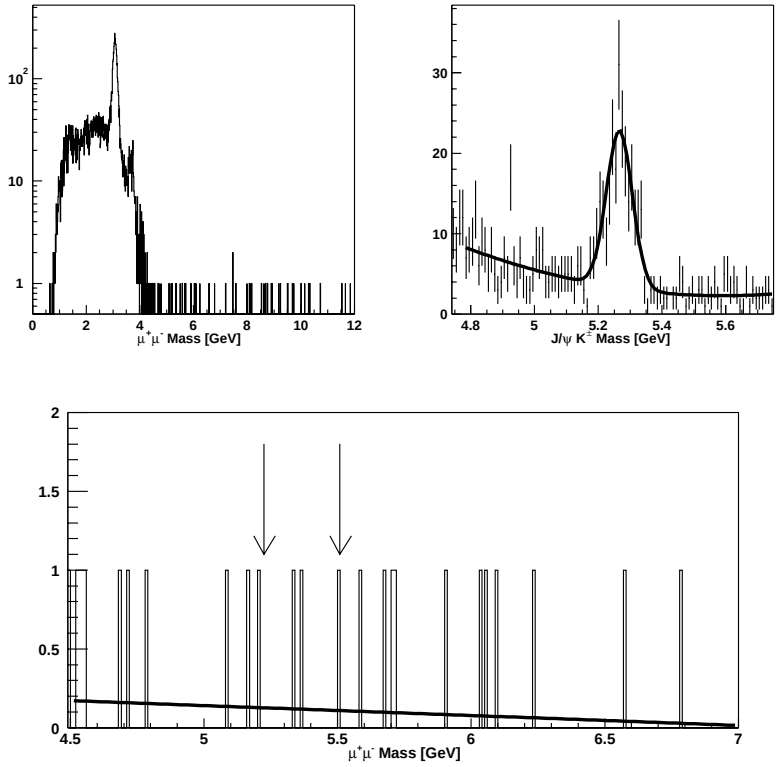

Figure III.1.15. Mass spectra after cuts for $B_s \to \mu^+\mu^-$ (upper left and bottom) and $B^+ \to J/\psi K^\pm$ (upper right). In the bottom plot, the $B_s \to \mu^+\mu^-$ signal region is indicated by arrows and the linear sideband fit is shown. The upper right plot shows the fit to $B^\pm \to J/\psi K^\pm$ with a quadratic background shape

For three events with a background of 3.42, the 90% C.L. upper limit on the number of signal events n_{UL} is 4.03 using the method of Reference [4]. We use the reaction $B^{\pm} \to J/\psi K^{\pm}, J/\psi \to \mu^+\mu^-$ to determine the number of B_s decays. To set an upper limit on BR($B_s \to \mu^+\mu^-$), we calculate

$$\frac{n_{UL}}{n_{B^{\pm}}} \frac{\varepsilon_{\mu\mu K}}{\varepsilon_{\mu\mu}} \frac{BR(b \to B^+)}{BR(b \to B_s)} BR(B^+ \to J/\psi K^+) BR(J/\psi \to \mu^+\mu^-), \qquad (0.1)$$

where n_{B^+} is the number of $B^{\pm} \to J/\psi(\to \mu^+\mu^-)K^{\pm}$ events in the data, $\varepsilon_{\mu\mu K}$ is the selection efficiency for $B^{\pm}$, and $\varepsilon_{\mu\mu}$ is the selection efficiency for the signal. The $B^{\pm} \to J/\psi K^{\pm}$ candidates are selected using the same requirements as for the signal, except that the $\mu^+\mu^-$ mass is required to be near the J/ψ and an additional track is required for the kaon. The fit shown in the upper right of Figure III.1.15 is used to determine $n_{B^{\pm}} = 198 \pm 17$. The ratios $\frac{n_{UL}}{n_{B^{\pm}}} \frac{\varepsilon_{\mu\mu K}}{\varepsilon_{\mu\mu}} \frac{BR(b \to B^+)}{BR(b \to B_s)}$ are computed using Pythia and the DØ detector simulation. The result is BR($B_s \to \mu^+\mu^-$) < 1×10^{-6}. Taking into account systematic uncertainties raises the limit to 1.1×10^{-6} [4]. The dominant systematic effects include uncertainty in the background (23.2%), Monte Carlo statistics (11.6%) and branching ratio uncertainties (12.2%). Currently, this is the world's best limit on $B_s \to \mu^+\mu^-$. DØ should be able to collect a data set at least 20 times larger than our current sample, and we expect to significantly improve upon this limit.

As a cross check, we have also reconstructed the decay $B_s \to J/\psi\phi,\ \phi \to K^+K^-$. Figure III.1.16 shows the reconstructed mass for the $\mu^+\mu^-K^+K^-$ candidates. A clear peak is evident at the B_s mass. Using these events we find a limit consistent with our earlier number. However, because of the increased statistical error from the $B_s \to J/\psi\phi$ decays and the large uncertainty on the $B_s \to J/\psi\phi$ branching ratio, we quote our limit using the $B^{\pm} \to J/\psi K^{\pm}$ normalization.

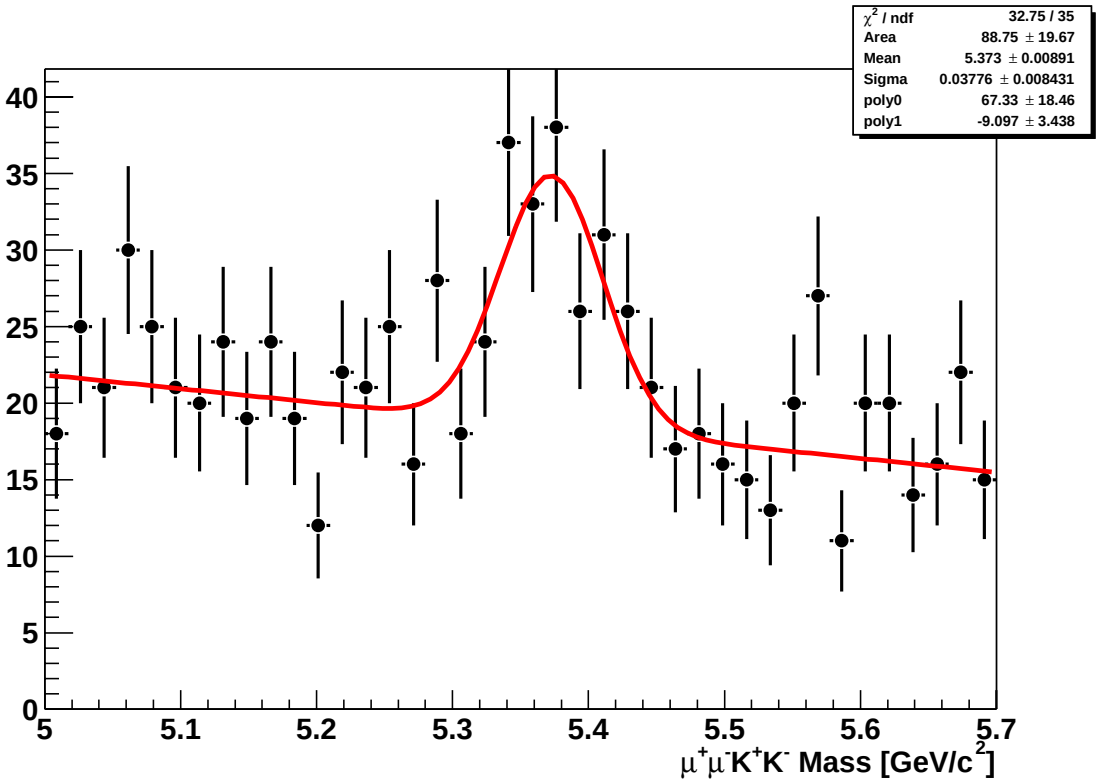

Figure III.1.16: $B_s \to J/\psi\phi$ candidates. The fit results in 89 +/- 20 candidates.

W-boson plus jets studies and searches for $HW \to l\nu b\bar{b}$

In preparation for a search for $HW \to l\nu b\bar{b}$, postdoc Peter Tamburello investigated the properties of jets produced in association with a W-boson using $W \to \mu\nu$ data. The purpose of this study is to understand the ability of the Monte Carlo to reproduce the data. Both the Pythia and Alpgen/Herwig generators are used in these comparisons.

Before examining jet distributions, we made detailed comparisons between data and Monte Carlo for $Z \to \mu^+\mu^-$ and $W \to \mu\nu$ events. The data were skimmed by requiring at least one muon with $P_T > 8$ GeV/c. Muons are required to have at least four hits in the wire chambers and two hits in the muon counter scintillators. To obtain a sample of isolated muons, we exclude muons with large amounts of calorimeter energy near the muon and large P_T from tracks in the vicinity of the muon. Potential biases to the jet distributions are avoided by only using events from the single muon trigger. With this sample we plot the dimuon mass in events with a pair of isolated muons (Figure III.1.17). A clear $Z \to \mu^+\mu^-$ peak is evident. To account for the difference in resolution between the data and the Monte Carlo, we smeared the Monte Carlo P_T resolution by 2.7 times the uncertainty returned by the track fit. This resolution smearing seems to reproduce the width of the Z-boson peak well. After normalizing the luminosity using the number of events in the Z-boson peak, we find good agreement between the shape and number of events in the low mass region of Figure III.1.17.

$W \to \mu\nu$ candidates were chosen from the same muon skim. In Figure III.1.18 the transverse mass of events with an isolated muon and missing E_T is plotted. Again, the agreement between the data and Monte Carlo is good. The expected number of W events, after accounting for the luminosity, cross section, trigger and reconstruction efficiencies is approximately 8800, which closely agrees with the data.

With reasonable W and Z-boson signals, we turn to the jets in the W–boson events. Jets are found using the 0.5 cone algorithm with $|\eta| < 2.5$. The number of 20 GeV jets per event is shown in Figures III.1.19 and III.1.20 and shows reasonable agreement between the data and the Monte Carlo. The transverse momentum of the leading jet in the data (before jet E_T cuts) is compared to Pythia and to Alpgen in Figure III.1.21.

To compare the jet distributions between data and Monte Carlo, we require at least two jets with $E_T > 20$ GeV. The data is compared the Alpgen W_{jj} Monte Carlo which includes QCD contributions. In each case the Monte Carlo is normalized to the area under the data distribution. The scalar sum of the E_T of the two highest-E_T jets is shown in Figure III.1.22, and the dijet mass of the two highest-P_T jets is shown in Figure III.1.23. In these last two figures, one sees that there are significant discrepancies between the data and the Monte Carlo. We are still investigating these effects, though they may hint at deficiencies in the Monte Carlo generators and not in our understanding of the data. These studies are continuing and better understanding of these events will help us as we begin to search for $HW \to l\nu b\bar{b}$ in the future.

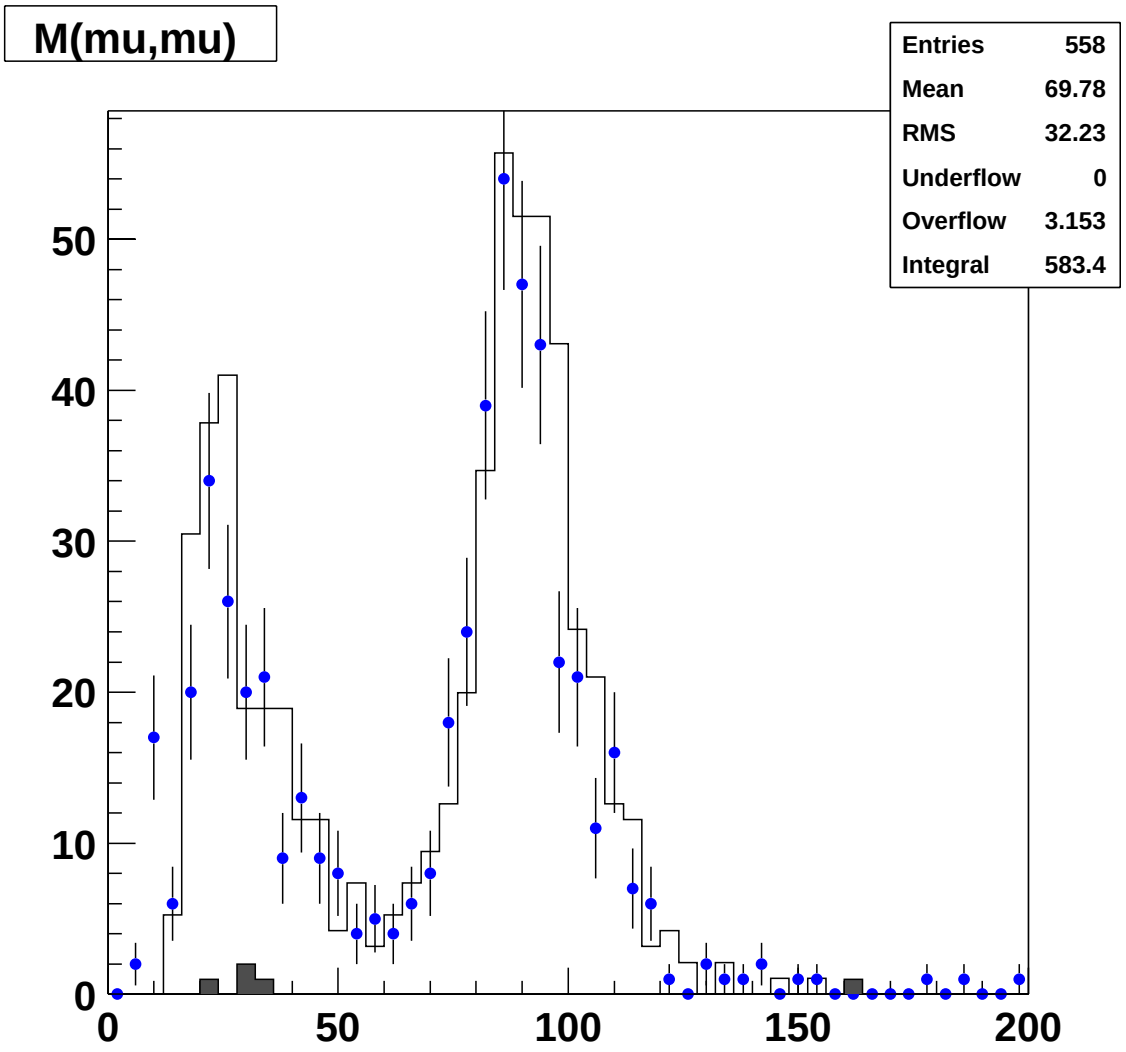

Figure III.1.17. The dimuon mass distribution for pairs of good-isolated muons. The normalization is the same as that used for inclusive *W*–boson events.

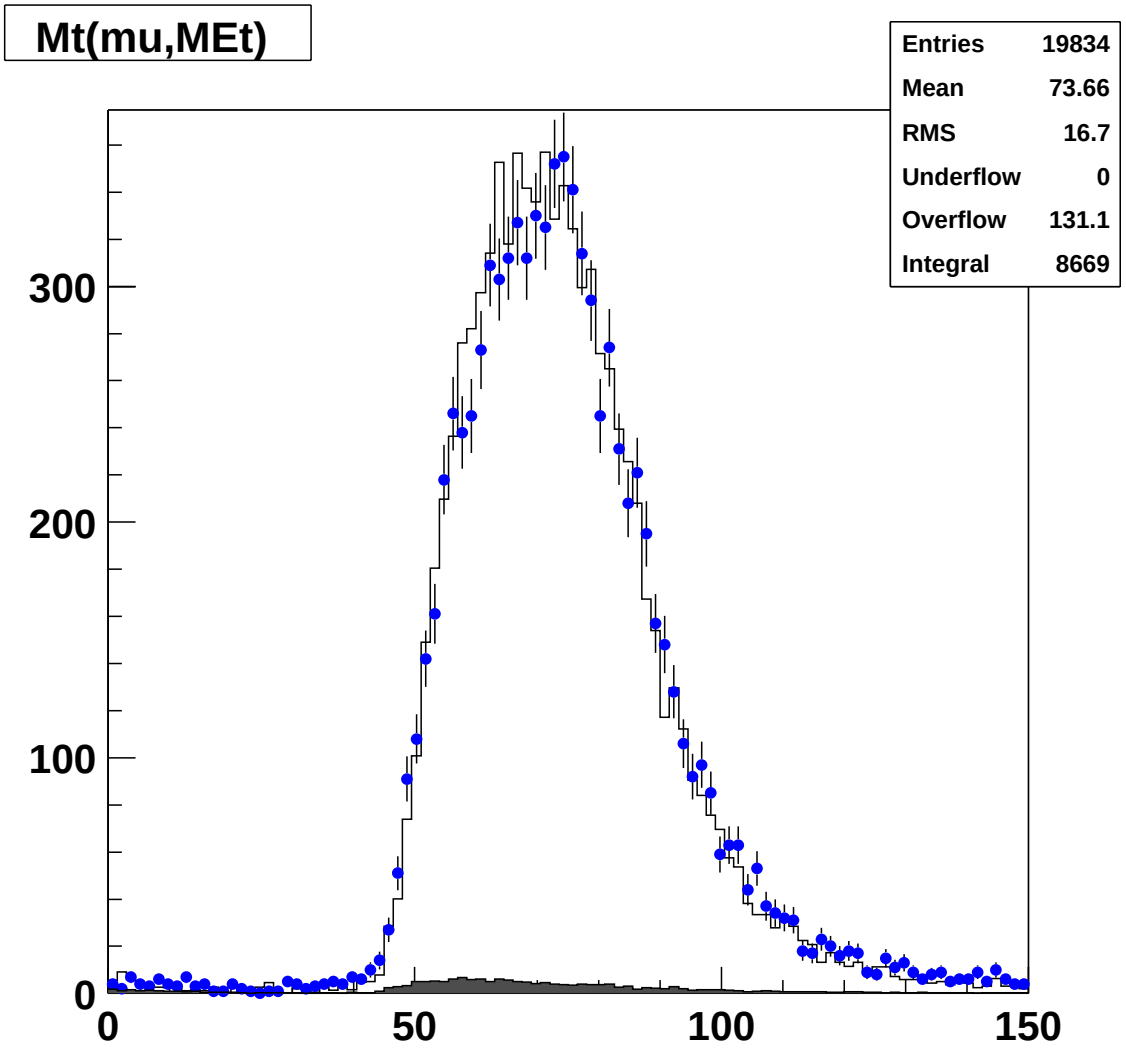

Figure III.1.18. Transverse mass of the *W*–boson candidates. The points are data. The filled histogram is QCD background estimated from data. The open histogram is the sum of Pythia and QCD.

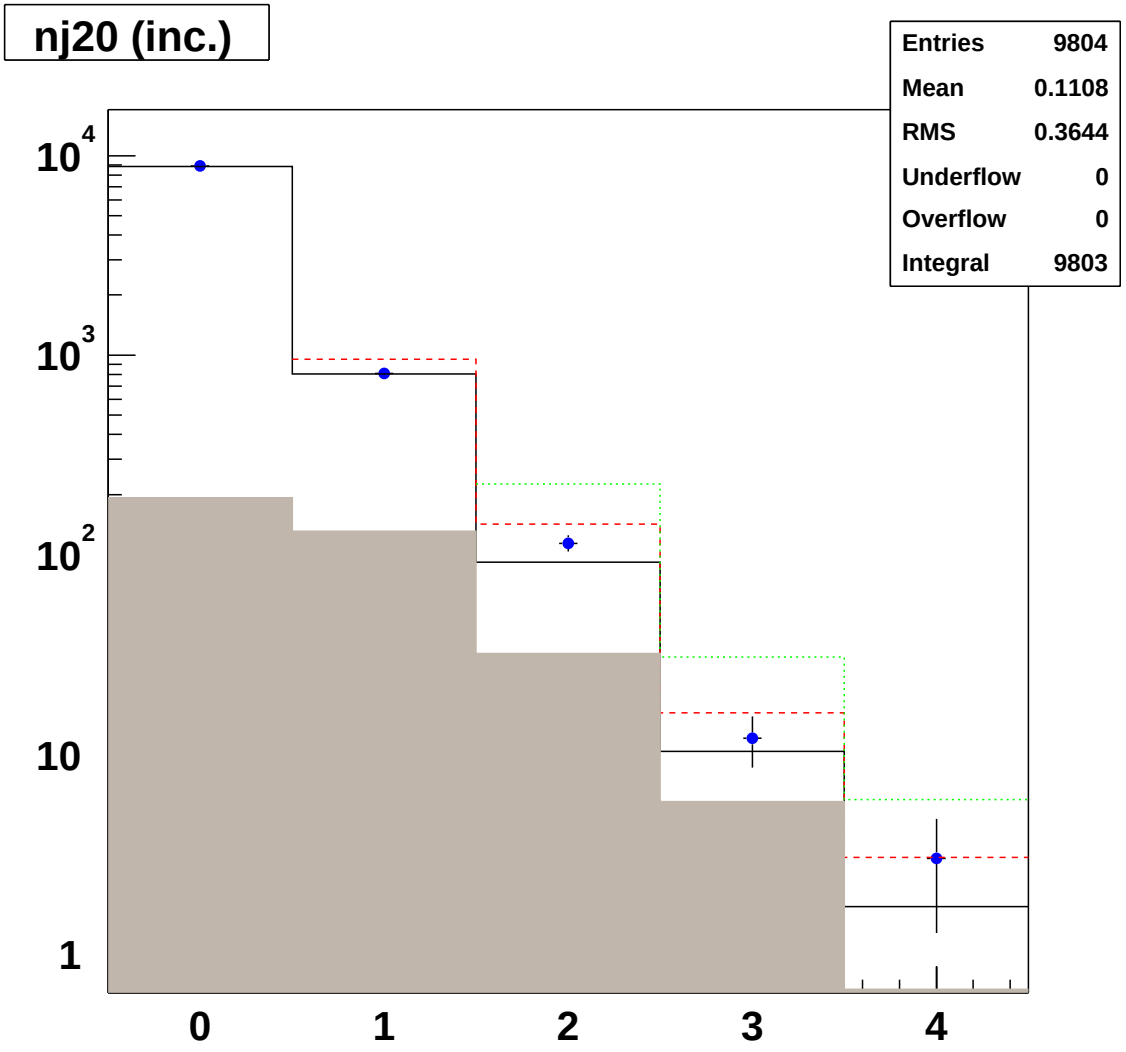

Figure III.1.19. The inclusive jet multiplicity for 20 GeV jets, shown for data (points), Pythia (solid), Alpgen W_j (dashed), Alpgen W_{jj} (dot-dashed), and QCD (hatched). The Monte Carlo distributions include QCD.

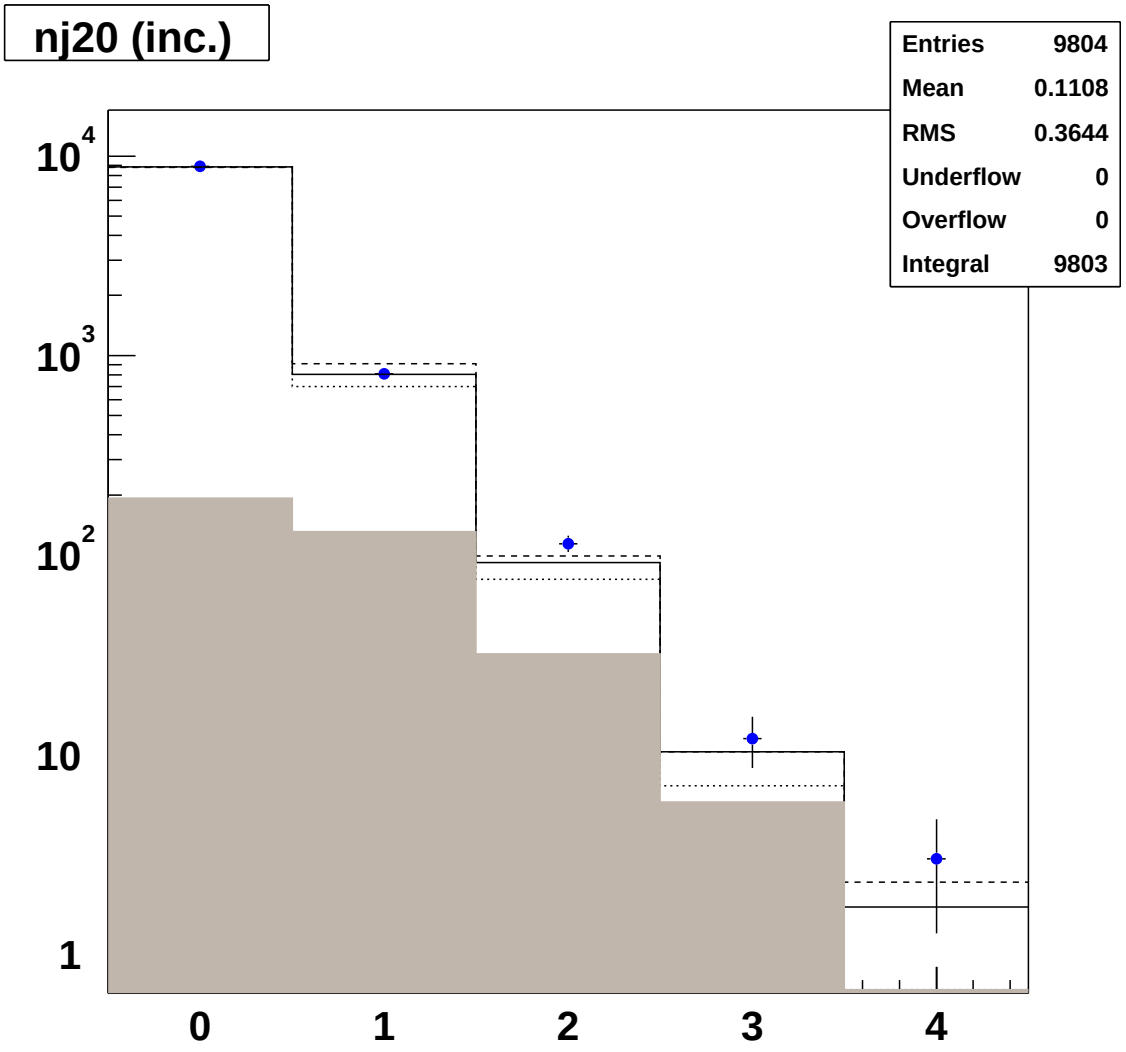

Figure III.1.20. The inclusive jet multiplicity for 20 GeV jets. Data (points); Pythia with nominal jet scale (solid), one σ high jet scale (dashed), and one σ low jet scale (dotted); and QCD (hatched). The Monte Carlo distributions include QCD. The Monte Carlo scale error and the data scale error were combined in quadrature.

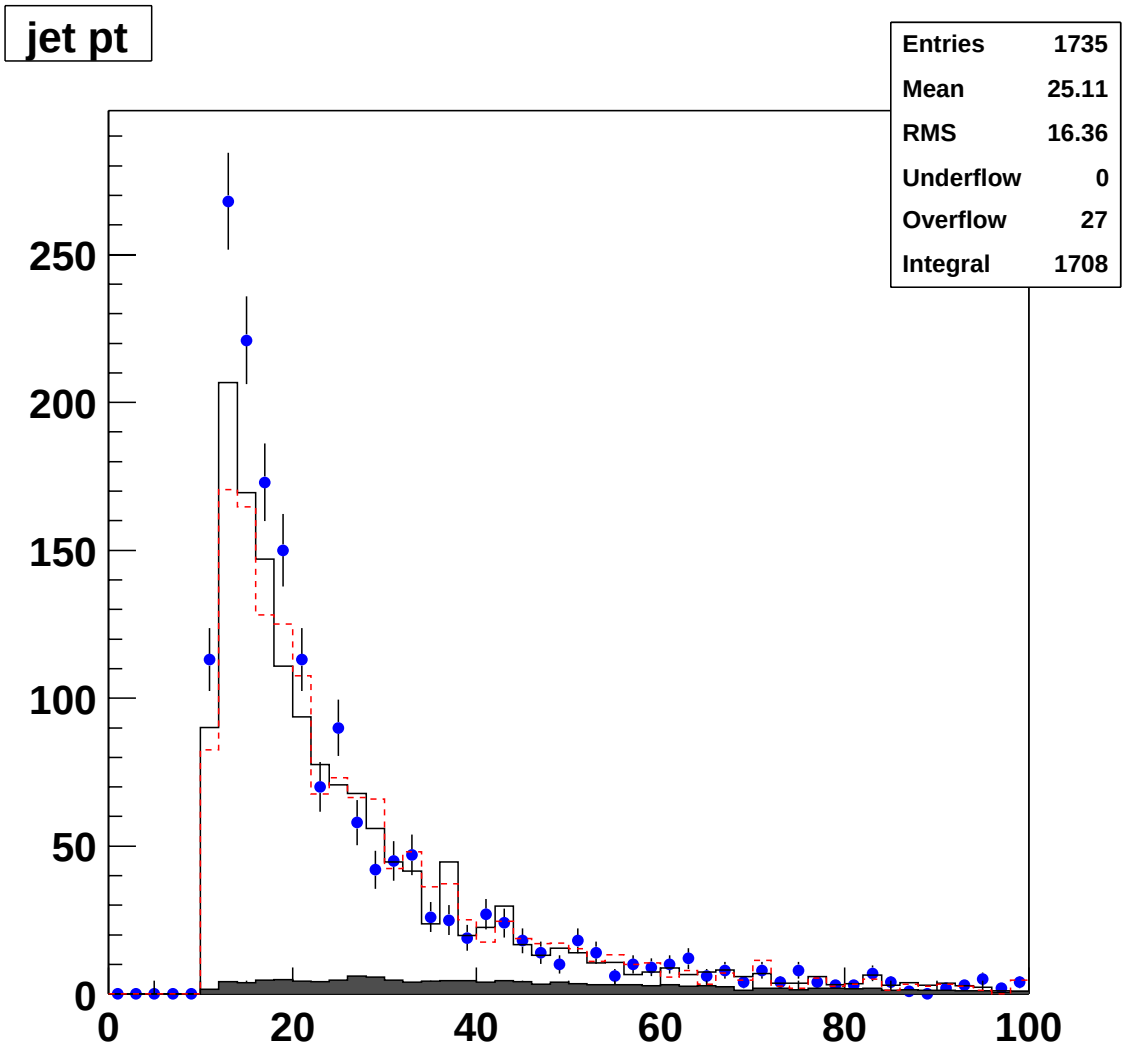

Figure III.1.21. E_T of the leading jet. The points are data. The filled histogram is QCD. The solid histogram is QCD plus Pythia. The dashed histogram is QCD plus Alpgen (single jet).

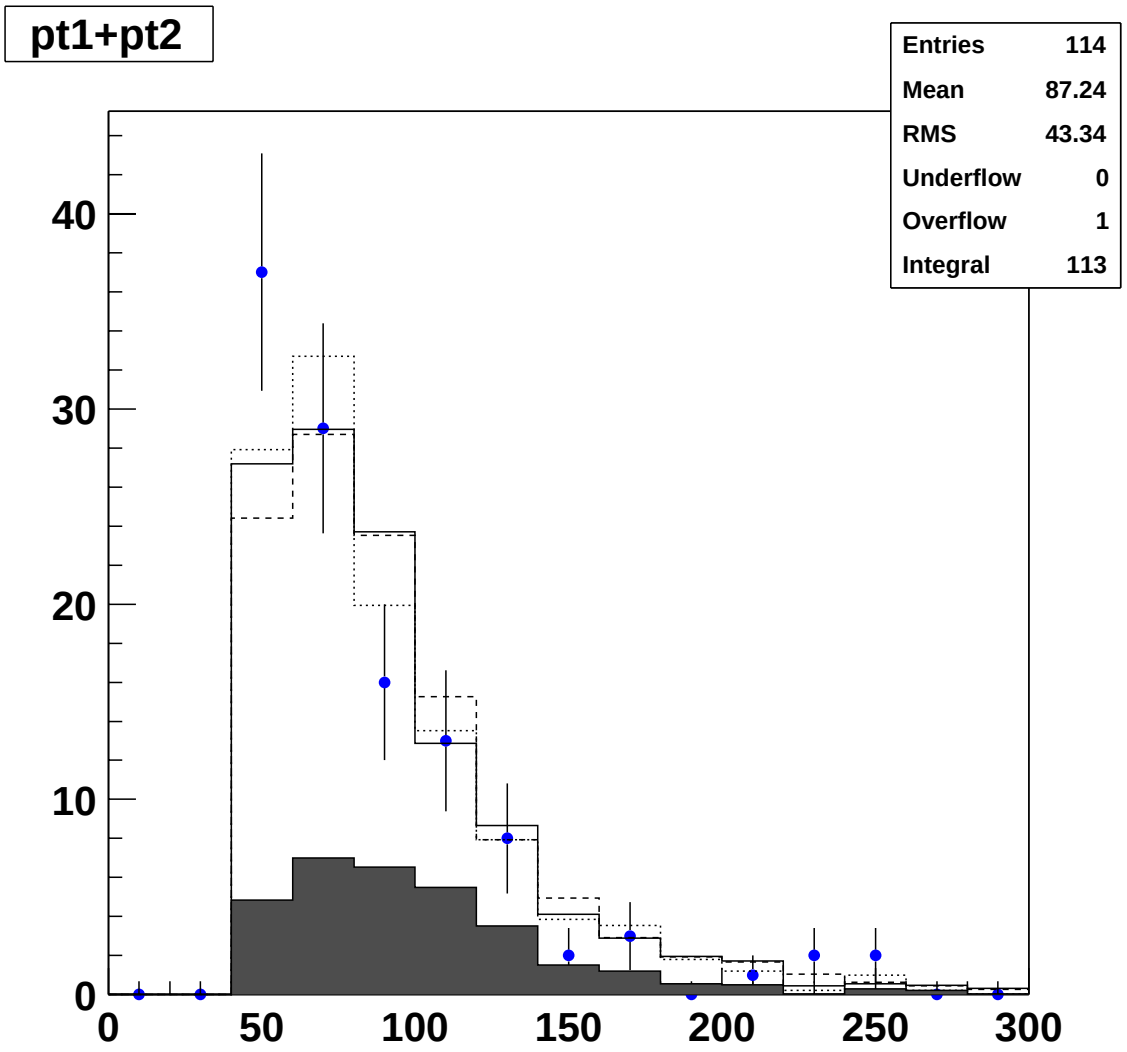

Figure III.1.22. E_T of the first jet plus the E_T of the second jet. Data (points), background with nominal (solid), high (dashed), and low (dotted) jet energy scale. For each jet scale, the Monte Carlo is normalized so that the Monte Carlo plus QCD distribution has equal area to the data distribution.

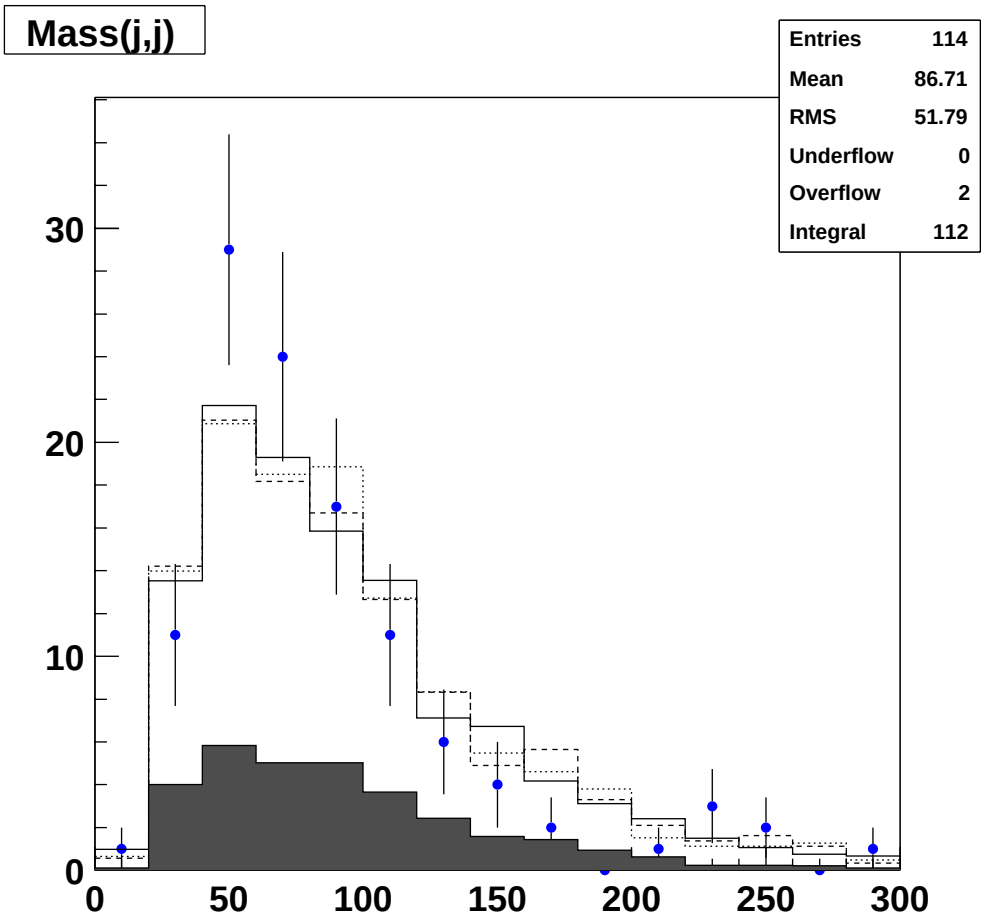

Figure III.1.23. Dijet mass. Data (points), background with nominal (solid), high (dashed), and low (dotted) jet energy scale. For each jet scale, the Monte Carlo is normalized so that the Monte Carlo plus QCD distribution has equal area to the data distribution.

References

[1] K. S. Babu and C. Kolda, Phys. Rev. Lett. **84**, 228 (2000). P.H. Chankowski, L. Slawianowska, Phys.Rev. **D63,** 054012 (2001). C. Bobeth, T. Ewerth, F. Kruger, J. Urban, Phys.Rev. **D64,** 074014 (2001). C. Bobeth, T. Ewerth, F. Kruger, J. Urban, Phys.Rev. **D66,** 074021 (2002). A. Dedes, H.K. Dreiner, U. Nierste, Phys.Rev.Lett. **87,** 251804 (2001). Gino Isidori, Alessandra Retico, JHEP **0111,** 001 (2001). A.J. Buras, P.H. Chankowski, J. Rosiek, L Slawianowska, Phys.Lett. **B546,** 96 (2002). R. Dermisek, S. Raby, L. Roszkowski, R. Ruiz de Austri, JHEP **0304,** 037 (2003). R. Arnowitt, B. Dutta, T. Kamon, M. Tanaka, Phys.Lett. **B538,** 121 (2002).

[2] The CDF Collaboration, F. Abe *et al.*, Phys. Rev. **D57**, 3811 (1998).

[3] G. Buchalla, A. J. Buras and M. E. Lautenbacher, Rev. Mod. Phys. **68**, 1125 (1996).

[4] G. Feldman and R. Cousins, Phys.Rev. **D57** (1998) 3873-3889.

III.1.4 DØ Service – Level 1 Muon Trigger (L1MU)

Overview

Arguably the most important contribution the University of Arizona has made to the DØ experiment to date is the Level 1 Muon Trigger (L1MU). Ken Johns developed the conceptual design. A team consisting of Ken Johns, electrical engineer Joel Steinberg, postdoc David Fein, and grad student Rob McCroskey pushed the design through the prototype, preproduction, production, and installation stages. Postdoc Freedy Nang and grad student Pete Johnson wrote much of the early L1MU simulator code and online software. In summary, an excellent team from the University of Arizona took sole responsibility for a $1M project and successfully delivered it to DØ.

Our contributions did not end with the delivery of the L1MU trigger to the experiment. Critically, our team also took responsibility for commissioning, integration, certification, monitoring, trouble-shooting, and maintenance of the L1MU trigger. We also took responsibility for the continued development and maintenance of the trigger simulator, online software, and physics analysis software associated with the L1MU trigger. The current team holding these multiple responsibilities consists of Ken Johns, postdoc Stefan Anderson, and graduate students Rob McCroskey and Jeff Temple. Each works on aspects of both L1MU hardware and software. Noah Wallace made important contributions to the L1MU online software during his tenure. Support at Arizona is provided by senior engineer Joel Steinberg and technician Chris Leeman.

These manifold tasks are critical to the continued successful operation of the L1MU trigger in Run II. As with many other detector systems on the experiment, an incredible amount of hard work continues to be poured into understanding and maintaining these systems. The L1MU trigger is no exception to this. It is important for the reviewer to understand the large time commitment the above activities entail. The outstanding support we provide for the L1MU trigger continues to be one of our most important service contributions to DØ.

After a very brief description of the L1MU trigger system, we give examples of this valuable support below. The current status of the L1MU trigger is that it is fully operational and being used for physics triggers. One crate of installed L1MU trigger cards is shown in Figure III.1.24. Nearly all of our envisioned L1MU triggers are available, including those that match tracks from the Level 1 Central Fiber Tracker Trigger (L1CTT) with hits in the muon detector scintillators.

L1MU Trigger System

The Level 1 Muon Trigger (L1MU) looks for patterns consistent with muons using hits from muon wire chambers, muon scintillation counters and tracks from the Level 1 Central Track Trigger (L1CTT). Field Programmable Gate Arrays (FPGA's) are used to perform combinatorial logic on roughly 60,000 muon channels and up to 480 tracks from the L1CTT for every bunch crossing. Data from the detector front-ends are transmitted on custom Gbit/s serial links over standard coaxial cable. The serial link receivers and FPGA's are located on VME cards that reside in four custom VME crates on the detector platform.

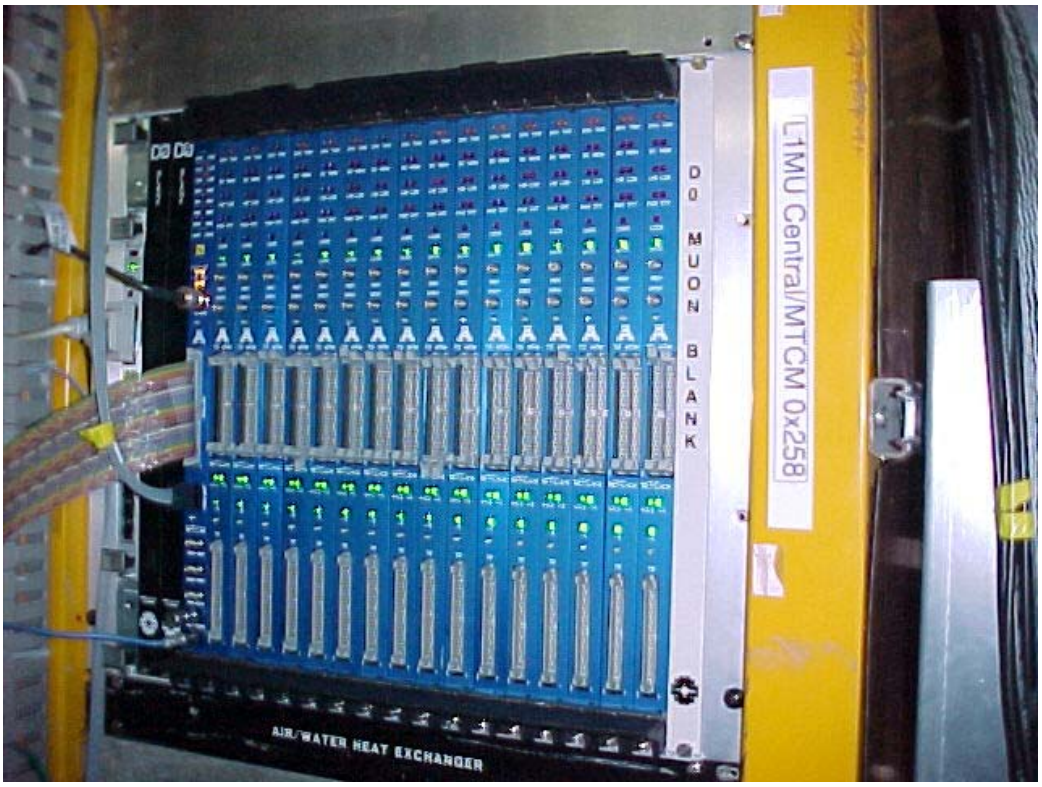

Figure III.1.24. A crate of L1MU trigger cards installed in the DØ collision hall.

The muon system (and L1MU) is divided into central, north, and south regions. Each region is furthur divided into octants in phi. Front-end data from each octant are processed by two L1MU trigger cards (Figure III.1.25). The scintillator trigger cards (MTC05) match particle tracks from the L1CTT to muon scintillator hits. The wire trigger cards (MTC10) match scintillator-confirmed track stubs in wire chambers between the three layers of the muon system. The octant decisions from each MTC05/MTC10 pair in a region are summed in the Muon Trigger Crate Managers (MTCM's, see Figure III.1.26) and sent to a global trigger manager (MTM). The MTM forms 256 global L1MU triggers and sends up to 32 of these to the Trigger Framework for inclusion in the Level 1 physics trigger. The download of the specific triggers is handled via EPICS software.

All detector inputs to L1MU use Gbit/s serial links, which transmit data over up to 150' of Times Microwave LMR-200 coaxial copper cable. The links are based on the AMCC S2042/S2043 fiber-optic transmitter/receiver pair and use an amplifier/equalizer circuit on the receiver to correct for the attenuation of the signal over the coaxial cable. The transmitters and receivers are 1.5" x 2.2" daughter cards that are mounted on the muon front ends and on the L1MU trigger cards. Each serial link can transmit up to 16 x 7 = 112 bits every 132 ns bunch crossing. All MTC05, MTC10, and MTM trigger cards use a common motherboard with sixteen serial links and different flavor daughter cards that perform the MTC05, MTC10, and MTM logic. The

motherboard, MTC05 flavor card, and serial link receivers are shown in Figures III.1.27and III.1.28.

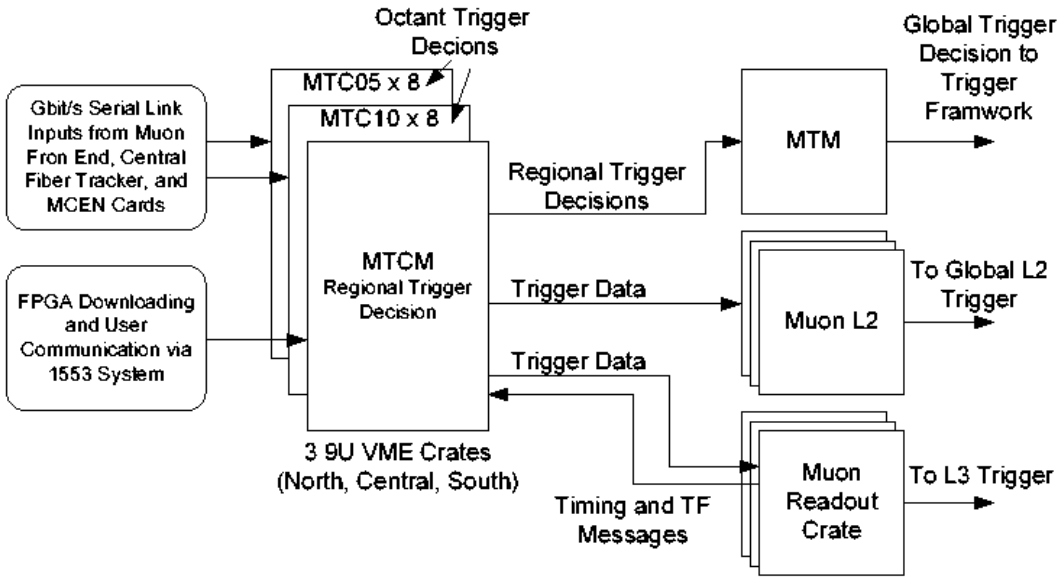

Figure III.1.25. Level 1 Muon Trigger system overview. Each octant has two trigger cards that process muon detector hit information and L1CTT tracks for that octant. The octant triggers for a given region are then summed on the MTCM and sent to the MTM, which combines the three regions and sends up to 32 triggers to the Trigger Framework.

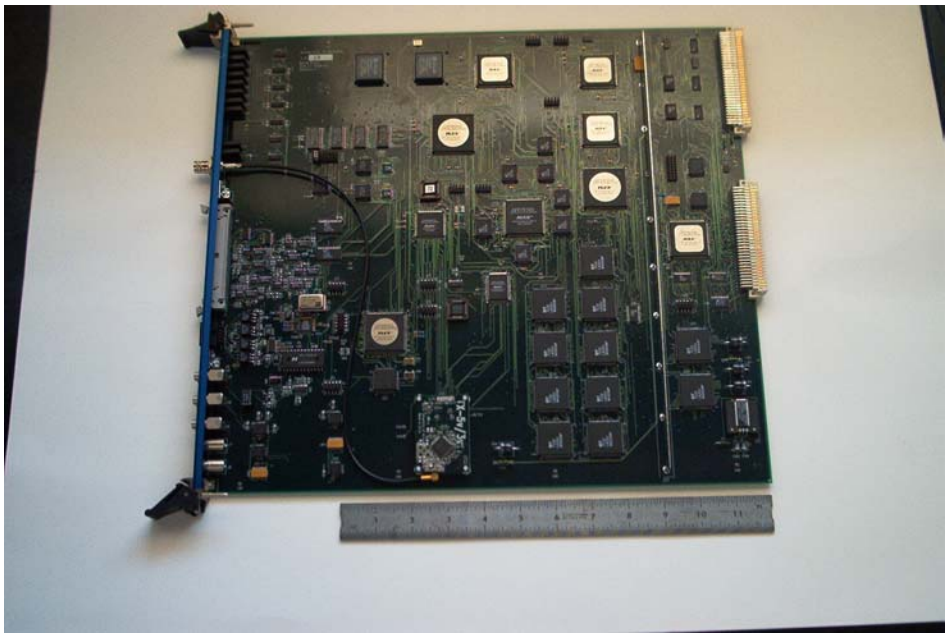

Figure III.1.26. Photograph of the Muon Trigger Crate Manager (MTCM) card.

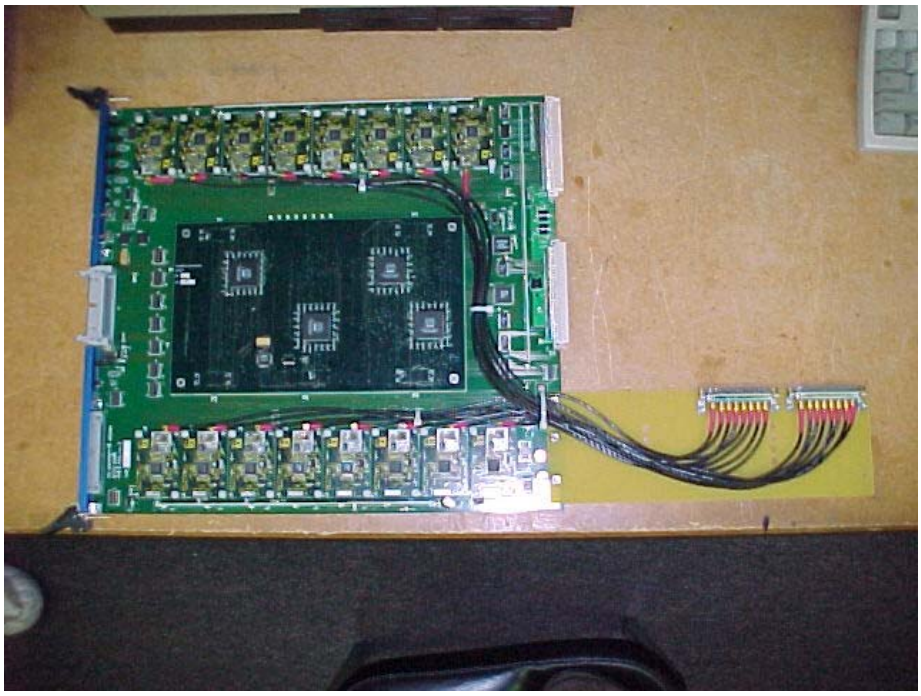

Figure III.1.27. Photograph of the L1MU motherboard, MTC05 daughter card, and serial link receivers.

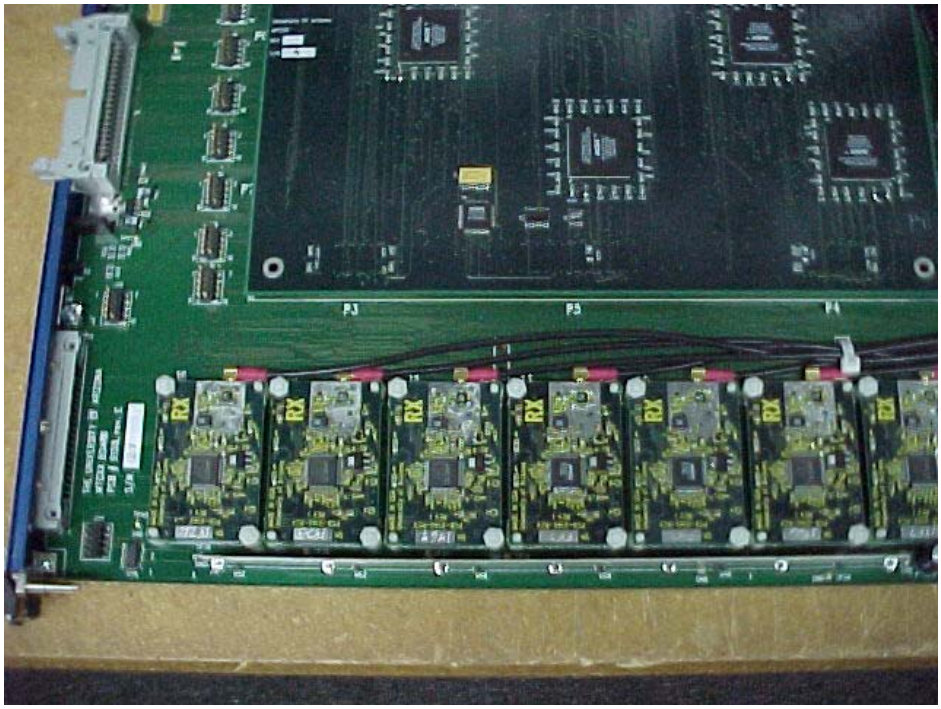

Figure III.1.28. Closeup photograph of the L1MU motherboard, MTC05 daughter card, and serial link receivers.

The MTC05 cards match tracks from L1CTT to hits in the muon scintillator system. Each octant trigger card receives tracks from the L1CTT for the ten 4.5 ˚ sectors in that octant plus one sector of overlap on either side. Each sector sends its six highest P_T tracks to L1MU, and each track contains the phi position in the outer layer, P_T value, and track curvature in the central magnetic field. The triggers formed by the MTC05 cards include loose (track matched to A-layer scintillator hits) and tight (track matched to a scintillator road using hits inside and outside the toroid iron) for four P_T thresholds (roughly 1.5, 3, 5, and 10 GeV/c). Loose and Tight scintillator-only triggers are also formed. The logic has been implemented on four 484-pin Altera ACEX 1K100 FPGA's and has a total latency of 13 x 18.8ns = 235 ns.

The MTC10 cards form triggers based on wire hits. In the central region, the hits from the wire chambers (PDT's) are sent directly to the trigger cards. The hits for each layer are used to form track stubs, or centroids, which are then used to confirm scintillator hits in each layer. Triggers are formed by matching centroid-confirmed scintillator hits between layers. In the forward region, the centroid finding is done by separate centroid-finding cards (MCEN's), which subsequently send the centroids to the MTC10 cards. (The MCEN cards were built by Boston University.) The MTC10 cards then use the centroid-confirmed scintillator hits to form Loose (A-layer) and Tight (A and B-layer) triggers. The MTC10 logic has been implemented on seven Altera ACEX 1K FPGA's (three 1K100, three 1K50, and one 1K30). The latency in the central region is 29 x 18.8 ns = 550 ns, while in the forward region the latency is 23 x 18.8 ns = 430 ns.

The data from the various front end systems arrive asynchronously at L1MU and must be synchronized before triggers can be formed for a given event. To accomplish this, all received data are written directly into FIFO's which are initially empty. When all FIFO's are not empty (i.e., they have all received data for the first bunch crossing), the data are read from the FIFO's and sent to the MTC05, MTC10, or MTM flavor cards for trigger formation. In addition to synchronizing the data for a given event, the trigger cards also buffer the input data and trigger decisions pending global Level 1 (L1) and Level 2 (L2) trigger decisions. The input data and trigger decisions are stored in Dual Port Memories (DPM's) and a pointer to the data is written into a FIFO. When an L1 or L2 Accept is received, the pointer is used to read the data for a particular event. The L1MU trigger can also send all of the received input data from the detector front-ends to aid debugging. Data is sent to L2 and L3 using the Cypress Hotlink chipset CY7B23/33 over “Astro cable” from AMP.

L1MU Trigger Hardware

As mentioned above, the L1MU trigger is completely operational. L1MU triggers can be formed from muon multiplicity, muon detector hits (scintillator hits and/or wire hits), L1CTT tracks, P_T threshold (from the L1CTT tracks), quality (single detector layer or coincidence between layers), and detector region. Examples of trigger hardware progress follow.

Trigger hardware progress focused on reliable readout of the L1MU trigger cards. We fixed several small issues relating to the readout of the trigger cards, including the interruption of an L3 message in order to send data to L2 and a glitch on a backplane signal that hindered trigger

readout from individual trigger cards. We also discovered and fixed a problem with the PECL clock drivers on the crate manager that had been damaged due to faulty extender cards. We are able to read the input data from the individual trigger cards and we have used this in commissioning the central wire chamber triggers and triggers using L1CTT tracks. We still have a few dark corners to sweep out that we will attack during the September 2003 shutdown.

New firmware was added which forms triggers using scintillator hits that have matched tracks from the L1CTT and triggers using scintillator hits that have wire chamber confirmation. New logic for the latter was needed to compensate for the late arrival of tracks from the L1CTT that put the overall trigger latency over budget. Octant-matching logic between scintillator triggers with matched L1CTT tracks and scintillator triggers with wire chamber confirmation was developed for the crate managers. This required a larger FPGA for the crate managers, which was installed during the January 2003 shutdown.

We maintain working L1MU test stands at Fermilab and Arizona. We maintain working trigger card replacements at Fermilab. If a trigger card goes bad during running (and very few have) we replace the trigger card at the next access. The suspect trigger card is then tested on the Fermilab test stand. If the problem can be quickly identified, the card is fixed and retested. Trigger cards with more difficult problems are sent back to Arizona for more thorough debugging.

Because the Muon Trigger Test (MTT) card plays a vital role in our maintenance operation, we recently designed and fabricated new MTT's to replace the existing ones. The existing MTT was the first card we built and now contains many obsolete parts. In addition, the layer alignment of the existing MTT was less than perfect which led to occasional, spurious problems. The new MTT's are currently being assembled and debugged.

L1MU Trigger Simulator

Another critical piece of the L1MU trigger system is the L1MU trigger simulator.
The L1MU trigger is fully simulated in C++ as part of the DØ trigger simulator. The L1MU simulator (tsim_l1muo) uses the digitized readout of the muon system and the results of the L1CTT simulator as inputs. The simulator allows us develop and optimize the various trigger algorithms that eventually become FPGA firmware on the L1MU trigger cards. Single muon and physics Monte Carlo events are used to determine detector acceptance and trigger algorithm efficiencies.

Most crucially though, the L1MU trigger simulator serves as the primary method by which we certify the L1MU trigger hardware. This is carried out as follows: detector hits in the collider data are processed through the simulator to produce L1MU simulator trigger decisions which are then compared event-by-event and bit-by-bit with the L1MU hardware trigger decisions in the collider data. Certification means achieving perfect or near-perfect agreement between the simulated and hardware L1MU trigger decisions. Presently this method of certification gives better than 99% agreement between the two. This simulator-hardware comparison is also run online and used to monitor the performance of the L1MU trigger during data-taking. No other trigger system in DØ uses such online monitoring.

Some examples of recent progress in the L1MU trigger simulator are: increasing the efficiency of the trigger logic in the central bottom region where the detector acceptance is sparse (done), adding octant matching between triggers that have scintillator hits with matching L1CTT tracks and triggers that have scintillator hits with wire chamber confirmation (done), moving to an RCP-based trigger logic to increase compatibility with the FPGA logic used in the hardware (in progress), and adding wire chamber confirmation for scintillator hits in the forward region (done, by Boston University).

A few of our many results from the L1MU trigger simulator are given in Figures III.1.29 and III.1.30. In both figures, the ptxwtlx trigger is a two-layer scintillator road and an A-layer wire chamber centroid in the same octant and the pt4wlxx trigger is a high P_T track matched to an A-layer scintillator hit. Figure III.1.29 (III.1.30) shows the trigger efficiency of these triggers as function of P_T (η) using single muon Monte Carlo events. In these plots, the denominator is the number of Monte Carlo muons that have the minimum number of hits in the muon system to reconstruct a medium muon. The numerator is the number of events in the denominator that had a simulated trigger.

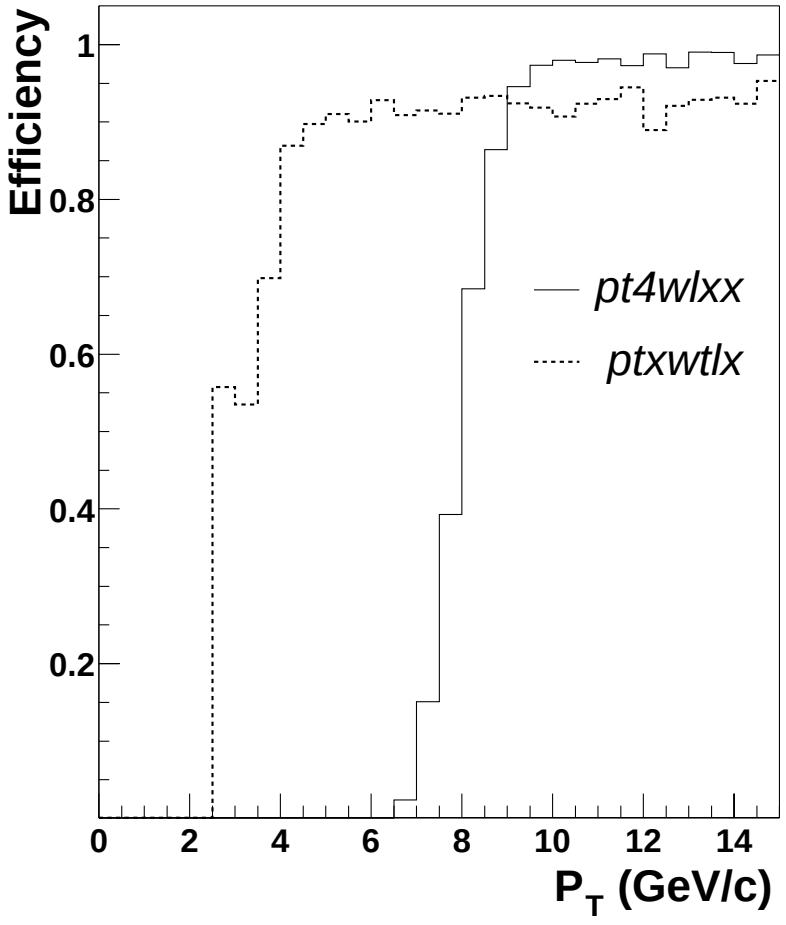

Figure III.1.29. Trigger efficiency as a function of P_T for the ptxwtlx and pt4wlxx triggers.

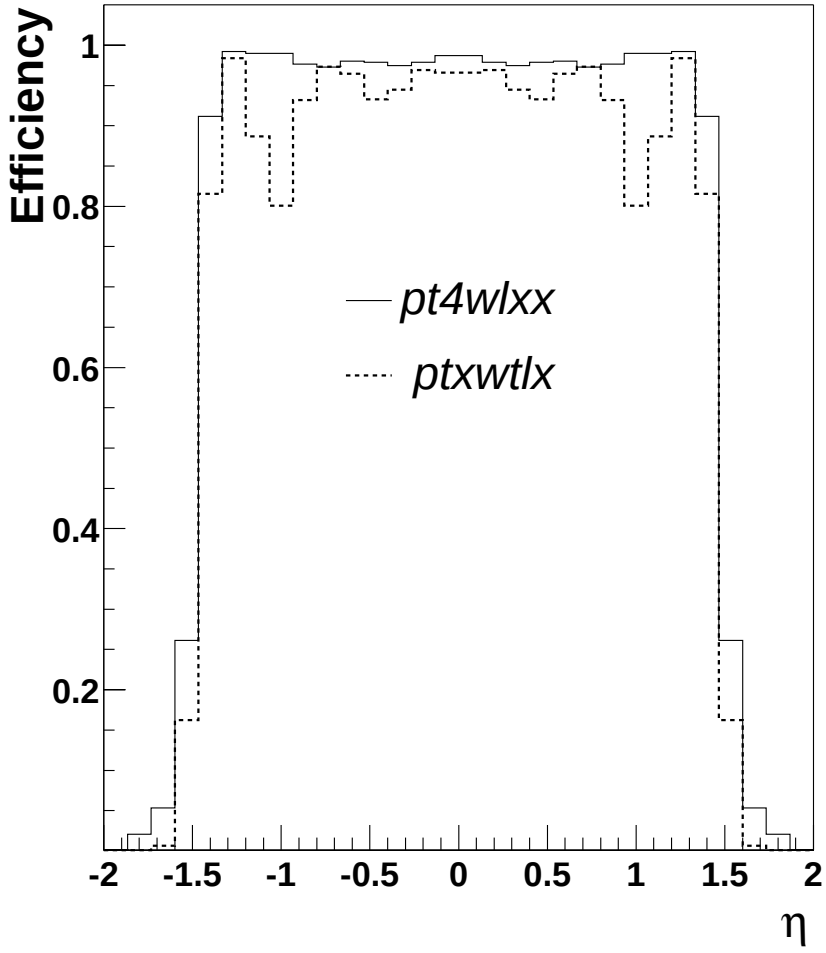

Figure III.1.30. Trigger efficiency as a function of η for the ptxwtlx and pt4wlxx triggers.

L1MU Online and Monitoring Software

Currently one of the highest priorities on DØ is to keep data-taking efficiency above 90%. To help achieve that goal, graduate student Jeff Temple led the effort by the L1MU group to develop numerous online monitoring tools as well as easy-to-use tools for control room shifters.

Online monitoring of the L1MU trigger uses trigger rates, octant trigger occupancies, and hardware/simulator comparisons to quickly detect problems with the trigger. Shifters record the rates of monitor triggers at the beginning of every run and verify they are within limits. Synchronization triggers which are formed on all 48 trigger cards are monitored continuously by the DaqAI program, which notifies shifters when these rates have gone out of range. During every run, occupancy plots for every trigger card are formed and checked against a template for discrepancies.

In addition to shifter monitoring, expert plots are produced every hour which include full hardware/simulator comparisons for every trigger card. Since the simulator uses the readout of

the muon system as input, these plots can also detect readout problems in the muon system itself, especially in cases where hits are sent to L1 but not to the event readout. Rate versus luminosity plots are also formed from the shifter checklist every four hours. All of these results are summarized on a web page (Figure III.1.31) which is checked several times daily by the L1MU group. Figure III.1.32 shows output from the L1MU trigger simulator-hardware comparison. Agreement between the simulator and hardware results at the 99% level is noted.

Much of the day-to-day operation of the L1MU system is handled by shifters, most of whom are not detector experts. To facilitate untrained personnel controlling a complex system, the L1MU group developed GUI's that allow the shifters to monitor power supply status, rack protection systems, and trigger rates. A common problem is that when a muon detector front end goes bad, its input to the L1MU trigger must be disabled. A GUI was written to allow the shifters to quickly and reliably remove (or add) muon front end systems from the L1MU trigger. The GUI also gives "one-button" configuration of the entire L1MU system in case of power outages or other problems. Some screen captures of these GUI's are shown in Figures III.1.33 and III.1.34.

In addition to daily monitoring, the L1MU group maintains a 24-hour on-call expert. The expert responds to questions about the system status and fixes any problems that may appear. Because of the close tie between the muon front ends and the L1MU trigger, many of these problems are general in nature (readout issues, muon front end problems). The addition of the trigger configuration GUI dramatically reduced the number of calls we receive, as many of the problems involve removing a bad muon front end from the L1MU trigger.

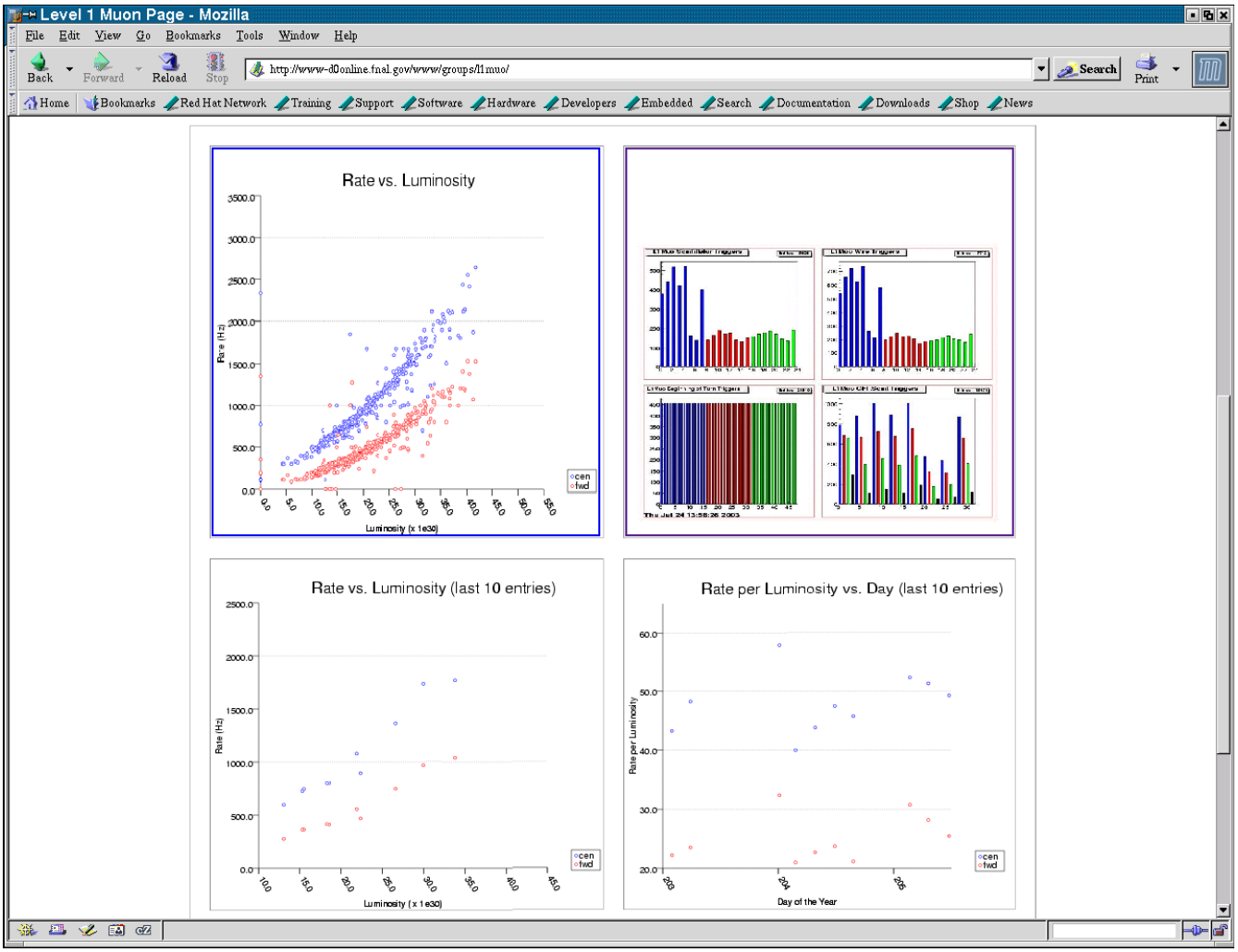

Figure III.1.31. Screen capture of the L1MU monitoring web page.

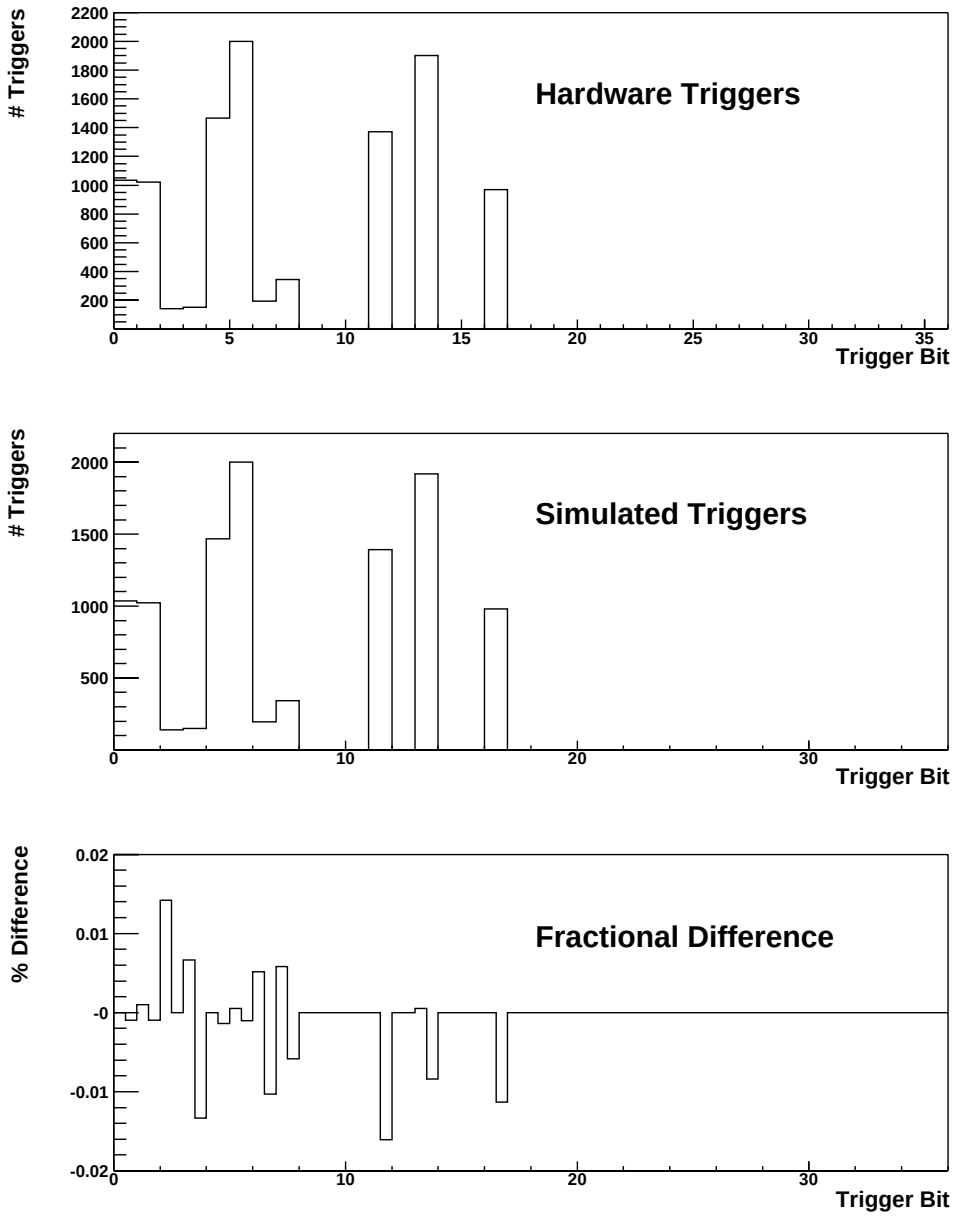

Figure III.1.32. Plot showing the number of triggers found in the L1MU hardware, the number of triggers found by the L1MU simulator, and the fractional difference.

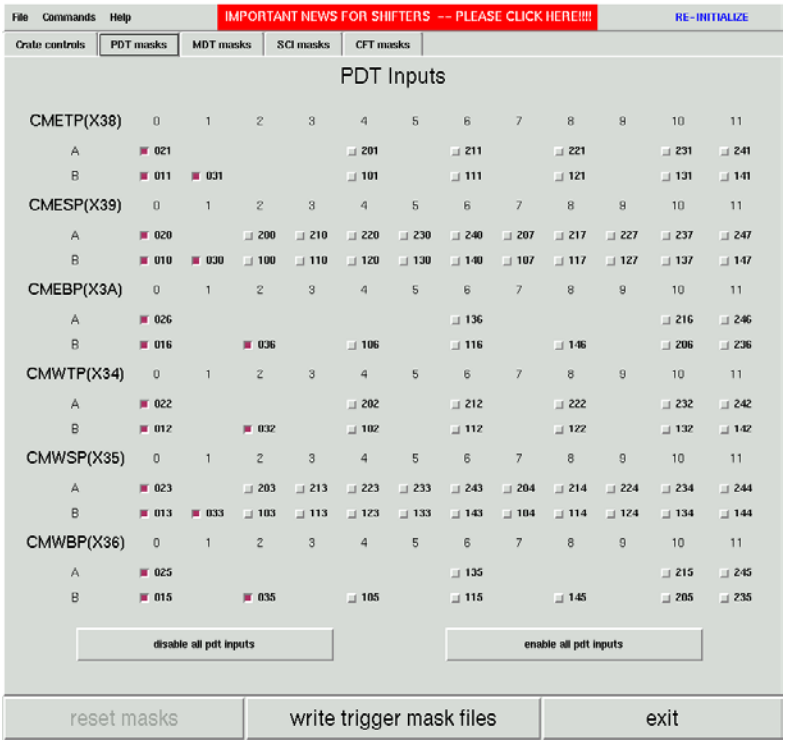

Figure III.1.33. Screen capture of the L1MU PDT input disable GUI.

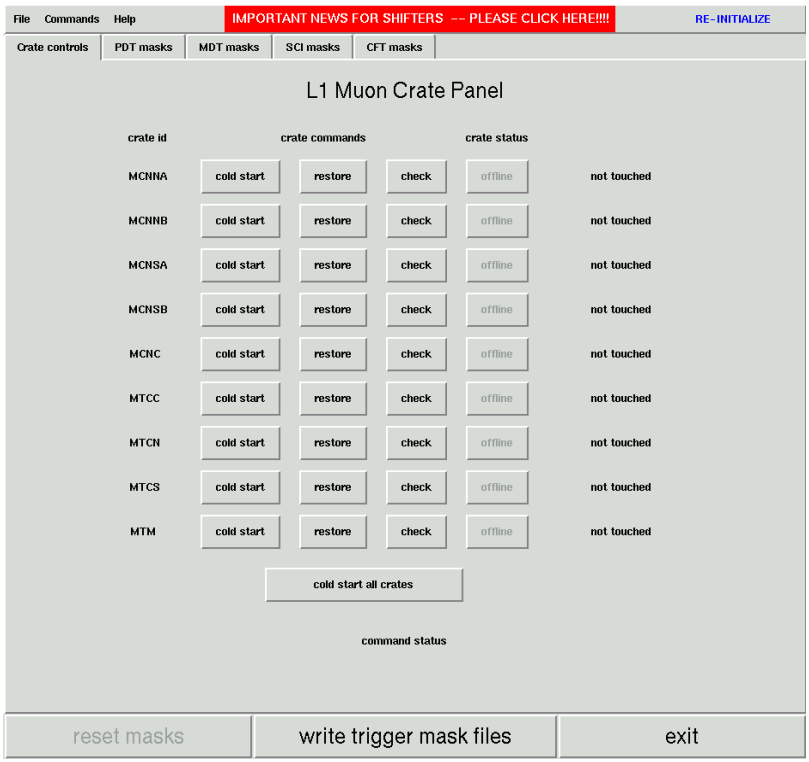

Figure III.1.34. Screen capture of the L1MU control GUI.

L1MU Results from Data

We constantly evaluate L1MU trigger efficiencies and purities using data. C++ code was developed to write summary L1MU information to TMB (Thumbnail) files. (TMB's are essentially DST's.) Code was also developed to write summary L1MU information to the ROOT files created from the TMB's. Finally, code was developed to analyze the summary L1MU information at the ROOT level. Below we give only a sample of recent results.

The L1CTT trigger was effectively commissioned in December 2002; hence a good portion of L1MU data analysis was devoted to understanding these triggers. For efficiency studies we make use of data collected with calorimeter-based triggers. Two triggers we focused on were TTK(1,10) and mu1pt4wlxx. The former trigger is an L1CTT track with $P_T > 10$ GeV/*c*. The latter trigger is a TTK(1,10) track matched to an A-layer scintillation counter.
The denominator of our efficiency calculation is the number of offline reconstructed muons. The numerator is the number of offline reconstructed muons that satisfied the trigger condition. Figures III.1.35 and III.1.36 show the trigger efficiency curves for the TTK(1,10) and mu1pt4wlxx triggers.

Note that the TTK(1,10) efficiency is over 55% for muons having P_T less than the threshold value of 10 GeV/c. This suggests that the L1CTT may be firing on tracks that are unrelated to the candidate muon. The efficiency plateaus at 84% for muons having $P_T > 15$ GeV/c. The mu1pt4wlxx trigger efficiency is lower, plateauing at 73%. It also shows an non-zero efficiency below 10 GeV/c, but at about half the rate seen for TTK(1,10).

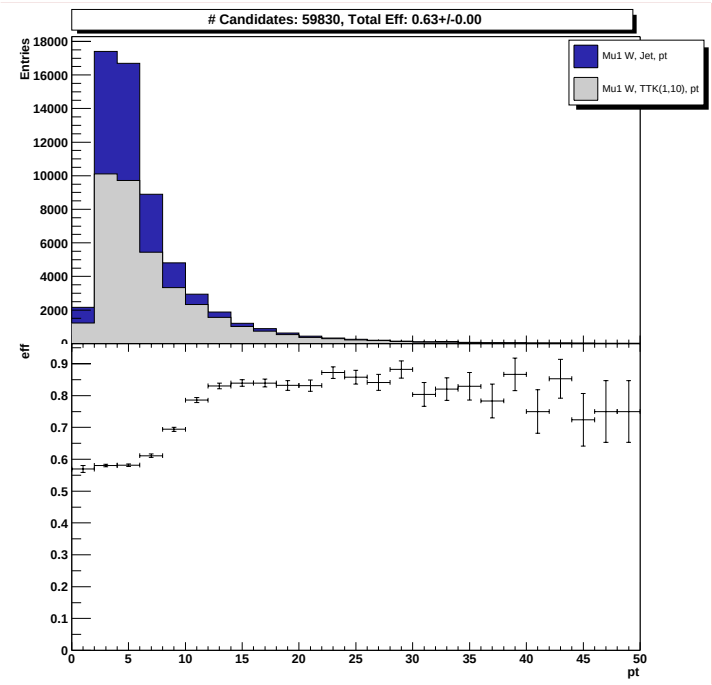

Figure III.1.35. Trigger efficiency as a function of P_T for the L1CTT trigger TTK(1,10).

Figures III.1.37 and III.1.38 show the relative trigger efficiency between mu1pt4wlxx and TTK(1,10) as a function of phi and pseudorapidity for muons with $P_T > 10$ GeV/*c*. In Figure III.1.37, a drop in efficiency is noted for $|\eta| > 1$. This suggests that the L1MU trigger roads may need to be expanded to include additional scintillation counters at forward η. The inefficiencies observed in Figure III.1.38 arise from the lack of A-layer scintillation counters in the bottom of the DØ detector.

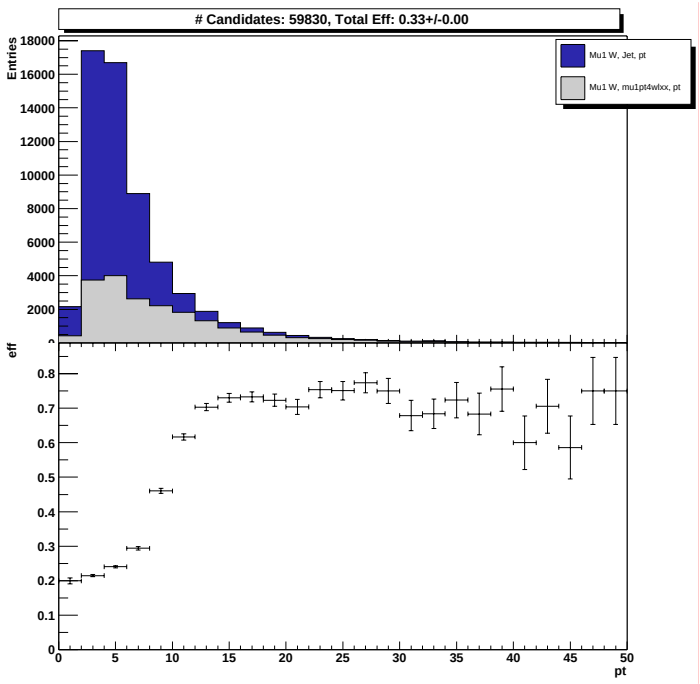

Figure III.1.36. Trigger efficiency as a function of P_T for the L1MU trigger mu1pt4wlxx. This trigger matches a TTK(1,10) track from L1CTT with an A-layer scintillation counter.

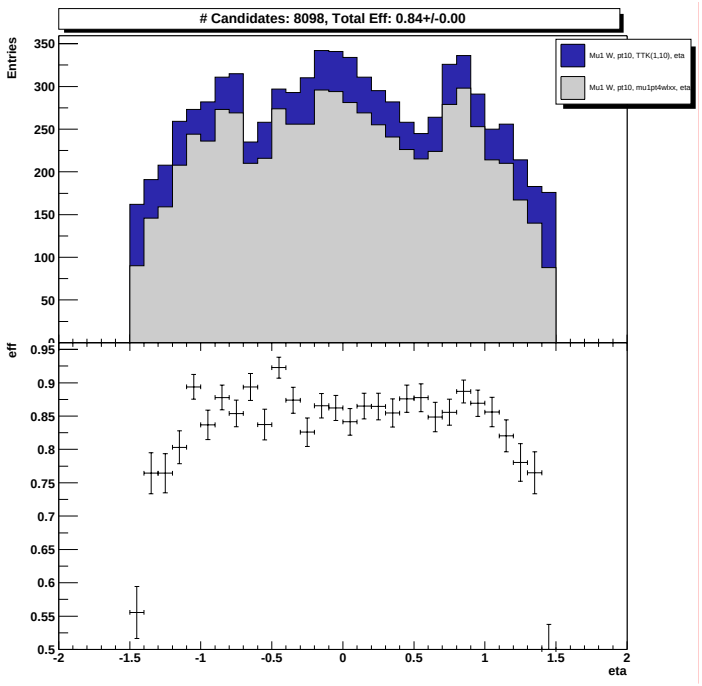

Figure III.1.37. The relative trigger efficiency of mu1pt4wlxx and TTK(1,10) as a function of η.

.

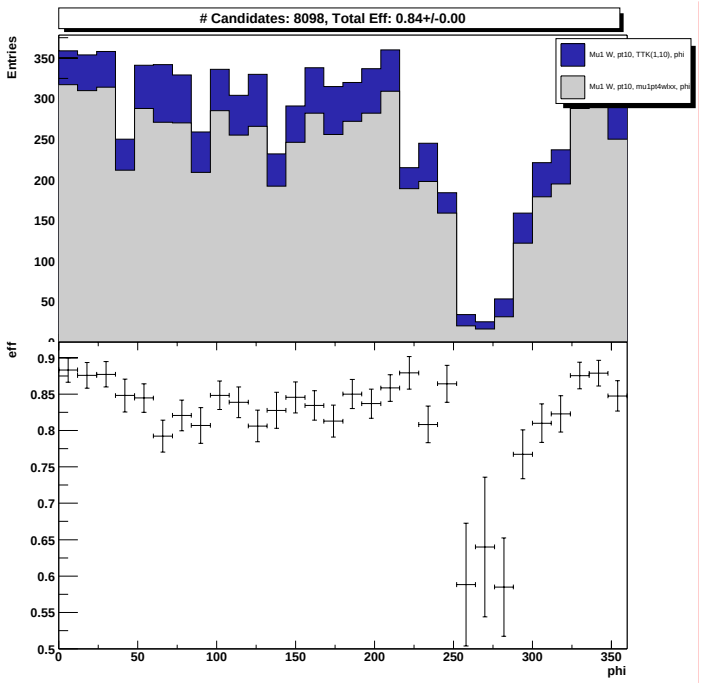

Figure III.1.38. The relative trigger efficiency of mu1pt4wlxx and TTK(1,10) as a function of φ.

A final example of L1MU data analysis is the L1MU trigger mu1ptxwtlx. This was the high P_T single-muon physics trigger used before the L1CTT was commissioned. It requires a scintillation counter road in the A and B-layers (inside and outside the toroid iron) and a wire chamber centroid in the A-layer. The efficiency is defined as above. Figure III.1.39 shows the relative efficiency between mu1ptxwtlx and mu1ptxwtxx as a function of pseudorapidity. The latter trigger does not require the wire chamber centroid in the A-layer. We see that the efficiency of requiring a wire chamber centroid in the A-layer is currently 96%.

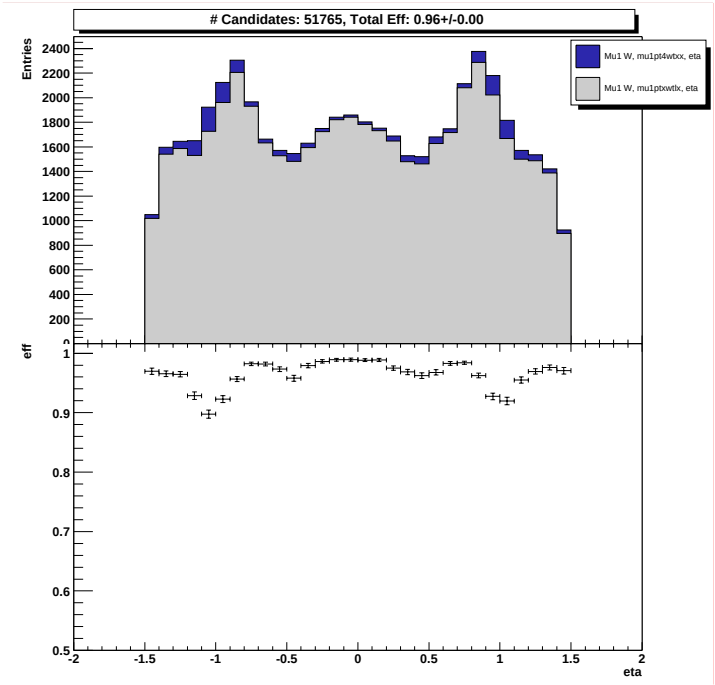

Figure III.1.39. The relative trigger efficiency of mu1ptxwtlx and mu1ptxwtxx as a function of η.

We end with some results on the purity of various L1MU triggers. The denominator of purity is the number of events satisfying a particular L1MU trigger. The numerator is the number of events satisfying a particular L1MU trigger and having an offline reconstructed muon in the same detector octant. Purities for various L1MU triggers are given in Table III.1.7. Note that the L1MU triggers are selecting mainly good muons at L1.

Trigger	Purity
mu1ptxctxx	0.61
mu1ptxbtxx	0.78
mu1ptxwtxx	0.72
mu1ptxwtlx	0.75
mu1pt4wlxx	0.44
mu1pt4wllx	0.54

Table III.1.7. Measured purities for various L1MU triggers.

III.1.5 DØ Service – Tracking Studies, L3, and Data-taking Shifts

In addition to the manifold services we provide in support of the Level 1 Muon Trigger, we also make contributions that have high impact in other areas of the experiment. Here we describe our service activities in tracking reconstruction (Erich Varnes), L3 examine and tracking (Elliott Cheu and Peter Tamburello), data-taking shifts (many of us), and editorial boards (Ken Johns).

Measurement of Tracking Efficiency

In the summer of 2002, one of the primary challenges facing DØ was charged track reconstruction. DØ's tracking system differs from those at other hadron collider experiments in that it is composed entirely of solid-state devices (silicon microstrips form the inner layers, while the outer layers are composed of scintillating fiber). This design offers excellent hit resolution and fast signal readout, but the cost and material required limits the number of layers one can build.

As DØ's initial data was analyzed, the track reconstruction efficiency was found to be inadequate, but it was not clear whether the problem was due to failures in the readout electronics, deficiencies in the reconstruction algorithm, or a fundamental limit of the detector's design. A reliable way to measure the tracking efficiency with high statistics was needed to diagnose the situation.

To achieve this, we take advantage of the fact that the DØ calorimeter and muon toroid have a thickness greater than ten nuclear interaction lengths over the entire fiducial volume, meaning that any track detected in the outer layers of the muon system can be identified as a muon with high purity. Therefore one can obtain a measure of the track reconstruction efficiency by taking a sample of muons identified in the muon system, and asking how often a track pointing toward that muon was reconstructed.

There are several effects that potentially bias the result of such a measurement. Firstly, the muon undergoes a significant amount of multiple coulomb scattering in traversing the calorimeter and toroid material, so the central track may not extrapolate exactly to the muon. Secondly, some muons may be due to cosmic rays that do not pass through the tracking volume. Both of these effects would cause the tracking efficiency to be underestimated. However, there is also a possibility that another charged particle in the event is close to the muon. In that case, the algorithm might declare a match even if the muon track was not reconstructed, thereby overestimating the efficiency.

The analysis is designed to minimize the first two effects and correct for the third. The size of the matching window is chosen empirically to be about 3σ in both the η and ϕ directions, rendering the fraction of tracks missed due to spatial mismatch negligible. Placing tight requirements on the timing and direction of the muons reduces cosmic ray contamination to a negligible level.

To determine the likelihood that a matched track was due to a charged particle other than the muon, we also look for tracks in a control window the same size as the matching window. If the

muon is isolated from jet activity, the control window is centered 90^o in φ from the muon. If the muon is within a jet, the control window is adjacent to the matching window in the same jet. The fraction of muons for which a track appears in the matching window is called the measured efficiency ε_M, and the fraction for which a track appears in the control window is called the random efficiency ε_R. To extract the true efficiency ε_T we note that the measured tracking efficiency is the sum of two terms:

$$\varepsilon_M = \varepsilon_T + \varepsilon_T \left(1 - \varepsilon_R\right)$$

so that:

$$\varepsilon_T = \frac{\varepsilon_M - \varepsilon_R}{1 - \varepsilon_R}$$

The true efficiency can therefore be calculated on a bin-by-bin basis for each histogram that is generated.

Results of the analysis for isolated tracks and tracks within jets are shown in Figures III.1.40 and III.1.41. For isolated tracks it is clear that the previous algorithm had significant difficulty in finding tracks in the central region, which the current version has remedied to bring the overall efficiency for finding an isolated track to about 98%. Similar improvement is seen for finding tracks in the more complex environment of a jet, though the overall efficiency is only slightly above 90% for these tracks, indicating that further algorithmic improvements may be beneficial.

These techniques for measuring the tracking efficiency have been incorporated into D∅'s quality control program that checks the performance of the detector and reconstruction on a run-by-run basis.

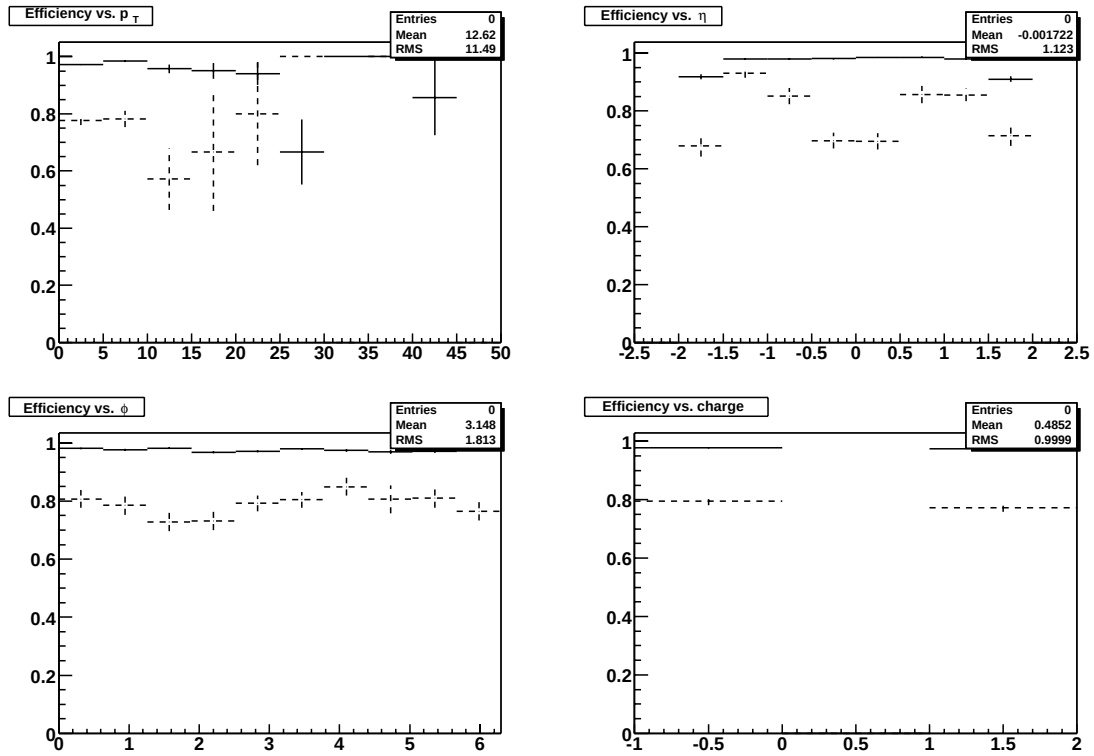

Figure III.1.40: Efficiency for reconstructing isolated tracks, as measured using single muons. The solid lines show the result using DØ's current track reconstruction algorithm, while the dashed lines show the result for the previous version. It is clear that the previous algorithm had a deficiency in the central region of the detector, which has now been fixed.

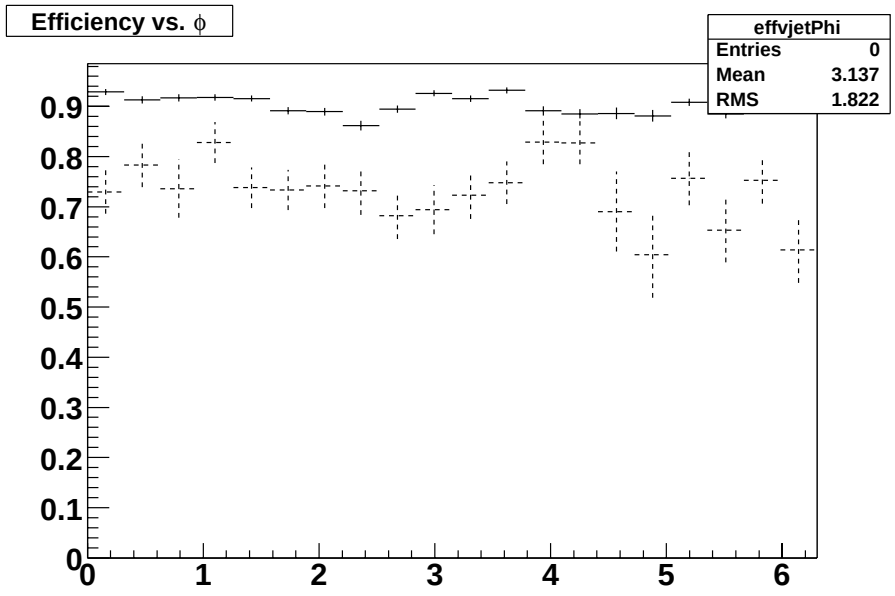

Figure III.1.41: Efficiency for reconstructing tracks within jets as a function of the jet φ, using DØ's current algorithm (solid lines) and the previous version (dashed lines).

Level 3 Examine

The Arizona group (Elliott Cheu and Peter Tamburello) has taken on the responsibility for developing and maintaining the Level 3 (L3) trigger examine. This system is used online to monitor the quality of objects found by the L3 trigger system and to quickly spot problems associated with the L3 trigger. We developed a framework that is able to display histograms in real time. These histograms are displayed in a custom browser and overlaid with reference histograms. A confidence level for the agreement between the data and the reference histogram is displayed to help shifters determine the quality of the data. This system also produces plots that are linked to the DØ web site as part of "DØ Live" so that anyone with access to a web browser can, in real time, get a snapshot of the data in the DØ control room. The trigger examine is now run during all shifts and has been useful in helping to spot problems with the data quality.

As an offshoot of this project, we have also been involved in developing software to allow shifters to take shifts remotely. This is useful since now collaborators in other parts of the world can remain active in DØ. Also, remote shifts allow people in different time zones to cover unpopular (i.e. owl) shifts. Recently we were able to modify the existing global monitoring software so that it can access histogram files on the online machines via a secure (kerberized) connection. This allows one to have the full power of the global monitoring software on a local desktop. The software has been fully implemented, and remote shifters are just now beginning to use the remote software during their shifts. Because of our experience with the global monitoring software, we are now responsible for maintaining this piece of code.

Our group has also been active in developing the L3 thumbnail framework. The thumbnails are a compressed data format that is meant to allow DØ to maintain a large data set on disk. We have developed the structure required to include the L3 information in this reduced data set. The L3 thumbnail information is now part of the standard thumbnail output and will be useful in order to allow trigger studies at the thumbnail stage.

Most of the physics at DØ either depends on or substantially benefits from tracking in the L3 trigger. For example, the only way to control the rate of an inclusive single muon trigger is to require a matching central track. The offline tracking algorithms use about eight seconds per event, while the time available for the L3 nodes to make a decision is about a tenth of a second. L3 therefore uses a separate fast algorithm. This algorithm is very efficient for high P_T tracks that leave hits in each layer of the CFT, but it is limited to the CFT fiducial region, approximately $|\eta| < 1.6$, and is sensitive to hit inefficiency, particularly in the two outermost layers.

We have been investigating ways to extend the coverage to the forward region and improve the robustness against hit inefficiency. Figure III.1.42 shows the η distribution of charged particles with $P_T > 1$ GeV/c in a $Z \to \mu^+\mu^-$ Monte Carlo, as well as the subsets of these particles that pass through five or more CFT layers, and all eight CFT layers. We find that most of the five, six, and seven layer tracks can be recovered by modifying the track seeding algorithm, resulting in an overall efficiency improvement of about ten percent in the Monte Carlo. The gain may be greater

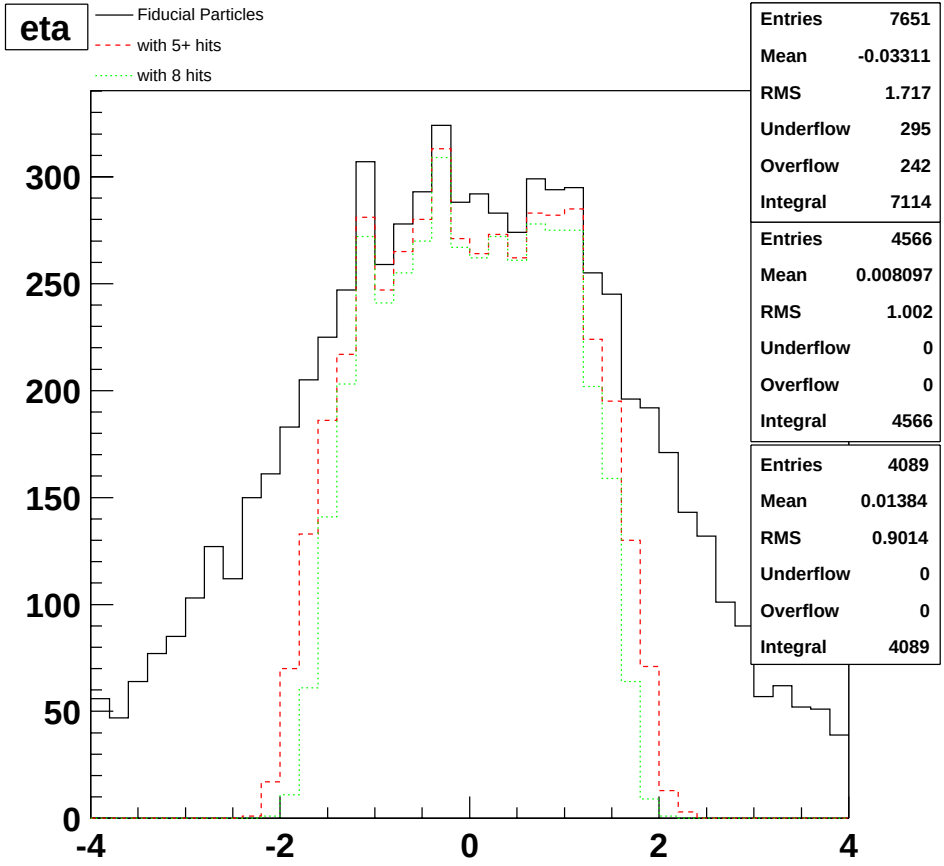

Figure III.1.42: The η distribution of charge particles with $P_T > 1$ GeV in a $Z \to \mu^+\mu^-$ Monte Carlo (solid), the subset of these leaving five or more CFT hits (dashed), and eight CFT hits (dotted).

in real data where the hit efficiency in the fibers is less than 100%. In addition, it may be possible to make use of the forward silicon disks in a fast algorithm. Our studies are continuing.

Data-taking Shifts

Many members of the Arizona DØ group run data-taking shifts in the control room or remotely (for Global Monitor (GM) shifts). Ken Johns, postdoc Stefan Anderson, and graduate students Jeff Temple and Rob McCroskey run captain and muon shifts. Notable is that Jeff Temple and Rob McCroskey serve as shift captains as graduate students. Even more remarkable is that Rob McCroskey held the responsibility of Deputy Run Coordinator while the current Run Coordinator and Deputy were out of town for several weeks. That our graduate students have been tapped for these positions is recognition of their knowledge of the experiment and responsible nature. Elliott Cheu and postdoc Peter Tamburello run GM shifts both in the control room and remotely.

As documented by the DØ Run Coordinator, Arizona's shift load from April 2001 to June 2003 is 1.54. This means we have run 54% more shifts than our minimum requirement. It also gives another indication of our deep involvement in running the experiment.

Editorial Boards

Ken Johns is chair of the editorial board for the analysis "Search for $t\bar{t}$ Resonances in the Leptons plus Jets Channel". The principal author of this paper is Supriya Jain of TIFR, India. The editorial board is charged with approving the physics results of an analysis for talks at conferences. It is also charged with approving the draft of the paper for publication before circulation to the collaboration for review, after the collaboration review, and after comments are received from the journal referees and have been incorporated by the author(s). The result of this paper were used to exclude the existence of a leptophobic topcolor particle with mass $M_X > 560$ GeV/c^2 and width $\Gamma = 0.012\ M_X$. This limit exceeds that of CDF. This paper was recently passed to final review of the spokespersons before submission for publication in Physical Review Letters.

III.1.6 DØ Service – Level 1 Calorimeter-Track Trigger (L1CalTrack)

Overview

In order to exploit the discovery potential of the DØ experiment, the Tevatron must run at the highest luminosity possible. While the initial luminosity provided by the Tevatron in Run II is only modestly higher than in Run I, there is a well-defined upgrade plan to increase the luminosity by a factor of ~3 by early 2005 and ~7 by early 2007. The increased luminosity will place increased pressure on the DØ trigger system at all levels.

In particular, the present L1 Accept rate of 1500 Hz is already a factor of ~3 below the Run II design goal, primarily because of the front-end busy rate of the tracking electronics and limited processing power at Level 2 (both problems are being addressed). In order to keep the most important physics triggers unprescaled as the luminosity increases, additional rejection power must be brought to bear at Level 1. To this end, both the Level 1 Calorimeter Trigger (L1CAL) and Level 1 Central Tracker Trigger (L1CTT) will be upgraded in the coming years.

Another trigger upgrade for higher luminosity, for which Arizona holds full hardware and software responsibility, is the L1CalTrack trigger. Ken Johns conceived of and leads this project. He is joined in this effort by Erich Varnes, graduate students Bryan Gmyrek and Vernon Miller, engineer Joel Steinberg, and technicians Chris Leeman and Semra Bekele. A large fraction of the L1CalTrack hardware is to be completed in the upcoming grant year. Hence support for our student technicians who play critical roles in testing and debugging trigger cards is particularly important.

The goal of the L1CalTrack trigger is to exploit matches in the φ position of tracks from the L1CTT trigger with that of EM and jet objects from the L1CAL trigger in order to reduce the L1 trigger rates of EM and tau triggers. Information from the Central Preshower (CPS) and Forward Preshower (FPS) detectors is also used. Monte Carlo studies show that the improvement in the reported φ position from 90º to 11.25º of EM objects can reduce medium P_T electron triggers by a factor of 2-3. Additionally, large factors of rejection (10-70) can be achieved by matching track triggers with calorimeter towers of modest energy. This latter is important in triggering on hadronic tau decays such as in $H \rightarrow \tau\tau$.

L1CalTrack Hardware

The implementation of the L1CalTrack trigger uses the **existing** Level 1 Muon Trigger (L1MU) architecture with small modifications. The L1MU trigger, designed, built, and commissioned by the University of Arizona, matches the φ position of tracks from the L1CTT trigger with that of muon objects derived using muon scintillation counter hits. Similarly, the L1CalTrack trigger is designed to match the φ position of tracks from the L1CTT trigger with calorimeter objects (EM objects and jets) from the L1CAL trigger. The huge advantage of this implementation is that the L1MU trigger has been successfully running since the start of Run II. Thus issues such as synchronization,

buffering, outputs to L2 and L3, electronics testing, monitoring, power supplies, and rack infrastructure have proven, working solutions.

Because the architecture of the L1CalTrack trigger is similar to that of L1MU, even a brief description is avoided here because of duplication. One can refer to the L1MU Hardware section of this progress report for details. In addition to making some small fixes to the existing L1MU design and replacing a few obsolete parts, there are essentially three differences between L1CalTrack and L1MU. The first is that FIFO's and DPM's are now incorporated inside FPGA's rather than discrete components. This greatly reduces the number of chips on the L1MU trigger cards. The second is that by exploiting the latest FPGA technology, we can design one universal flavor board that can be used for MTC05, MTC10, MTM, and CalTrack trigger algorithms. The third difference is that additional inputs were added to the L1MU trigger cards. In fact these were added to the new, universal flavor board.

L1CalTrack Status

Until recently, our primary efforts were in documentation and design. We wrote the L1CalTrack sections of the Conceptual Design Report and Technical Design Report for the Run IIb trigger upgrade. We produced talks for Temple (August 2002) and Lehman (September 2002) reviews that were part of the project approval process. We prepared technical documentation for the upcoming Production Readiness Review (July 2003). On the design side, we began making the changes, some of which were described above, to the L1MU schematics. We also began testing and debugging a new Muon Trigger Test (MTT) card that we will use for bench testing of both the L1CalTrack and L1MU systems.

In the Spring 2003, we began a prototyping phase and we recently sent the prototype universal flavor board to a vendor for assembly. We also ordered several long lead-time items such as our custom VME backplane, power supplies, and (fire retardant) signal cables.

As mentioned above, a majority of L1CalTrack fabrication, assembly, and testing will take place later this year and in the next grant year. Highlighting a few dates from the official schedule:
Fabrication and Assembly of Preproduction MTCxx Trigger Cards--October 2003
Fabrication and Assembly of Production MTCxx Trigger Cards--May 2004
Fabrication and Assembly of Production Universal Flavor Boards--December 2003
Fabrication and Assembly of Production MTCM Crate Managers--November 2003
In fact we are approximately one-two months behind the official schedule however still very far ahead of a 2005 completion date.

Recent L1CalTrack Simulation

We hold responsibility for all online, offline, and simulation software for the L1CalTrack trigger, responsibilities we successfully assumed for the L1MU trigger. Fortunately much of the online and offline software for L1MU can be modified in a straightforward way for the L1CalTrack trigger. In the next year we hope to complete the C++ code for the L1CalTrack trigger that will be used in the D∅ trigger simulator. Again, we will use the existing C++ code for the L1MU trigger as a starting point. In the last year, Erich Varnes and graduate student Vernon Miller worked to improve L1CALTrack algorithms studies.

In these studies, the Monte Carlo, detector simulation, and trigger simulation machineries were brought to bear. In particular, the response of the upgraded L1CAL trigger was used rather than the existing one. The background is modeled by Pythia inclusive QCD events. The signal is modeled by Pythia $H \rightarrow \tau\tau$ decays, where the τ decays hadronically. This is a signature that would not be accepted by the lepton-based Level 1 triggers that are currently running in D∅, and also one that appears most similar to the QCD dijet background.

There are several variables that can be used to define triggers that select signal events while reducing background. Both the L1CAL and L1CTT triggers have four energy or momentum thresholds, so one has flexibility in determining the set of tracks and calorimeter clusters to use in defining a match. One can also require the track trigger to be isolated. This helps in distinguishing τ candidates, which tend to have low track multiplicities, from hadronic jets.

One trigger algorithm for $H \rightarrow \tau\tau$ ignores matches between a calorimeter cluster that passes only the lowest-energy threshold and a track that passes only the second-lowest P_T threshold, requires that the track be isolated, and demands that there be more than one such match in an event. The background rate for this algorithm is estimated from simulation to be 125 Hz at luminosities of $2 \times 10^{32} cm^{-2} s^{-1}$, while the trigger efficiency for signal is 32%. In the future we will further explore the flexibility allowed by the L1CAL and L1CTT trigger information to determine if an even more attractive solution can be found.

III.2.1 KTeV at the Fermilab Tevatron

The Arizona group, consisting of E. Cheu, J. Hamm, S. Taegar and J. Wang, played a very significant role on the KTeV experiment. During the KTeV run, we were responsible for the neutral trigger and the online splitting system. When data taking was completed in 2000, we turned our attention to the CsI calibration and various data analyses.

The Arizona group spearheaded the effort for developing an online data splitting system that was used during the 1999 data taking. This system allowed each event to go to a particular tape set based upon information obtained during level 3 processing. Calibration of the data and access to the data was significantly improved after we implemented this system compared to analysis of the 1996-1997 data. Our group has worked on a significant part of the CsI calibration of the 1999 data sets and has now completed its calibration-related tasks.

The Arizona group has completed work on a number of important analyses and continues to work on one remaining topic. We have completed an alternate analysis of $\mathrm{Re}(\varepsilon'/\varepsilon)$, complementary to the main analysis headed by the U. Chicago group. Along with an undergraduate, T. Uchizawa, we have made major contributions to the analysis of $K_L \to \pi^0 e^+ e^- \gamma$. Our two graduate students, J. Wang and J. Hamm, are responsible for analysis of the $K_L \to \pi^0 \gamma\gamma$ and $K_L \to e^+ e^- \mu^+ \mu^-$ decays, respectively. In particular, the $K_L \to e^+ e^- \mu^+ \mu^-$ result represents the best measurement to date of this decay mode.

KTeV Analysis

Alternate Analysis of $\mathrm{Re}(\varepsilon'/\varepsilon)$

The main goal of the KTeV experiment is the measurement of the direct CP violating parameter, $\mathrm{Re}(\varepsilon'/\varepsilon)$. In 1999 both the KTeV and NA48 experiments published new results on $\mathrm{Re}(\varepsilon'/\varepsilon)$. [1,2] The NA48 experiment also announced a result based upon their 1998 data in 2000. All of these results indicated a non-zero value for $\mathrm{Re}(\varepsilon'/\varepsilon)$. However, agreement between these three results was not very good, and, until recently, the situation regarding direct CP violation remained somewhat unclear. Because of the importance of this measurement and the disparity of the results, the Arizona group embarked upon a new analysis of $\mathrm{Re}(\varepsilon'/\varepsilon)$ with the 1997 KTeV data set using a reweighting-based acceptance correction. The first KTeV result was based upon approximately one-eighth of the total data set taken primarily in 1996. The new data set comprises about 3/8 of the total KTeV data set.

The value of $\mathrm{Re}(\varepsilon'/\varepsilon)$ is determined from a double ratio of the four $K \to \pi\pi$ decay modes. However, an acceptance correction must be applied to each of the decay modes before determining $\mathrm{Re}(\varepsilon'/\varepsilon)$. In the KTeV experiment, the acceptances for the four modes are very different due to the large difference in the K_L and K_S lifetimes, and the

difference in acceptance between charged and neutral decays. The standard KTeV $\mathrm{Re}(\varepsilon'/\varepsilon)$ analysis utilizes a detailed Monte Carlo simulation to correct for the acceptance differences. The acceptance correction is on the order of 90×10^{-4}, which is large compared to the value of $\mathrm{Re}(\varepsilon'/\varepsilon)\sim 20\times10^{-4}$.

As a check of the standard analysis, we lead a small group, including two postdocs from Fermilab, to perform an alternate analysis of the 1997 $\mathrm{Re}(\varepsilon'/\varepsilon)$ data. To correct for the acceptance, we used a reweighting method, similar to that used by the NA48 experiment. In this method, the K_L decays are reweighted so that the K_L decay distribution matches the K_S decay distribution. Since K_S and K_L decays with the same p and z nominally have the same acceptance, the acceptance will cancel in the ratio of reweighted K_L to K_S decays, and reliance upon any Monte Carlo is reduced. The effect of this reweighting can be seen in Figure 1. Before reweighting by the proper lifetime, the track illuminations between the K_L and K_S decays are very different. However, after reweighting, the two track illuminations show excellent agreement.

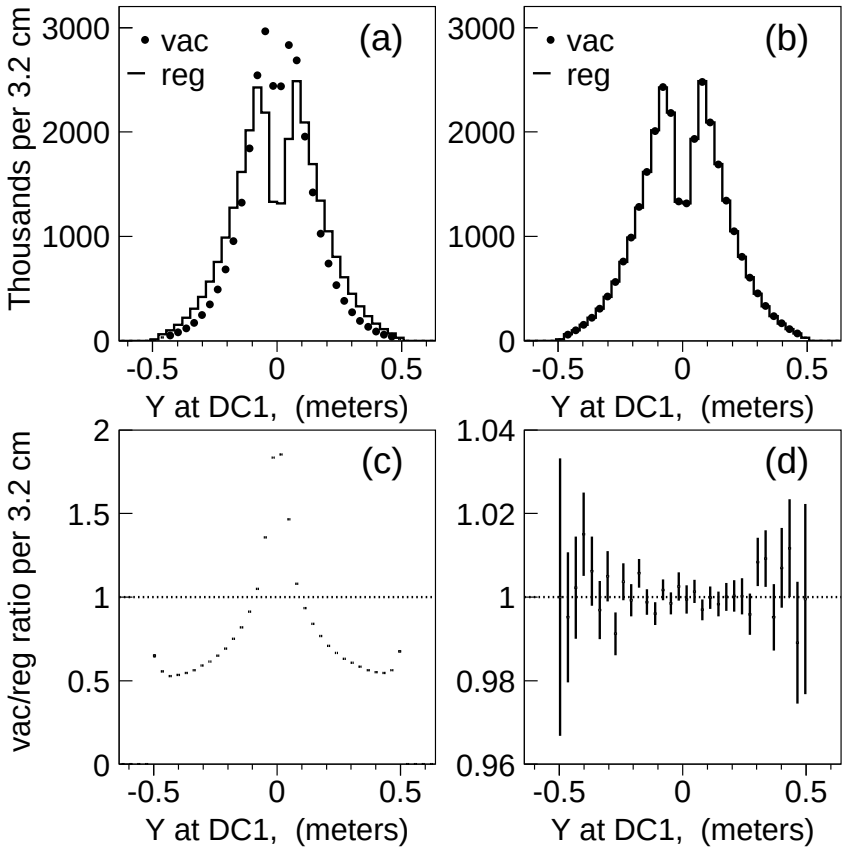

Figure 1: Track illuminations for events a) before and b) after applying the reweighting function for $K_L\to\pi^+\pi^-$ events. The dots represent the KL decays while the K_S decays are the histogram. The K_L/K_S ratio is shown in c) and d). Note the different vertical scales for plots c) and d).

One disadvantage of this reweighting method is that the K_L events far downstream of the target receive a very low weight. Also, decays upstream of the KTeV regenerator are not used. In the standard analysis these upstream events are included. These two effects increase the statistical error on $\mathrm{Re}(\varepsilon'/\varepsilon)$ by a large amount compared to the standard analysis. We found that the statistical error using the reweighting method is approximately 1.7 times worse than in the standard KTeV analysis. However, given the discrepancies between the earlier KTeV and NA48 experiments, a second analysis of the KTeV data remains very important.

Using the reweighting method, our group determined $\mathrm{Re}(\varepsilon'/\varepsilon) = (21.32 \pm 2.90 \pm 3.98)\times 10^{-4}$. The U. Chicago analysis found $\mathrm{Re}(\varepsilon'/\varepsilon) = (19.8 \pm 1.7 \pm 2.4)\times 10^{-4}$. The increase in the statistical error results from the loss of sensitivity introduced by the reweighting method. In principle, the systematic errors of our method should be comparable if not better than the Monte Carlo based method. However, we found some parts of the analysis were unexpectedly sensitive to the selection criteria. In spite of these issues, the good agreement between the two KTeV methods helped to increase the confidence in the recent KTeV result. This analysis has been included in a paper recently published in Physical Review D.[3]

Measurement of BR($K_L \to e^+e^-\mu^+\mu^-$)

The $K_L \to e^+e^-\mu^+\mu^-$ decay proceeds via a two-photon intermediate state, and, therefore, contains information about the $K_L \to \gamma^*\gamma^*$ form factor. Knowledge of this form factor, along with the $K_L \to \mu^+\mu^-\gamma$ branching ratio, can be used to compute the CKM matrix element V_{td}. In addition, it has been suggested that if a CP violating component of the $K_L\gamma\gamma$ vertex exists, its contribution can be measured by analyzing the angular distribution between the e^+e^- and $\mu^+\mu^-$ decay planes in the $K_L \to e^+e^-\mu^+\mu^-$ decay. Furthermore, the same data set can be used to search for lepton flavor violation via the decay $K_L \to e^\pm e^\pm \mu^\mp \mu^\mp$.

The first KTeV analysis of this decay mode only used our 1997 data, resulting in a sample of approximately 40 candidate $K_L \to e^+e^-\mu^+\mu^-$ events. The E799-I experiment had seen one candidate event. For the 1999 data, studies by J. Hamm indicated that simultaneously modifying the trigger and lowering the magnetic field would increase the acceptance for this mode by about 20\%. We recently completed the analysis of the combined 1997 and 1999 data sets resulting in a final sample of 132 events. The final resulting invariant mass distribution is shown in Figure 2, with a clear peak at the kaon mass, and very little background. With this data set we have been able to make the first measurements of the $K_L \to \gamma^*\gamma^*$ form factor using this decay mode. The results are consistent with other measurements from $K_L \to \mu^+\mu^-\gamma$ and $K_L \to e^+e^-e^+e^-$. Other

measurements including searching for CP violation in $K_L \to e^+e^-\mu^+\mu^-$ and lepton violation via $K_L \to e^\pm e^\pm \mu^\mp \mu^\mp$ have been performed, although there is no evidence for either phenomenon. This work was recently published in Physical Review Letters.[4] J. Hamm completed his thesis on this topic in 2002.

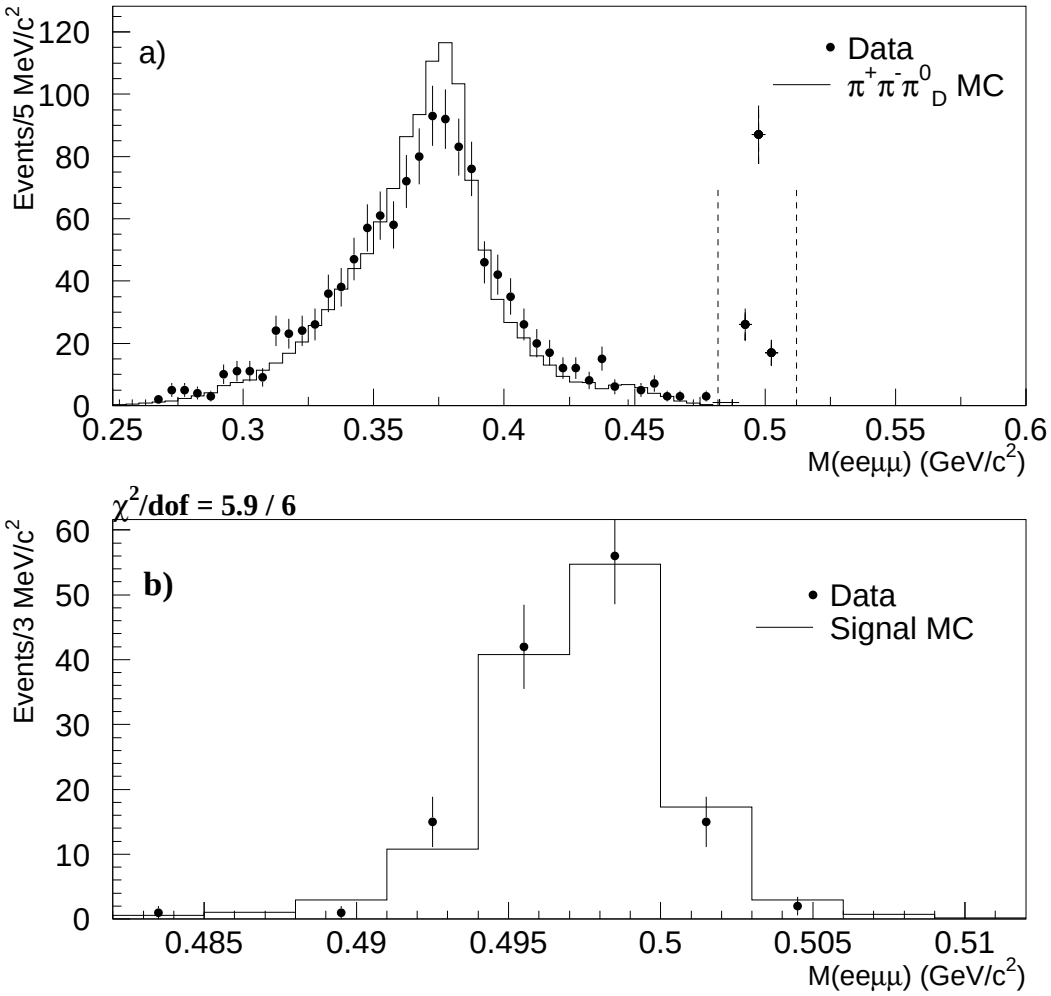

Figure 2: Reconstructed (eemm) mass for KL-> eemm candidates.

Measurement of BR($K_L \to \pi^0\gamma\gamma$)

One of the main goals of the KTeV rare decay program is to search for the decay, $K_L \to \pi^0 e^+e^-$. This decay mode contains a direct CP violating amplitude and measuring this mode would provide another means for discovering direct CP violation. The $K_L \to \pi^0 e^+e^-$ decay also contains a CP conserving amplitude, and measuring $K_L \to \pi^0\gamma\gamma$ is important for untangling this contribution.

The Arizona group was responsible for analysis of the 1996-1997 $K_L \to \pi^0\gamma\gamma$ data. In our analysis we found approximately 800 $K_L \to \pi^0\gamma\gamma$ events, an order of magnitude improvement over the previous world sample. Using this sample of events, we calculated a branching ratio of $(1.68 \pm 0.06 \pm 0.08)\times 10^{-6}$ to be compared with the previous measurement of $(1.70 \pm \pm 0.3)\times 10^{-6}$. In the 1996-1997 data, we determined a_v = $-0.72 \pm 0.05 \pm 0.06$. This variable parameterizes the level of vector meson contributions to the $K_L \to \pi^0\gamma\gamma$ and is significant since the level of CP conserving contributions to $K_L \to \pi^0 e^+ e^-$ has a strong dependence on the value of a_v. Our work on the 1996-1997 data set was published in Physical Review Letters. [5] Figure 3 shows the $\gamma\gamma$ invariant mass distribution for our candidate events. Recently, the NA48 group has published [6] a result which is somewhat in disagreement with our 1999 result. They find BR($K_L \to \pi^0\gamma\gamma$) = $(1.36 \pm 0.5)\times 10^{-6}$.

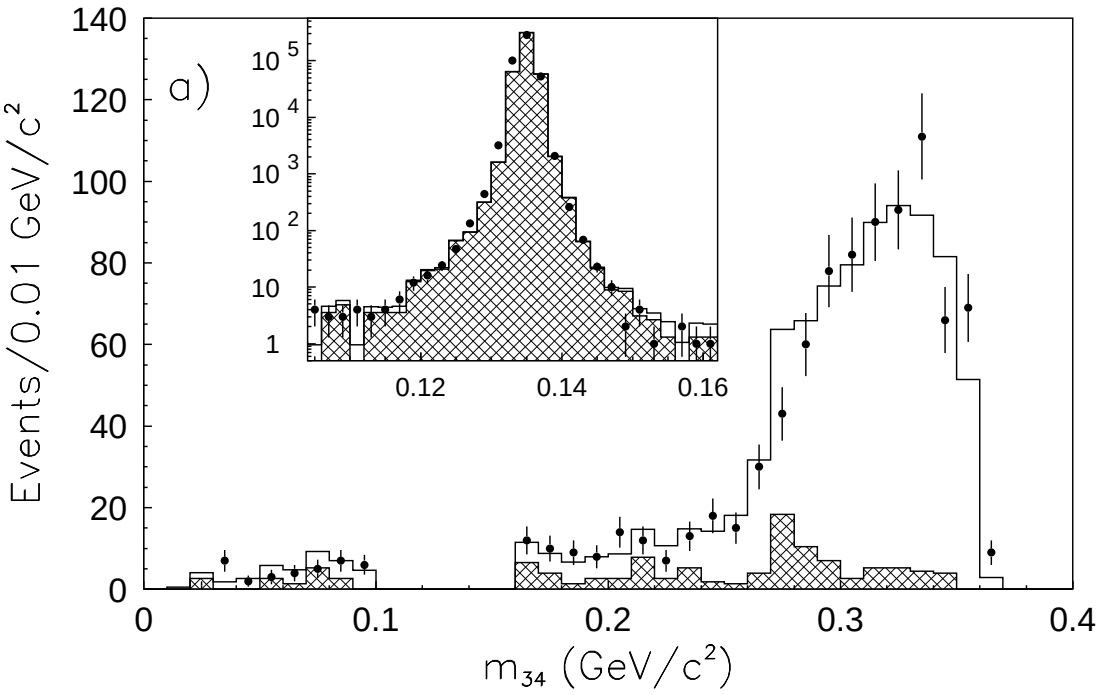

Figure 3: Invariant $\gamma\gamma$ mass distribution for $K_L \to \pi^0\gamma\gamma$ candidates. The dots are the data, while the histogram is the Monte Carlo. The hashed area represents the sum of $K_L \to \pi^0\pi^0$ and $K_L \to \pi^0\pi^0\pi^0$ events. The inset shows the excluded region from 0.1-0.16 GeV/c^2 which is dominated by $K_L \to \pi^0\pi^0$ events.

J. Wang has been working on the combined 1996-1999 data set. To date we find our 1999 data consistent with our previous result, and have not discovered any reason for the discrepancy between the NA48 and KTeV results. We have also been concentrating on better understanding the backgrounds to the $K_L \to \pi^0\gamma\gamma$ signal.

Future KTeV Plans

For this proposal we plan to complete the analysis of the $K_L \to \pi^0\gamma\gamma$ data set. By including the 1999 data, we should be able to obtain a result with comparable statistics to the NA48 result. We are only requesting funding to support travel to regular KTeV meetings and to support the computer infrastructure required for the $K_L \to \pi^0\gamma\gamma$ analysis.

References

[1] A. Alavi-Harati *et al.*, Phys. Rev. Lett. **83** 22 (1999).

[2] V. Fanti *et al.*, Phys. Lett. **B465**, 335 (1999).

[3] A. Alavi-Harati *et al.*, Phys. Rev. **D67** 012005 (2003).

[4] A. Alavi-Harati *et al.*, Phys. Rev. Lett. **90** 141801 (2003).

[5] A. Alavi-Harati *et al.*, Phys. Rev. Lett. **83** 917 (1999).

[6] A. Lai *et al.*, Phys. Rev. **B536** 229 (2002).

III.3 ATLAS at the LHC

It is now almost 10 years since we joined the ATLAS collaboration and took the task of providing the liquid argon forward calorimeters (FCal). In the following sections we describe 1) how it all began, 2) the unique features of the ATLAS forward calorimeter system, 3) the challenges and responsibilities we chose, 4) the ATLAS forward calorimeter construction project, 5) related R&D projects, 6) the various test beam runs to prove the concept and to provide input into various detailed decisions, and 7) the various checks and tests we are performing to verify that the FCal will work properly in the new high luminosity environment of a hadron collider.

III.3.1 A bit of history

We like a challenge. The one component of a collider detector which must operate in the harshest radiation environment is the forward calorimeter. We set out to develop an approach to provide the best calorimeter performance under the worst conditions. We soon converged on liquid argon calorimetry because it is inherently radiation tolerant.

In 1989 the Arizona group submitted an R&D proposal to the DOE to develop techniques for robust liquid argon calorimetry to meet the challenges of high luminosity hadron colliders. But recognizing that the positive Argon ions could build up in a conventional 2 mm liquid argon gap and distort the electric field (and therefore the signal), we focused on significantly smaller gaps to avoid this problem. Once funded, we began what led to the forward calorimeter concept for ATLAS using a novel electrode structure with a number of benefits.

Along the way we produced a prototype for the GEM forward calorimeter which we tested in a beam at Brookhaven in the summer of 1993. Then, at the invitation of ATLAS people at CERN, we took this prototype to the CERN North Area to try out higher energies. We were sitting at our data acquisition computer witnessing excellent performance from our device as Congress killed the SSC in October of 1993. Flush with our own success but devastated by the loss of the SSC, we made discreet inquiries about joining ATLAS. While members of the ATLAS liquid argon community were encouraging, the ATLAS decision makers were more cautious. We worked up our test beam data and made a presentation to the ATLAS Calorimetry Panel in January of 1994 at CERN. This Panel was charged with recommending to the collaboration which technologies were best. The Panel had nearly finished its work. The forward calorimetry decision was all that remained and that was nearly completed. Three Russian groups had coalesced their competing proposals and had produced a credible scenario using a high pressure gas ionization device located far downstream from the interaction point (IP). When we presented our test beam data, we suggested that our device might be located closer to the IP but we didn't sketch out a full proposal. The Panel was not impressed and gave a tentative nod to the Russians with a caveat. “If some group can make the case for a smaller forward calorimeter closer to the IP then we would be interested in hearing it.”

While disappointed that our test results didn't generate more interest, we at Arizona took

this as a challenge. We had already developed what became known at the "Integrated Forward Calorimeter" for GEM. The concept was an even better match to the ATLAS detector layout. It included not only the novel electrode structure using liquid argon technology but also a powerful scheme to 1) minimize backgrounds in the sensitive muon system (approximately two orders of magnitude better), 2) provide significantly better position and energy resolution due, in part, to fewer significant transitions going from one calorimeter structure to another, 3) far more practical experiment-wide shielding configurations, 4) much easier access to the inner parts of the detector, 5) larger $|\eta|$ coverage, and 6) a much smaller device allowing higher quality with a much lower overall cost. Figure III.3.1 shows the FCal "tube" electrode structure.

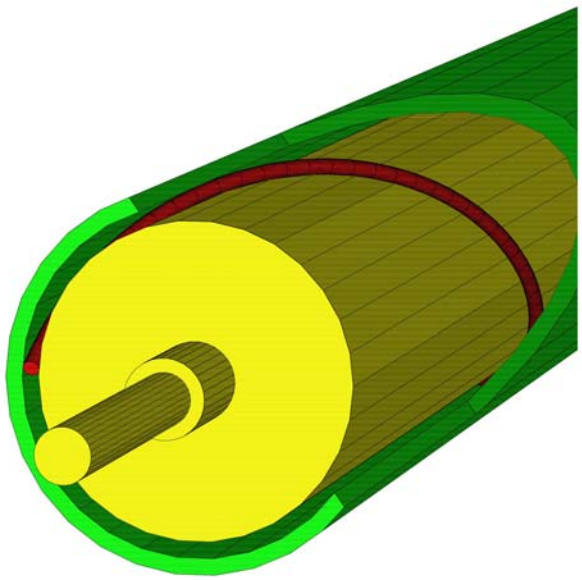

Figure III.3.1: A GEANT-generated cut-away view of the end of one of the 12,260 electrodes for each (of two) of the electromagnetic FCal modules. Liquid argon fills the gap between the outer tube and the inner rod. A helically wound PEEK fiber electrically insulates the rod from the tube. Charged particles in showers ionize the Argon atoms. The electrons then drift in the electric field to the rod. The electrical pulse is picked off the connector pin in the end of the rod.

Our technology was manifestly radiation hard and we were able to positively demonstrate that it would not only survive the highest luminosities at the LHC but would also provide exceptional performance. Other groups were pushing technologies they claimed would be "adequate" or "good enough".

We prepared several reports for the next Calorimetry Panel Meeting in March of '94. One of these laid out the Integrated Forward Calorimeter concept and the others provided supporting material. These were well received but there was clearly skepticism by some Panel members. The Panel responded with a list of seven rather probing questions and gave us an unrealistically short time to provide answers. They apologized for this but explained they were forced to make their decision before the end of the summer. We went into crash mode. We initiated several studies at once and enlisted help from most of our group. But in addition we were able to contract for help from contacts at Martin Marietta and Los Alamos on some practical matters. We were also helped by Hans

Hoffman, the new ATLAS Technical Coordinator, who understood (better than the physicists) the problems faced by shielding, access, etc.

Figure III.3.2: Each FCal1 module is made up of a stack of 18 matrix plates, each with 12,260 holes. These holes all line up when the plates are stacked. Each plate is 25 mm thick. After the matrix is assembled, a 450 mm long electrode is inserted into each hole. Three such matrix plates are shown here. The large hole in the middle of each plate is where the accelerator beam pipe passes through the FCal.

About this time our Russian competitors were joined by Nikos Giokaris from Rockefeller who had been pushing high pressure gas for some time. Much to his credit he had lots of test beam results, something the Russians had little of. But by this time we were beginning to convince even the skeptics that our scheme provided considerable advantages for the whole experiment. We were proposing not just a detector technology but a rather comprehensive concept for the ATLAS detector which fit comfortably into the existing framework. Not much of the ATLAS concept required changing (by chance) but we provided a well-conceived rationale for what was previously a somewhat haphazard design-by-committee.

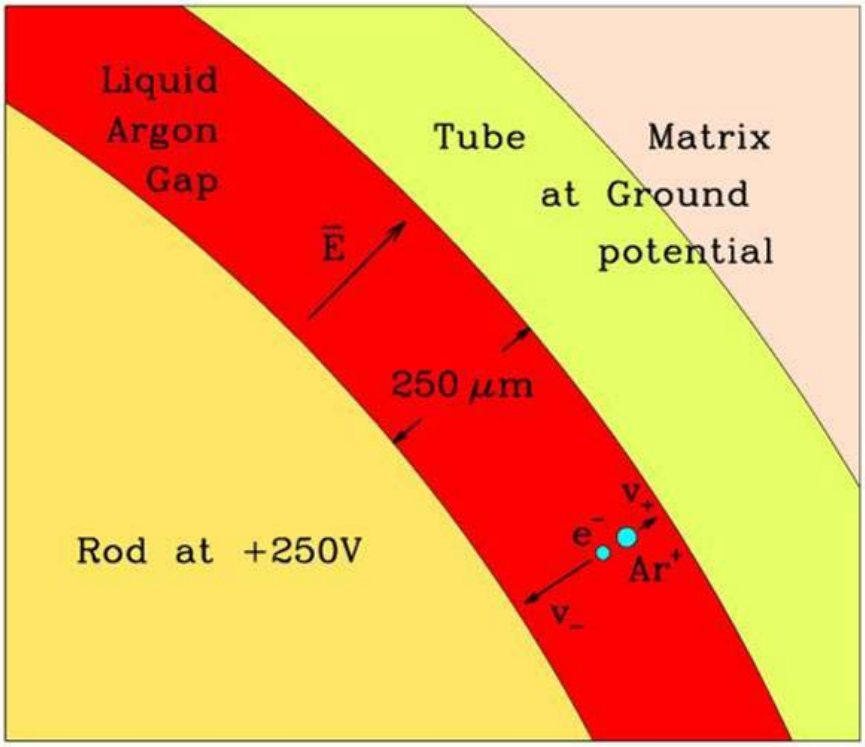

Figure III.3.3: This extreme closeup of the narrow (about 250 μm) liquid argon gap shows one ionized Argon atom. The electron is drifting towards the rod in an electric field of 1 kV/mm. The positive Argon ion is drifting towards the tube wall at a velocity about 10^4 times slower.

We were unaware of the Panel's views when Shupe, Shaver, and Rutherfoord met with the Committee at CERN in late June to present the answers to their questions and results of further studies we'd performed. We spent most of the day giving talks and there was lots of discussion. We were lucky that some of the experts the Panel had assembled agreed with our assertions. (Leif Shaver and John Rutherfoord had brought a Geiger Counter along and had taken readings on the airplane. This led to a mini-tutorial on radiation exposure in which many committee members were very interested but had little background, much to our surprise. We were amused that they preferred we use units of rads and rems rather than Grays and sieverts.) In mid-afternoon the Panel invited us to leave so they could confer privately. We were invited back in an hour and we listened to the chair explain their decision. After about 20 minutes we still didn't know the outcome. It was only when the chair turned to the Russians and asked what they wanted to contribute to ATLAS, now that their high pressure gas forward calorimeter was no longer favored, that we understood the result.

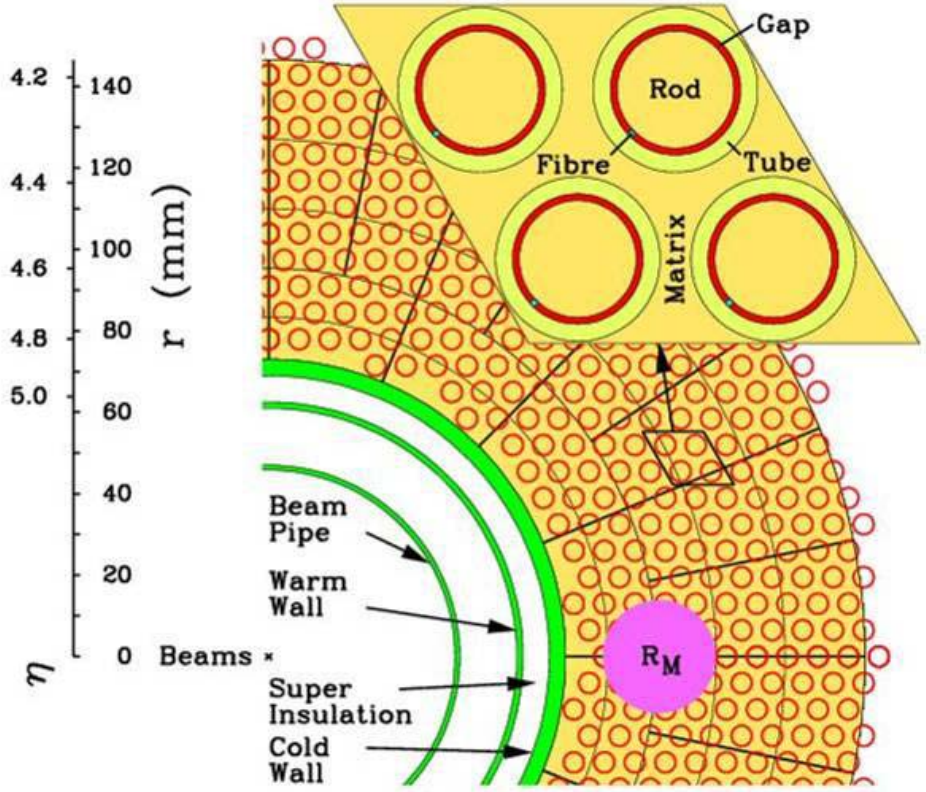

Figure III.3.4: A close-up drawing of the front face of one electromagnetic FCal module. The small open circles represent the tube electrodes. The larger filled circle (labeled R_M) shows the size of the Moliere Radius. The module extends outward (not shown) to a radius of 450 mm. The accelerator beam tube and the warm and cold walls of the cryostat are indicated. A blow-up front view of four electrodes appears at the upper right.

We were then asked to form a collaboration and to head the forward calorimeter effort within ATLAS.

Arizona became famous as a US group which was able to contribute more than just technical expertise and resources to ATLAS. We had shaped the ATLAS detector in a fundamental way, leaving our imprint on the overall design of the experiment. Since then we've completed three test beam runs (on schedule), we've completed the module production at Arizona, and we're in the midst of the "final assembly" phase at CERN. The intensely competitive technology wars of 1994 are now well behind us.

Figure III.3.6 shows not only the forward calorimeter within the ATLAS detector but also its relationship to some of the other systems which the "Integrated Forward Calorimeter" concept affected. These include the massive shielding, the inner regions of the end cap

toroids, and the high |η| edges of the muon chambers.

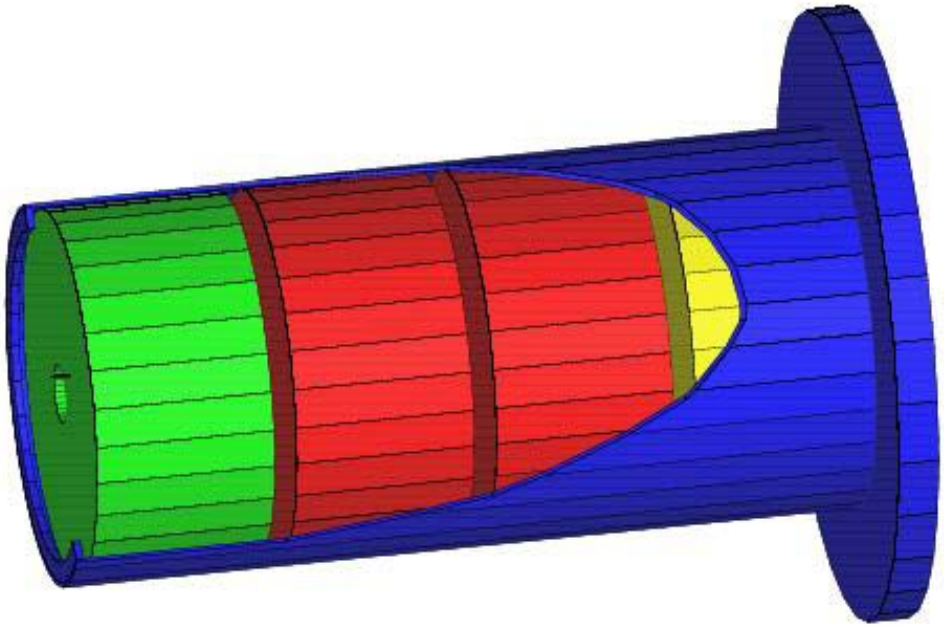

Figure III.3.5: Each of the two ATLAS Forward Calorimeters is composed of three modules. From left to right they are as follows: FCal1 is the "EM" module facing the IP. The absorber material is copper. FCal2 is the first hadronic compartment with absorber material of tungsten. FCal3 is the second hadronic compartment, also of tungsten. Following these modules is an uninstrumented "plug" to help in shielding the muon system. The three modules and plug are shown in a GEANT generated drawing inside the support tube which is a structural member of the endcap cryostat.

III.3.2 The Arizona Personnel Involved in ATLAS

Professors Michael Shupe and John Rutherfoord lead the Arizona involvement in ATLAS. Research Scientist Peter Loch joined Arizona in 1992 as a post doc and devotes full-time to the ATLAS FCal project. Salaries for these physicists are paid by the university and by this grant. Engineer Leif Shaver joined us in 1989 and works full-time on the ATLAS FCal project. He is the technical coordinator for the whole FCal project and heads the engineering at Arizona and the collaborating institutions. His salary is paid by the University. Daniel Tompkins is an electronics engineer who is overseeing the FCal cold electronics. His salary is paid partly by the University and partly by this DOE grant. In past years the non-University portion of his salary was sometimes paid by our LHC funding. Alexandre Savine is a technical programmer with physicist training who joined us in 1993. His salary is paid by our LHC funding. A number of short-term technical staff have worked with us on the FCal project. These include Deborah

Koolbeck, Teresa Embry, Peter Truncale, Kenneth Green, and Michael Starr. These people are or were all paid by LHC funding although Teresa Embry has, at times, been paid by this grant by special arrangements between P.K.Williams and Bill Willis of Columbia University who is project manager for the U.S.ATLAS contribution to ATLAS.

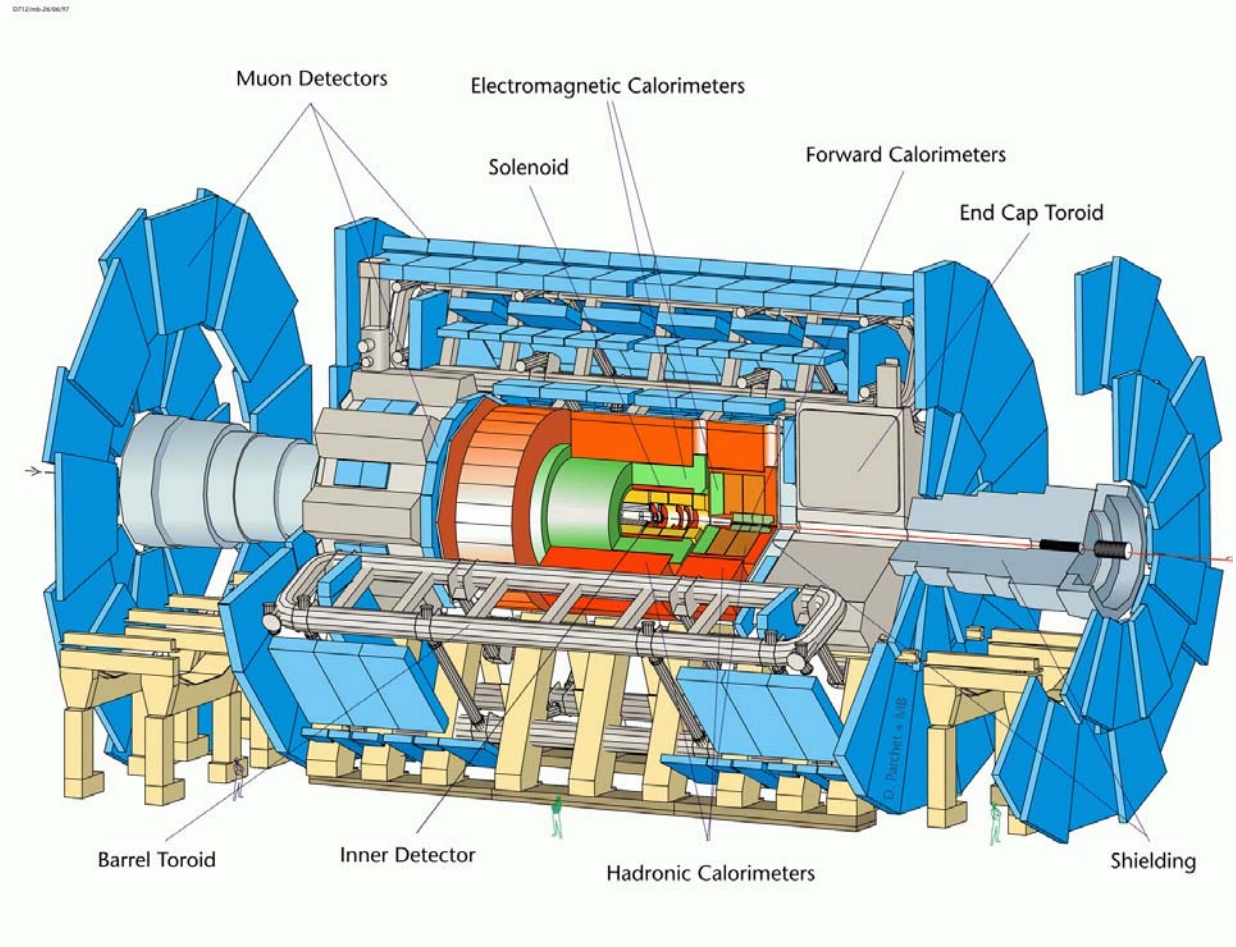

Figure III.3.6: The full ATLAS detector with parts cut away at one end to reveal the forward calorimeters. Also shown is the massive shielding which provides sufficiently low backgrounds in the muon chambers to keep occupancy to acceptable levels and yet allows muons coverage out to $|\eta| = 2.7$. For scale, notice the people on the floor of the cavern.

Over the years a large number of very enthusiastic undergraduate students have worked on various aspects of the FCal project. The largest effort went into the module construction. All student labor was carefully supervised with strict QC guidelines. Teresa Embry, through her high standards and insistence on producing the best result possible, has instilled in our students an impressive degree of diligence. They all feel appreciated and show unusual dedication to the success of the FCal1 modules. All student labor was paid by our LHC funds.

III.3.3 The FCal Construction Project

Arizona receives LHC funding from the DOE for the ATLAS FCal project and related work. The total FCal project cost will be a little over $3M spread over the years through FY 2004, with a sharp peak in the years 1999 and 2000. Small additional funds cover test beam runs and some help we provided Brookhaven on preamplifier testing, now complete. Here we define the scope of this effort.

Arizona has specific construction responsibility for the two FCal1 modules and all of the FCal cold electronics. This includes the concept, design, construction, installation, debugging, commissioning, operation, and maintenance. It also includes conceptual design of the FCal2 and FCal3 modules and the final assembly procedures and tooling at CERN. The LHC funding covers tasks and deliverables through the commissioning phase.

When Arizona established the ATLAS FCal group and invited Canadian and Russian groups to join, we defined the responsibilities as above for Arizona. Our Canadian colleagues (Bob Orr and group at University of Toronto and Gerald Oakham and group at Carleton University) have constructed the FCal2 and FCal3 modules to our conceptual design and our Russian colleagues (Valerii Khovansky and group) have provided the tungsten rods for FCal2 and FCal3. (When it became apparent that ITEP would have financial difficulties in fulfilling all of its commitments, Rutherfoord arranged for Professor Ting-Yang Chen and his collaborators in a consortium of universities centered around Nanjing University, to fill the gap.) All groups are participating in the installation and commissioning. Arizona provides project management as well. John Rutherfoord is the leader of the effort and Leif Shaver is the chief engineer.

Arizona also provides the technical leadership for the project. Weekly conference calls allow the FCal collaborating institutions to work coherently and to share information. We have led the various test beam runs as described later and all the data analysis to date has taken place at Arizona. (We expect our Canadian and Russian colleagues to take a role in data analysis in the future.)

Because the FCal construction project is funded separately from this University Grant, we will weight our progress discussion a bit on the side of those aspects of our ATLAS involvement not completely covered by the project funds. These include the more intellectual aspects of the FCal development and much of the R&D. But because the physicists (supported on the base program) have devoted a lot of time to the construction project we will report this activity too.

III.3.4 FCal Modules

After years of design work, reviews, costing exercises, and detailed planning, we started construction of our FCal1 modules in March of 2001. The copper matrix plates (see

Figures III.3.2 and III.3.7) started to arrive from the contracted machine shop. The first step was to check that these plates all met the specifications. A set of measurements determined our acceptance criteria and these measurements are all now stored for posterity. These measurements included the inner and outer diameters, the thickness, and flatness of the plates. We also carefully checked a large sample of electrode holes to make sure their diameters were within geometric tolerance. Most importantly, we stacked pairs of plates to check that the holes lined up.

Next the plates were carefully cleaned in a three-stage process and any remaining machining "whiskers" were removed. Each plate has a unique serial number stamped on the outer periphery which allows us to track it through the full construction process. The plates were then stacked one next to another in our clean room on a specially constructed "carrier" and bolted together.

In parallel with the preparation of the matrix plates, we kept our electrode tube processing assembly line moving. Upon delivery, a sample of tubes was carefully measured to determine if they met the specifications. The liquid argon gap is determined by the ID of the tube and the OD of the rod so these dimensions are particularly important to us. All of these measurements were recorded through a computer interface and analyzed. A description of these measurements, the data itself, and all the various analyses of these data have been written up in a polished form for future reference. While the tube manufacturing company would not bid on our job if we specified too tight a tolerance on the ID, we knew from experience that they were able to far exceed the tolerance they would agree to. Our measurements on the production tubes bore this out.

We next removed the occasional burrs left when the manufacturer cut the tubes to length. Then the tubes were left to soak in a kerosene solution to soften the drawing compound left from the manufacturing process. We then passed all the tubes through a rigorous 6-stage cleaning procedure, each step of which is carefully specified so that different crews perform the exact same procedures. Particularly difficult was to remove this drawing compound from the inside surface of the tubes. Embry researched this problem ahead of time and developed the procedures and standard tests. If tubes failed the inspection tests after a first cleaning then they were recycled through the full cleaning procedure again.

By the time the matrix plates were stacked we has a stock of cleaned tubes stored in sealed tubs with dry nitrogen gas circulated throughout. By the summer of 2001 we were inserting tubes into the FCal1C matrix. (FCal1C is the first of the two modules. FCal1A is the second.) The matrix plate at the read-out end of the module has special swage groves machined into the tube holes. Each swage groove had a ridge in the center of the groove to cut into the OD of the tube when it is "swaged" into place. A custom-designed and produced "swage gun" was used to expand a short section of the tube into this groove to make a positive electrical contact with the matrix. We had a lot of trouble with this swage gun. We were able to insert and swage a little over 100 tubes per day.

When all the tubes were inserted into the matrix and swaged into place, we swabbed each tube, again, by a specified procedure, and inspected the swab to check for grime, debris,

or particulate. If there was any sign of such contamination, we repeated the swabbing procedure until the tube passed.

When the electrode rods were delivered we conducted the same exacting metrology on them. But in this case the job was easier because there was only the OD and length to measure, no ID. As before, OD measurements were taken on a sample of rods at six locations and angles along the rod. Again we were very pleased that the dimensions of the rods were well within the specified tolerances. The bottom line on all these measurements of the tubes and rods is that we predict the liquid argon gap to be precise to better than 3%. The reason for the upper limit is that our measurement precision enters into the estimate. (See section III.3.6 for additional measurements of this critical parameter.)

In parallel with the preparation of the matrix and tubes, we had our machine shop drill a hole in the end of each rod. Into this hole the readout pin is inserted at a later time. Rods, returned from our shop, were then sent through the same cleaning procedure as our tubes. We had less trouble with the rods because it is easier to clean an outer surface than an inner surface. After cleaning, the rods were "pinned" (i.e. the signal pins were inserted into the holes) and then stored in similar sealed tubs with dry Nitrogen atmosphere.

By the time the tubes were inserted into the matrix we had a sufficient stock to start the next step of the assembly procedure. The PEEK fiber, located on a spool conveniently suspended next to the module, was affixed to the signal pin of a rod and the rod was then inserted into a tube in the matrix. During insertion the rod was rotated so that between 12 and 14 windings of the PEEK fiber were distributed along the length of the electrode. The picture in Figure III.3.7 is a close-up of the matrix taken during rod insertion. This operation started in October of 2001 and extended through February of 2002.

After several rows of rods were inserted we subjected them to our HV test. The nominal high voltage in the liquid argon is 250 V. But we find that our electrode structure is so robust that we can run a typical electrode up to about 1300 V before it breaks down. However this is not true of all electrodes. Some have minute particulate in the gap which leads to breakdown at lower potentials. We defined our HV test such that we subject the electrode to 600 V for a short time and check the current draw. In the dry Arizona air the current draw is typically below a microAmp (but in the damp CERN atmosphere a good electrode might draw tens of microAmps). If an electrode draws current in the milliAmp range we pull the electrode apart, swab the tube, wipe the rod, and replace the PEEK fiber. Then we re-assemble the electrode and try the HV test again. This has proved to be a critical test and it is not easy to get all 12,260 electrodes to pass this test at any given time.

In September 2001 the matrix plates for the FCal1A module started to arrive and we started our metrology and cleaning procedures on them in parallel.

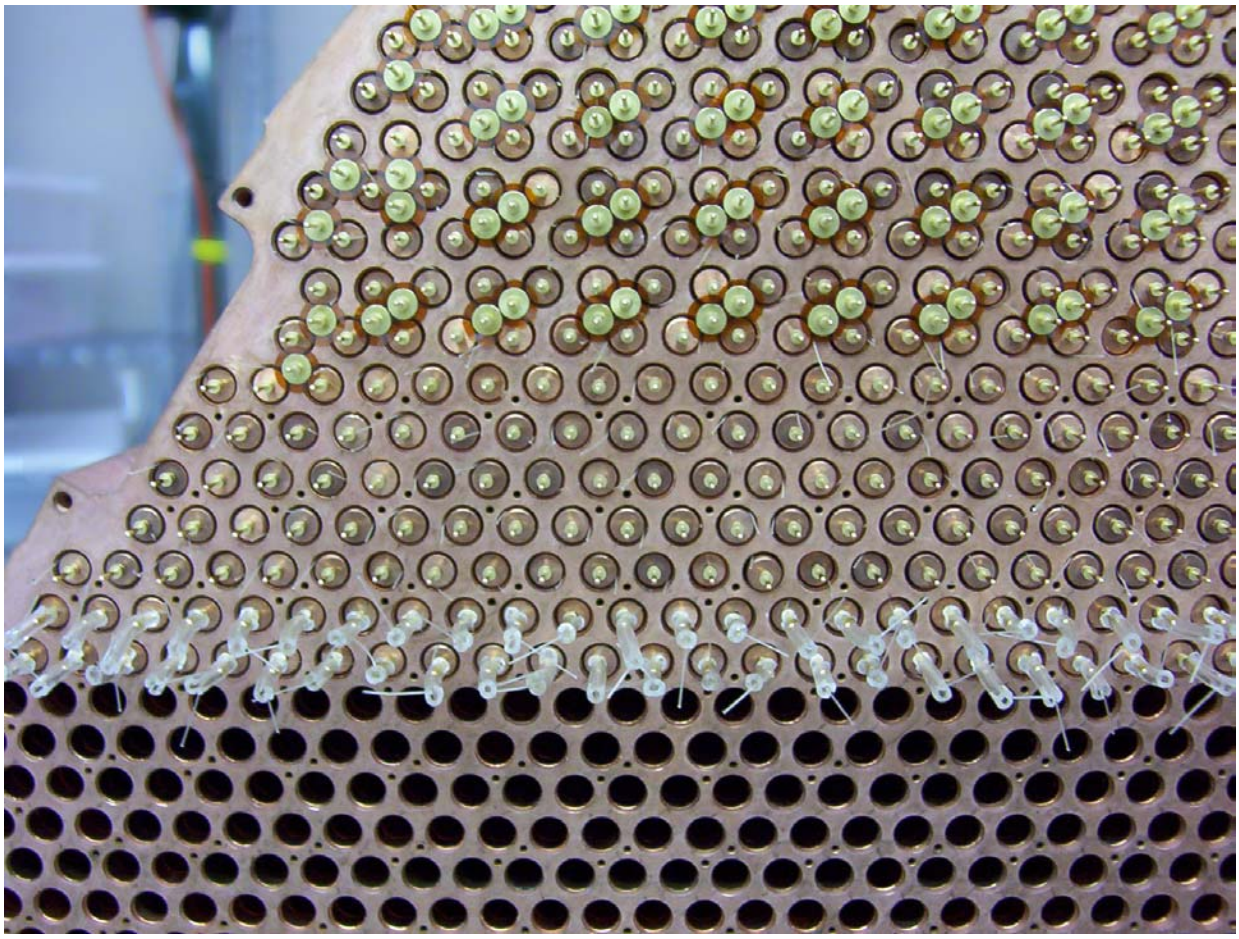

Figure III.3.7: Photograph of the face of the FCal1 "EM" module showing the progression of electrode insertion. At the bottom of the picture only the tubes (which don't show very well in this picture) have been inserted and swaged into groves in the end plate for good electrical contact. Above this are two rows of rods which have just been inserted. Each still has the tygon tubing on the readout pin which holds the PEEK fiber wound in place. The next five rows above this are of tubes which are undergoing HV testing to check that they are properly insulated from the tubes and matrix. In the upper portion of the picture the electrodes are completely assembled. The washers and ground pins are in place. To set the scale, the distance between nearest neighbor electrodes is 7.5 mm.

The FCal1C module was officially completed on 25 February 2002 but we kept repeating the HV tests for quite a while trying to rid the module of any failures. For this extended testing we built a special, small cleanroom so that we could make space to start construction on FCal1A in the regular clean room. The stacking of the FCal1A matrix started in April and was completed in June.

We shipped the FCal1C module to CERN in mid-June. We found that US ATLAS has no policy on shipping insurance so we decided to insure the module for $1M. It would not be possible to recover from catastrophic loss because schedule delay would be the

most serious consequence. But insurance would help us recover from damage less severe than full loss of our module. The cost of the insurance was about $4500.

As the FCal1C module was delivered to the North Area at CERN the fork-lift operator dropped the module on its end. He failed to position the crate against the ends of the forks and the fork-lift truck started to tip forward under the weight. The crate slipped off the ends of the forks and flipped over 90 degrees, falling a distance less than 1 meter to the ground. We had debated about what precautions to take against rough handling and how robust our shipping container should be. We ended up with a steel-tube box frame with a shaft through the beam hole of the module. The module was held on this shaft via two expansion hubs, one at each end. The crate fell with the shaft vertical. We were slow to unpack the damaged crate because we didn't want to void the insurance. So only after a representative from the insurance company arrived, about a week later, did we remove the sides of the crate to look inside. Despite an accident far more severe than we had ever imagined, there was little damage. The expansion hubs gave a bit and the module slid down the shaft about 30 mm. But the module did not hit the steel tube frame. A few electrode rods fell out of their tubes but there was little other damage. It delayed us about two months and required some extra manpower to repair the electrodes. We also had additional HV failures, probably due to the accident. And because we planned to re-use the steel-tube box frame, shaft, and hubs, some repairs to these were also necessary. The insurance company paid our claim of $20k and they are now trying to collect damages from the rigging company.

After the cycle of HV tests and electrode repairs converged we returned to our planned activity. This included capacitance measurements of the electrodes. These are discussed in the section on electrical tests below.

The FCal1C module was then cabled up. Four electrodes are ganged together via a connector with sockets which slip over the pins in the electrode rods and ground pins in the matrix. Also attached to this connector is a 25 Ω cable which carries the signal to the electronics. The FCal2C and FCal3C modules also arrived at CERN from Canada and were cabled up. In November of 2002 we conducted a "cold test" of the three modules. For this test we connected the HV, placed the modules into the H1 cryostat, filled it with liquid Argon, and ramped up the HV to its nominal value of 250 V. During this test the FCal1C module developed 10 shorts. At the end of the test we turned off the HV and then turned it on again. Three shorts went away but five new ones appeared for a total of 12 shorts.

At the next meeting of the ATLAS Liquid Argon group all the subsystems were asked to summarize the results of their cold tests. As a fraction of the volume each subsystem within the liquid Argon group had approximately the same percentage of dead volume of about 0.3%. But we were not satisfied. Embry, who spent the year at CERN, went over the whole FCal1C module again and again carefully cleaning and HV testing every electrode. She finally began to understand the origin of the failures and how to avoid the problem. During the recent test beam run, reported below, we repeated the "cold test" and found only one short out of the 12,260 electrodes. This is extraordinarily good,

almost too good to believe. We don't expect to be able to repeat this performance. But we are hopeful that the FCal will be a bit better than the other subsystems in terms of HV failures.

During the work on the FCal1C module at CERN, the FCal1A module made good progress back at Arizona. The home team repeated the same procedures already polished on the FCal1C module. All tubes were inserted into the FCal1A matrix by the end of July 2002 and all were swaged by the beginning of September. The rigorous tube swabbing was completed by the beginning of November. Electrode rods were prepared in parallel and rod insertion started immediately. HV testing was done during insertion and the whole procedure was concluded by 18 February 2003. This was the official end date of module construction. The FCal1A module was shipped in mid-March and arrived at CERN by the end of March without mishap. HV tests, capacitance measurements, and cabling have now been completed. We are presently in the midst of mapping checks and reflection tests.

III.3.5 FCal Cold Electronics

Key to the success of the newest generation of liquid argon calorimeters is the ability to cleanly (this means with low inductance) pick the small electronics signals off the electrodes and quickly transmit them to the remote front-end electronics outside the cryostats. The necessary small gap in the ATLAS FCal leads to high capacitance electrodes and demands low impedance cables. The need to reduce the electronics channel count requires summing electrodes together which further increases the effective electrode capacitance, exacerbating the problem. However we do this summing via an optimal, elegant, and simple method which matches the impedances of the cables and increases the noise by only the square root of the number of channels. We employ transformers which usually lack the high frequency bandwidth required in these applications. However an old technique, unknown to most modern electronics people, employs a "transmission line" transformer which has some excellent features including channel-to-channel uniformity. Being completely passive, it is possible to do this summing inside the cryostat with little overhead. This is the scheme we've adopted. The summing is performed on "transformer summing boards" which are a part of the cold electronics, the other major Arizona responsibility. These boards are positioned at the downstream end of the cryostat at a radial distance just outside of the FCal. The HV distribution is done on these same boards. There are 28 such boards at each end of ATLAS.

A big advantage of our transformer summing scheme is that it allows us to mate to the same electronics readout adopted by the rest of the liquid argon calorimeter system. The only differences are 1) the level 1 trigger sums are different from *every* system and 2) our calibration signals will be introduced directly into the preamps rather than at the electrodes.

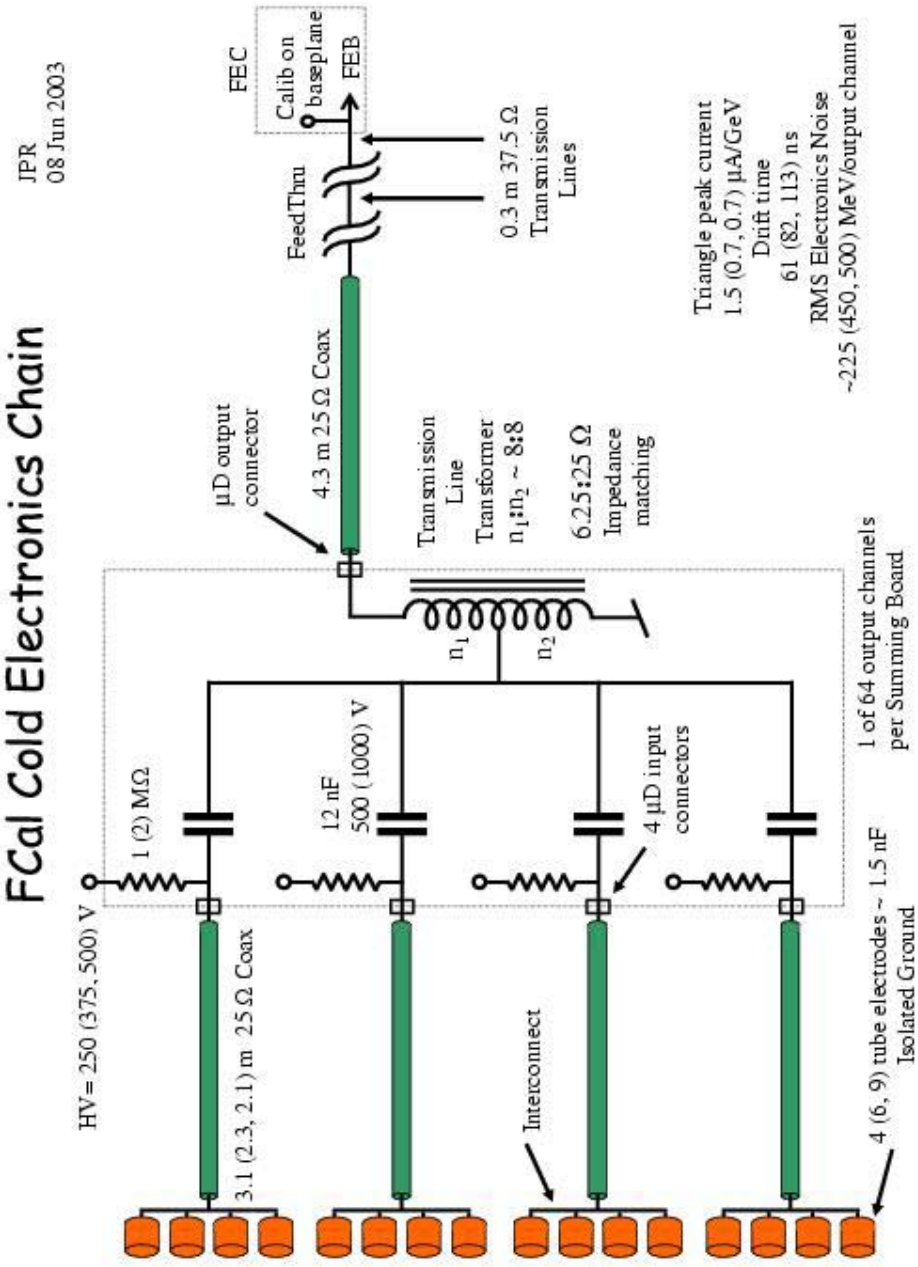

Figure III.3.8: FCal Cold Electronics Chain from electrodes to warm electronics. If the figure is viewed from the side then at the left are the electrodes which are electrically equivalent to low impedance transmission lines. These electrodes are ganged together and the signal travels up the "cold cables" to the summing board. This is where the HV is distributed and the signals summed via a transmission line transformer (here modeled by an Auto Transformer which is an approximation to the low frequency behavior of the actual transformer).

For our Module 0 test in 1998 we constructed five such boards with home-made transformers. Performance was excellent but since then the space allotted to these boards contracted a bit, requiring a more compact design. While the cross talk was quite low (~0.5%) we realized it would be difficult to make cross-talk corrections because information is lost during the summing. Savin proposed a simple re-arrangement of the pin assignments at the inputs to the summing boards that would reduce the cross talk even further, limit the largest cross talk to channels that are ultimately summed together, and allow a more deterministic correction. Rutherfoord optimized the values of the HV protection resistors to allow the HV supplies to survive with more shorts and Tompkins came up with a cleaner layout. We have now implemented these changes, placed all the orders, received all the parts, contracted for board stuffing, and received the completed boards. The boards for the FCalC modules are presently in the liquid Argon at the CERN North Area for our Calibration Test Beam Run, currently in limbo, awaiting additional beam time in September. We have experienced no problems with these boards.

Figure III.3.8 shows the cold electronics chain from the FCal electrodes to the warm electronics. Arizona is responsible for the cold cables and the summing boards for all of the FCal modules. Other ATLAS collaborators are responsible for the pigtails (the 4.3 m coax from the summing board to the feedthrough), the feedthrough, etc.

We have QC tested and characterized all 224 plus spares of our cold cable harnesses mentioned above. Each harness is composed of 64 Axon 25 Ω coax cables with polyimide dielectric and polyimide insulation for radiation hardness. A central element of our cold cable test station is a Time Domain Reflectometer (TDR) which measures the cable impedance at selected positions along the wire and provides results in computer readable format. We designed and assembled a complete, stand-alone test station to automate all the data taking and recording. Peter Loch oversaw the whole operation and took much of the data himself. Dan Tompkins designed and built the computer controlled switching box and relay boards that went in the cryostat. Ken Green loaded and unloaded each batch of 10 cable harnesses in the cryostat and managed the liquid Nitrogen dewars to fill the cryostat. The data allow us to determine the cable impedance as a function of distance along the cable and to estimate the Ohmic resistance at room temperature and at liquid Nitrogen temperatures. Once we had the procedure working smoothly it took two days to cycle through 10 harnesses. Some of that time was waiting for the cryostat to warm up so we were able to do up to three loads per week. Counting inefficiencies, the whole testing program was completed in just three months.

At this time all of the cold cable harnesses are now installed on the modules and those for the C-end are in the test beam cryostat along with the summing boards noted above.

III.3.6 FCal Electrical Tests

Over the last two years, Savin, Tompkins, and Rutherfoord have developed a battery of electrical test stations to probe the FCal module and the cold electronics. Several of these have already been mentioned above.

The HV trip test is relatively simple and very incisive. It consists of a simple Bertan HV power supply with current trip protection. We add probes to make convenient connection to the electrodes or we use custom break-out boxes when the cold cables are attached to the module. No computer control or data recording is involved in this test. It is a simple pass/fail test with a process sheet to help insure that all operators perform the same test.

The capacitance measurement test station consists of a impedance meter with precision probes interfaced to a PC running LabVIEW. The LabVIEW program knows the layout of electrodes on the FCal front face. It prompts the operator to connect the probes either to the next FCal electrode, to a standard capacitor, or to a "blank" so that the probe capacitance can be measured alone. It also requires the operator to return to one electrode repeatedly in order to track any drift. All the data is recorded by the PC in a way that makes it easy to correct mistakes, leave for lunch, or to switch from one FCal module to another and then back again. Savin did all the programming and taught other team members in its use. Rutherfoord took metrology data and calculated the expected capacitance for all the FCal modules before the data was available. He also performed various corrections to the data based on the measurements of the standards and blank. The results agree well with the predictions. The spread in measurements is one indication of the electrode-to-electrode gap variation, averaged over the electrode. For FCal1 this variation is about 0.7%, an impressive uniformity. This means that the sampling fraction of the calorimeter is uniform to this level. If an electrode has smaller than average gap then the collected charge is smaller than average, the drift distance is smaller, the electric field is larger than average because the potential across the gap is fixed by the HV supply, and the capacitance is larger. Because we do not measure the collected charge but the current integrated over a time shorter than the drift time, these effects tend to cancel making the signal even less sensitive to channel-to-channel variations than the 0.7% might indicate. This is another indication that the FCal electrode structure, despite the exceptionally small gap, is a precision electrode. These capacitance measurements are a key ingredient in a long list of effects that contribute to the translation of the current pulse from the electronics to an energy deposit in the calorimeter.

The Cold Cable Harness Test and Characterization Station consists of a Time Domain Reflectometer (TDR), a computer-controlled switch box, ten relay boards, and a PC. A step-function pulse is sent down a cable and the reflections are recorded on the PC (after some processing). There is a choice in the processing the TDR does and we selected the impedance option. The TDR calculates the impedance of the cable as a function of the time the step-function pulse travels down the line. It can convert this time to distance if we tell it the propagation velocity. We found that out 25 Ω cables have an impedance closer to 26 Ω and we have a measure of the Ohmic resistance too. We have recorded this data for every coax cable in every cold cable harness. It will be particularly important when we correct our calibration data for impedance mismatches with the preamp input.

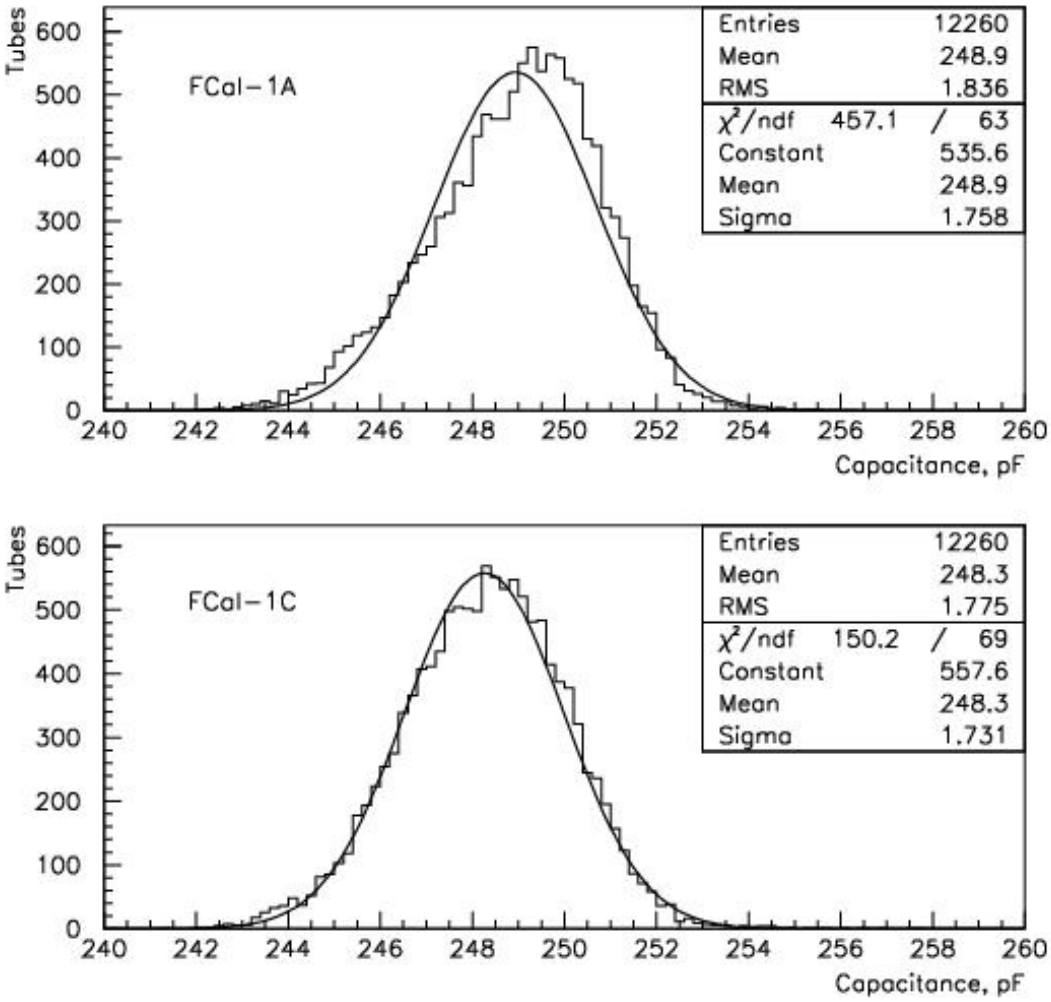

Figure III.3.9: Capacitance measurements of the FCal1 electrodes.

The Reflection Test Station consists of the same TDR, switch box, one relay board, and PC. In this surprisingly incisive test the TDR sends a step-function pulse down a coax cable to the electrodes and records the reflections. We can see details that are easy to interpret by the trained eye. In particular we can see the difference between a disconnected electrode and a broken ground braid. Shorts show up easily. Good channels are remarkably uniform in their reflections. During our Calibration Test Beam Run this summer (see below) we tried this test from the warm electronics base plane. We sent signals down through the feedthrough to the summing board and then to the electrodes. We were able to determine which electrode in the FCal1C module was shorted and we found one other fault, a broken ground braid, that we had not seen by any other means. We intend to use this test several more times as we prepare the modules for installation into the cryostat. In particular there is a critical point at which we connect the pigtails to the summing boards just before we close up the cryostat. We will conduct

reflection tests from the base plane to check that we have made these connections properly. At this point we can still correct faults before it is too late. Rutherfoord is simulating the setup in SPICE to mimic the behavior of the TDR. This allows us to replicate the anomalies we see to further confirm our understanding of the problems.

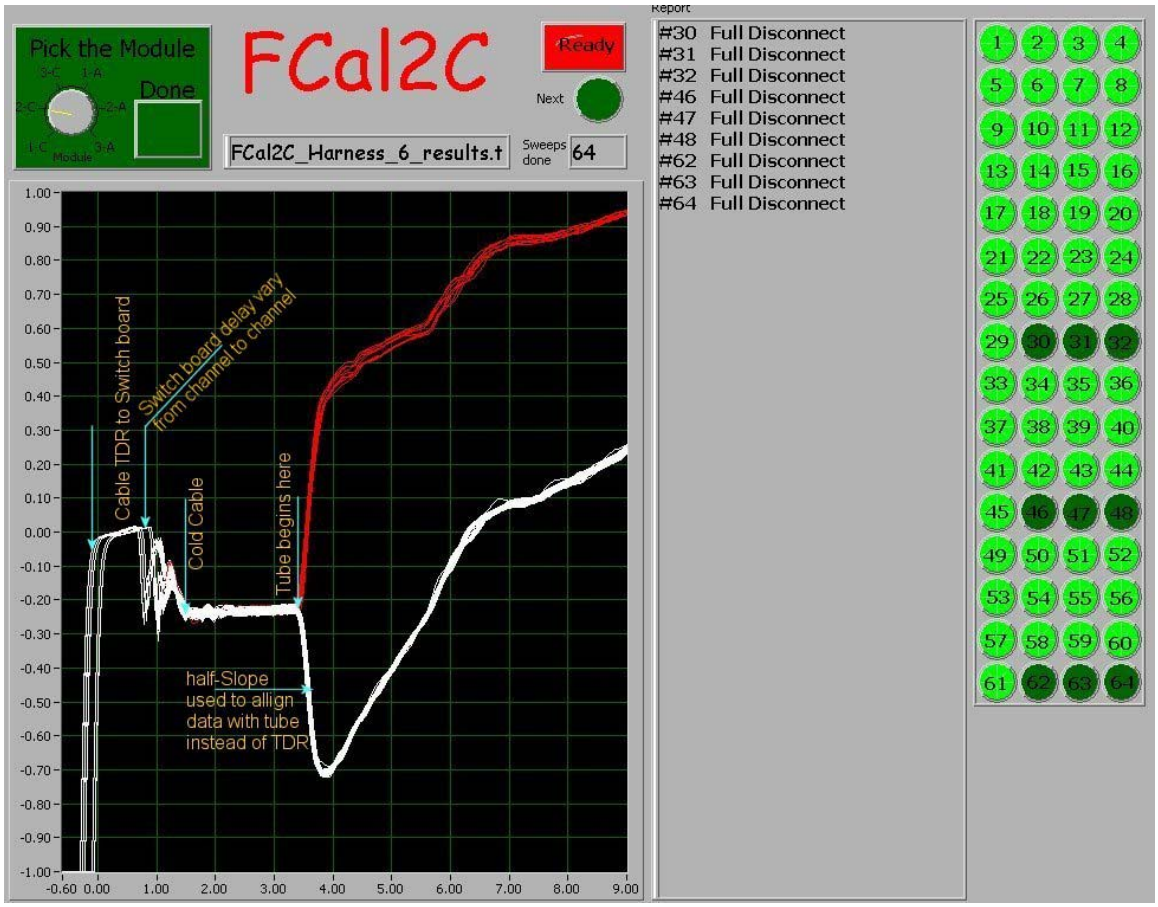

Figure III.3.10: Screen shot of the LabVIEW program "Reflection Test Station" with representative traces and commentary superimposed.

III.3.7 Radiation Damage Testing

For many hadronic processes pseudorapidity η is the preferred kinematic variable. ATLAS covers the range $-4.9 \leq \eta \leq +4.9$. Over nearly two thirds of this range particles first pass through the ATLAS inner tracker, then the ATLAS liquid argon accordion EM calorimeters, then the ATLAS Tile hadronic calorimeters, and finally the ATLAS muon system. But for more than one third of this η coverage the Forward Calorimeter is the only detector device that the collision products will see. The reason is obvious. At the highest values of $|\eta|$ the energy and flux of particles from the approximately 20 interactions per bunch crossing is so large that most detector technologies can not cope

and will not survive.

Bunch crossings occur every 25 ns at the LHC. At design luminosity 7 TeV of energy is deposited in each forward calorimeter from the products of minimum bias events in each bunch crossing. (It is just a coincidence that this energy happens to coincide with the LHC beam energy.) This amounts to about 40 watts in each FCal1 module. (The FCal1 module is made out of copper, rather than brass or some other material, in order to transport this heat away from the hot spots, preventing boiling the Argon.) At EM shower maximum near $\eta = \pm 4.9$ this amounts to about 1 MGy/year. And near hadronic shower maximum (near the interface between FCal1 and FCal2) the neutron fluence is about 10^{16} neutrons/cm^2/yr.

Such considerations went into the choice and placement of materials in the ATLAS forward calorimeters. While the liquid argon, the absorber matrix, and the readout signal pins are manifestly radiation hard, other components, though mechanically able to withstand the dose, could conceivably poison the argon.

A large program of materials certification was concluded near the beginning of our present 3-year grant so we will simply report here that all materials passed with no hints that radiation would lead to poisoning. Loch and Shupe calculated all the above numbers and Rutherfoord negotiated all of the radiation testing.

III.3.8 Ion Loading Measurements and Simulations

In a liquid argon ionization, sampling calorimeter the shower particles ionize the argon atoms, producing free electrons in the liquid. Without these free electrons, liquid argon is otherwise an excellent insulator. These electrons drift in the applied electric field and induce a current in the circuit connected to the electrodes. Also drifting far more slowly are the positive argon ions. They are too slow to contribute to the fast electronics signal. In fact they are so slow that, under constant bombardment by showers from the products of minimum bias events, the positive ions tend to build up in the electrode gap and produce space charge effects. Rutherfoord has calculated this effect quantitatively and has predicted the effect this build-up has on the signal. He has been able to derive analytic expressions for the signal shape under simplifying assumptions and has a detailed simulation to include all the effects which might modify the analytic results. A draft report has been available for some time now and this work was published last year in NIMA. Basically the signal is unaffected as the luminosity is increased until a threshold is passed. After that, as the luminosity increases further, the signal amplitude is degraded dramatically.

Some parameters affecting the signal in the face of this positive ion build-up are not well known. Therefore the on-set of the signal degradation cannot be predicted with certainty. So Shupe conceived a method to test the effect in our lab with a small liquid argon gap and a high energy, high activity beta source. In the device Shupe's student, Ron Norton, designed and built, the gap width could be adjusted and the electric field changed to map

out the behavior. Norton also purchased two sealed Sr(90) sources with activity differing by a factor 10. One gap electrode was composed of a stretched, thin copper foil so that we could bring the beta source close to the gap. In this way we were able to minimize the energy loss by the betas in traversing the liquid argon and electrode material before they entered the liquid argon of the gap. Even so the ionization on the side of the gap with the source is significantly larger than at the other side. This is a different situation from what we will see in ATLAS where the ionization in the gap will be nearly uniform over dimensions comparable to the gap size.

Rutherfoord has written a simulation program with less symmetry, i.e. more dimensions, than the simulations described above. CPU time requirements for this new simulation are so excessive that we wouldn't have been able to get results were it not for the US ATLAS PC farm at BNL. At this time we have completed all the conditions necessary for detailed comparisons with the data we took with the sources. We are hoping to constrain the parameters well enough to make firm predictions for the maximum luminosity ATLAS can withstand. We are fairly confident, however, that our design parameters are conservative enough that the LHC won't be able to drive us to these limits.

When Norton left Arizona Rutherfoord took over this R&D project and has involved two graduate students and one undergraduate in this work.

But the measurements show an unanticipated effect which prevents us from extracting the high quality data we expected. The effect seems likely due to some unusual contaminant (not Oxygen) which slowly collects (via gettering?) on the electrodes building up a semi insulating layer of very large capacitance. It is imperative that we understand this effect and we intend to pursue it until we do.

In the meantime Rutherfoord has designed and built two electrodes identical to the FCal tube electrodes except that they are a bit shorter in overall length and the rods have a 12 mm length hollowed out, leaving a 250 μm wall. He then contracted with a Russian nuclear power company to produce two foils each with a Strontium 90 beta source evenly distributed on one surface and then rolled up such that the surface with the source is flush with the cavity wall when sealed inside the rod. One source is 50 mCi and the other 2 mCi to act as a control. Over the 10 mm length of the foil the electrode with the hot source will behave roughly as one of the FCal electrodes in ATLAS during 10^{34} cm^{-2} s^{-1} instantaneous luminosity near EM shower maximum at $|\eta| = 4.5$. Once the problem described above is solved Rutherfoord intends to run for months with these two electrodes in liquid Argon, observing their HV curves and current as a function of time. We expect to show that our forward calorimeter concept is solid and robust.

III.3.9 Interfaces

Because of the central role the Integrated Forward Calorimeter plays in ATLAS and because of our collaborative style to help insure the success of the whole experiment, the Arizona group has stayed involved in several interrelated areas of ATLAS where we can

help. The next section describes some of our larger involvements, i.e. the ATLAS radiation backgrounds in the experiment and the cavern, the shielding design and engineering, especially of the plugs 1, 2, and 3, and the accelerator beam pipe. Here we mention in passing some smaller responsibilities we have taken on.

What we call "the FCal support tube" is a structural member of the end cap cryostat. It is not the weight of the FCal that dictates the thickness of the wall of this tube but the forces exerted on it by the cryostat under certain extreme conditions. We participated in the conceptual design of the two end cap cryostats and some of the engineering. We also have given guidance and advice on the heat leak calculations through the walls of these cryostats. And, in collaboration with some of our Canadian colleagues, we have developed an advanced model with which we estimate the overall heat flow within the cryostat. We constructed a model of the feedthrough and measured the electrical breakdown potential in the vacuum region between the flanges under various failure modes.

Shaver twice visited the Italian factory where the end cap cryostats were being constructed, carrying a full-size model of one matrix plate of the FCal1 module to make sure it would fit in the support tube, first for end cap C and then for end cap A. At the same time he was able to advise on more general cryostat issues.

We have prototyped early versions of some of the front-end electronics including the preamps, shaper, calibration pulser, trigger sums, and baseplane. We purchased the first low-impedance, radiation-hard coaxial cables from industry. We were the first to research and specify a rigorous testing procedure for the production preamps and made first contacts with companies which certify circuits under extreme conditions. All of this information and experience we passed on to those responsible for the front-end electronics.

III.3.10 ATLAS Background Radiation: Simulations, Shielding Design, and Shielding Engineering

Overview – 1994 to the Present

In 1994 the Arizona *integrated forward calorimeter* concept instigated a major redesign of the ATLAS forward region and changed the nascent ATLAS radiation shielding plan. As a part of the crash effort that Spring to convince the ATLAS Calorimeter Review Panel of the virtues of our design, Mike Shupe took on the project of simulating the radiation backgrounds in the ATLAS detector. This task was made easier for us because the GCALOR code, the melding of Tony Gabriel's CALOR shower code with GEANT, had just been written by Christian Zeitnitz, then an Arizona postdoc working on an early prototype of the FCal. By 1994, this code had already been exercised in the conceptual design of shielding for the GEM detector, proposed for the SSC. Shupe's task was to quickly generate a complete description of the ATLAS geometry appropriate for radiation calculations, and run the simulations (on machines that were very slow by today's standards) in time for a succession of review Panel meetings.

Before 1994, Alfredo Ferrari at Milan had provided the only radiation background simulations for ATLAS. He had taken over the FLUKA shower code from Johannes Ranft and improved it to do the same low energy neutron transport. He used his own geometry package in a stand-alone program that was not readily available for use by others. We were lucky that Alfredo agreed with our shielding concepts, and this motivated him to perform his own simulations to compare with ours. The agreement was better than we might have expected (10 to 20 per cent in total neutrons and photons), considering the uncertainties in the parameters in these packages.

In the period from 1995 to 1998, Ferrari provided the majority of the radiation background calculations for ATLAS, with Arizona confirming the major results and doing periodic studies to optimize specific materials or dimensions. But in early 1998, Alfredo left ATLAS to work with Carlo Rubbia on his many efforts, and Arizona became the only source of radiation calculations for ATLAS. Unfortunately, at the same time ATLAS was just embarking on the realistic engineering design phase for the shielding --- to take it from the 'physicists design' to the engineered design that would ultimately be fabricated. This implied a large increase in the level of detail and the number of options to simulate.

In March of 1998, Mike Shupe was appointed Convenor of the ATLAS Radiation Backgrounds working group and, in concert with the Shielding Engineering Group lead by Werner Witzeling, began meeting with ATLAS engineers in all subsystems and upgrading the GEANT/GCALOR description of the detector. The summer of 1998 marked a period when mechanical gaps and more realistic materials were introduced to the design, and when a number of the cladding concepts had to be redone to avoid penetrating structural areas of the shield. The number of volumes in the geometry description grew by roughly a factor of two, and has continued to creep upward in the intervening years in response to increased engineering definition.

Fortunately, after a lull of about one year, ATLAS was able to resume comparing GCALOR and FLUKA simulations. Ian Dawson, now at the University of Sheffield, had been working with Graham Stevenson on beamline activation studies in the 1997-98 period. He agreed to shift to doing ATLAS full simulations, and Ferrari was willing to hand over his full FLUKA description of ATLAS to Ian. Ian spent some time converting the geometry description to a new input format (ALIFE), so that it would be more convenient to modify. Since mid-1999, we have been able to do comparison runs again. But given the large number of simulations to be done, Ian focussed on inner detector levels and optimization of the moderator block in front of the forward calorimeter, while Shupe simulated several hundred design variants for the electronics gaps, beamline configurations, and forward region shielding elements--from behind the FCAL to the end of the ATLAS cavern. The detector and detector support designs were themselves evolving up through 2002, and there were several epochs of redesign, followed by corresponding reoptimization of the shield.

In this engineering phase, analyzing design modifications required changing dimensions or materials incrementally, often one parameter at a time. This led to a very large number of options to simulate--and neutron transport simulation is extremely CPU intensive. Fortunately, the U.S. ATLAS Computing Center at Brookhaven appeared in the year 2000, ultimately with 128 CPU's in the 450-850 MHz range. Since 1998, when serious engineering design began on ATLAS shielding, more than 500 geometry simulations (baselines and their options) were done using GCALOR. Each simulation required of order 2400 CPU hours on the Brookhaven machines, producing approximately 60 k simulated events per option, running with a duty factor of roughly 75% on 50 CPU's over the span of three years, ending in May 2003.

ATLAS considered the results of these calculations so critical to detector design and operation that the ATLAS Radiation Task Force (RTF) of ~25 collaborators, convened by Martine Bosman, was formed at the behest of Torsten Akesson in the summer of 2000 to crosscheck and certify the simulations. Geometry models and materials descriptions used in each subsystem were checked by people from each subsystem group. Assistance was provided in assessing the many sources of uncertainty in the transport codes, detector model, and tabulated functions (damage, counting efficiency, error rate, etc.) so that safety factors might be assigned in a consistent fashion. Between 2000 and the present, the core group in the Taskforce became Martine Bosman (Convenor), Vincent Hedberg (head of Shielding Engineering (following Werner Witzeling) and activation specialist), Ian Dawson (FLUKA simulations, inner detector, transport code comparisons, etc), and Mike Shupe (GCALOR simulations, shielding design optimization, radiation damage tabulations, etc.). The Taskforce also received strong contributions from Ivan Stekl (cladding optimization studies), Mikael Morev (activation simulations, with Hedberg), Serguei Baranov and Leandro Nisati (muon detector response detailed GEANT simulations and muon trigger response, with Martine Bosman).

The Radiation Task Force activity is culminating as this grant request is being written. The core Task Force members had this as their primary research activity for large blocks

of time since the summer of 2000, and many others have made similar large commitments to making this a successful effort. The large RTF Summary Document is in final draft, and will be released to ATLAS in August, 2003. There is also an ATLAS Web page with the complete results from GCALOR, FLUKA, the activation studies, the muon detector studies, etc., at the following web site, for collaboration and public access:

//atlas.web.cern.ch/Atlas/GROUPS/PHYSICS/RADIATION/RTF_SummaryPage.htm

The Radiation Task Force has fulfilled its mission of supporting the engineering design of the ATLAS radiation shielding through to its completion, and is being disbanded as the RTF Summary is released. However, there are a number of issues which will require future simulation work at Arizona and elsewhere, that will be outlined in the ATLAS paragraphs in Section III of this proposal. At this point, we turn to reporting what has been done in the course of this project.

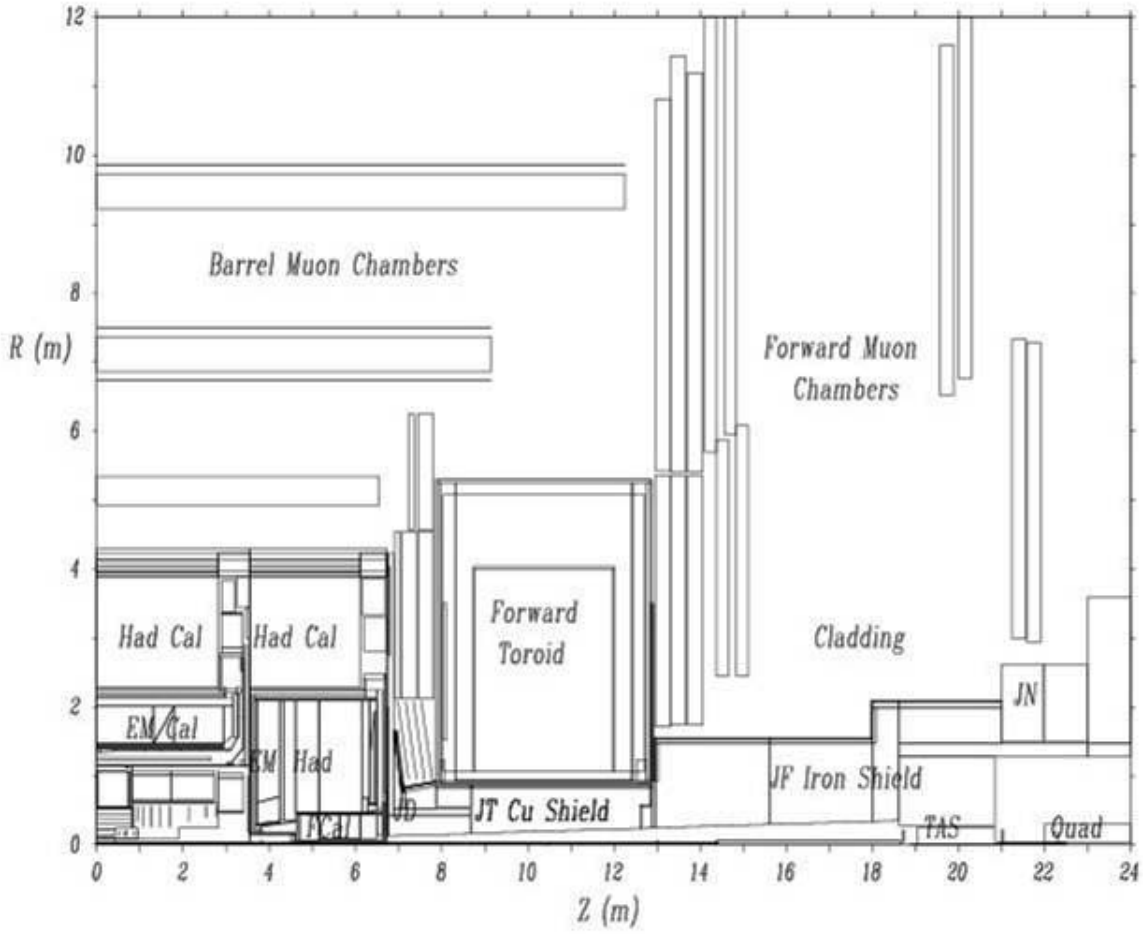

Figure III.3.11: View of one quadrant of ATLAS with forward region labels

Arizona Shielding Design Concept for the Forward Region

Figure III.3.11 shows a cross-section of one quadrant of ATLAS, with the various detector and shielding zones labeled. We will use it to point out the strategic elements of the forward region shielding design developed at Arizona.

The ATLAS Forward Shielding Region begins behind the endcap calorimeter and extends through the forward toroid, past the TAS absorber and final focus quadrupole, to the cavern wall. It naturally divides into four regions:

(1) the Flux Return Disk and Hub, `JD' (Z = 6.7 m to 7.8 m);
(2) the Forward Toroid Radiation Shield, `JT' (Z = 7.8 m to 12.9 m)
(3) the Massive Forward Shield, `JF' (Z = 12.9 m to 21.0 m)
(4) the Shielding Nose On Support Tube, `JN' (Z = 21.0 m to 23.0 m).

The integrated forward calorimeter design proposed to ATLAS in 1994 by the University of Arizona was to be installed in the endcap calorimeter cryostat at about 4.5 m from the IP, instead of a standalone far-forward calorimeter at 13 m. One of the primary features of the design was to make the whole ATLAS calorimeter a hermetic container of the flux from the interaction point up to $|\eta| = 4.9$, and to allow the calorimeter interaction lengths to provide much of the shielding depth needed to protect the open, low mass, muon system from background radiation. This also allowed for massive shielding to be placed behind the FCal, extending to the shielding around the TAS collimator. And, finally, it allowed for the FCal bore itself to be designed to act as a large aperture collimator, restricting the forward streaming particles to flow toward the TAS shield, and reducing the flux heading for the inner and middle forward muon detectors (small and large 'wheels', respectively).

In the far-forward design being proposed in 1994, there was no room for adequate shielding inside the bore of the forward toroid, and the rates in the muon system were predicted to be two orders of magnitude higher in that design compared to the integrated design proposed by Arizona. The muon system would not have operated in such a radiation environment.

Calorimeter Radiation Shielding Engineered at Arizona

Before proceeding with more detailed descriptions of the radiation backgrounds work done at Arizona, we would like to highlight the independent effort by our group engineer, Leif Shaver, in designing and supervising the production of the calorimeter shielding plugs in the ATLAS endcap cryostats. (See, for example, the photo of shielding plug 2 in Figure III.3.12.)

There are three copper shielding 'plugs' inside each endcap cryostat to increase the integrated absorbing material between the IP and the muon system. Arizona played a key role in this shielding concept and in the geometry of the cryostat. So it was natural for us

to follow through to design these plugs. Leif Shaver produced the drawings in consultation with the responsible CERN people and put them into the official ATLAS computer archive. Australian groups at Sydney and Melbourne were awarded these plugs as a part of their common fund contribution, and Leif worked closely with Goeffrey Taylor of Melbourne in the final fabrication of the plugs.

All three plug types are placed inside the liquid argon of each endcap cryostat. Plug 1 lines the inner face of the rear cold wall, thickening the calorimeter in front of the muon CSC and TGC detectors. Plug 3 sits behind the third FCal module, to attenuate the radiation punching through into the forward region beamline cavity. Plug 2 closes a gap between these two, sitting behind the HEC calorimeter modules and abutting the FCal summing boards. It helps reduce the flux of particles at the position of the electronics.

Leif Shaver made numerous trips to Australia to collaborate in the search for the best alloy, fabrication technique, and foundry. As pieces were fabricated, he traveled again to assist in their certification: dimensions, uniformity, and surface quality. And finally, he is in the process of overseeing their installation at CERN (along with his many other tasks involving FCal module installation and testbeam work).

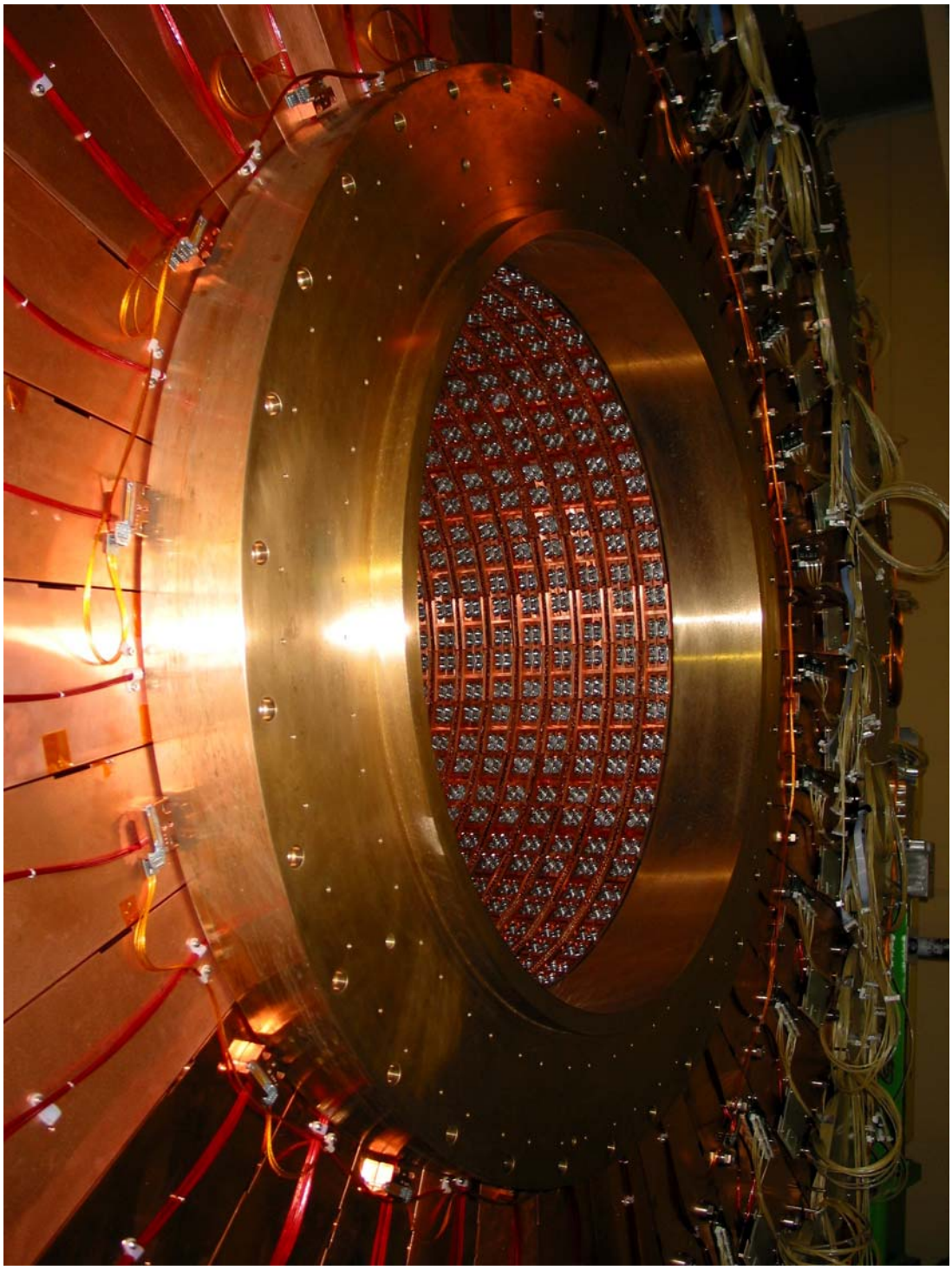

Figure III.3.12 Shielding plug 2, mounted on back of HEC calorimeter

Results from the ATLAS Radiation Background Calculations

We now turn to a capsule report of the performance of the ATLAS shielding design resulting from the simulation work at Arizona and the work of the ATLAS Radiation Taskforce and ATLAS shielding engineers. The results presented in this section are from GCALOR calculations done on the final shielding design for ATLAS, between January and May, 2003, and referred to as the 'January 2003 Baseline Geometry'.

Figure III.3.13 is an example of a recent contour plot showing total neutron flux in ATLAS in the current baseline geometry, and is typical of the outputs from GCALOR simulations for ATLAS done for many years. But the products of each simulation run are now considerably more numerous than in the past. In addition to the traditional flux maps (such as the one below) of a large variety of particle species, we now accumulate spectra for 8 categories of particles divided into 25 logarithmic energy bins of 1/3rd decade each. These spectra may be applied directly, or used to calculate detector counting rates, silicon damage rates in units of 1 MeV equivalent neutron flux, and single event upset and single event damage rates.

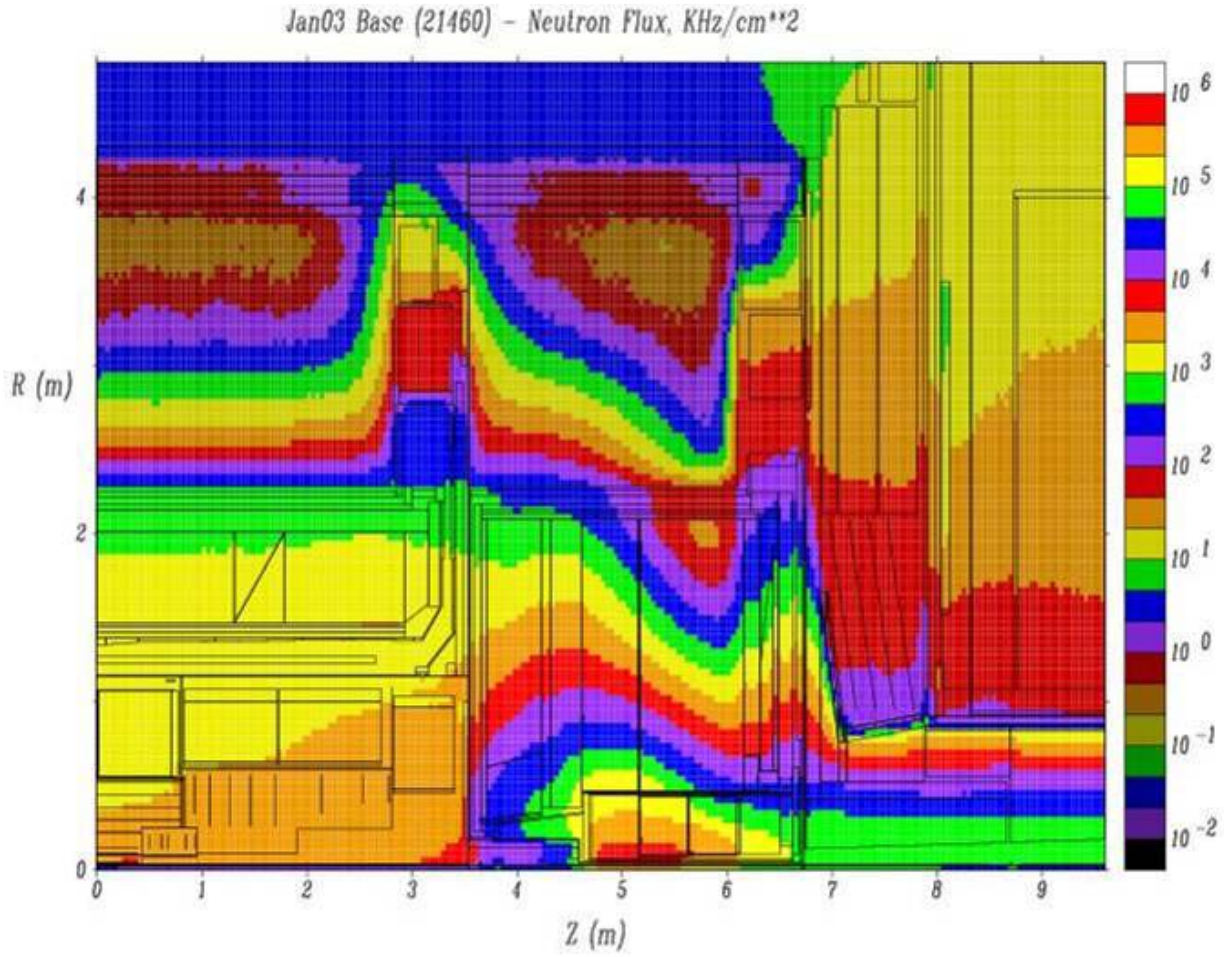

Figure III.3.13: Total neutron flux in ATLAS inner detector and calorimeters

If we consider the total neutron and photon flux maps (Figure III.3.14), zoomed to look at the inner detector, calorimeters, and inner muon region, we see a number of features that have been at the focus of the shielding design.

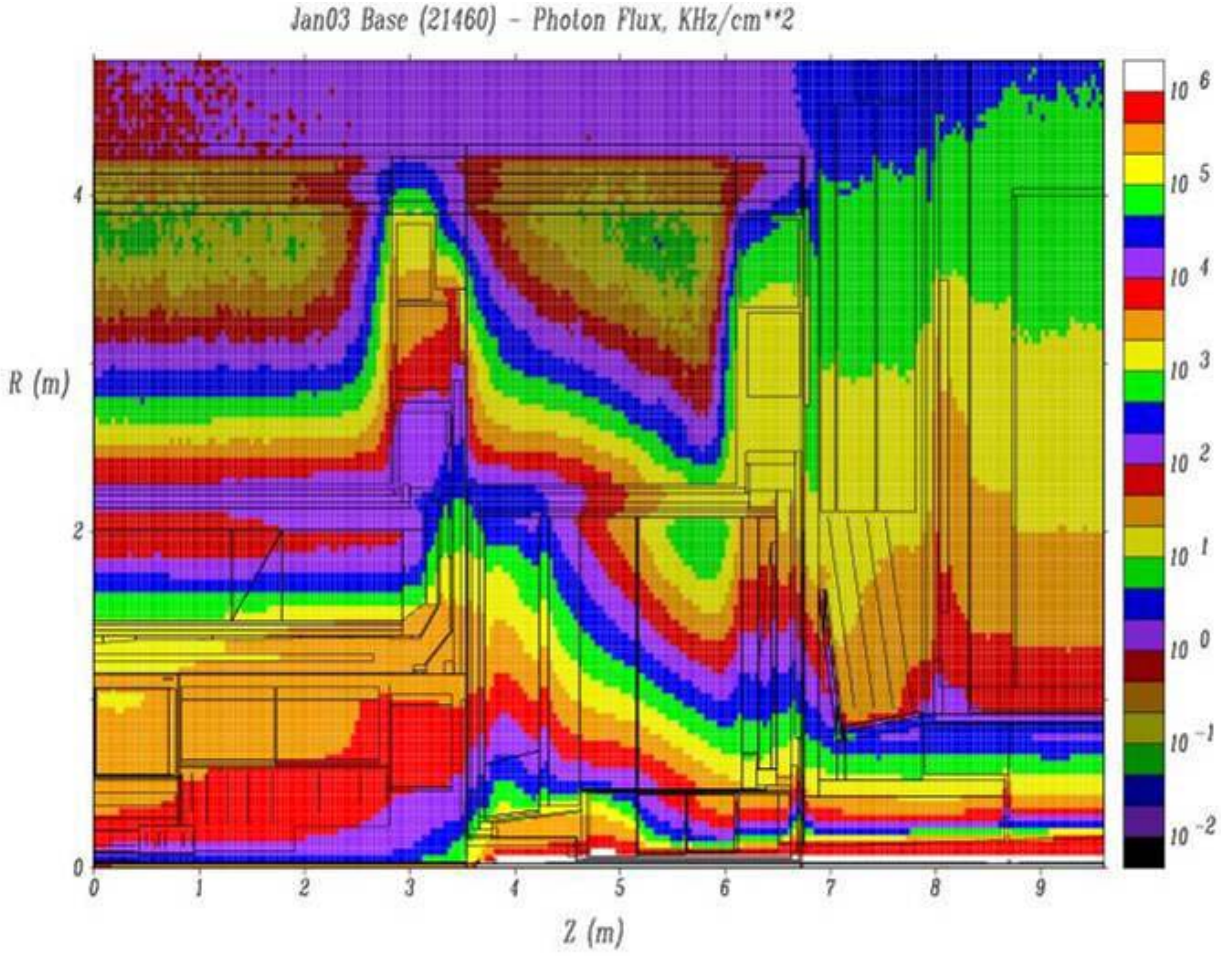

Figure III.3.14: Total photon flux in ATLAS inner detector and calorimeters

1) Both maps show the hot spot in the first and second FCal modules. The neutrons emphasize hadronic shower maximum at z = ± 5.1 m, almost between the modules, and the photons show electromagnetic shower development peaking earlier, around 4.9 m. The photon map also shows photon production in the ion pump at z = ± 3.85 m, and in the beamline structures. In effect there is a 'searchlight beam' of photons streaming from the rear bore of the FCal, but the shielding boundary inside the JN shows that it is relatively well contained.

2) All particle fluxes in the inner detector show the trend that they increase with |z| along lines parallel to the beamline. This shows up clearly in the photon map, and results from IP particles undergoing secondary interactions in the beampipe, and from interactions of low energy charged particles curling in the magnetic field of the solenoid (while coasting forward). In the neutron map, this trend is less

pronounced because there is also an appreciable flux of albedo neutrons from the face of the endcap calorimeter.

Also, the map (Figure III.3.15) of high energy hadrons, shows that those from the IP, predominantly charged pions, undergo very little change in z for fixed r, and we can approximate these fluxes as depending only on radius, and dropping off as 1/r.

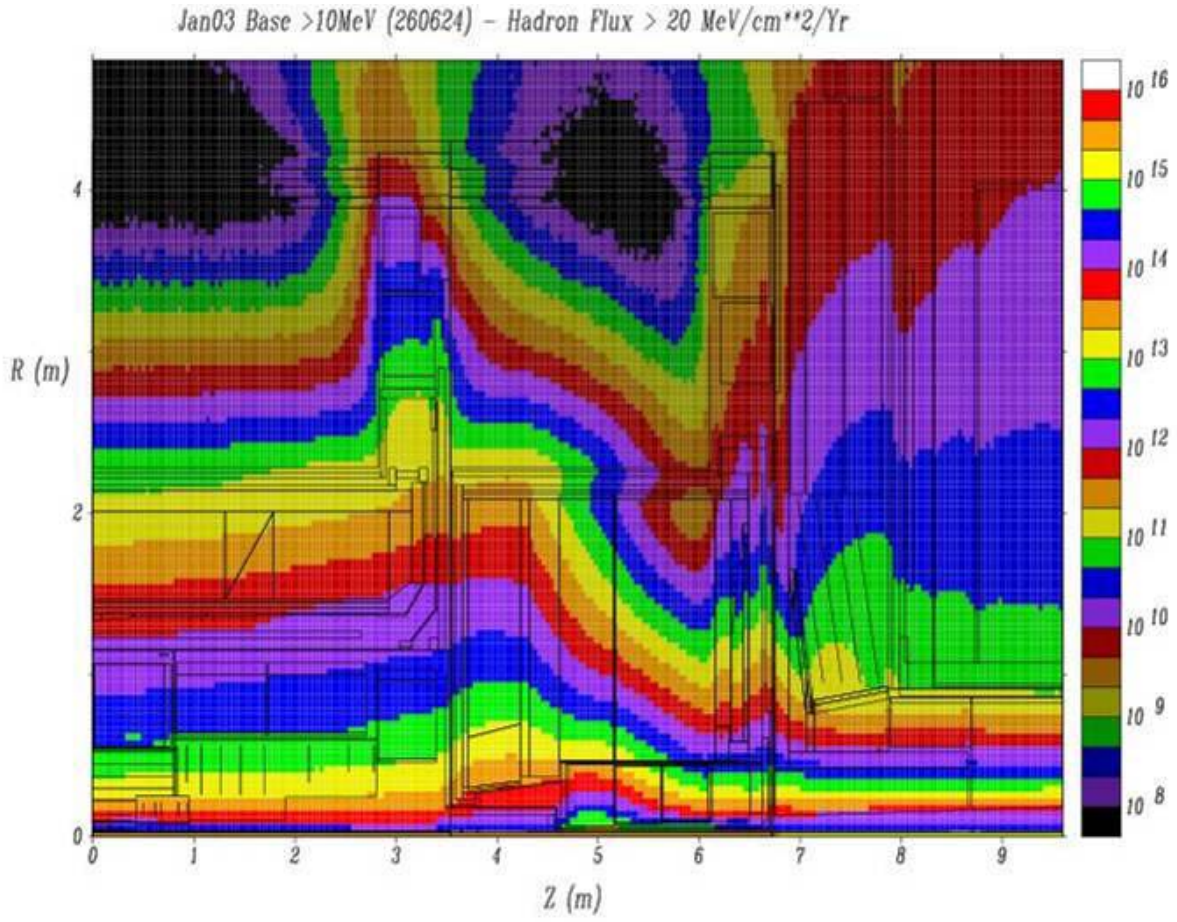

Figure III.3.15: Flux of hadrons above 20 MeV in inner detector and calorimeter

(3) The barrel/endcap services gap shows up clearly in the photon map (Figure III.3.14). One can see the 'low density channel' between the cryostats in the region from z = 3.3 to 3.8 m, populated by aluminum cryostat walls, liquid argon, services, and vacuum. As one moves outward, beyond r = 2 m, where the EM barrel modules end, this channel widens into the gap between the TileCal modules, from z = 2.8 to 3.5 m, filled with cryostat feedthroughs, electronics crates, and services. At larger r, the channel narrows again where the TileCal small modules are placed on the face of the extended TileCal. If we look at attenuation in the services gap, we see that the neutrons and photons are relatively well contained, with little 'plume' into the inner muon system, while hadrons > 20 MeV are able to penetrate into the inner muon

system. Note, however, that the hadron plume from this gap is still considerably smaller than the plume entering the barrel region behind the back of the forward calorimetry.

(4) Another low density channel shows up most clearly in the total neutron plot (Figure III.3.13). In the LArg endcap calorimeter, behind the HEC modules, the layers between z = 6.1 m and 6.8 m, where the JD flux return disk appears, are: liquid argon with cabling, copper plug 1, aluminum cold wall, vacuum, aluminum warm wall, and air gap. There is also a smaller gap between the back of the FCal plug (plug 3) and the JD copper core. As with the barrel/endcap gap region, neutrons, photons, and other fluxes can feed outward through this channel, again to encounter cryostat feedthroughs, crates and services, ultimately working their way to the muon system *in front* of the JD disk.

(5) The behavior of backgrounds at the JD thin corner where the CSC's are mounted is also evident from these plots. The neutron plots show that the 8 cm cladding zones on the faces of the JD cone and hub are doing their job. The neutron flux contours follow the cladding faces in a very reasonable fashion, and this extends into the JTT region, where the 4 cm polyboron insert is also performing well. The photon fluxes, are, however, more 'interesting'. Near the inner front of the CSC's they mirror the contours of the neutrons, showing that we are seeing mostly capture gammas at this point. But as one moves toward the forward toroid, additional photon flux is seen coming through the thin JTT, not associated with neutrons. These we interpret to be the products of hadronic shower development resulting mostly from beampipe secondaries hitting the inside of the JTT core: in simulation, this flux reduces sharply as beampipe material is removed. Finally, the high energy hadron flux in the CSC region looks like punchthrough from paths through the dense shielding materials, and could only be reduced by putting more dense material in this region. The global optimization points to the use of cladding on the JD because it gives large reductions in neutron and photon rates, whereas 8 cm of additional dense shield does little to reduce high energy hadron rates.

We now turn our attention to the muon system, and introduce maps zoomed out to show a full quadrant of ATLAS. The global optimization of radiation backgrounds in the Forward Shielding Region is dominated by one central feature of the shielding envelope: the outer radius of the JT Forward Toroid Radiation Shield is by far the thinnest part of the shield. The rest of the forward shield outer envelope lies approximately along the line of $|\eta| = 2.7$, but the forward toroid shield copper and its support tube must end at a radius of 915 mm in order to provide clearance for the toroid coils, and this introduces a notch in the outer envelope of the forward region shield. The effect is that neutron and photon fluxes in the inner and middle forward muon stations consist of two components: flux coming through the adjacent shield (JD for inner, and JF for middle), AND flux spilling into this region from the nearby JT region. For photons, the flux from the JT dominates.

In this region, we shall begin discussion with the map of hadron flux > 20 MeV, shown in Figure III.3.16, to emphasise the properties of the dense 'core' sections of the shield.

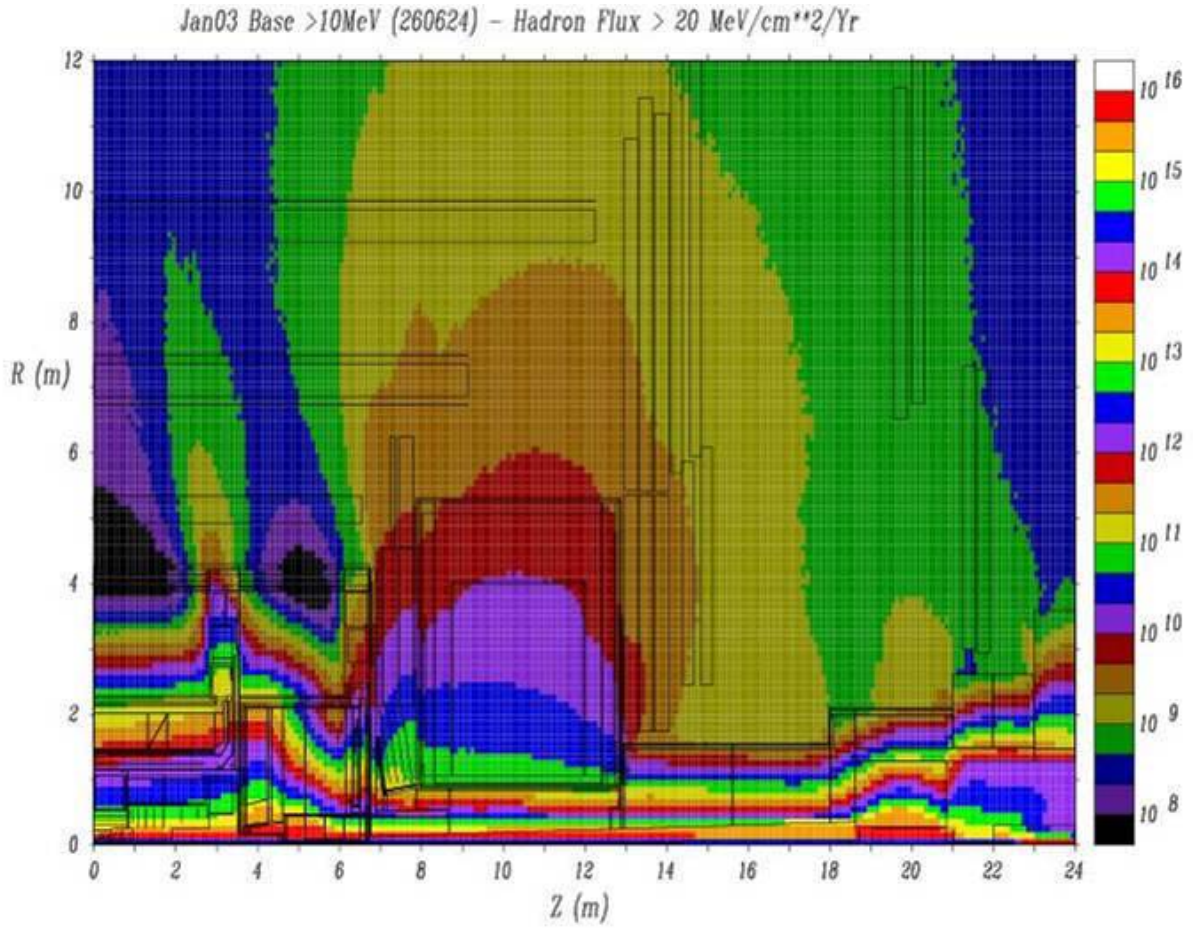

Figure III.3.16: Flux of hadrons above 20 MeV in the ATLAS detector

If we look at the prominent features in this map we see the following.

(1) The JD corner and the JT core are the thinnest sections of dense shielding leading into the muon system. Although there is no sharp boundary between sources, we see that the JD corner is seeing punchthrough from the back of the endcap calorimeter, and radiation feeding outward from the region of the FCal plug, up the low density channel at the back of the endcap. As we move further downstream into the JTT we see that the flux contours are becoming more parallel to the beamline. This signals the appearance of radiation coming from the beampipe 'line source' of secondaries,

hitting the inside of the JD and JTT, and punching through the copper core of the JTT. In fact, this map at low statistics shows tracks pointing back to these sources, and there is a remnant of this pattern at the back outer edges of the contours in this map above. Note that the high energy hadron rate through much of the volume of the muon system is dominated by the large plume of radiation coming through the JT

(2) The JF massive shield is doing an excellent job shielding the TAS collimator hot spot. In the middle MDT region, the level of radiation coming through the JF shield is very low compared to that coming through the JT. (At the JF corner, one must be careful, because the contributions become comparable, and optimising the JF cladding inside the big wheel has helped lower the rates there.) In the zone immediately outside the TAS, at 20 m, there is a small plume punching through the shield. But this does not reach the outer MDT's because it is intercepted by the JN cast iron shielding disks. The conclusion is that the stepped design of the JF shield, while much reduced in tonnage, cost, and complexity compared to earlier conical designs, has enough dense shielding in the right places to make its high energy hadron background contributions negligible compared to other sources.

(3) It was noted earlier that hadrons > 20 MeV emerge from a plume outside the barrel/endcap services gap. This feature is seen more clearly in this map, but it is also even more apparent that its contribution to the hadron rates is small compared to that from the JT plume.

As a side note, why is the dense material of the massive forward shield cast iron instead of (denser) steel? As early as 1994 it had been realized that steel, though dense ((= 7.8), has the disadvantage that it is very transparent to neutrons in the region of its resonance windows. This situation is improved greatly if the shielding iron includes 2% (by weight) or greater of carbon. The neutrons scatter elastically from the carbon and the resulting reduction of their kinetic energy (moderation) shifts them through the resonance windows and greatly increases their attenuation. It was realized that the carbon would reduce the density of the iron, so a composition including 5% carbon with a density of
7.5 was used up until 1998. In the summer of 1998, advice from Claude Arnaud lead to the use of more realistic materials in the simulations. For iron: cast irons which have densities in the range 7.1 to 7.2 and carbon fractions 3.2% to 3.8%. The carbon fraction is more than adequate to achieve neutron moderation, but the loss of density means an overall loss of about 4% of the shielding depth. Note that the fractional changes in background fluxes might be considerably smaller or larger than this fraction since they are often coming from the tails of showers developing in the shield.

We next look at the neutron and photon maps for the muon region.

□ SHAPE * MERGEFORMAT □□
in the ATLAS detector

Since we have discussed these fluxes
here on the rest of the muon system. I
cladding on the JF massive shield, anc
the JT toroid are doing an excellent jo
In fact, the green plume emerging fro
coming through beyond where all clac
mass. The outer forward MDT's are l
where they experience the same green
necessary). These levels are really no
the much higher rates in the inner forv
as operating levels.

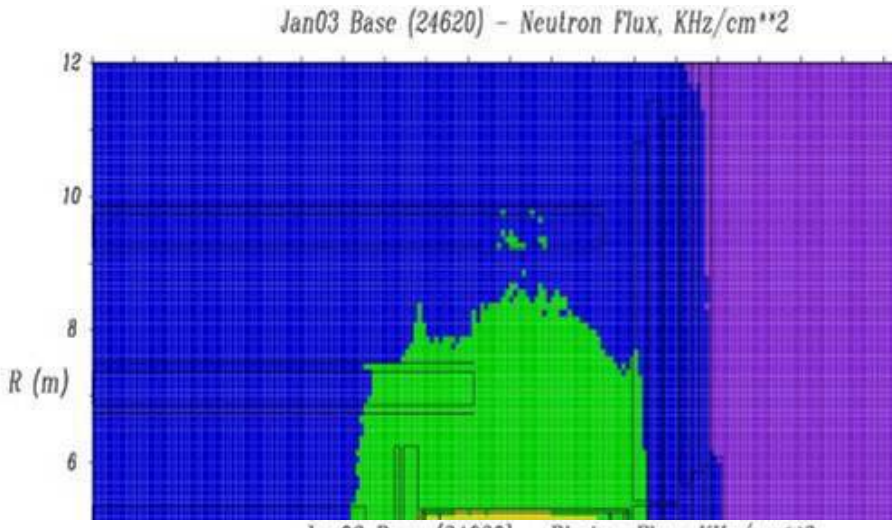

□ SHAPE * MERGEFORMAT □□
in the ATLAS detector

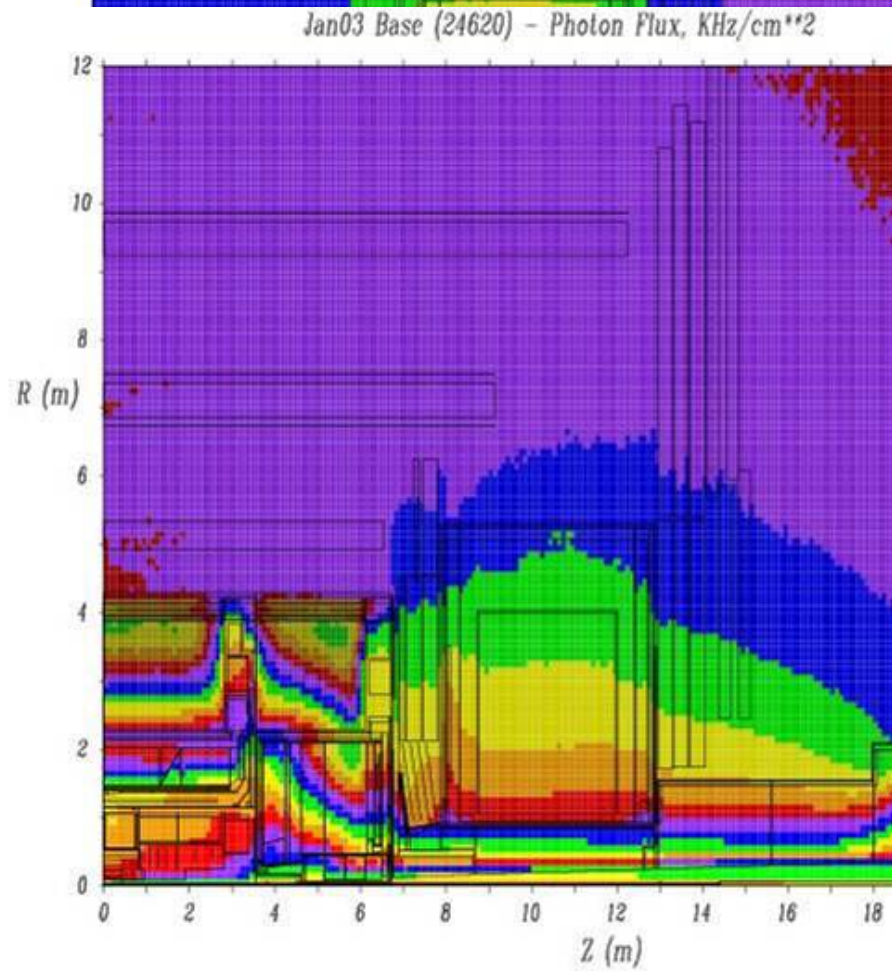

Once again, the photon maps (Figure
the TAS region, we see the photon co
are predominantly capture gammas as
approaches the JT, the situation is ana
contours 'blow out' from the shieldin
indicating that they are caused by sho
beampipe line source.

This concludes our quick summary of
leading to the baseline geometry of Jar
shielding.

III.3.11 Beam Tests

We have conducted a number of beam
Calorimeter over the years. The "proo
1993 were already mentioned in the H
brass prototype with 192 electrodes an

We conducted another beam test in the summer of 1995 with a full depth (26 X0) brass prototype with 384 electrodes. The purpose of this test was to try out the two competing approaches to the electronics read-out of the liquid argon calorimeters with the forward calorimeter. Rutherfoord had already determined that the FCal would try to use the same electronics as the rest of the Liquid Argon Calorimeter System to the extent possible. But this choice had not yet been made by ATLAS management. At this time there were two proposals. 1) A GaAs FET preamp to be located in the liquid argon near the electrodes was proposed by the Milan group. It promised exceptionally low noise performance but would be subjected to higher radiation levels and would be impossible to service. 2) The competing proposal was to use a common base transistor preamp outside the cryostat. Conventional wisdom suggested that this latter solution would have poor noise performance because the capacitance of the cable would add in parallel with the detector capacitance. On the other hand the preamp would be located in a region with lower exposure to radiation and it could be serviced several times per year.

Things were changing quickly at this time. It had only recently been realized that with the very fast shaping necessary with any readout electronics at the LHC only a short section of the cable would contribute to the detector capacitance in the calculation of the noise. So the cable could be any length, to the extent that the Ohmic resistance could be neglected (and this is small at the temperatures of liquid argon). This is called the 0T (zero transistor) solution because no transistor is located on the calorimeter.

At Arizona we designed and built our rendition of the 0T Solution but with the capability to accommodate the cold GaAs preamp solution. Our Russian collaborators supplied silicon cold preamps for this test. But the performance of the 0T solution was already so good that we found it difficult to put full effort into the competing version. The noise levels from the two electronics versions were comparable and the other considerations argued forcefully for the 0T choice.

Loch and Savin analyzed this data with some suggestions and guidance by Rutherfoord. We got a lot of very nice performance results from this test. But it was all with electrons because we only had a prototype of the EM module.

Therefore in the summer of 1998 we conducted a test with our engineering prototypes of our FCal1 EM module and Toronto's FCal2 first hadronic module. We also constructed a "warm tailcatcher" just downstream of the cryostat. This was a crude iron/scintillator sandwich calorimeter used to estimate the energy leaking out of the FCal2 module. These engineering prototypes were each one quarter of 2π, i.e. a 90° section of the full module but had all the features of the actual modules, now fully designed but yet to be built. And by then all the electronics choices were made and early versions constructed. Again we built the accompanying electronics system but this time using components that the other liquid argon groups were also using in their test beam runs. Out of 2300 electrodes we had only one short. At the end of the run we decided to conduct a destructive test and ran the voltage up to 675 V (from the nominal 250 V). We developed three more shorts. This was a very satisfying result showing, again, that the electrode

concept is quite robust despite the exceptionally small gap of 250 μm.

The engineering prototype worked well so we changed almost nothing and proceeded with procurement for the actual modules. But the highlight of this test beam run was the performance parameters.

While the major thrust of the test beam run was to measure the response to hadrons, we nevertheless were interested in the electron response to see how well we might do with gammas from π°'s and to determine some fundamental parameters of the device such as the e/MIP and e/h ratios. We have measured electrons in earlier prototypes and are relatively confident we understand the EM performance for our new technology. We were pleasantly surprised when even the on-line results were a bit better than expected. Linearity is better than approximately 0.5%. These results are comparable to those from devices designed for precision calorimetry unhampered by the requirement of surviving the harsh forward region.

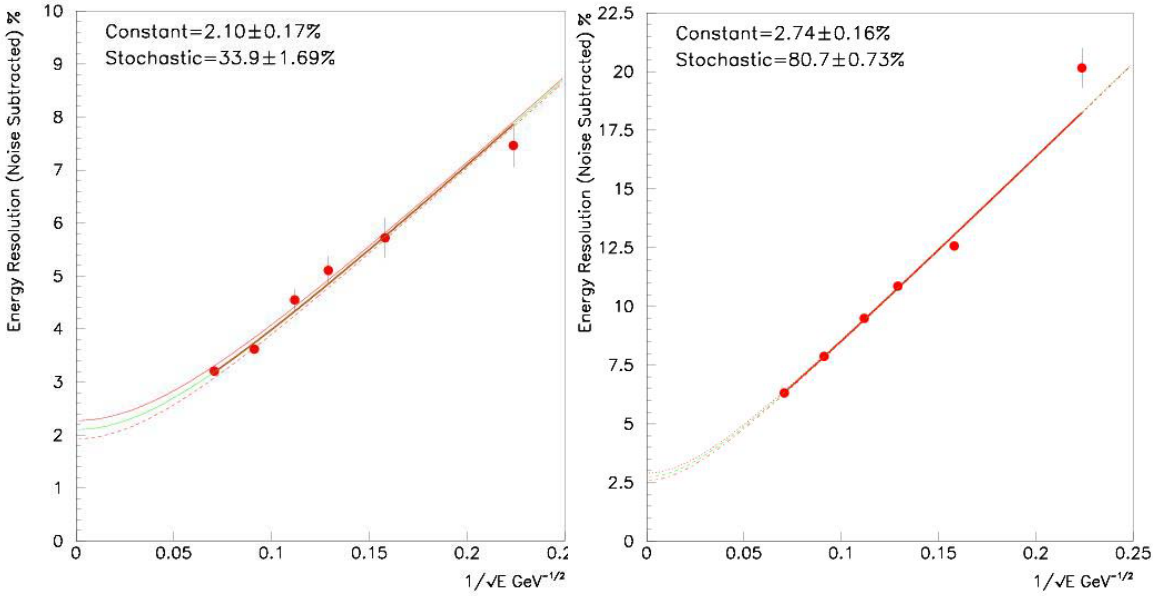

Figure III.3.19: Percent energy resolution versus 1/√E. Electron response is on the left and pion response on the right. Since this is a calorimeter designed for the highest energies, it is the constant term that is most interesting.

The electron energy resolution is shown in Figure III.3.19. Because our calibration system was precise only at the 3% level we didn't gain-correct any of our electronics channels which are expected to be uniform to better than 2%. Had we a more precise calibration system we might have made channel-to-channel gain corrections and improved the resolution a bit. It is possible that the constant term is dominated by the channel-to-channel electronics variations.

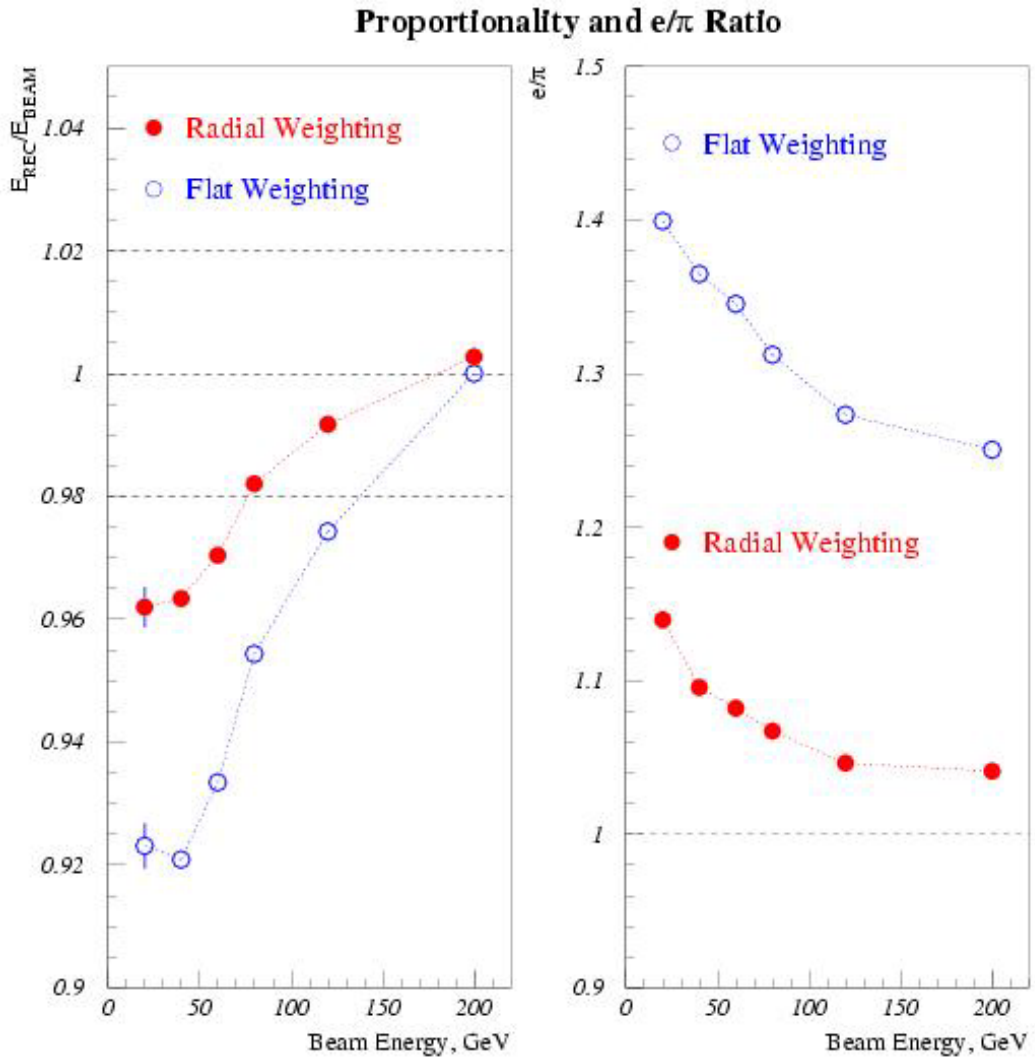

Figure III.3.20: Deviation from Proportionality on the left and e/π on the right with and without radial weighting. In each case radial weighting gives significantly improved results.

Savin invented a new hadronic weighting scheme which is simple and very intuitive. It differs from the famous H1 weighting scheme in that the weights do not vary from event to event and it is more appropriate to our geometry in that it works best with fine transverse segmentation but coarse longitudinal segmentation. For energy deposited along the axis of the shower a weight equivalent to the electron response is assigned. For channels away from the axis a larger weight is applied to boost the hadronic component up to the EM scale. Because we had a small amount of coherent noise, the weighting scheme applies a negative weight for very distant channels, providing an optimized coherent noise subtraction (which is very small, almost negligible). In ATLAS this distant noise contribution will be dominated by pileup noise which also has a coherent

component. The pion energy resolution obtained with this weighting scheme is shown on the right of Figure III.3.19. Note that the constant term is nearly the same as for electrons. This is surprisingly good performance. Our goal was a constant term of better than 7% and we have exceeded this goal by a rather large margin.

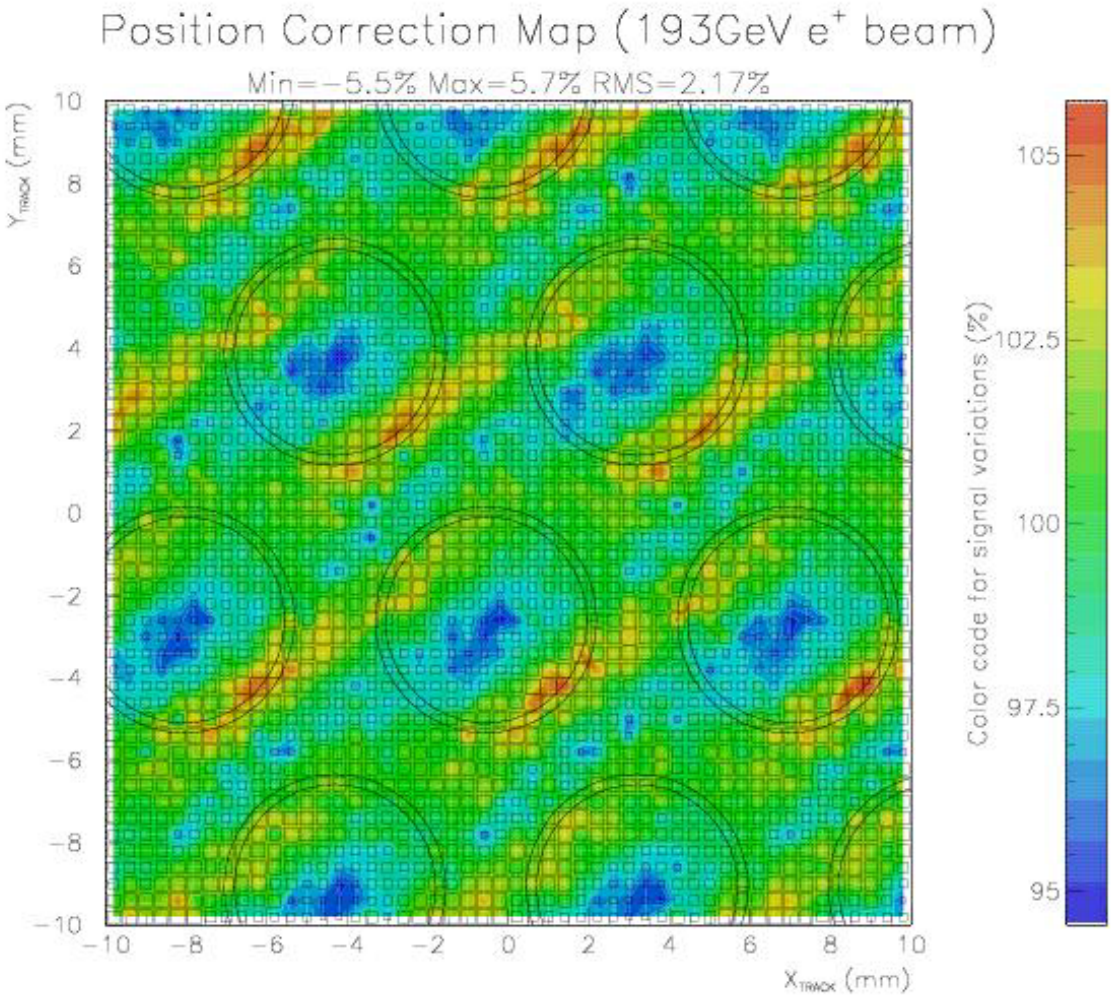

Figure III.3.21: Response variations across the face of the FCal1 module. Note the expanded scale to show the rather small variations.

This new weighting scheme also improves the linearity (or proportionality since the intercept should be at the origin) of the pion response. Figure III.3.20 shows the deviation from proportionality with 1) the usual (flat) weighting (using just an e/π correction) and 2) with Savin's new radial weighting scheme. Also shown is the e/π ratio without and with the new scheme. In all cases this rather logical scheme gives significantly improved performance. A description of this weighting scheme can be found in A.Savine, "Hadronic Energy Resolution Improvement in High Energy Physics", Proceedings of the IX International Conference on Calorimetry in High Energy Physics, Ed., B.Aubert, J.Colas, P.Nedelec, and L.Poggioli, Annecy, Frascati Physics Series

(2001).

Because the tube electrodes in our forward calorimeter have axis nearly parallel with the incident particles, there is the potential for channeling of particles down the low density gap, producing anomalously large signal. We didn't expect to see a very large effect because the gap is so narrow (250 μm), the Moliere radius is large (see Figure III.3.4), and the density of liquid Argon is not that low. But to test this possibility we used the precision mwpcs in the test beam to track electrons to the front face of the FCal1 module. Figure III.3.21 shows the response of the module to electrons as a function of impact point. The peak-to-peak variation in response is approximately ± 5.6 % and the rms is about 2.2 %. The lowest response occurs when an electron hits the center of a rod in the electrode and the maximum comes when the electron is aimed at the gap such that the shower tends to stay in the gap. Electrons in the test beam lie in a plane normal to the front face of the module and intersecting the plane of the front face in a line from lower left to upper right in the figure. This is why the contours tend to point in this direction. The energy resolution data shown in Figure III.3.19 has a position variation correction. The ATLAS accordion calorimeters also have a position dependent response variation and they correct for this effect as we do. However we won't be able to make such a correction in ATLAS because there is no tracking in front of the FCal (as opposed to the accordion) and the position determination from energy sharing in neighbor calorimeter channels, while excellent in the test beam, is compromised at high luminosity due to the pileup noise. But the forward calorimeter is designed to detect jets. Using EM showers observed in the test beam we have combined them with Pythia min bias events in a simulation of the EM energy in a jet and find that the position dependent contribution to the energy resolution washes out because several photons average over the position variation. The simulation results show that the EM energy resolution shown in Figure III.3.19 can be interpreted as the energy resolution for the EM portion of a jet.

Our most recent beam test is in progress as we write this progress report. It is called the "FCal Calibration Test Beam Run" because one of our goals is to determine the calibration constants we will use in ATLAS. When we first planned this test the final analog electronics was to be available and the electronics group was to operate their electronics for us as a part of their validation process. But the electronics is behind schedule and we were forced to use the "Mod 0" version of the electronics without the anticipated help. It was also planned that we would have inserted our modules into the cryostat support tube, a major step towards preparing the FCal for ATLAS. But it became apparent that difficulties and delays with the cryostat would force us to change this part of the plan too. We constructed a temporary support for the three modules and are now behind our final assembly schedule. But we anticipate catching up this fall.

Because the FCal is at small angles to the beam and because there is no tracking in front, the conventional in situ calibration schemes are difficult. So we rely, more than the other subsystems, on this test beam calibration. We are well aware of the experience of the D0 collaboration who found approximately 5% shift in calibration in going from test beam to collision hall so we are taking several precautions along the way. One is to keep the same calibration pulser board to use again when we are in place in the cavern.

Other goals of the test beam run are 2) to scan the inner (high |η|) edge of the FCal to determine how energy is lost down the beam pipe and how energy scatters to the other side. This latter (cross-over) effect gives a false E_T signal. And 3) we will repeat the "cold test" of last November in which the FCal1C module had 10 shorts (satisfactory to ATLAS but not acceptable to us).

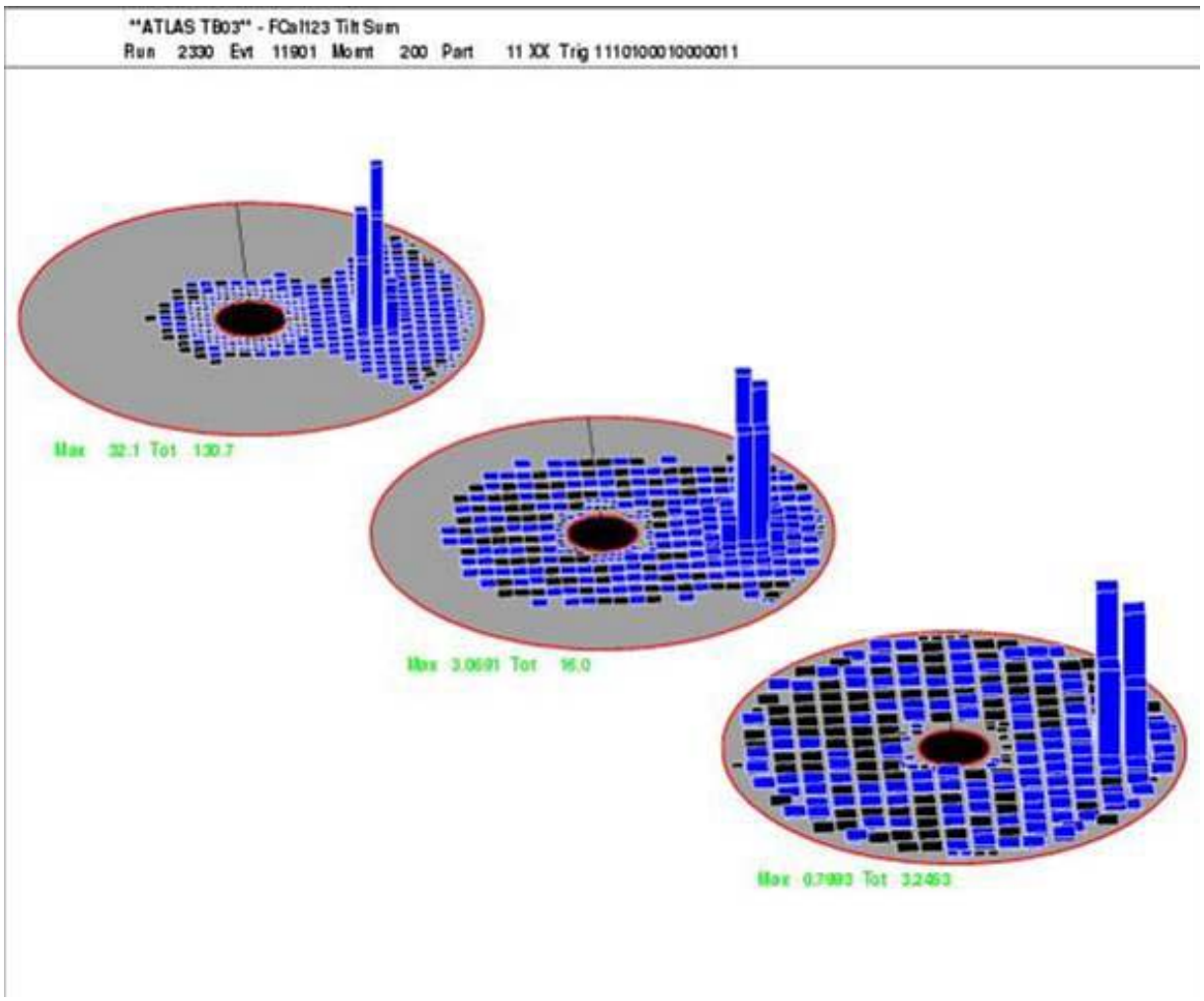

Figure III.3.22: Lego plots of energy deposit in the three FCal modules. FCal1 is at the upper left and FCal3 is at the lower right. Note that not all of FCal1 and FCal2 are instrumented.

Figure III.3.22 is a monitoring display written by Mike Shupe which shows energy deposit in each of the modules. Each lego represents a readout tile and the height of the lego is proportional to the energy deposit. (Each module has a different overall constant of proportionality for ease of viewing only.) Note that only parts of FCal1 and FCal2 are instrumented. This was because we did not have enough cabling and feedthroughs

available for this test. We were forced to purchase cables (pigtails) and bought all we could afford. But it is clear that we have encircled the beam hole so we can study the "cross-over" effect mentioned above and we have full coverage for showers in one quadrant, the region we used for the calibration data.

The display program can be used in many modes. In the one shown here we have accumulated several thousand events. So the transverse size of the energy deposit, particularly in FCal1, reflects the size of our beam spot which we purposely choose to be large so that we get roughly uniform illumination over at least one readout tile. Another convenient mode is to use it in "one-event-display" mode so that we can *see* single events. It is instructive to watch event after event in a mixed electron/hadron beam.

At this time we have accumulated a large data set (about 1 TeraByte including pulser and pedestal data) but only at the higher energies of 80 to 200 GeV. The sample includes both electrons and pions (we set the differential Cerenkov counter to identify pions and there is some separation of electrons via synchrotron radiation losses). But an accelerator magnet failure curtailed our planned run and we lost all of our anticipated low energy running. We requested and were granted an extension in September. The modules are now sitting quietly in the cryostat, still full of liquid Argon, and all of our beam counters, mwpcs, scintillator tail catcher, muon counter, electronics, and daq are in place awaiting the September run. We hope to pick up where we left off with little, if any, setup.

We have lots of preliminary data on linearity, energy resolution, etc. but a full analysis will take a long time because all the detailed data we take demands that we make optimal use of this information. For instance, this is the first time that we have taken seven (and sometimes up to 32) samples of the pulse from each channel. This requires that we understand the pulse shape in great detail. Reconstructing the pulse shape from our samples is already a challenge and we nearly have this in hand after some instructive but less than optimal attempts predicted strange features which disappear when the correct procedure is used. Using SPICE models of the electronics and detailed descriptions of the FCal modules, Rutherfoord made predictions of the pulse shape and amplitude (i.e. the calibration constants) ahead of the run. All the on-line analysis programs use these constants and, so far, we don't have sufficient precision to change this prediction and our precision is now at the 5% level. This encourages us to believe that we may be able to understand our calorimeter in enough detail to obtain a reliable calibration from this data. The multiple samples also require that we handle the electronics noise in an optimal way. Rutherfoord has calculated the autocorrelation function from the electronics model and theory and Loch has obtained it from the data. This allows another comparison which shows us in a sensitive way how well we understand our readout chain. So far we see that there is room for improvement but we are close.

While only seven sixteenths of FCal1C and five eights of FCal2C are read out, all channels can be connected to HV. This allowed us to repeat the "cold test" of last November, which we did while we were waiting for the accelerator to be repaired. We already knew there was one short in the instrumented portion of FCal1C which gave us some confidence that we had improved over the first cold test. When we applied HV to

the un-instrumented nine sixteenths of FCal1C no further shorts appeared. Needless to say we were pleased with this result, particularly Embry who spent so many weeks carefully re-cleaning the module after the first cold test.

In September we plan to take data from 60 GeV down to as low an energy as is practical, perhaps as low at 10 GeV.

Another feature of this test beam run is that we are using a "semi-on-line" analysis and monitoring program in the ATHENA framework, a prototype of the official ATLAS analysis framework. Loch has been using this framework for some time now and the version he prepared for the test beam is very impressive. Others in our group are determined to learn this framework with the short-term goal of analyzing our test beam data and, in the long-term, to be well positioned to analyze ATLAS data.

Mike Shupe monitored most of the runs as we took them and caught several problems quickly which we were able to fix. He has also performed preliminary analysis of a lot of the data as noted above. Savin also monitored the data for noise, cross-talk, and particle ID to make sure all was as expected. When he found small anomalies we either were able to understand them or correct them.

All indications are that this Calibration Test Beam Run is a success, …. So far.

III.3.12 FCal Project Management

More so than with other ATLAS construction projects the FCal requires a lot of management. This management falls into several categories.

Arizona leads the ATLAS FCal project. Included in the collaboration are two Canadian universities, Carleton and Toronto, and one Russian institute, ITEP/Moscow. These report to us and we represent the FCal project within ATLAS. John Rutherfoord heads this organization and Leif Shaver is the FCal Technical Coordinator. We arrange and chair the bi-monthly FCal meetings and we hold almost weekly engineering conference calls to thrash out details. We are responsible for financial reporting, progress reports, schedules, milestones, and for anticipating and warning of glitches, if there are any. We also occasionally ask for help and the ATLAS collaboration has been very generous. For instance we received lots of help when the FCal1C module was dropped from the fork-lift truck. And when the electronics group was not ready with their final front end electronics for our present test beam run, they volunteered experts from various labs who gave us lots of valuable advice.

Arizona is also the technical and intellectual leader of the FCal collaboration. However in recent years our Canadian and Russian colleagues have become more than competent and some are now playing impressive roles within the group. The FCal2 and FCal3 modules have turned out to be excellent devices and the credit goes to our foreign friends.

US ATLAS has evolved a management structure to oversee the US contribution to the ATLAS experiment. Starting from scratch with almost no experience in managing large projects, the Project Office at Brookhaven has evolved in fits and starts. Since we're almost across the continent from them, communication is vital as their views of their role changes.

While the FCal project within the US is not one of the larger contributions to ATLAS, it nevertheless requires crisp management appropriate to the scale of the effort. We have had five or six technical people working on various phases of the project at the peak of production. In addition there are physicists and students playing key roles. And while the FCal is not a particularly challenging device to construct (one of its virtues is its relative simplicity) there are many parts requiring several operations and a lot of record-keeping so that we can track and evaluate progress. All of this work requires advanced planning and a lot of oversight. This is largely worked out and implemented. A large remaining job is to organize and store all our production data and records in an official data base for access by any ATLAS collaborator.

III.3.13 FCal Software Work

The Arizona group is heavily committed to the FCal construction project but is looking forward to the physics. Over the last few years we have been struggling to find a way to get more involved in the development of the analysis software so that we will be well positioned to analyze the first data from ATLAS. So far our requests to the DOE for help with this goal have not been successful. Thus our involvement with software development has been modest. Nevertheless it has been significant.

Peter Loch produced the geometry description of the FCal using the GEANT4 Simulation Toolkit, and delivered the reconstruction program for the FCal in the standard ATLAS object-oriented software framework ATHENA. He is also a member of the ATLAS/GEANT4 Physics Validation Project, for which he reported results at the CALOR2002 Conference and in ATLAS collaboration-wide plenary meetings.

Recent software activities concentrate on the cluster and jet reconstruction. Here important contributions from Arizona are support software for object navigation, developed in close collaboration with S.Rajagopalan and H.Ma at BNL, and a complete re-design of the jet reconstruction software. The latter effort originally started at a small workshop in Tucson in Summer 2001, initiated and organized by Loch., and is now nearing completion. The working group includes ATLAS colleagues from the Enrico Fermi Institute at Chicago, ANL, and TRIUMF. In the course of this project Arizona assumed sole or shared responsibilities for several software packages in ATHENA.

Arizona also contributed significantly to the first ATLAS Calorimeter Calibration Workshop, held at Ringberg Castle, Germany, in July of 2002. Loch is a member of the Physics Advisory Committee and was responsible for the agenda. This workshop was the first in a planned sequence of similar meetings, for which we will continue to contribute.

Near future plans for contributions to ATLAS software include a complete re-design of the calorimeter reconstruction software, a project in which we already established a strong lead position. This is reflected in the fact that Loch is now the Reconstruction Software Coordinator for the ATLAS Liquid Argon Calorimeters, therefore also continuing as a member of the ATLAS Liquid Argon Software Steering Group. It is expected to not only improve the efficiency of the reconstruction software in this project, but also to add important features like 3-D cell clustering. This particular effort was initiated at Arizona and we carry the main responsibility for software design and algorithms.

The present ATLAS test beam activity concentrates on the FCal Calibration Test Beam Run as noted above, followed by the Combined Test Beam Run scheduled for summer 2004. This run is sometimes called the "Crack Studies" because it will allow us to study the transition between the Accordion EM calorimeter followed by the Hadronic Endcap Calorimeter and the FCal. Arizona has taken the lead in planning for this run and Loch is expected to be the run coordinator.